Development of a Laser Based Surface Profilometer Using the Principle of Optical Triangulation

by

David Collins, BEng

This thesis is submitted as the fulfilment for the requirement of the award of degree of

MASTER OF ENGINEERING (MEng)

by research from

DUBLIN CITY UNIVERSITY

Supervisors: Dr. Dermot Brabazon
Professor Mohie El Baradie

August 2005

Table of Contents

Table of Figures

List of Tables

Abstract

The metrology industry is constantly looking for new ways to accurately and quickly inspect and digitise surface topographies including the calculation of surface roughness parameters and generating point clouds (a collection of 3-dimensional points which describe a surface or surfaces) for modelling or reverse engineering purposes. Many types of profilometer systems currently exist and the past decade has seen the rise in popularity of optical based systems, however most optical profilometers are expensive to purchase and to maintain. The development of optical profilometers can also be exceptionally complex depending on the type of system and its fragility may not make it suitable for most workshop or factory floor applications. This project covers the development of a profilometer using the principle of optical triangulation.

The developed system has a scanning table area of 200 by 120 millimetres and a vertical measurement range of five millimetres. The position of the laser sensor above the target surface also has an adjustable range of 15 millimetres. A control program was developed to automatically scan user selected part and surface areas. This new system was characterised in terms of dimensional accuracy. The maximum cosine error of the system was measured at 0.07°. Dynamic accuracy of the system was measured at 2μm in the Z-axis (height) and at approximately 10μm in the X and Y axes. Good dimensional correlation between scanned parts (coins, screws, washers, and fibre optic lens moulds) were achieved. Testing of the system will be also discussed, including the limitations of the profilometer and possible improvements to the system.

Chapter 1 Introduction

The main aim of all manufacturing processes is to produce a required quantity of goods, which have a specified level of quality. Surface measurement systems have been around for over half a century and until about 20 years ago practically the whole of this industry was based on contact style probe systems. With the development of more advanced electronics and signal processing, high quality optical components and the refinement of lasers and focused light technology, it has become possible to employ sophisticated vision equipment as a metrology tool.

The most basic of these systems is possibly the triangulation method; a design on which the system developed in this thesis is based. Triangulation is a very simple approach to the surface measurement problem, yet it can be highly effective. Further research on laser triangulation systems, specifically in the areas of advanced image acquisition, beam scanning/sweeping, and intelligent optics is of vital importance to the metrology industry to further increase the performance of optical metrology systems.

The first section in this thesis will discuss many different types of surface inspection and measurement techniques as well as their advantages and limitations. Various methods and techniques for deflecting and moving the laser beam over the target surface will be described.

The second section of the thesis will describe in detail the development, construction, and testing of a laser profilometer capable of a vertical resolution of $\approx 2\mu m$.

1.1 Surface roughness & defect inspection

Why measure surface roughness? Well, for many engineering applications the type of surface texture is closely related to the function, especially if that surface will come into moving contact with another surface. A very smooth surface is not necessarily the most desirable surface finish, and it is important to look at a number of factors before deciding on the surface finish of a component.

A classic example is the effect of surface roughness on lubrication - for efficient lubrication to take place between two parts a film of oil must be maintained between them and it has been found that the roughness valleys are essential. Another example are lip seals, sometimes used on motor vehicle axles. The seal is interposed between the differential housing and brake mechanism. If the finish on the shaft is too smooth it may allow lubricant to escape under the seal, while on the other hand, if it is too rough, it may cause abrasion of the seal, and lead to its failure.

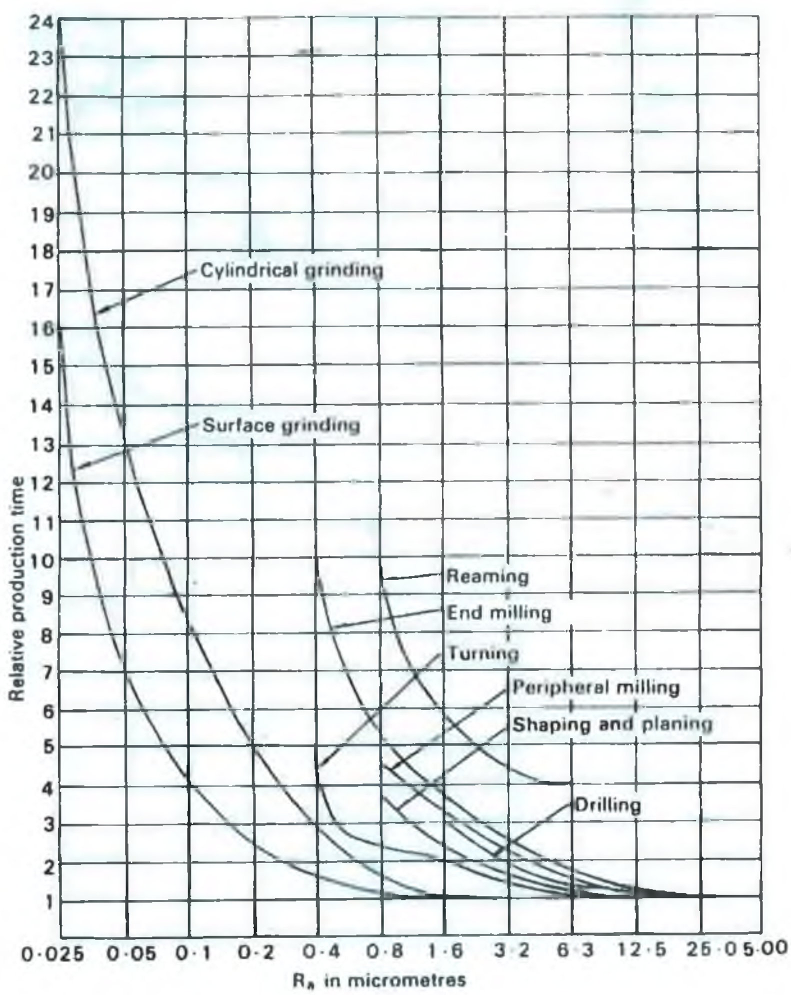

Figure 1.1 - Relative production time necessary to produce different surface finishes[1]

The time and operation required to achieve a better surface finish can lead to increased cost, see figure 1.1 and table 1.1. It may not be cost effective (or necessary) to produce a part with a high surface finish. Improving a surface finish more than is necessary adds considerably to a components production time and cost, while it may only fractionally improve its performance.

To measure the finish or texture of a surface requires inspection, where all deviations of a component from its design specification can be detected. Depending on the results from the surface measurements it may be necessary to alter the production process. Surface texture is like the fingerprint of manufacture and it is an important means of control. Examination of the texture of a machined surface will often reveal tool or machine defects, incorrect machine or tool settings, or deficient operating procedures. For example, tool wear, material stress, and incorrect machining conditions all leave their mark on a surface. In order to alter the process, the cause of each fault or flaw must be identified, and then corrected.

Generally speaking, most surfaces produced by common manufacturing processes have a surface texture that is regular over most of its area. This means that a profile recorded from a line (achieved either through stylus or laser triangulation) across the surface will differ only in detail from a parallel-recorded line a small distance away. The parallelism of these two lines is important due to the direction of the surface's lay. A surface's lay refers to the predominant nature of the surfaces texture and is usually a function of the particular production method used. The geometry of the lay is made up of striations or peaks and valleys aligned in the direction that the cutting tool was drawn across the surface and can take on a number of forms.

Most of the time, a single trace along a line or track across a surface is enough to obtain a profile that is typical of that surface, and thus assess the surface roughness. Occasionally however, it is necessary to calculate the surface roughness over an entire area. It is possible to measure surface texture across a large area using a stylus, however it can get quite tedious as many traces need to be recorded, each one only spaced a fraction from the last. Similarly, triangulation scanning of such a surface may appear equally tedious, however, because it is a non-contact technique, it is possible to scan very quickly, the only limiting factors being the sampling rate, mechanical integrity of the scanning rig, and the speed at which either the sample or laser beam can be moved. As compared with a contact type system, an optical triangulation system will be able to scan much faster across the surface, however the relative speeds of both systems will vary depending on the complexity of the surface, scan area, and required resolution for example.

Table 1.1 - Machining roughness characterisation for various methods of material removal[1]

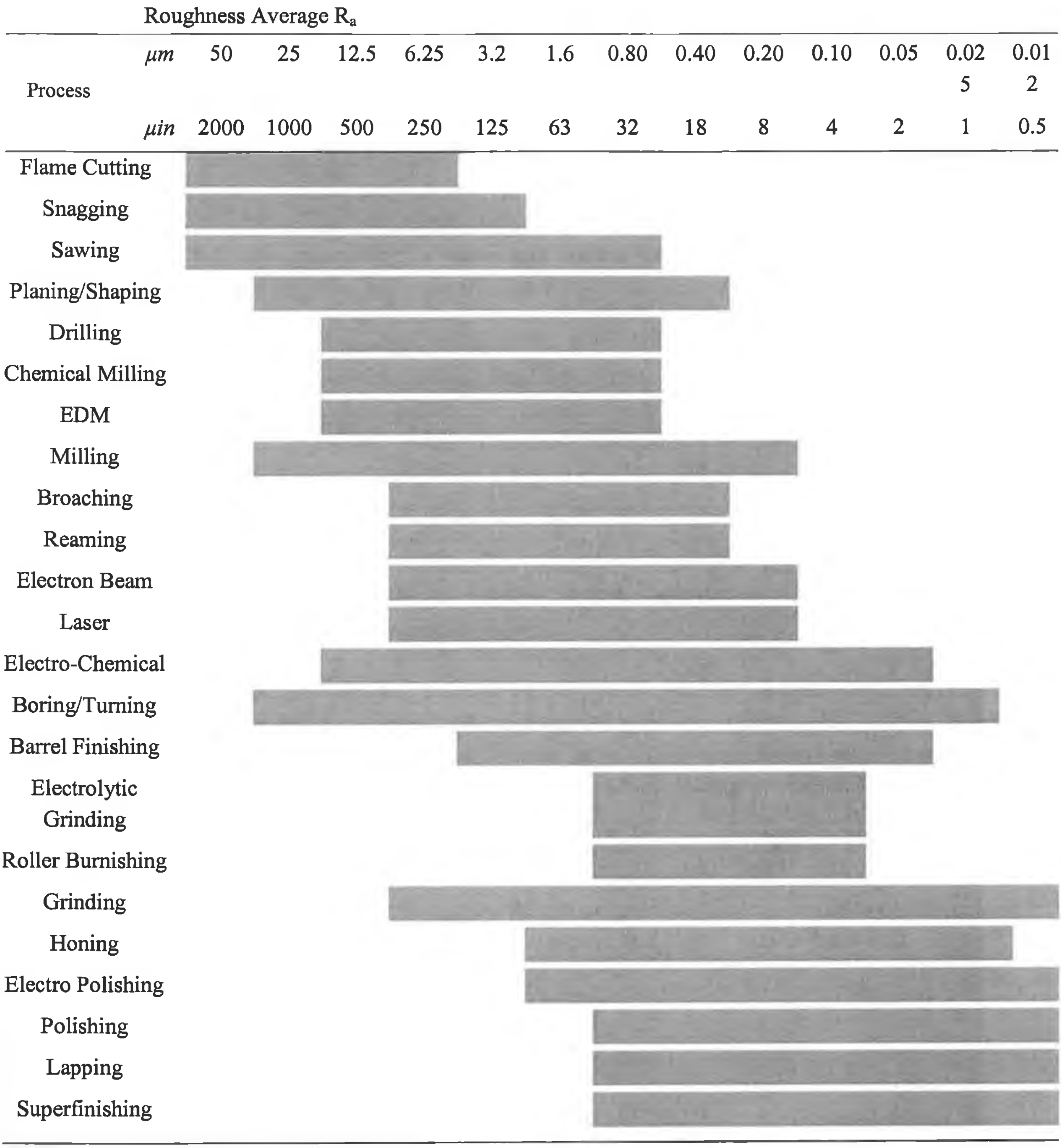

1.2 Stylus based surface profiling

It has been said of surface profiling that in order "to see where we are going next, we must know where we have been"[2]. The very first stylus type profiling instrument was described by Schmaltz in 1936[2,3].

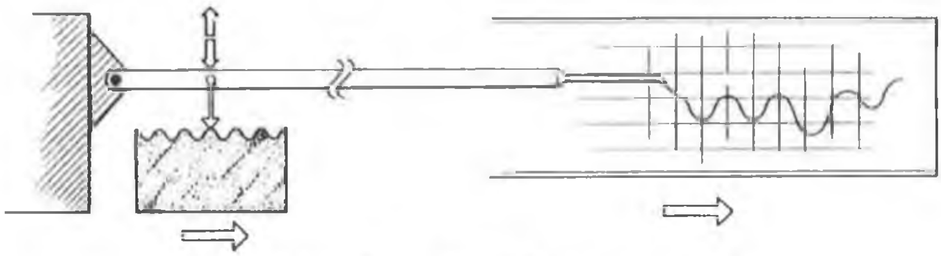

Figure 1.2 - A simple profiling instrument[1]

A simple contact inspection instrument is illustrated in figure 1.2. The instrument itself is made up of a lever, which has a pivot at one end. At the end of the lever is a stylus, which is used to trace the profile of the target surface. On the opposite end (pivoted end) of the lever is a plotting device or pen. The vertical 'excursions' of the stylus are recorded through the pen at a greatly increased magnification (for example x5000). By moving the stylus across the surface at a constant speed and by moving the paper at a higher speed (so that the individual surface irregularities can be separated clearly) it is possible to accurately map the various surface profiles, see figure 1.3.

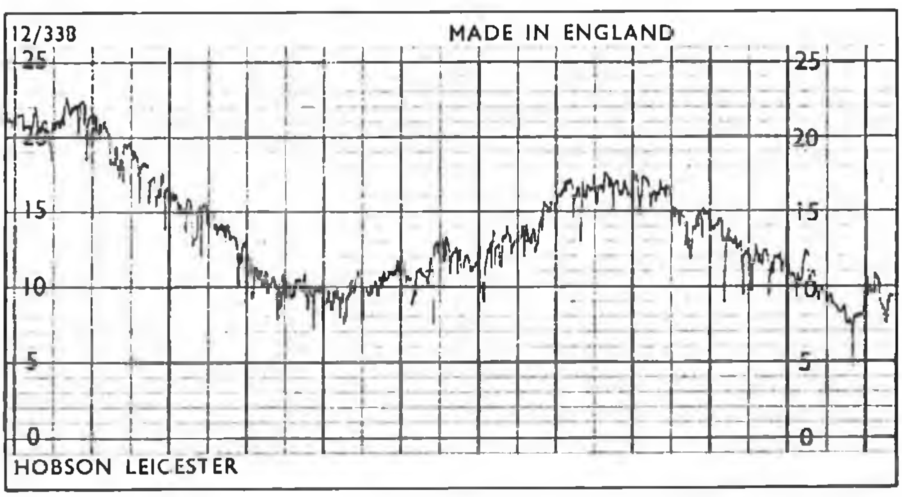

Figure 1.3 - Typical surface profile graph[1]

From the late 1930's onwards, the Rank-Taylor-Hobson (RTH) Talysurf instruments, models 1 to 6, epitomised the progress of the traditional surface roughness profilometer and together with their two sister devices, the Form Talysurf and the Talystep, they embraced the direction of the evolution of profiling stylus devices.

The Talystep was essentially designed for step height measurements and it made a new stride towards low amplitude, low wavelength measurement capability. The Form Talysurf evolved in a different direction, covering macroscopic profiles (form measurement) – its unique feature being the ability to measure both roughness and form in one pass due to the use of an interferometric transducer, conferring high range and resolution simultaneously.

Further advances in the stylus profilometer are still possible however. It is possible to reduce the flank slopes of the styli by reducing the included angle of the stylus cone, but this would have to be a trade-off with the tip radius. What has happened though is that the vertical resolution has improved significantly through the improvement of active filtering and the overall design of the inspection device reducing both electrical and mechanical noise. In addition, more powerful software (higher acquisition and sampling rates for example) is being developed year-by-year further increasing the performance of the latest contact styli instruments. Inspection requirements beyond the abilities of the smallest styli (typically with tip radii of around 0.1μm) are being explored using devices such as Scanning Tunnelling Microscopes (STM) and Atomic Force Microscopes (AFM)[4].

National Physical Laboratory's (NPL) Nanosurf-2 was the successor to the earlier profilometer, the Nanosurf-1 which itself came about through the need to inspect the internal bore surfaces of the mirrors on the Wolter X-Ray microscope[5]. The construction of the Nanosurf-1 included a Talystep head fitted with a stylus, which was offset from the axis of the transducer. The head was fitted to a precision slide-way/carriage assembly and could provide linear scans up to 15mm long. The Nanosurf-2 was constructed using the experience base provided by the Nanosurf-1 however it was fully optimised for stability through insensitivity to thermal, vibrational, and other extraneous inputs that would be detrimental to the systems performance. The head assembly again, was essentially a Talystep head, however many of the parts were replaced with identical parts constructed from Invar, Zerodur, and fused silica. The reference loop of the instrument was also contained mainly in Zerodur (almost zero rate of thermal expansion) and was kept as short as possible. A diamond (conical shape) stylus was interfaced with the transducer by a thin walled silica tube (in place of the aluminium tube used on the Nanosurf-1)[4]. The inspection and levelling table was mounted kinematically on a precision specimen carriage. In turn, the carriage was supported by dry polymeric bearing pads.

Horizontal motion of the carriage was achieved through the use of a remotely mounted DC motor linked to a micrometer head. The carriage was not moved directly however. Motion was achieved via an intermediate carriage, which forms a non-influencing drive system. The stylus was brought into contact with the target surface though the use of another micrometer, which adjusted the height of the measuring head.

Using this instrument, the typical measured noise level during stationary operation was reported to be in the region of 0.05nm rms and noise levels during dynamic tests were in the region of 0.084nm[4]. Tests were also carried out on the effects of mechanical and airborne vibration and it was shown that for an airborne shockwave, the Nanosurf-2 system was 30 times less sensitive than the Talystep system. Thermal step tests of the transducer showed a response of around $50nmK^{-1}$ while the linear slide showed a height deviation of 1.5nm during successive start-ups. In addition, the slide showed a reproducibility of 1.5nm rms over successive 40mm long scans, while scans of 5mm showed a reproducibility of better than 0.25nm rms.

The ultimate tool in stylus profilometry is the atomic force microscope. It records surface profile by measuring the interaction forces between the target surface and the instrument tip, the gap between the two being only around 1nm. Depending on the surface, forces may be either repulsive or attractive. The use of extremely fine, delicate tips (such as ion sharpened diamond styli) is possible as the force acting on the tip is only of the order of 10^{-10}N. To acquire an image the microscope raster-scans the probe over the sample while measuring the local load on the tip. The resulting image can be represented on a television screen and it consists of many rows or lines of information placed one above the other. In its repulsive "contact" mode, the instrument lightly touches a tip at the end of a leaf spring or "cantilever" to the sample. As a raster-scan drags the tip over the sample, some sort of detection apparatus measures the vertical deflection of the cantilever, which indicates the local sample height. Thus, in contact mode the AFM measures hard-sphere repulsion forces between the tip and sample. In non-contact mode, the AFM derives topographic images from measurements of attractive forces; the tip does not touch the sample. AFMs can achieve a resolution of 10pm, and unlike electron microscopes, can image samples in air and under liquids. In principle, AFM resembles the record player as well as the stylus profilometer. However, AFM incorporates a number of refinements that enable it to achieve atomic-scale resolution[6,7]:

- Sensitive detection
  AFMs can generally measure the vertical deflection of the cantilever with picometer resolution. To achieve this most AFMs today use an optical lever, a device that achieves resolution comparable to an interferometer while remaining inexpensive and easy to use

- Flexible cantilevers
  A high flexibility stylus exerts lower downward forces on the sample, resulting in less distortion and damage while scanning, see figure 1.2c. For this reason AFM cantilevers generally have spring constants of about 0.1 N/m and very high resonant frequencies to respond quickly to surface topography changes. Two 100μm long V-shaped cantilevers are shown in figure 1.4.

- Sharp tips

  AFMs generally use one of four types of tip, three of them are shown in figure 1.5. The standard tip is a 3 µm tall pyramid with a ~30 nm end radius. The electron-beam-deposited (EBD) tip can image steep, high structures by scanning force microscopy[8]. Improvements on this have been achieved with an electron-beam-induced deposit of carbonaceous material made by pointing a normal tip straight into the electron beam of a scanning electron microscope. The Supertip (not shown here) offers a higher aspect ratio (it is long and thin, good for probing pits and crevices) and sometimes a better end radius than the normal tip. Finally, Park Scientific Instruments offers the Ultralever tip, which is based on an improved microlithography process. Ultralevers offer a high aspect ratio typically with a ~10 nm end radius.

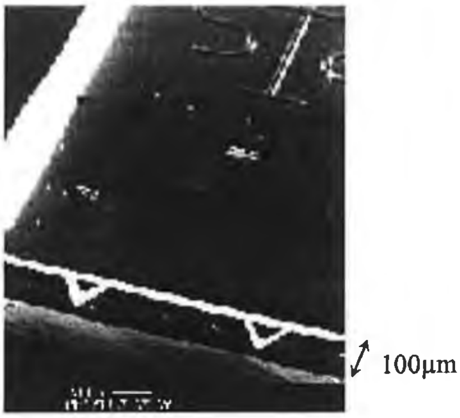

Figure 1.4 - Electron micrograph of two 100µm long V-shaped cantilevers[9]

(a) (b) (c)

Figure 1.5 - (a) Standard tip (b) EBD tip (c) Ultralever tip[9]

- High-resolution tip-sample positioning

  Piezoceramics make it possible to create three-dimensional positioning devices of arbitrarily high precision. Most scanned-probe microscopes use tube-shaped piezoceramics because they combine a simple one-piece construction with high stability and large scan range. Four electrodes cover the outer surface of the tube, while a single electrode covers the inner surface. Application of voltages to one or more of the electrodes causes the tube to bend or stretch thus moving the sample.

- Force feedback

  The presence of a feedback loop is one of the subtler differences between AFMs and older stylus-based instruments such as stylus profilometers. The AFM not only measures the force on the sample but also regulates it, allowing acquisition of images at very low forces. The feedback loop consists of the tube scanner that controls the height of the entire sample; the cantilever and optical lever, which measures the local height of the sample; and a feedback circuit that attempts to keep the cantilever deflection constant by adjusting the voltage applied to the scanner.

One point of interest: the faster the feedback loop can correct deviations of the cantilever deflection, the faster the AFM can acquire images; therefore, a well-constructed feedback loop is essential to microscope performance. AFM feedback loops tend to have a bandwidth of about 10 kHz, resulting in fast image acquisition times[9].

1.3 Contact vs non-contact inspection

There are a number of advantages and disadvantages associated with contact and non-contact measurement or inspection systems[11,12].The basic fundamental difference between contact and non-contact measurement is that contact gauging instruments measure what they can touch, while non-contact gauging instruments measure what they can 'see'. Examples of equipment used in contact measurement include callipers, micrometers, or CMM (Coordinate Measuring Machine) equipment. Each of these must touch the part in order to measure it. Non-contact measurement sensors usually involve the use of optical sensors (such as CMOS or CCD cameras) and/or lasers. Typical machine vision systems have a video camera on the product line, which captures images of each product, sending them to a computer for analysis. Laser sensor systems use diffusely reflected light from the part to measure features on a component. In order to avoid ambiguity, the word reflection used in the context of reflected laser light is to be taken as diffuse reflection rather than specular reflection unless otherwise stated.

One concern for non-contact measurement is whether or not it is rugged enough for use in the manufacturing or production environment. Also, if the part or surface is covered with grease, dirt, or fluids (such as coolant), this may also create a considerable problem for non-contact measurement. Contact gauging may be more appropriate in a situation such as this. Generally speaking, contact gauging is far more rugged than non-contact gauging. Rod Leehy, Quality Engineer at Nypro Inc[11] - *"A contact machine might be more robust to go out to the manufacturing environment...although vision is used on the floor. Non-contact sees a piece of dirt and says that's part of the part...you can pick up stray points and get bogus readings with vision systems a lot easier than you can with contact because it's not actually physically touching something"*. Having said this however, due to the harsh conditions, which are found in some industrial environments, in addition to the continuous motion or fluctuations in products (size, orientation, etc) on the line, non-contact inspection systems are often preferable[13].

Charles Seifert of Metrology Products Group, GSI Lumonics, comments on the use of non-contact equipment on manufacturing lines with constant product changeover[11] - *"If the line changes product all the time, then there's a large advantage to using laser and non-contact. It's more apt to be adapted to product changeover. Contact gauging requires a lot of setup and calibration to change over and, if not, then a lot of design went into it, and that's very expensive"*.

Touch trigger probes have become very advanced, in terms of both probe technology, and also through the use of powerful software packages. Modern styli can have contact pressures of less than 10g and can be used to measure soft materials without damaging the model or the pattern that is being scanned. In addition, the tip radius of a typical CMM ball stylus can be as low as 0.3mm and pointed styli can have tip radii as low as 0.1mm. This virtually eliminates problems associated with sharp corners that can sometimes be a major stumbling block for contact probe systems. When used with a fine step over distance, the combination of a small styli and a low contact force means that a user can collect highly accurate data from a range of complex surfaces.

In comparison, laser-scanning (or indeed other methods of optical scanning) systems may have trouble with such complex surfaces. Deep or near vertical faces present a huge problem for laser systems, especially when the depth of the surface is outside the measuring range of the device. The scanned data often requires extensive post-capture processing in order to generate workable data, and although this may improve the overall quality of the recorded information, it is usually at the expense of accuracy and loss of sharpness on pointed geometries or corners. For optimum operation, the laser head needs to be aligned perfectly perpendicular to the target surface – this is suitable for surfaces of low relief, but for structured surfaces or steep vertical faces the laser head should be re-aligned and re-datumed in order to collect accurate data. Generally speaking, for a misalignment of 5° between the laser and target surface, the error influence will be around 0.05% of the measuring range. This increases to 0.12% for a 15° misalignment, and 0.5% for 30°[11]. A further disadvantage of laser-based systems is the need to remove 'rogue' points which usually is not necessary when using a contact probe. In addition, most laser-based scanning requires the user to setup a fixed grid format prior to scanning or digitising a surface.

Contact measurement or inspection is acceptable for rugged materials such as steel. Unlike more fragile materials and components, steel will not be indented or damaged when probes touch it. However, if the working material or part is delicate, such as an electronic component, then non-contact measurement may be more suitable. It is also important to note that non-contact measurement of such a part is ideal from the point of speed. High volumes of small parts can be measured very quickly using non-contact equipment. According to Stephen Kress of Cognex Corp, spark plugs, gaskets, syringes, contact lenses, bottle caps, and tips of ballpoint pens are some examples of products that are ideally suited for non-contact inspection. Each of these products is high volume, and so requires rapid measurement. Contact gauging would be unsuitable, as it would disrupt the flow of the manufacturing process.

Optical sensors and non-contact techniques are finding greater applications for inspection tasks, not just because of their non-contact nature, but also due to their high response speed, excellent resolution, and ever increasing ruggedness[11].

1.4 Optical interferometry

Interference is the term given to the phenomenon by which light waves (in this case) interact with one another both constructively and destructively producing an intensity maximum or minimum of the resultant wave respectively[32,33]. Collectively, the distribution of these fringes is called an interference pattern, the bright regions occurring where the waves add together to produce an intensity maximum, and the dark regions indicate areas of intensity minimum[34,35]. Optical interferometers employ a 'common path' method, where two interfering beams are reflected from different parts of the target surface thus making the interferometer sensitive to vertical displacement[23]. Using interferometric techniques, the required sensitivity to the variations in height of the target surface can be measured by gauging the path difference between the two interfering beams. This in itself will vary according to the profile of the surface as the interference beams move across it. The parameters which bound the operation of this type of system in measurement of surface roughness depends on the wavelength of the light used, and the numerical aperture of the probe beam optics. The longest surface wavelength across the target surface that can be measured depends on the optical configuration of the measurement instrument.

Optical interferometry provides an extremely powerful tool for the measurement of highly finished surface profiles, however care must be taken in the interpretation of the recorded results, as they are directly dependant on the energy distribution within the interfering beams and the actual characteristics of the surface roughness under examination. The 'common path' design of these instruments makes them relatively insensitive to environmental conditions enabling high measurement stability while also making them simple to apply in a practical sense.

1.4.1 Laser and white light interferometry

Interferometry is an extremely powerful tool for optical measurements[16,17]. Currently most interferometry is performed using a laser as the light source. The primary reason for this is that the long coherence length of laser light makes it easy to obtain interference fringes and interferometer path lengths no longer have to be matched as they do if a short coherence length (white light source) is used. The ease with which interference fringes are obtained when a white light source is used is both good and bad. It is good that it is easy to find laser light interference fringes, but it can be bad in that it can be too easy to obtain interference fringes and any stray reflections will give spurious interference fringes, which can result in incorrect measurements. The principle behind interferometry is not a new technology - it is a combination of older white light interferometry techniques and modern electronics, computers, and software to analyse, filter and improve the quality of the acquired data. This has produced extremely powerful measurement tools, which can accurately measure and inspect objects and surfaces.

The shape of an object can be measured by means of a white light interferometer. White light from a source is collected by a lens and is passed through a beam splitter where it is divided into two beams - one beam is directed towards a reference mirror and the other towards an object mirror. The reflected beams are brought together and the resulting beam is displayed on a screen, see figure 1.6.

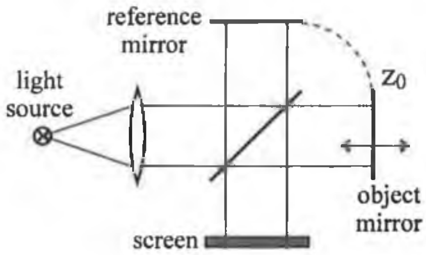

Figure 1.6 - Typical setup of a Michelson interferometer

If the object mirror is moved on its z-axis the light intensity on the screen will vary. The modulation of the intensity is strongest when the light waves superimpose coherently, this is given as position z_0. Light from the object and reference mirrors takes the same time to reach this point and it lies in the reference plane. White light interference appears if the object mirror lies in the position z_0 or its immediate locality. The range in which the light interference may be observed is determined by the size of the coherence band of the light source. For example, thermic light sources have short coherence bands of approximately 3μm, while on the other hand the coherence bands of lasers range from a few centimetres to several kilometres. To use this technique to inspect surfaces the object mirror is replaced by the target surface (see figure 1.7). Coherent light is reflected from the diffuse surface and the intensity distribution is displayed on the screen as speckle. Although speckle is a typical effect for laser illumination, it can also be achieved by white light, once the condition of coherence is fulfilled - this condition of sufficient temporal coherence is achieved if the target surface roughness is smaller than the coherence length (band) of the light source. To fulfil the condition for spatial coherence, the coherence area on the target surface must be larger than the area contributing to one speckle.

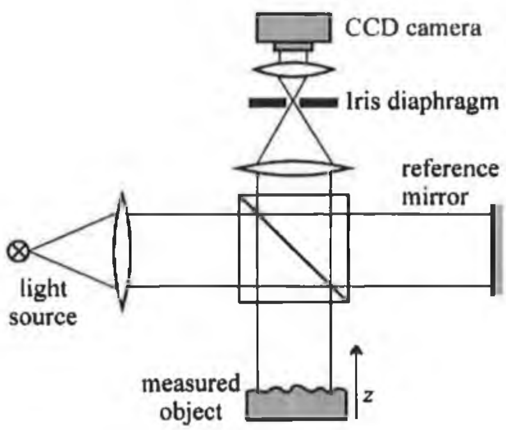

Figure 1.7 - Interferometer setup for profile height measurement

Like the object mirror, if the target surface is moved on its z-axis so that it passes the reference plane each particular speckle will display the intensity modulation as described earlier. The speckle intensity is modulated with the period of $\frac{1}{2}.\lambda_S$ where λ_S is the mean wavelength of the white light source. The image is continuously recorded and processed during the measurement by a CCD camera. As the target surface is moved in its z-axis, each position at z_0 is recorded. This value together with the known coordinates (x,y) of the pixel describes the geometrical position of each recorded point on the measured surface The collection of all these points being the geometrical shape of the surface itself. By processing this data it is possible to generate a 3D image of the scanned surface.

Currently, one of the leading innovations in laser interferometry is the Conoscan 3000 produced by Optimet of Danvers, MA[18,19]. Illumination of a 3-dimensional object yields a characteristic wave front that is determined by the topography of the object, however ordinary cameras are not phase-sensitive, thus they can only capture 2-dimensional images. Recent progress in surface scanning technology by a team of scientists at Cal Tech University has led to the development of a new and revolutionary type of laser scanning measurement system called conoscopic holography, discussed below.

It is a non-contact 3-dimensional surface measurement technique and can create extremely precise 3-dimensional digital images of virtually any surface, including previously difficult to measure components. It can do this at very high speeds and at standoff distances once considered totally unfeasible. It is suitable for measuring surfaces with a roughness, R_a, down to 0.5μm and is also vibration insensitive.

In classical holography, an interference pattern is formed between a reference beam and an object beam using a coherent light source. The two beams propagate at the same velocity but follow two different geometrical paths, creating a Gabor Zone Lens (GZL). An older technique using holographic interferometry made use of the wave (amplitude and phase) pattern emanating from the target object by combining it with an off-axis carrier wave. The interference of these two coherent wave fronts could be then recorded on a photographic plate. In order to measure surface displacement (roughness), two such wave patterns must be recorded when the object is in its original and displaced states. These two patterns are then combined to give and interference fringe pattern or interferogram. The fringe patterns represent surface contours of equal displacement. Each successive fringe pattern is actually a change in the displacement of the object, equal to approximately half the wavelength of the incident light source used during the recording process. By far, the biggest downfall of this technique was its inability to measure displacements on different planes.

However, during conoscopic holography, the two beams are replaced by the ordinary and extraordinary components of a single beam traversing a uni-axial crystal. It is an incoherent and collinear interferometric technique. This has the ability to produce holograms even with incoherent light whose fringe patterns can be measured very precisely to determine the exact distance to the point measured, such as on a component (i.e., the absolute distance to any point is retrieved by counting the fringes in the interferogram – this can be done on a CCD detector or camera by placing the appropriate optics before and after the crystal).

This idea has been marketed with the Conoscan 3000. The Conoscan 3000 has the ability to measure the X, Y and Z components of a part, analysing in detail it's angles and radii, and it can do this with practically any material, rubber, plastics, fabrics, and shiny metallic parts. The system can measure blind holes with internal cross piping, tiny radii, or even steep angles and intricate contours. What sets the Conoprobe apart from other holographic systems, is that it is collinear, rather than having object and reference beams that follow separate paths. This is what enables the probe to measure intricate features. The probe can measure up to 700 points per second whilst in motion[18].

During most scanning applications the systems precision and repeatability is greater than 1/8,000 of the working range. It can also measure narrow, deep slots and holes of diameter <1mm, and depth to diameter ratios of 25:1. The system can also measure angles very close to the grazing incidence and the 'forbidden' zone extends only 5° from normal incidence in all directions, giving the user the ability to measure at angles from 0° to 85°.

1.4.2 Heterodyne interferometric profilometer

Figure 1.8 shows the principle of operation of the heterodyne profilometer[16]. The system operates by focusing two orthogonally polarized beams (He-Ne laser) onto the target by means of a Zeeman beam splitter and scanning lens. The focus is held on the surface by an autofocus system.

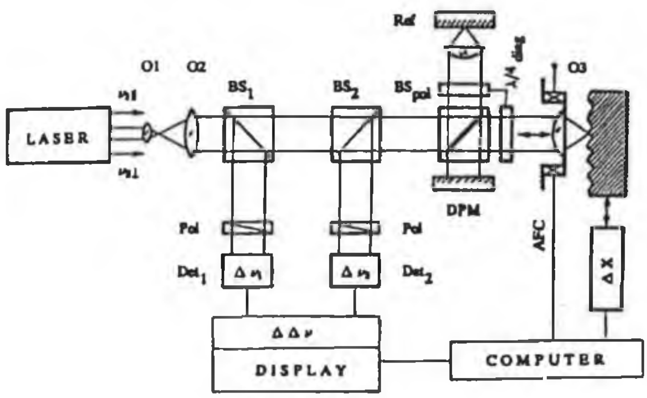

Figure 1.8 - Heterodyne interferometric profilometer[16]

The system is not of differential type, but instead measures the profile height directly from the target surface. The scanning head in this particular system is mounted on an air-bearing slide way of 300mm travel. Profile measurements in the 10 to 40nm range can be readily obtained, and surface roughness measurements in the sub-nanometer range may be obtained after high-pass filtering (cut-off wavelength in the region of 100 to 500μm) of the raw profile data. Surfaces with irregularities within the spot width, having large local slopes, or having sharp corners or edges are extremely difficult to be profiled accurately.

1.5 Laser-based inspection systems

Previous optical surface scanning systems (ones that did not use lasers) were forced to use inefficient high power linear type lamps in order to provide a sufficiently strong light intensity for high speed scanning[20,13]. Recently, in the past 10 years, laser systems have become much more rugged and are suitable for use in the harshest of manufacturing and inspection environments.

Lasers are able to offer a significant improvement in surface scanning performance, specifically in their resolution, speed, and reliability. Laser scanning measurement systems can achieve high resolutions because the maximum resolution of the system is directly proportional to the size of the projected laser spot. In addition, because the object is being illuminated by intense laser light for very short periods, laser scanning produces a very low signal to noise ratio (SNR). It is also possible to select a specific angular scattering range due to the directionality of laser systems, thus improving defect detectability.

Some of the drawbacks of laser based systems have already been covered in section 1.3, however some of the advantages of laser-based systems over other optical systems are listed below:

- Higher resolution
- Extremely fast scanning speeds
- High contrast image acquisition
- Brightness
- Increased depth of field
- Improved spectral filtering capabilities
- Small size (i.e., diode lasers)
- Increased lifetime (over conventional lamp sources)

1.5.1 Basic laser theory

The acronym LASER stands for Light Amplification by Stimulated Emission of Radiation. Lasers operate on the principle of stimulated emission. See figure 1.9. Stimulated emission occurs by achieving a significant population inversion in atomic or molecular energy states. This is a precondition for laser action. Electrons will normally reside in the lowest available energy state. They can be elevated to excited states by absorption, but no significant collection of electrons can be accumulated by absorption alone since both spontaneous emission and stimulated emission will bring them back down to a lower energy state. A population inversion cannot be achieved with just two levels because the probability for absorption and for spontaneous emission is exactly the same. The lifetime of a typical excited state is about 10^{-8} seconds, so in practical terms, the electrons drop back down by photon emission about as fast as you can pump them up to the upper level. In gas lasers excitation can take place through either electrical discharge or optical pumping.

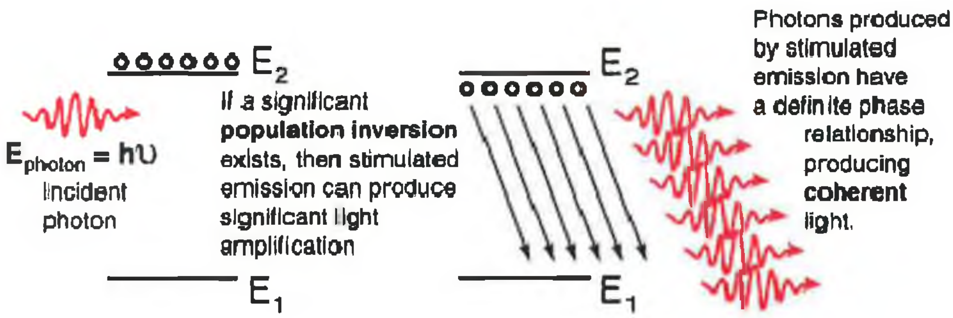

Figure 1.9 - Photon production by stimulated emission

- Electrical Discharge
  Applying high voltage to electrodes at both sides of the tube containing the gas causes electrical breakdown through the gas. Electrons are ejected from the cathode, accelerated toward the anode, and collide with the gas molecules along the way. During the collision, the mechanical kinetic energy of the electrons is transferred to the gas molecules, and excites them.

- Optical Pumping
  Exciting a laser medium by optical pumping, requires that the absorption spectrum of the medium will be similar to the emission spectrum of the pumping source, so that a big amount of the radiation will be absorbed. Conventional light sources used for optical pumping have a broad emission spectrum, so only a small part of the light is used in the excitation process. Because gas atoms absorb only a small portion of the spectrum, optical pumping is not generally an efficient method for gas lasers.

The absorption spectrum of solids is wider than the absorption spectra of gases, so the pumping efficiency of solid state lasers by conventional light sources are higher than that for gas lasers. Thus gas lasers are usually excited by an electric discharge. To excite a gas laser by optical pumpingit is beneficial to use an optical source with very narrow bandwidth, which fits the narrow absorption spectral lines of the gas. A good source for optical pumping of a gas laser is another laser. This method is used for pumping Far-Infra-Red (FIR) gas lasers by a CO_2 laser. The characteristics of lasers (discussed below) that make them ideal for optical inspection are radiance, collimation, monochromaticity, and coherence.

Radiance is an important property of laser beams. Lasers can achieve high radiance at relatively low power output levels[21]. The radiance of a laser source (or of any light source) is the power emitted per unit area of the source per unit angle[22], units are in watts per metre, per steradian. Generally speaking, lasers have a very high radiance output - high radiance meaning that the beam has a very small divergence angle (unless the source power is very large), which is in turn linked to the directionality (collimation) of the beam.

Light from a typical laser emerges in an extremely thin beam with very little divergence. Another way of saying this is that the beam is highly "collimated". The high degree of collimation arises from the fact that the cavity of the laser has very nearly parallel front and back mirrors, which constrain the final laser beam to a path that is perpendicular to the mirrors. The back mirror is made almost perfectly reflecting while the front mirror is about 99% reflecting, letting out about 1% of the beam. This 1% is the output beam, which you see. The light is passed back and forth between the mirrors many times in order to gain intensity by the stimulated emission of more photons at the same wavelength, see figure 1.10. If the light is the slightest bit off axis, it will be lost from the beam.

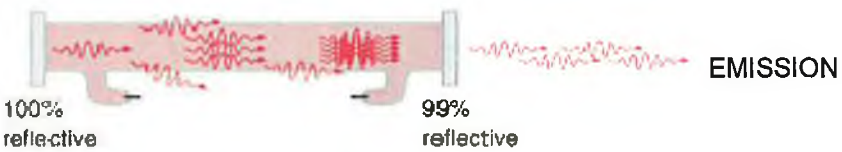

Figure 1.10 - Collimation of a laser beam

The highly collimated nature of the laser beam contributes both to its danger and to its usefulness. One should never look directly into a laser beam, because the highly parallel beams can focus to a dot on the retina of your eye, causing almost instant damage to the retina. This capacity for sharp focusing means that the laser is a very useful tool in optical inspection.

Another important property of laser light is monochromaticity. The light from the laser typically comes from one atomic transition with a single precise wavelength hence the light has a single spectral colour and is almost the purest monochromatic light available. That being said, however, the laser light is not exactly monochromatic. The spectral emission line from which it originates does have a finite width, if only from the Doppler effect of the moving atoms or molecules from which it comes. Since the wavelength of the light is extremely small compared to the size of the laser cavities used, then within that tiny spectral bandwidth of the emission lines are many resonant modes of the laser cavity.

Coherence is one of the unique properties of laser light. It arises from the stimulated emission process, which provides the amplification. Since a common stimulus triggers the emission events, which provide the amplified light, the emitted photons are "in step" and have a definite phase relation to each other, see figure 1.11.

This coherence is described in terms of temporal coherence and spatial coherence, both of which are important in producing the interference, which is used to produce holograms. Ordinary light is not coherent because it comes from independent atoms, which emit on time scales of about 10^{-8} seconds. There is a degree of coherence in sources like the mercury green line and some other useful spectral sources, but their coherence does not approach that of a laser.

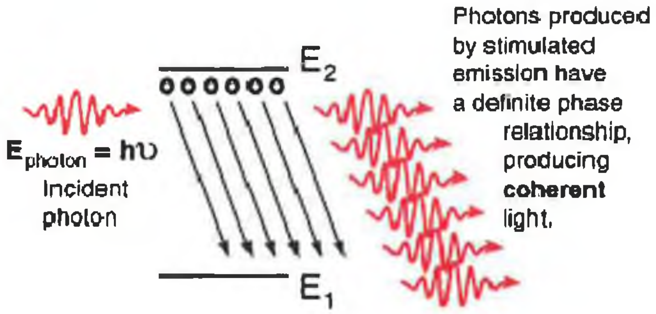

Figure 1.11 - Coherence of laser light

1.5.2 Common lasers types

Currently there are many different types of lasers available for industrial use, each class having its own unique characteristics[21]. The application of lasers in industry ranges from surface coating, to surface inspection, to surface forming. Lasers can be divided into groups according to different criteria:

- The state of matter of the active medium: solid, liquid, gas, or plasma.
- The spectral range of the laser wavelength: visible spectrum, Infra-Red (IR) spectrum, etc.
- The excitation (pumping) method of the active medium: Optic pumping, electric pumping, etc.
- The characteristics of the radiation emitted from the laser.
- The number of energy levels, which participate in the lasing process.

The active medium of the laser plays a major role in how the laser operates and its characteristics. The material used as the active medium determines:

- Laser wavelength
- Preferred pumping method
- Order of magnitude of the laser output
- The efficiency of the laser system

Also, there are two basic requirements for laser action, population inversion between the upper and lower energy levels, and the active medium must be capable of emitting the collimated laser light, i.e. it must be transparent to the output wavelength. The active medium determines most of the laser properties; hence the laser name is often derived from the name of the active medium.

A brief description of the most common laser types used today is given below[21]:

Helium-Neon (HeNe) laser

- Electrically pumped gas laser – energy transfer from electrons to HeNe atoms.
- Beam (red) wavelength of 632.8nm and infrared lines at 1.15 and 3.39μm.
- Output from a fraction of 1 mW to 50mW.
- Electrical efficiency $\approx$ 0.1%.
- Operating life $\approx$ 15,000 – 20,000 hrs.
- Most commonly used in barcode readers, CD and DVD equipment, and laser printers.

CO_2 molecular lasers

- Laser operation is based on the rotational, vibrational, and electronic levels of molecules.
- Molecular lasers are capable of generating very high powers with high efficiency (>10%).
- CO_2 lasers with outputs in excess of 20kW are commercially available.
- High output CO_2 lasers are most commonly used in material processing applications, such as metal cutting, welding, etc.

Solid State (Nd:YAG, Nd:Glass, Cr:Ruby) Lasers

- Lasing atoms are embedded in a host transparent material (solid).
- Population inversion occurs through optical pumping.
- Many solid-state lasers must be cooled – usually water-cooled.
- Solid-state lasers find use mostly in range finders, targeting equipment, and other tactical military equipment as well as in material processing and the medical sector.

Semiconductor (GaAs) Lasers

- Semiconductor lasers are the most common type of laser in use today.
- Advantages: ruggedness, cheap.
- Disadvantages: Generally limited to low power applications
- Semiconductor lasers, or laser-diodes are effectively formed between junctions of p-doped and n-doped materials.
- The resonator is often formed by polishing the end faces of the semiconductor.
- Laser emission is stimulated.
- Beam wavelength of 0.33μm (ultra violet) to 40μm (infra red).
- Output is typically in the mW range.

1.6 Methods of surface inspection using laser speckle

Speckle is a result of interference from a coherent beam of radiation from one or any number of point light sources. It is identified as a random arrangement of light and dark spots on the incident surface as these beams interfere with one another, both constructively (light spot) and destructively (dark spot). An object viewed under highly coherent light will be granular in appearance due to the speckle pattern. Laser speckle is created by the coherent nature of a single laser beam and was first discovered in the 1960's when the earliest lasers were created. Initially, it was thought that this phenomenon was due to a source of noise in the laser itself and was considered parasitical, however, soon after its discovery, the full potential of speckle was realised.

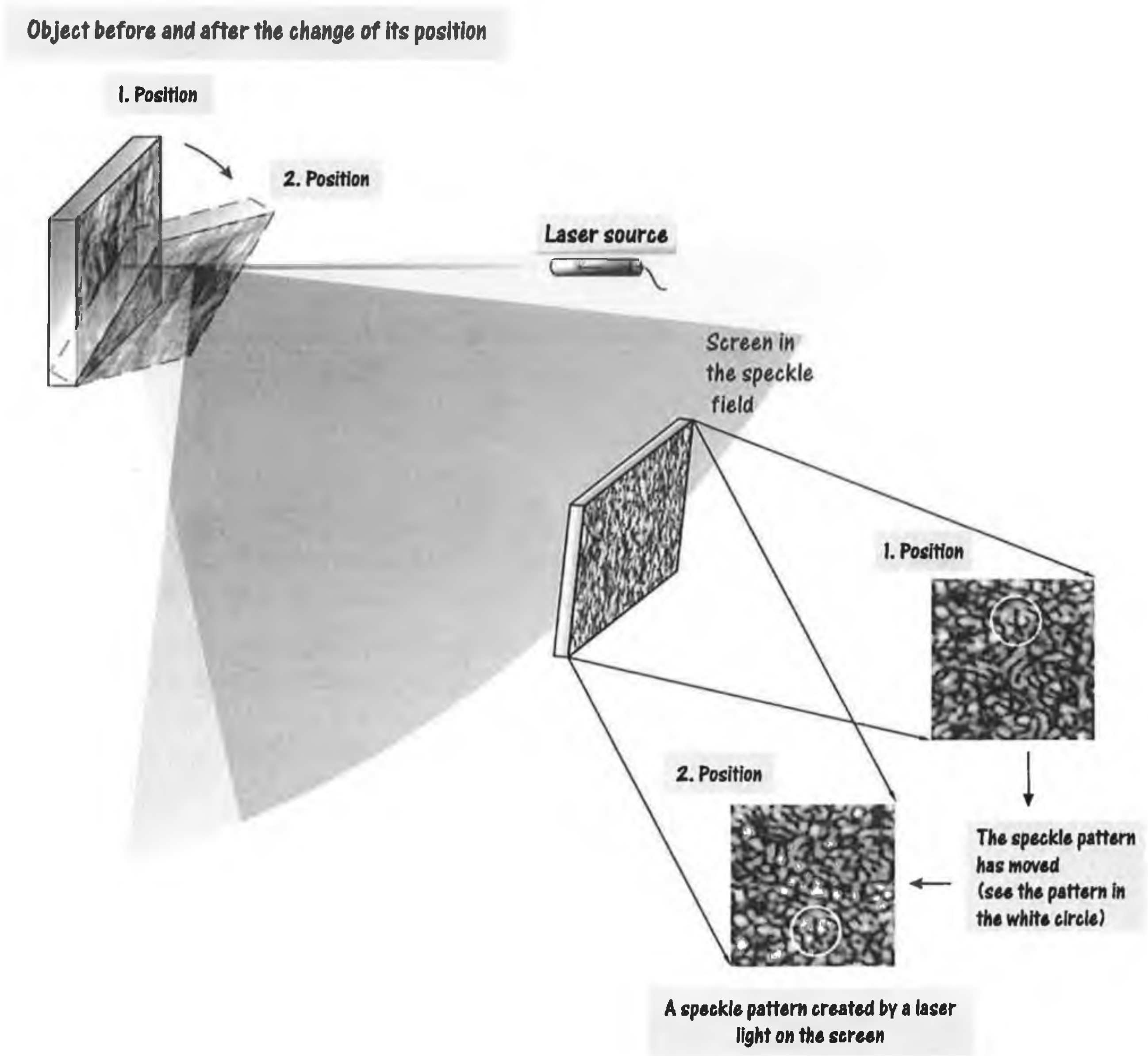

Figure 1.12 - Principle of laser speckle[24]

When the object or target surface (i.e., the surface illuminated by the laser light) undergoes any kind of movement (rotational, translational etc.) or deformation (bending, shearing etc.), the speckle viewed in the observation plane will move and/or change structure, see figure 1.12.

The following speckle techniques can be used to inspect surfaces and measure surface roughness by studying the correlation of two separate speckle patterns obtained from the same target surface. This is achieved by either changing the orientation or the wavelength of the incident laser beam.

1.6.1 Surface roughness measurement by the correlation of two speckle patterns

The target surface is illuminated with a plane wave from a laser (see figure 1.13) and two speckle patterns are obtained, each with two distinct angles of incidence, which are recorded successively on a photographic plate (the speckle patterns recorded are translated relative to one another). Changing the angle of incidence, θ, does not produce any decorrelation under the above conditions. If the change in the angle of incidence is small enough, the speckle will simply be translated by a distance ξ_0 where;

$$\xi_0 = d.\mathrm{Cos}\theta.\Delta\theta$$

eq 1.1

and d is given as the distance between the target surface, S, and the photographic plate, H. As Δθ increases for a given value of θ, the speckle itself is not only shifted, but its structure changes due to the roughness of the target surface.

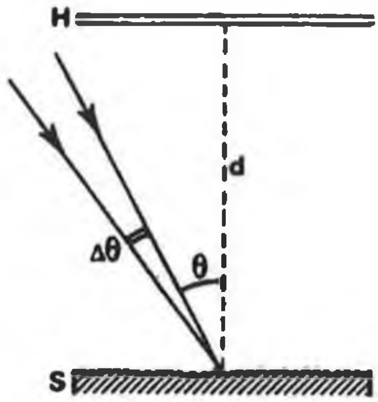

Figure 1.13 - Two speckle patterns obtained by changing the incidence of the laser beam

This is the principle of this technique – two successive recordings are made on the same photographic plate, H, the angle Δθ being the difference between the angles of incidence of the two laser beams.

1.6.2 Real-time measurement of surface roughness by the amplitude correlation of two speckle patterns

In the previous measurement, the surface roughness could be calculated by inspecting the contrast of the interference fringes, which were recorded on a graphic plate. Real-time measurements can be made by using intensity correlation of the beams amplitudes. To achieve this, the target surface is illuminated by two coherent plane waves from the same laser source. The incident laser beam is split by a beam splitter and a mirror shown in figure 1.14.

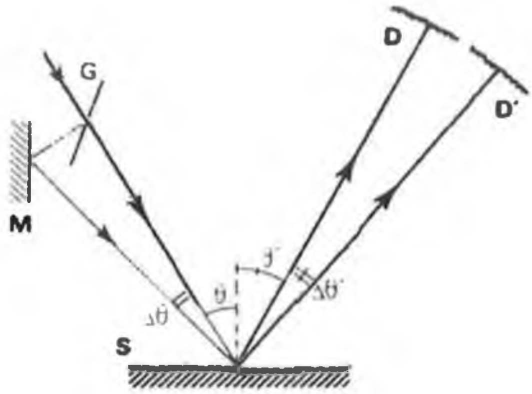

Figure 1.14 - Real-time measurement of surface roughness by amplitude correlation

For an incidence angle of θ a speckle pattern D is observed in the direction θ'. For an angle of incidence θ + Δθ, another speckle pattern D' is observed. This speckle pattern is related to speckle pattern D through a rotation of Δθ' and the two have a certain degree of correlation, where:

$$\Delta\theta' = (\mathrm{Cos}\theta \,/\, \mathrm{Cos}\theta').\Delta\theta$$

eq 1.2

To measure the correlation, the two speckle patterns are superimposed on one another. This is achieved by using a 2-beam interferometer such as a Michelson interferometer if Δθ and Δθ' are variable, or two Wallaston prisms if Δθ and Δθ' are fixed.

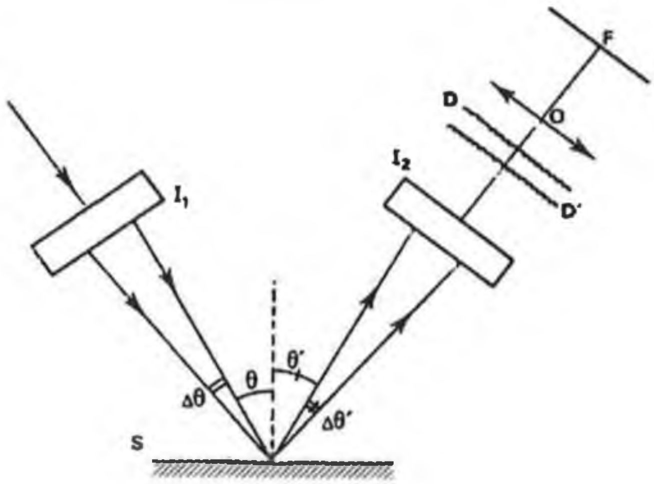

Figure 1.15 - Setup using two Michelson Interferometers

In the case where two Michelson interferometers are used (see figure 1.15), the second interferometer not adjusted for zero path difference, the two speckle patterns are shifted along the axis shown above. Interference fringes are observed at the focal plane of the lens O and their contrast is directly related to the correlation of the two speckle patterns, which in turn is proportional to the surface roughness of S. For rough metal surfaces where $\sigma > 1\mu m$, the contrast, γ, of the fringes is defined by:

$$\gamma = {}^{1}/_{2}\exp[-2((2\pi\sigma)^{1/2}/\lambda\ .\mathrm{Sin}\Delta\theta)^{2}]$$

eq 1.3

1.6.3 Surface roughness measurement of two speckle patterns obtained with two wavelengths

Rather than changing the orientation of the incident beam as discussed previously, it is also possible to change the wavelength, however this does not allow real-time measurement if only one laser source is used.

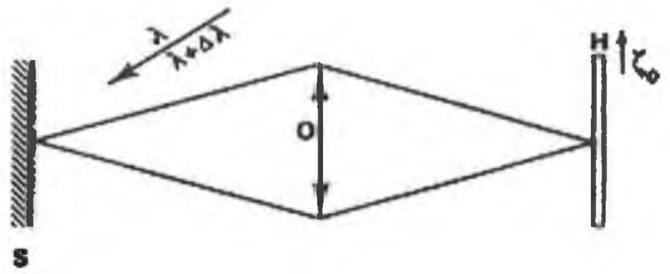

Figure 1.16 - Roughness measurement of two speckle patterns obtained with two wavelengths

The target surface, S, is illuminated with a laser of wavelength λ and an image of S is projected onto a photographic plate H through a lens O where a speckle pattern (which corresponds to λ) is recorded, see figure 1.16.

The photographic plate is translated by a small amount ξ_0, and the target surface is again illuminated, this time with a laser of wavelength $\lambda + \Delta\lambda$. The speckle pattern corresponding to this new wavelength is then recorded at H.

An alternative to the previous method is to avoid the need for lens O by recording the speckle at a finite distance as shown in figure 1.17.

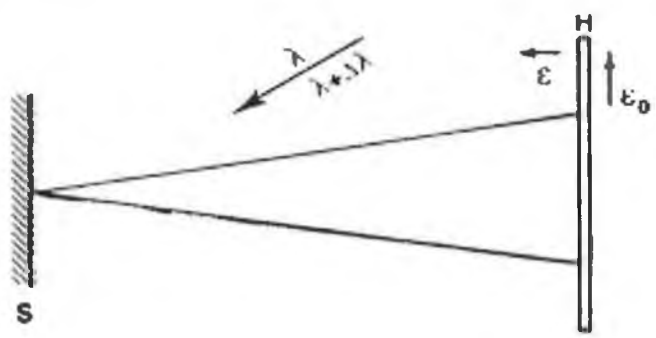

Figure 1.17 - Recording speckle at a finite distance

Again, the same procedure is followed, however, before illuminating the target surface S with a laser of wavelength $\lambda + \Delta\lambda$, the surface undergoes two translations ε and ε_0. The photographic plate is shifted by ε to compensate for the variation $\Delta\lambda$.

Under these new conditions two identical speckle patterns are obtained on the photographic plate if:

$$\sigma << \lambda^2/\Delta\lambda$$

eq 1.4

If this condition is not satisfied, the two speckle patterns are more or less decorrelated. Again, the spectrum of the photographic plate is observed as before, and the correlation of the speckle patterns (σ) may be deduced from the contrast of the fringes.

1.6.4 Surface roughness measurement with a source having a wide bandwidth

Maximum speckle contrast is achieved when a rough surface is illuminated by spatially coherent light. Reducing the temporal coherence while maintaining the spatial coherence will in turn reduce the speckle contrast.

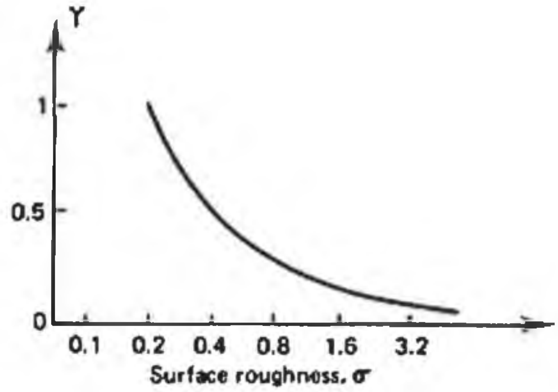

Figure 1.18 - Relationship between white light speckle intensity and surface roughness

The relationship between the speckle intensity and the surface roughness for any given coherence length is predominantly great when the variations in the surface roughness are in or around the same order of magnitude as the coherence length.

From figure 1.18, we can see that for white light, with a coherence length of approximately 1 to 1.5μm the surface roughness may be assessed by measuring the contrast of the speckle, provided the surface roughness is in the region of 0.2 to 3μm. The intensity of the speckle contrast may be measured by projecting an image of the target surface onto a small aperture, behind which there is a detector or transducer to record the level of the intensity. As the surface is translated in its plane the profile of the speckle intensity may be recorded.

1.7 Optical triangulation

Optical triangulation requires a light source, imaging optics to focus and receive the light, and some form of photo detector to provide an output relative to the position of the imaged light. The principle of optical triangulation can be seen in figure 1.19 below.

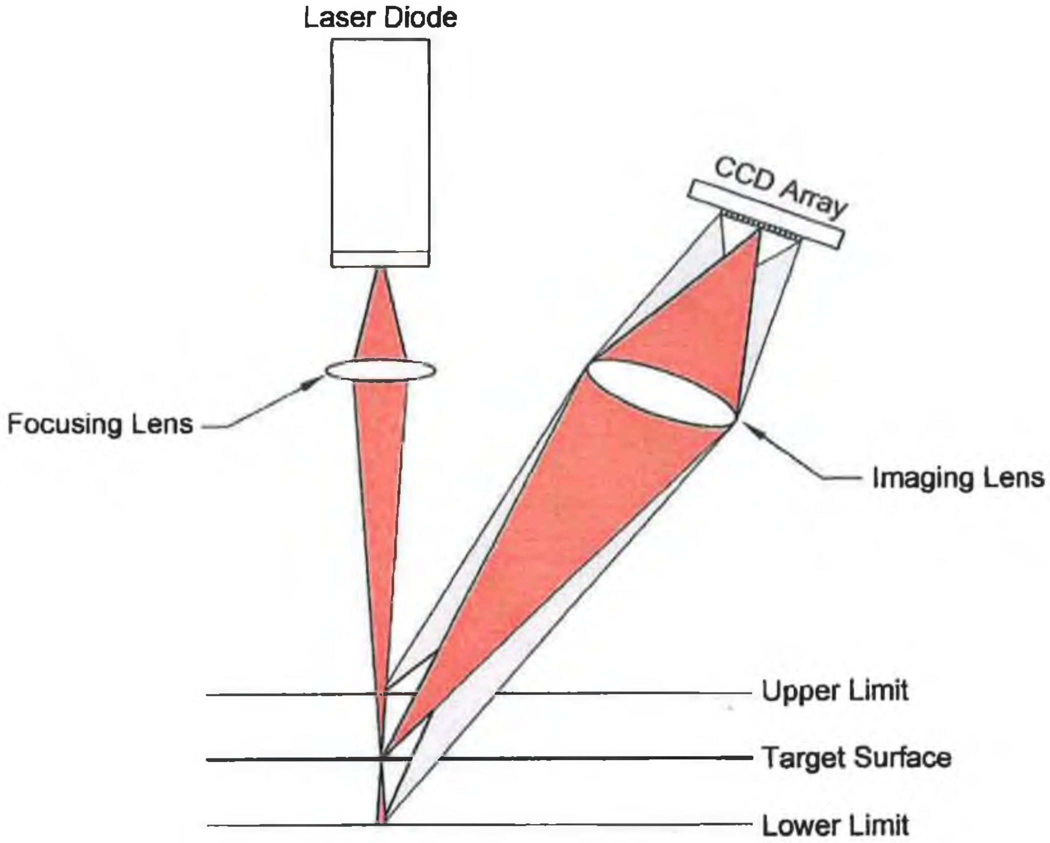

Figure 1.19 - Optical triangulation

The laser diode provides a collimated or focused beam of light which is projected onto the target surface through the focusing lens. The diffuse light or object spot is then captured (diffuse reflection) by the imaging lens and is focused onto a photo detector. Due to parallax, as the relative distance between the target surface and focusing lens changes, so too does the position of the imaged spot on the receiver or detector. The laser sensor is equipped with it's own signal conditioning electronics allowing linearisation and digital or analog signal conditioning. The output signal from the sensor is proportional to the position of the spot on the target surface.

The most critical component of a triangulation type sensor is the receiver element. There are currently three main types of photo detector or receiver employed in triangulation type sensors, the oldest device being the PSD, or Position Sensitive Device. When used under ideal conditions, a PSD sensor will perform very well, however, should the target surface vary in colour, texture or alignment, then the PSD runs into problems. These changes alter the centre of light distribution thus inducing a change in the output of the PSD device even though the true position of the spot has not changed.

In the case of a CCD array, the array surface is made up of rows of coupled photo capacitors, which individually accumulate charge as light lands on them. The voltage across each capacitor can be measured thus it is possible to ascertain how much light is falling on any particular area of the array. Since movement of the assembly with respect to the target surface will change the position of the imaged light on the CCD array through parallax, it is possible to accurately measure the distance between the focusing lens and the target surface. The effects of target alignment, colour, and texture variation are no longer issues since CCD devices work as a function of light intensity, not quantity. Some of the most modern CCD triangulation sensors only require about 1% of diffuse reflection from the target surface in order to operate. For some years CCD technology was limited in it's response time to constant surface variations, especially during high speed scanning. This limitation was more down to the speed of the sensor's microprocessor rather than the CCD. Today however this is no longer an issue and CCD devices can cope with high speed scanning as well as the aforementioned problems that limited the use of PSD. Laser triangulation and its limitations will be discussed further in section 2.5.

1.8 Methods of laser scanning

There are several methods of laser scanning or sweeping currently used today. In this particular context, laser scanning means the actual 'sweeping' motion of the laser beam over the target surface, and how that motion is achieved. This motion may be accomplished through a variety of means, including mechanical, acoustic (acousto-optical), or electric (electro-optical) among others. In turn, these specific types of scanning system may be further split into two groups; high-inertia and low-inertia scanning systems. Generally speaking, high-inertia systems include rotational (mechanical) systems as well as mirror/prism (mechanical) systems, while low-inertia systems include vibrational (mechanical) systems as well as electro and acousto-optical systems.

For the most part, the laser scanning motion is achieved through mechanical means, whether it be through the use of mirrors, or prisms. Mechanical scanners work by moving or oscillating an optical component, which is directly in the path of the incident beam from the laser. Depending on the arc or rotation of this movement, a laser beam may be moved backwards and forwards across a surface. The distance that the laser beam moves across the surface before it starts back the other way is equal to twice the amplitude of the scan. The amplitude of the scan may be varied through the use of different mirrors and prisms. Assuming that the rotational velocity of the oscillating/rotating surface remains constant, the speed of the scan and it's amplitude will be directly proportional. The actual physical motion of the optical components is usually accomplished through the use of electric motors or a galvanometer/coil arrangement. Due to the high inertia of the system, mechanical scanners tend to have very high stability with a low positional error. On the other hand, mechanical scanners tend to be very slow and difficult to control as compared with their electro or acousto-optic counterparts. Mechanical scanners tend to have a very rigid scan format, which may be complicated to change or adapt. Also, the bulky nature of mechanically rotational scanners may be outside of the physical parameters allowed, however mechanical scanners have some major advantages over other types due to their comparatively low cost, durability, and simplicity in design. A review of possible mirror and prism orientation set-ups and laser scanning methods have previously been presented [17, 26, 28, 29, 34].

1.9 Laser scanning motions & patterns

1.9.1 Laser scanning motions

The movement of a scanning motion may fall into one of three categories:

- Rotational
- Oscillatory
- Translational

The three primary scanning motions are shown in figure 1.20.

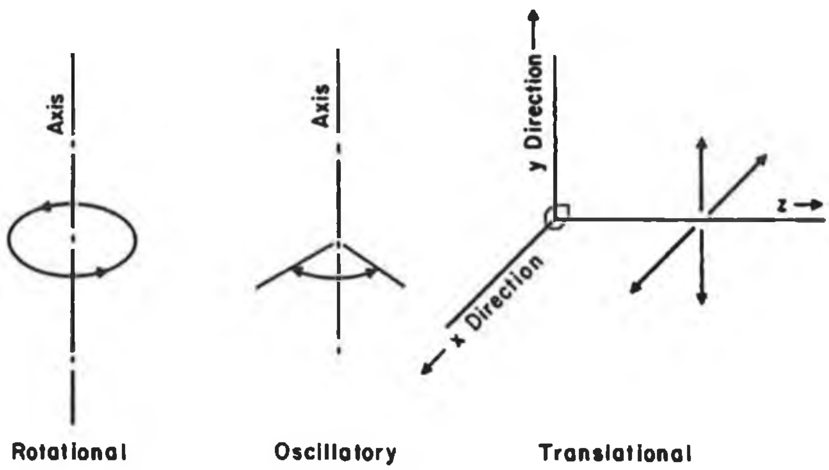

Figure 1.20 - Primary scanning motions[27]

Rotational motion is a simple, natural movement and is generally associated with mechanical scanners (which use mirrors or prisms to deflect the laser beam). Usually the angular velocity of the rotational motion is kept constant, however, depending on the device's parameters and the relative size of its optics, this speed may differ over a broad range. The limit of the rotational velocity is restricted by the stresses and loads associated with the systems mechanical components (such as bearings) and by the substrate material of its optics. See section 1.14.1 Mechanical considerations of laser based surface inspection.

Oscillatory motion is probably the most natural physical movement, however it can become quite complicated, especially when associated with mechanical scanners. Dynamic requirements of the system can change from simple harmonic motion (displacement varies sinusoidally with time) to reciprocating motion (displacement variation is in some other way, proportional to time), which has a saw-tooth or triangular type displacement over time, see figure 1.21 on the next page. With this continuously changing direction, speed, and acceleration, the dynamic movement of the system may become very complex.

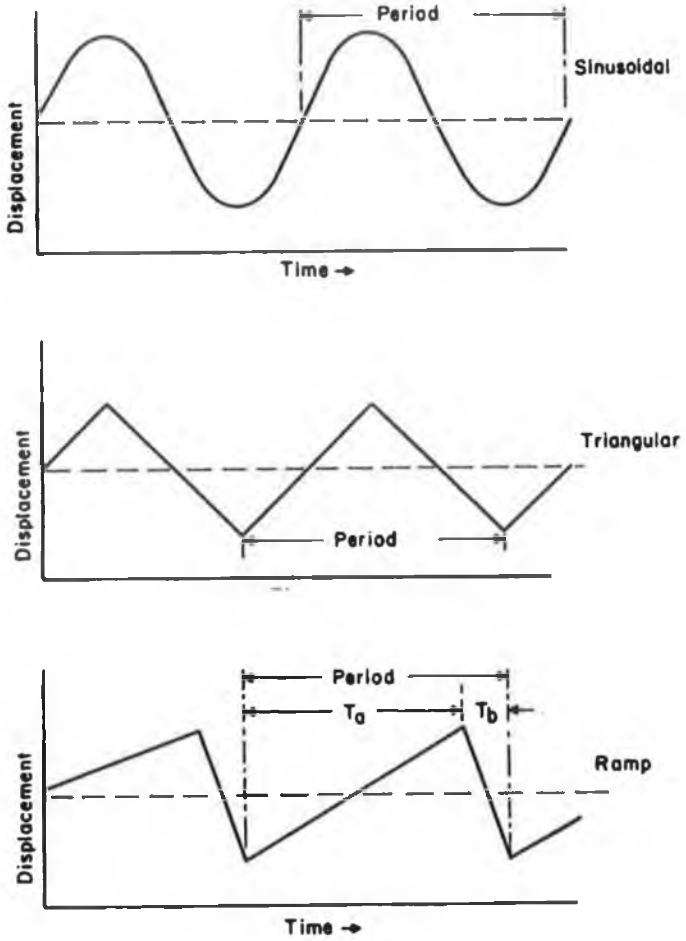

Figure 1.21 - Oscillatory motion[27]

Looking at figure 1.21 above, the change in displacement seems to take place at a particular instant in time suggesting an infinitely fast acceleration/deceleration, which is impossible. In reality, the corners of the saw-tooth/triangular waveform are rounded. Another important consideration when using the saw-tooth/triangular waveform for scanning, is that it is effectively composed of a series of simple harmonic motions, each having a frequency that is a multiple of the fundamental frequency. In other words, there is an interaction between the oscillatory rate and the natural frequency response of the system – depending on the design of the system, one may choose to operate close to or avoid the resonant frequency.

A translational or transverse motion is a simple sideways motion without any change of direction. It may also be considered as an arcuate (curved) motion, where the centre of rotation is an infinite distance away. An angularly scanning or sweeping beam from a rotating or oscillating mirror or prism can be converted to a transversing scanning beam through the collimation and focusing of the beam, see figure 1.22.

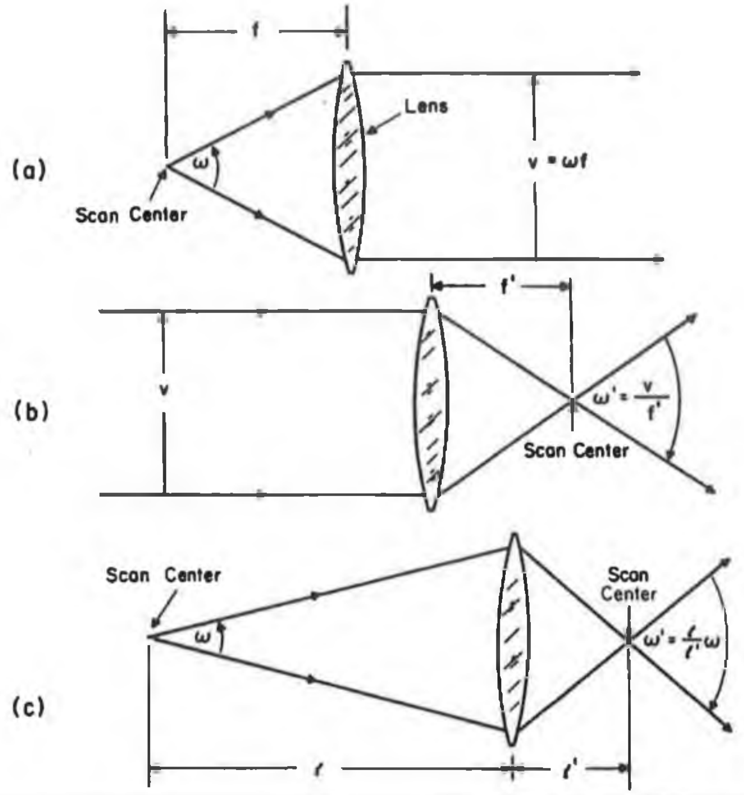

Figure 1.22 - (a) Angular movement, (b) traversing movement, and (c) magnification of a scanning beam[27]

Figure 1.22 shows how an angularly scanning beam may be turned into a traversing beam and vice versa, and also the magnification of the angle of deflection and angular velocity of the scan (ω = angular velocity, v = linear velocity).

1.9.2 Laser scanning patterns

There are numerous types of scan pattern that the laser beam can follow. These patterns are generally determined by the performance limitations of the scanning device and also from a cost efficiency perspective.

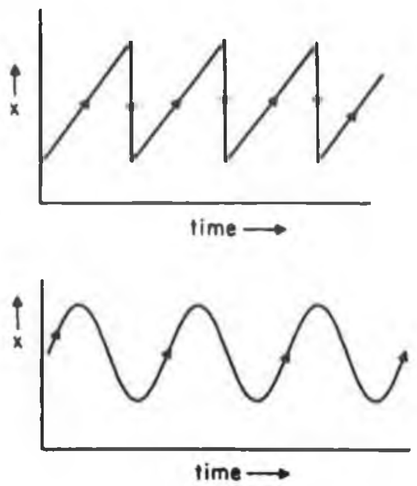

Figure 1.23 - Straight line scan[27]

The simplest type of scan is the straight-line scan (see figure 1.23 above), where the beam sweeps repetitively across the target surface at a constant velocity (acceleration = 0). Mechanical rotational or oscillatory scanning systems usually scan in a simple harmonic saw-tooth pattern made up of straight-line scans. This type of scan is easy to achieve on such a system as well as translational systems

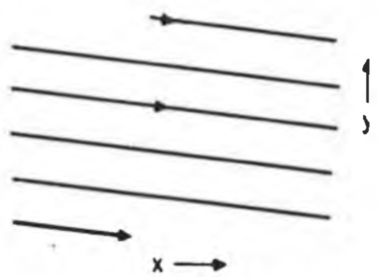

Figure 1.24 - Raster scan[27]

The raster scan pattern (see figure 1.24) is made up of two mutually perpendicular scanning motions running at a constant speed. One complete motion across the target surface by raster scanning is called a frame, and the amount of scans or lines in one frame is proportional to the ratio of the periodicies of the x and y-axis motions.

The lissajous scanning pattern in figure 1.25 is made up of two simple harmonic motions, again, in mutually perpendicular directions, producing a lissajous pattern. The actual pattern configuration depends on a number of factors associated with each of the harmonic motions – frequency ratio, phase differences, and amplitude.

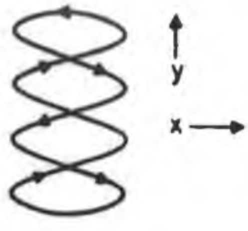

Figure 1.25 - Lissajous scan[27]

When observing the actual lissajous pattern, it will seem to move in the x-direction when the scan frequency in the y-axis, f_y, is greater than that of the x-axis frequency, f_x, and that f_y/f_x does not reduce to a whole number, for example with $f_y/f_x = 3.001$, the integral part, 3, determines the actual pattern configuration, while the decimal portion, .001, determines the rate of migration. Likewise, the pattern will exhibit movement in the y-direction when f_x is greater than f_y. In order for a patter to migrate at a uniform rate the ratio of the frequencies must be synchronised otherwise the pattern will drift, reverse, or speed up.

Figure 1.26 - Sinusoidal pattern[27]

A sinusoidal scan (see figure 1.26) is the combination of a simple harmonic motion and a constant scanning motion in two mutually perpendicular directions. The number of cycles (spatial wavelengths) per scan length is directly proportional to the ratio of the velocity of the constant speed and simple harmonic motions. If the ratio results in an odd number, then the pattern will be interlaced and it will have the appearance of a lissajous pattern. Again, the same general guidelines apply regarding the migration of the scanning pattern.

1.10 Technical considerations of laser based surface inspection

Due to its high quality and efficiency, a plane mirror can provide an effective means for scanning a beam of light. In order to be useful in scanning a beam of light, it is required that a mirror vibrate at a adequately high rate and over a sufficiently large angle (depending on the distance to the target surface), while at the same time being able to cope with the effects of high torque, i.e. while suffering low surface deformation. Mirror sizes are typically 10mm or smaller in width with a angular excursion of up to 40° and a step response usually greater than 100µs. To be an effective substrate for the mirror, the mirror material must be of a low mass (to help reduce inertia) and high stiffness (to help prevent deformation under inertial stress). It must also be fabricated and polished to an extremely high finish to provide efficient and controlled reflectance. Although glass remains one of the most effective substrates, more demanding tasks require the use of exotic materials and high technology fabrication techniques, such as in the manufacture of ultra-light weight beryllium mirrors. This section will deal mainly with mechanical scanning systems and the problems associated with mechanically 'sweeping' a laser beam.

1.10.1 Mechanical considerations of laser based surface inspection

Mechanical scanners tend to be very slow and difficult to control as compared with their electro or acousto-optic counterparts whilst they also tend to have a very rigid scan format, which may be complicated to change or adapt. In addition, the high inertia produced by the rotating components (which helps the stability) unfortunately greatly limits the systems performance. Also, the bulky nature of mechanically rotational scanners may be outside of the physical parameters allowed, however mechanical scanners have some major advantages over other types due to their comparatively low cost, durability, and simplicity in design.

As covered previously, another way of mechanically scanning a laser beam across a surface is through the use of a galvanometer type arrangement. A galvanometer works on the principle that a current carrying coil wrapped around a permanent magnet will tend to repulse one from the other. A mirror mounted on the coil of the galvanometer may be moved backwards and forwards by varying the amount and direction of the current passing through the coil, achieving in some cases a very high angle of deflection with little or no distortion of the incident beam. In addition, optical correction is kept to a minimum because the centre of deflection coincides with the axis of rotation of the mirror, also, due to the simple nature of the scan, two or more mirrors may be used together to scan the beam in a number of directions. However, galvanometer mirror arrangements are limited by a number of factors. Large scan angles can cause slow scan rates, simply because the mirror must deflect more to achieve the required scan angle. Likewise, high scan rates (>15Hz) are only achievable through small scanning angles, where the mirror is only deflecting very slightly.

Most optical devices are made from physical materials which have elastic properties (small as they may be) which have fundamental importance to the design and subsequent performance of the system[30]. The most critical material properties include stability, stiffness, and stress limitations. The stiffness properties of the material will determine the amount of deformation of the material during normal operation that may induce high inertial forces or temperature changes in the material; for example, plain mirrors tend to flex and warp when undergoing an oscillatory motion where the acceleration of the mirror is constantly changing.

When dealing with a system which must meet a high degree of repeatability we must also consider factors such as material stability with relation to temperature, and general degradation of the material and associated mechanical system. Further material regarding mechanical considerations of beam scanning have been previously presented [30, 34].

1.10.2 Optical considerations of laser scanning

1.10.2.1 Focused beam spot diameter

Theoretically, a focusing lens will focus a set of light rays from a point to another point, however in reality, lenses always focus light to a spot which has a finite size (the term 'point' suggests an infinitely small spot size)[27]. The size of the spot is dependent on a number of variables, the two most important being the quality of the lens (both in design and manufacture), and the wavelength of the light. A perfectly designed and manufactured lens will in fact focus light to a spot, which in turn is surrounded by collection of faint rings. The diameter of the spot is given by:

$$D_a = 2.44\,\lambda\,(l/A)$$

eq 1.5

where,
D_a = Beam diameter
λ = Wavelength of the light
l = Distance of spot from lens (for a collimated beam $l = f$, the focal length of the lens)
A = Lens aperture diameter

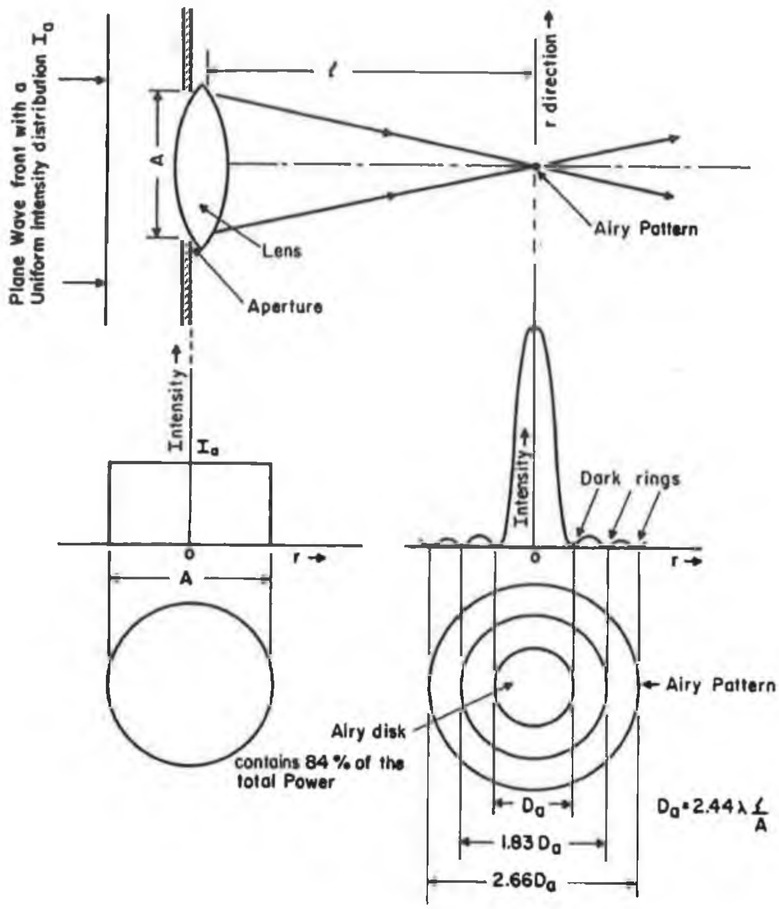

Figure 1.27 - Focused beam spot intensity distribution[27]

The actual intensity distribution of the spot is shown in figure 1.27. The series of light and dark rings is known as an Airy pattern, the central part of the pattern being known as the Airy disk. A lens that produces an Airy pattern is identified as being diffraction limited.

1.10.2.2 Focused Gaussian beam spot diameter

A beam or spot having a Gaussian intensity distribution is said to have an effective spot diameter, D_s, corresponding to 4σ, where σ is the standard deviation of a Gaussian beam intensity distribution[27]:

$$I = I_0 e^{-r^2/2\sigma^2} \qquad \text{eq 1.6}$$

where,
I = Spot intensity at radius r from axis of the beam
I_0 = Peak intensity

Specifically for a Gaussian beam, the effective spot diameter, D_s, is related to the effective beam diameter, D_b, as shown below.

$$D_s = (4/\pi)\,\lambda\,(1/D_b)$$

eq 1.7

where,

$$D_s = 4\sigma_s$$

eq 1.8

and,

$$D_b = 4\sigma_b$$

eq 1.9

1.10.2.3 Beam/spot power

Consider a beam whose Gaussian intensity distribution focuses to a spot which also has a Gaussian intensity distribution it can be seen that at the spot diameter of $4\sigma_b$ the intensity level has dropped to only 14% of the peak, see figure 1.28[27]. The central circle of the Airy disk holds roughly 86% of the total beam or spot power, thus 14% of the power of the beam lies outside the effective diameter of the spot. Table 1.2 shows the relative intensity and power against diameter for a spot size of eight millimetres and with a Gaussian distribution.

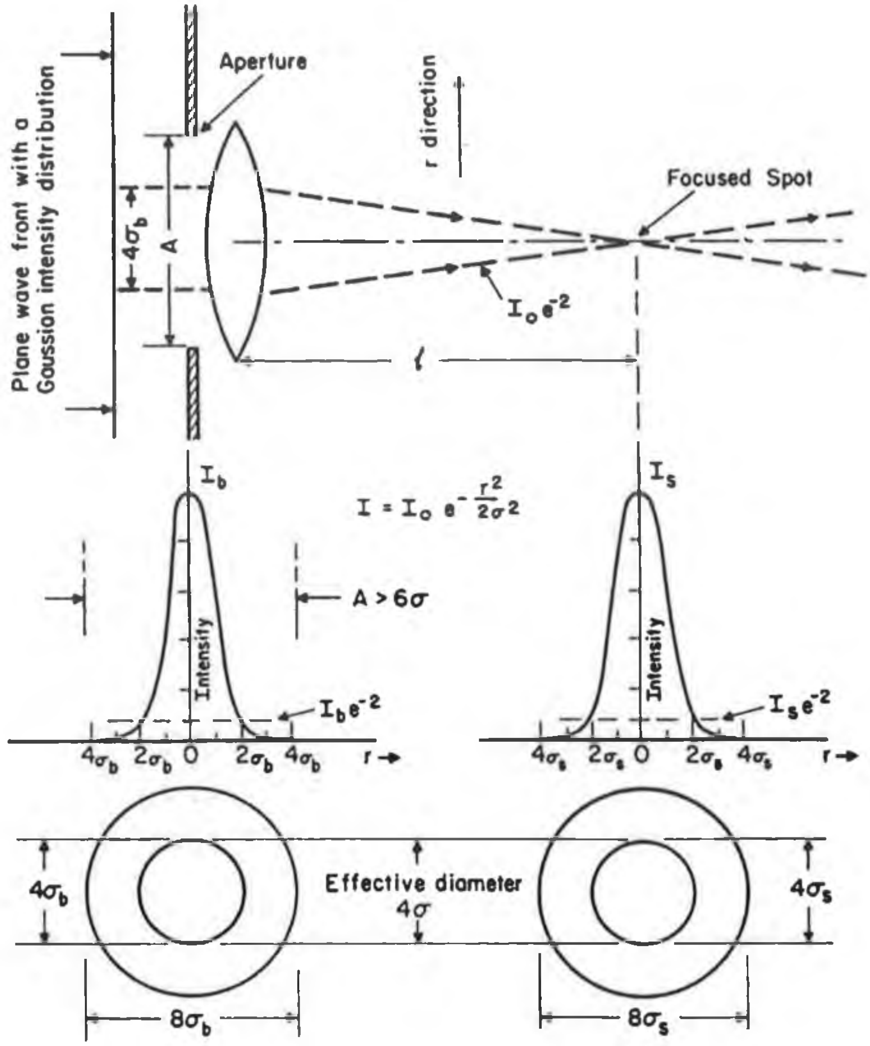

Figure 1.28 - Beam/spot power[27]

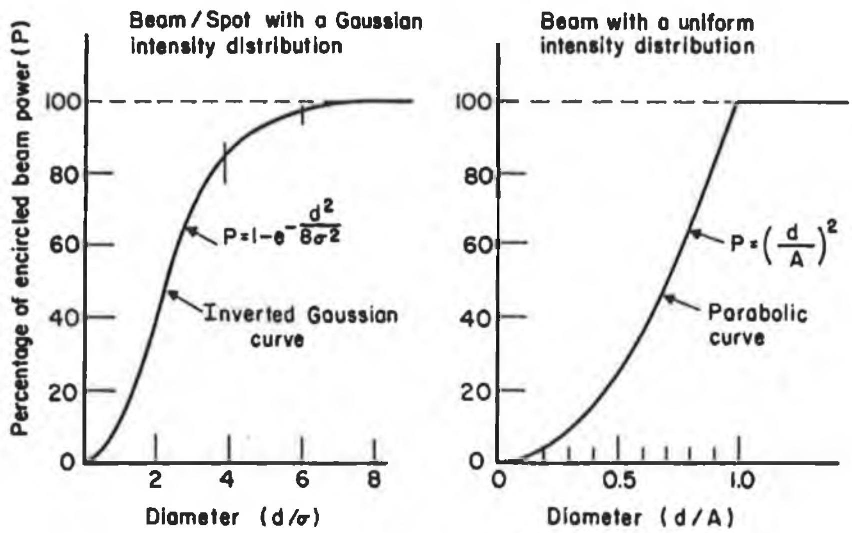

Figure 1.29 - Beam intensity distribution[27]

Table 1.2 - Relative intensity and power vs spot diameter for a Gaussian distribution[30]

Spot ∅	Intensity Level % I/I_0	Power % within Beam Spot ∅
1.00	94%	6%
1.52	75%	25%
2.00	61%	39%
2.35	50%	50%
3.33	25%	75%
4.00	14%	86%
6.00	1.1%	98.9%
8.00	0.034%	99.966%

1.10.2.4 Beam truncation

Truncation, or 'aperturing' of the laser beam is also an important consideration as the intensity of the distribution of the beam will also be truncated asymmetrically thus leading to variation in the effective spot diameter and spot shape[27].

Aperturing occurs because the mirror facets of scanning devices are themselves apertures, which project various different shapes when a beam falls on the mirror surface obliquely. When a beam (again, which has a Gaussian intensity distribution) passes through an aperture it will become increasingly truncated as the effective beam diameter becomes equal to and greater than the diameter of the aperture.

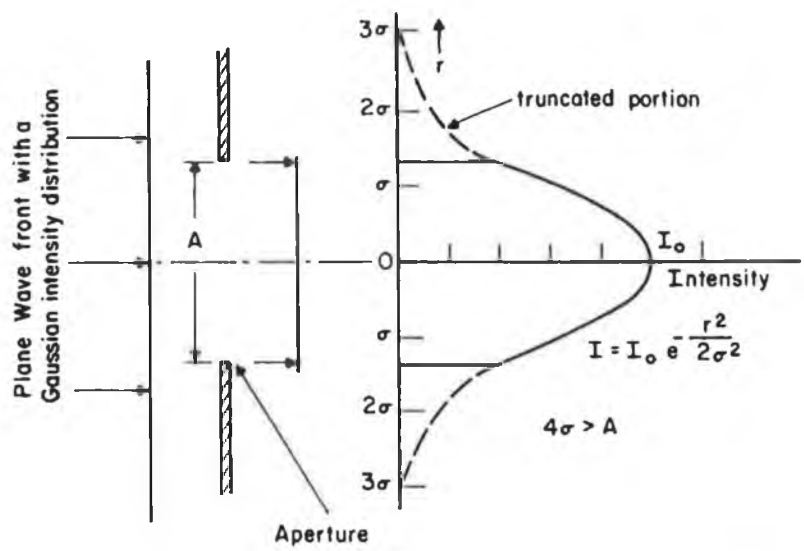

Figure 1.30 - Beam intensity distribution after passing through an aperture[27]

When the beam emerges from the aperture, its intensity distribution will neither be Gaussian nor uniform, hence the focused spot intensity distribution will not be Gaussian. As a beam passes through an aperture, the beam diameter will grow and the truncation of the intensity distribution will increase dramatically, however the intensity variation across the aperture will become more consistent, hence, as the beam expands and becomes even more truncated, the focussed spot will evolve into an Airy pattern the central spot becoming the Airy disk, see figure 1.30 above. In general, for beams truncated by apertures of different shapes, the effective spot diameter, D_s, is given by:

$$D_s = k\lambda(1/A) \qquad \text{eq 1.10}$$

where,
k = Constant (depending on aperture shape), $1 < k < 3$
A = Effective aperture dimension.

1.10.3 Electrical & control considerations

A rotating mechanical scanner has three states of motion; at rest (the scanner is in a stationary position), transient-state (where the motor/scanner is accelerating/decelerating towards a steady state velocity, a different operational steady state velocity, or a rest state), and steady-state (where the motor/scanner has a constant velocity and acceleration equals zero)[31]. The transient state is an unwanted state as it is not constant, therefore measurement or inspection usually does not take place during this time. Using an electrical drive coupled with a control system, this transient period can be controlled and kept to a minimum, although realistically it can never be eliminated entirely. In addition, during steady-state operation, there will also be a requirement to ensure that the system remains at this steady-state constraint with the minimum of variation. This can be done in two ways, by using either an open or closed loop controller. Open loop control systems rely entirely on the electromechanical characteristics of the scanning device and voltage inputs powering it. In contrast, the closed loop system is a servo-control structure and will continuously monitor the scanners parameters and will adjust them accordingly through the use of feedback to the controller, and on to the various scanning devices. This type of real-time control and requires the use of some type of encoder, capacitive, magnetic, or optical sensor.

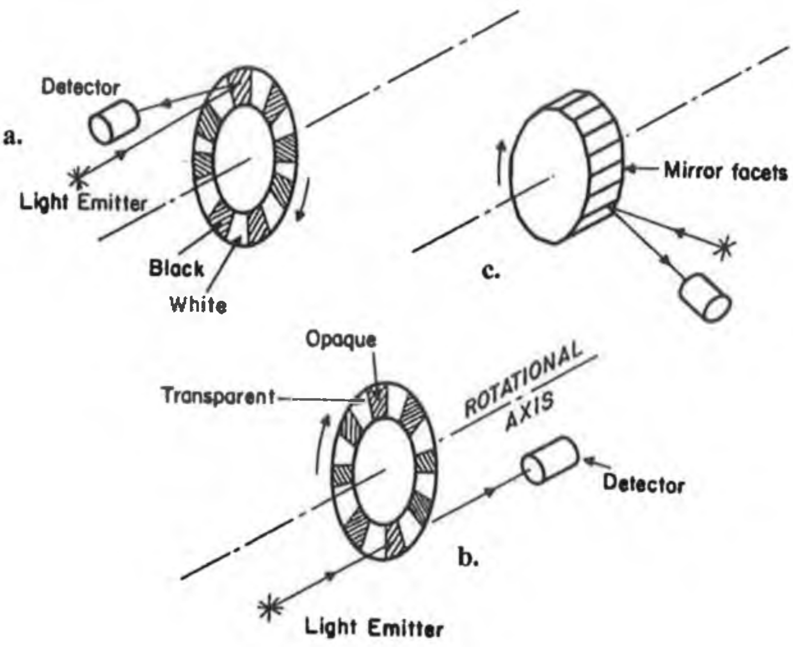

Figure 1.31 - Common optical encoders for scanning devices[30]

Optical encoders for scanning devices usually take one of the forms shown in figure 1.31. A disk, with equiangular black and white (a) or opaque and transparent (depending whether reflection or transmission is required) sections (b), or a multi faceted-mirrored rotor (c) is mounted on the shaft of the motor or on the axis of the scanning device. As the motor or scanner rotates, reflection or transmission will occur and the angular position of the motor or scanner can be established (assuming the start position is known first). These types of encoder can achieve exceptional resolution depending on the number of equiangular, mirror, or opaque sections. Table 1.3 on the next page details a comparison of the parameters of different motor types.

Table 1.3[30] - Comparison of the parameters of different motor types

		Motor Type					
		Induction			Reluctance		
Parameter	DC Motor	Squirrel Cage	Solid	Hysteresis	Squirrel Cage	Hysteresis	Brushless DC
Highest Speed	5000 rpm	30,000 rpm	150,000 rpm	150,000 rpm	30,000 rpm	150,000 rpm	30,000 rpm
Output Torque	High	High	High	Medium	Medium	Low	Medium
Rotor Heating	I^2r_m	Load Dependant	Load Dependant	Minor Loop	Load Dependant	Minor Loop	None
Speed Control*	Easy	Hard	Medium	Self Regulating	Hard	Self Regulating	Easy
Phase Lock**	Medium	Hard	Medium	Hard	Hard	Hard	Medium
Efficiency	High	Medium	Medium	Medium	Medium	Low	High
Power Factor	High	Medium	Low	Low	Medium	Low	High
Relative Cost	Low	Low	Medium	Medium	Medium	Medium	High

* Complexity for Simple Speed Control

** Complexity for Phase Locked Performance

1.11 Summary

This chapter has introduced the principle of utilising optical triangulation and laser light for the measurement of surface profile and surface digitisation. This has led on from a discussion of the development of manual systems for measuring surface roughness. Having developed the parameters of a measuring system, the next chapter introduces a new system developed, utilising the principle of optical triangulation, for these purposes.

Chapter 2 Profilometer development

The previous chapter indicated the need and principle behind both contact and non-contact profilometers. This chapter will discuss the design and prototyping of a profilometer using optical triangulation. The first section in this chapter deals with the mechanical design of the system.

2.1 Mechanical design

The complete system was designed with SolidWorks v2001 in order to minimise design changes after the production of piece parts had begun. By using a 3D modelling tool such as this it was possible to simulate the systems complete range of movement and detect any collisions or problems before production of the individual parts had begun. A picture of the developed laser scanning system is shown in figure 2.1. The laser scanning system is made up of a number of different assemblies. The system assembly drawings are presented in detail in Appendix E. The base assembly for the system is made up of a thick granite surface plate mounted on four elastic mountings to absorb vibration. Granite itself is a good medium for absorbing shock and vibration while also being much more dimensionally stable than either steel or cast iron. Granite also has a very low co-efficient of thermal expansion.

Figure 2.1 - Laser scanning system

The elastic mountings which the granite surface table sits on are constructed of rubber with a threaded bar protruding from the centre of one end. The mountings are fixed in threaded holes in the bottom of the granite table, see drawing ST-GR, Appendix C. These mountings were designed to protect sensitive machinery and equipment from shock and excessive vibration however they also allow a degree of relative movement thus reducing forces and tensions.

Four more elastic mountings were attached to the top surface of the granite table however these mountings differ from the previous one in that they have threaded bolts protruding from both ends. Fixed to the top of these elastic mountings was the $^{5}/_{8}''$ (15.875 mm) aluminium bolster plate to which the remaining main assemblies were attached. Fixed directly to the bolster plate was the Y-axis slide assembly, see Assembly Drg. #1 in Appendix E. The Y-axis slide was constructed from a single leadscrew stepper actuator assembly. This in itself is made up of a leadscrew (2mm movement per revolution) mounted on a length of aluminium extrusion. The whole leadscrew assembly was bolted through the aluminium extrusion onto the bolster plate. Aluminium was chosen as the main component material for the profilometer mainly because of it's machinability and low cost.

For added stability of the inspection table (which was mounted on the Y-axis leadscrew actuator carrier plate) two additional linear guides were mounted on the bolster plate, either side of the Y-axis slide assembly, see Assembly Drgs #2 and #4 in Appendix E. Two linear bearings support the inspection table and run along these guides, see figure 2.2.

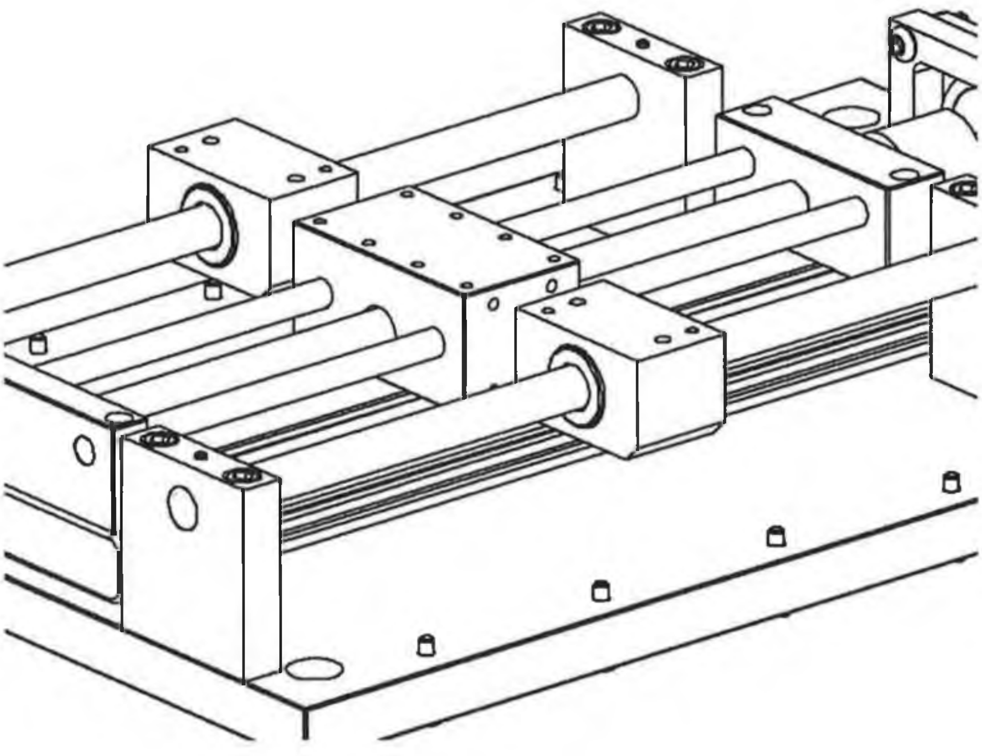

Figure 2.2 - Table assembly showing table linear bearings and guides

The inspection table was constructed from $^1/_4$" (6.35 mm) aluminium tooling plate, which has a total of 73 M3 tapped holes in it at a 17.5 x 18.4 mm spacing. These tapped holes allow specimens or samples to be mounted securely on the inspection table.

A stepper motor located at the opposite end of the leadscrew actuator assembly drives the leadscrew, which in turn drives the surface inspection table up and down the Y-axis. There are two stepper motors attached to the system, one to drive the Y-axis, shown in figure 2.3, and the other to drive the X-axis, shown in figure 2.4. The Y-axis carried the inspection table and the sample to be scanned. On the other hand, the X-axis carried the laser height measuring scanning head.

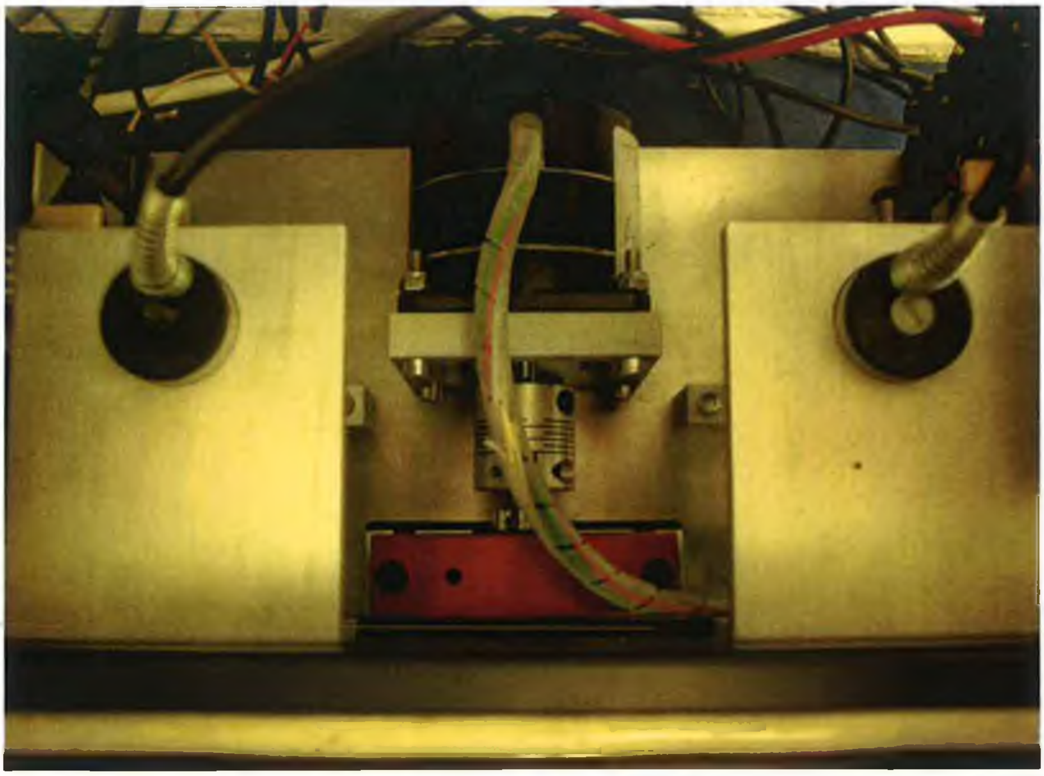

Figure 2.3 - Y-Axis stepper motor

Both of the motors were mounted in the same way (see Assembly Drg #3 in Appendix E) but in two different locations. The stepper motors were attached to an aluminium frame, which was in turn mounted in position using four small elastic mountings, again to absorb the vibrations from the stepper motors. The motors were coupled to the leadscrew drives through flexible couplings which allowed the motors to run non-concentric with the axis of each leadscrew without putting a shear load on the couplings or causing excessive vibration in the leadscrew bearings.

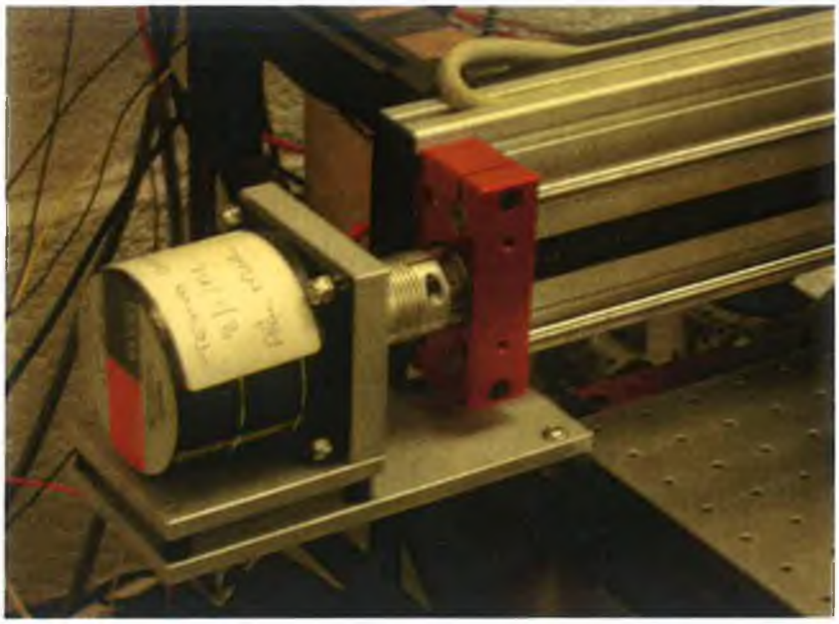

Figure 2.4 - X-Axis stepper motor

The frame assembly onto which the X-axis leadscrew assembly was fixed was also mounted onto the bolster plate. The frame was constructed from high tensile 20 x 20mm black anodised extruded aluminium alloy. The frame elements contained longitudinal grooves in the profile, which could be used in conjunction with many other connecting elements. The aluminium extrusion was chosen again due to it's machinability and because of it's modular design, allowing it to be easily fastened to other elements.

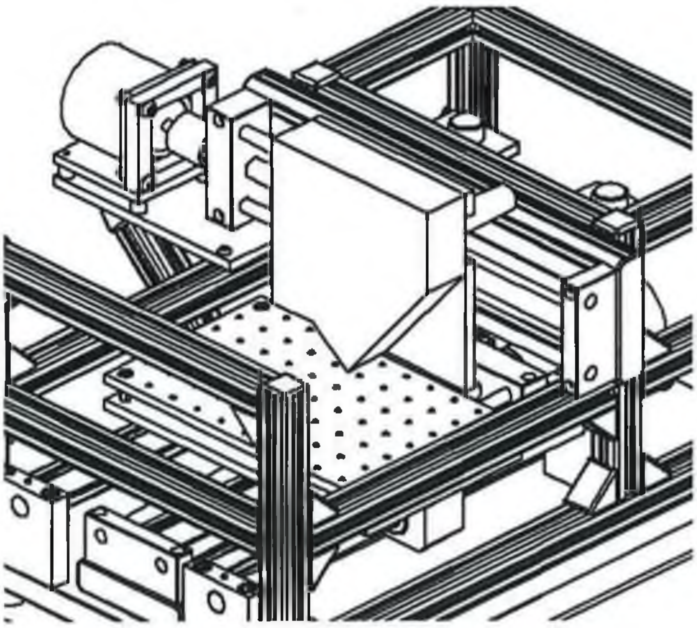

Figure 2.5 - X-Axis leadscrew assembly

The frame profiles also had a ∅4.2mm ID bore, which is suitable for use with an array of fastening elements. The frame assembly was designed such that the laser sensor and X-axis leadscrew assembly could be positioned at either end or at the centre of the system. Moving the laser sensor to the end of the system gives a broader scanning area since the X-axis assembly can also be mounted at on the end vertical members. For the purposes of the work presented in this thesis, the sensor and X-axis was located at the centre of the system, fixed to the centre pair of vertical frame members as shown in figure 2.5. Optimum areas of the surface inspection table for scanning operations are detailed further on in the thesis.

The laser sensor assembly was mounted on a manual linear stage, which was in turn mounted to the X-axis carrier plates. This linear stage was used to fine-tune the height of the laser above the table surface. The linear stage had a travel of ±7.5mm and could be locked in place during operation of the system.

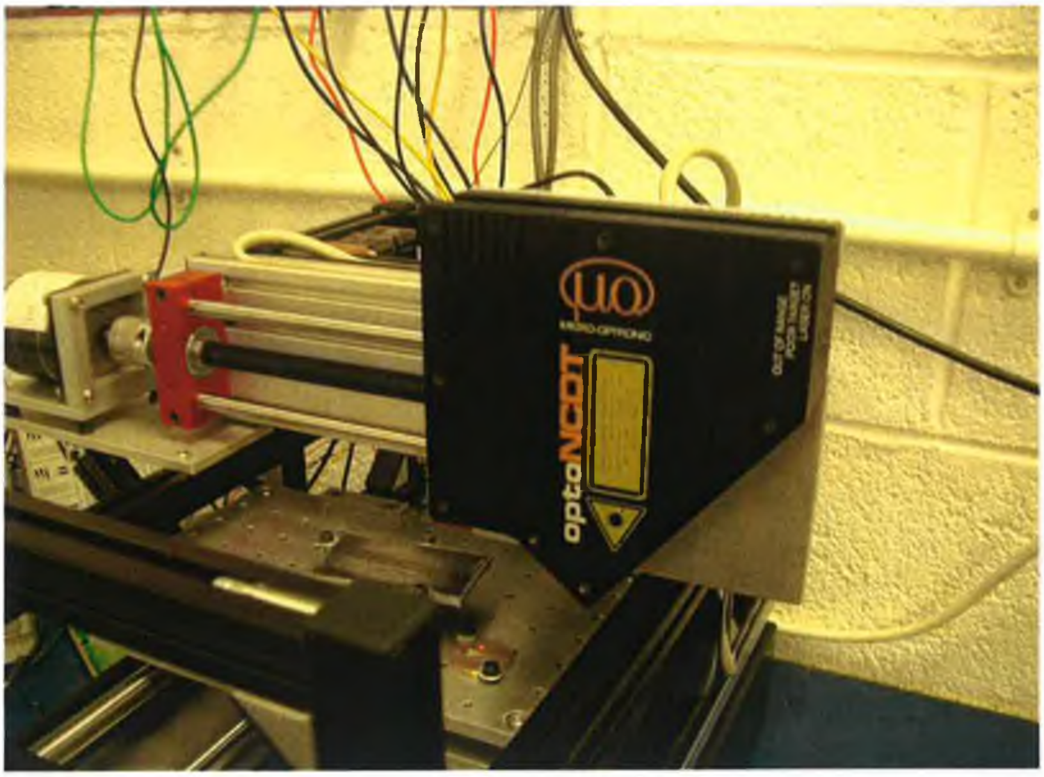

Figure 2.6 - X-axis leadscrew and laser displacement sensor

The laser displacement sensor attached to the linear stage was a Micro-Epsilon OptoNCDT 2000. The sensor operates on the principle of optical triangulation, which was detailed in section 1.7. A visible (laser diode), modulated point of light is projected onto the target surface[54]. The beam passes through a focusing lens which converges the beam to an average spot size of 90μm. The light spot is reflected onto a CCD array through an imaging lens. The position of the imaged spot of light determined from the CCD, is relayed as a real-time signal voltage (±5V_{DC}) which is proportional to the height of the laser sensor above the target surface.

The reflection factor range of the unit is very wide, from almost total absorption to almost total reflection. The system was designed so that continuous scanning could be possible as the part moved beneath the laser. Due to excessive vibration of the laser sensor during movement of the laser head assembly in the X-axis, it was decided early on during experimental work that the scans over target surfaces should be a straight line in the Y-axis. This vibration may have been caused by the moment acting on the laser displacement sensor assembly along the axis of the leadscrew. Because the leadscrew assembly is not supported by additional guides, this moment force could cause the sensor assembly to vibrate back and forth very slightly, and thus causing errors in the scan. One step in the X-axis would then be performed before recommencing the next straight line scan in the Y-axis. Two LVDTs (Linear Variable Displacement Transducers) were also attached to the X-axis leadscrew assembly to measure vibration of the X-axis during continuous scanning. The LVDTs measured minute changes in the height of the X-axis assembly above the bolster plate. The control program is detailed in section 2.2.4.

The signal from the displacement sensor was taken into the data acquisition (DAQ) card as a differential signal ranging from $-5V_{DC}$ to $+5V_{DC}$ corresponding to a height between –2.5mm and +2.5mm about the nominal. A 1kΩ load resistor was connected in series with the voltage signal and helped to reduce noise and stabilise the signal from the sensor. The total sensor output voltage range was $10V_{P-P}$ for a Z height range of 5mm. The recorded signal therefore needed to be divided by 2 to give the actual Z height measurement (e.g. $2V_{P-P}$ represented 1mm height differential). All graphed results including 3-D digitised surfaces were post processed to present the data on a micrometer or mm scale with the graphed points shifted to set the first height point acquired to zero, i.e. a datum shift of all data.

2.2 Electrical & control software development

The electrical design of the system was developed around the two stepper motors moving the axes and the voltage acquisition from the laser displacement sensor. Electrical wiring schematics of the individual motor circuits, power supply, and laser sensor circuits are given in Appendix D. Each of the I/Os from the motor control boards and laser sensor were wired back to a breakout box (terminal box), which was connected to the data acquisition card in the attached PC. In addition to simply acquiring data from the terminal box, the data acquisition card was also used to output drive voltages and a clock output to drive each of the stepper motors. Outputs from the data acquisition card were controlled using software developed in LabVIEW, a National Instruments graphical programming package. Similarly, the same program was used to record the output voltage from the displacement sensor. Overall, four different programs were developed for the scanning process – a main program for controlling the scanning system which could be used to execute a raster scan over a selected area, a smaller program used for positioning the laser spot at the start position before a scan, a 3D plot program which could display the digitised surface after scanning, and a program which could transpose the recorded data matrix for post processing.

2.2.1 LabVIEW v6.1

LabVIEW (Laboratory Virtual Instrument Engineering Workbench) is a graphical programming language in which functions represented by icons are connected together to write the program instead of lines of text. The programs or VIs (Virtual Instruments) used to drive the stepper motors and record the signal from the laser sensor were developed using LabVIEW 6.1. The program developed allowed to acquire the voltage output from the laser displacement sensor while simultaneous controlling the systems stepper motors.. The VI developed was designed to run autonomously. The scan characteristics could be input from the GUI main screen before each scan was recorded. The control program is presented in detail in section 2.2.4

2.2.2 Data acquisition card & break-out box

A SCB-68 break-out box and a PCI 6024E data acquisition (DAQ) and control card used in this work. The PCI 6024E card has a total of 16 single ended or 8 differential analogue inputs, 2 analogue outputs, 8 digital I/Os, and 2 clocks. Using this arrangement it is possible to acquire data for analysis in the LabView software environment. Figure 2.7 shows the layout of the SCB-68 board.

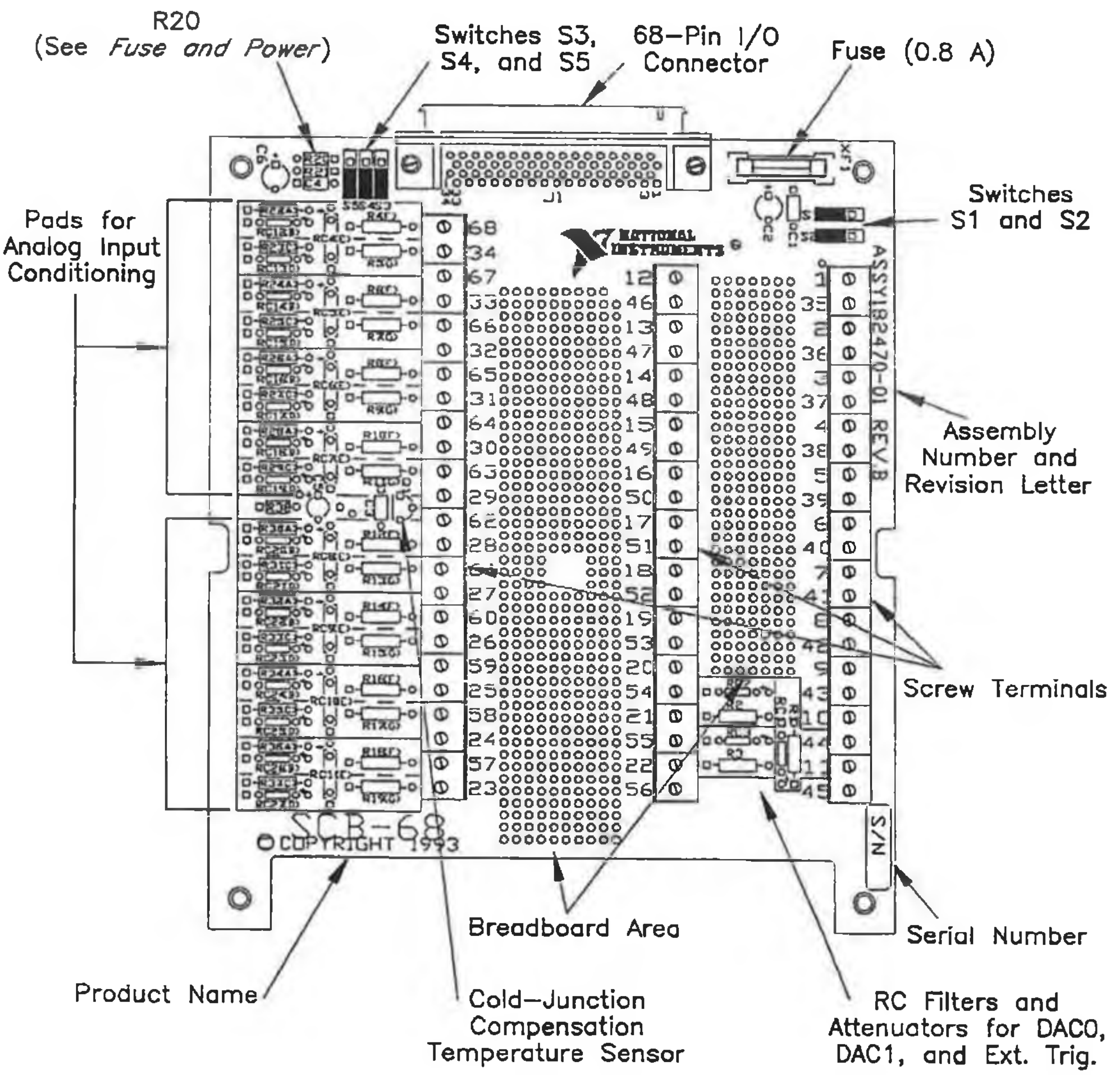

Figure 2.7 - SCB-68 board layout[10]

2.2.3 Stepper motors

The stepper motors were controlled by two IM483 stepper motor control boards. Each board was powered by a $+12V_{DC}$ taken from one of the 3 output 0-30V power supplies. Each IM483 driver board could be configured to output between 400 and 51200 steps per revolution, resulting in a leadscrew movement range from 3.9 x 10^{-2}μm to 5μm per pulse. The clock signal to drive the stepper motors was taken from the DAQ board and controlled via the LabVIEW software and the DAQ (data acquisition) card. The clock output form the DAQ card was selectively sent to either of the two motor control boards by sending a digital signal to a Phillips 3 to 8 line inverting demultiplexor. A single clock signal was output from the DAQ card to the demultiplexor chip. By sending a high or low signal to the enable inputs on the chip the output clock signal could be routed through up to 7 output channels (only 2 output channels were needed in this work). Using this method, either one of the stepper motors could be driven to move either the X or Y-axis in a positive or negative direction. The direction of rotation of each motor was selected by sending a low or high signal (+0V_{DC} or +5V_{DC}) to Pin 3 of the motor control board, see electrical wiring schematics in Appendix D. All surface and straight-line scans were run with 51,200 steps per revolution (256 micro-steps per step). Table 2.1 details the stepper motor control board settings.

Table 2.1 - Stepper motor control board settings

Micro Steps / Step	Dip Switch Settings				Steps / Revolution	µm / pulse
	1	2	3	4		
2	ON	ON	ON	ON	400	5
4	OFF	ON	ON	ON	800	2.5
8	ON	OFF	ON	ON	1,600	1.25
16	OFF	OFF	ON	ON	3,200	6.25×10^{-1}
32	ON	ON	OFF	ON	6,400	3.125×10^{-1}
64	OFF	ON	OFF	ON	12,800	1.56×10^{-1}
128	ON	OFF	OFF	ON	25,600	7.81×10^{-2}
256	OFF	OFF	OFF	ON	51,200*	3.906×10^{-2}

*For all incremental scans the motor control board is configured for 51,200 pulses/rev

2.2.4 Control methodology

Initial testing using a continuous scan method with a maximum data sampling rate (200 kHz) led to difficulties obtaining a constant scan rate due slowness in the speed of the PC. This also proved difficult to implement as the simultaneous collection of time stamps and measured points resulted in excessive memory usage for high resolution scans or scans over large areas.

Once the system had been set up various scans were made to test the program to ensure proper scan direction, scan step, number of scan increments, and scan measurements. One of the first 2D test scans was of a 20 Cent coin and the features on its surface proved to be very useful in determining system stability in both the X and Y axes. The coin was chosen simply for proving the principle of operation. The second version of the control methodology was straightforward. A finite number of pulses were output to either the X or Y-Axis motor, thus moving the laser scanner over the target surface or vica versa. Once this VI was activated the user would then activate an additional VI to record the voltage received from the laser displacement sensor's camera and save it to file. The second (data acquisition) VI was linked to the first VI so that it would terminate once the first VI had output the desired clock pulses to the active stepper motor.

The program was then developed further to use a fixed frequency scan of 1kHz. By using a fixed frequency it was possible to scan the target surface at a known constant speed and calculate the distance between each scan point taken. A number of test scans were run, again over the 20 Cent coin, however it was clear that the scanning frequency was erratic, varying between 700Hz to 1kHz. It was determined that a lot of the system memory was being used to write the data to file and that the changing available memory on the user PC was having an adverse effect on the scan frequency as less memory was available to deal with running the control and data acquisition VIs.

To overcome this problem a scan cycle was developed which moved across the target surface in steps. The voltage from the laser sensor was recorded after an increment rather than continuously. This type of scan ensured that height points were captured at the specified locations. It also allowed for a time delay to be introduced ensuring the axis movement had stopped before the height data was recorded. This scan methodology was further developed to allow raster-scanning patterns over the target area. This type of movement improved the accuracy of the system by ensuring the X-axis was stationary before data acquisition.

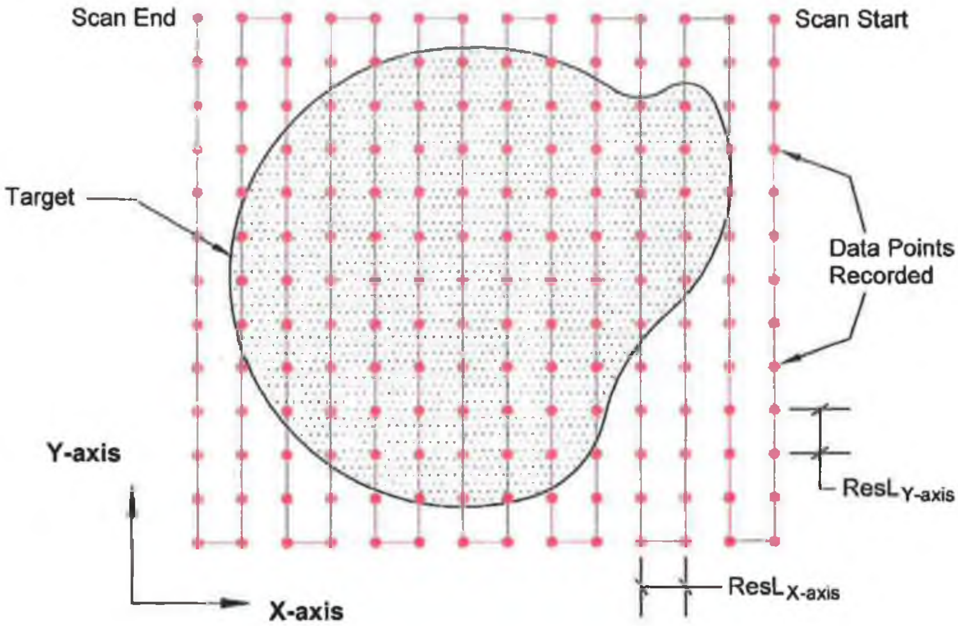

Figure 2.8 - Sample incremental raster scan

Figure 2.8 shows a sample incremental raster scan, each point representing a location at which a voltage is recorded from the laser displacement sensor. The distance from one of these points to the next is the incremental scan resolution, Res_L. The movement of the beam over the target surface is along the path traced from the scan start point to the scan end point as shown. The sample above is made up of fourteen passes in the Y direction. The lateral resolution of the scan will affect the quality of the surface information captured.

However, by increasing the lateral resolution so that each step size is small, a high-resolution image of the target surface can be achieved. Increasing the lateral resolution can however decrease the performance of the system on a number of levels and may actually be detrimental to the quality of the recorded data. The higher the resolution the more data points that must be recorded thus increasing the time it takes to scan a given area. In addition, using a small stepper motor and a high lateral resolution can lead to errors from sticking friction in the leadscrew assembly thus having an adverse effect on the integrity of the collected data.
Figure 2.9 shows the GUI or front panel of the main data acquisition program called *Scanner Controller Main*. Movement in both the X and Y-Axis can be manipulated through speed

(*Frequency*), distance (*Number of pulses* = number of pulses per increment) and the number of *Scan increments*. The lateral resolution (Res_L) is defined by the number of pulses per increment. For example, if the stepper motor controller has been set up to output 51,200 pulses per one revolution of the leadscrew, then 25.6 pulses is equivalent to a Res_L of 1μm (1 revolution of the leadscrew = 2mm linear travel). For all scans made during the testing of the system, the Res_L of both the X and Y-axis were kept equal. The *Number of Passes* required over the target surface is input by the program user below the motor settings. For a simple straight line scan in the Y-axis, the *Number of passes* would be set to 1 and the *Number of pulses* and *Scan increments in the X-Axis* would both be set to 0. The scan can be set to move in either the positive or negative X-Axis by clicking the *Reverse X Direction* button. The X-Axis direction is set to negative as default. The scan can be set up so that the program will run continuous scans by selecting the *Loop* button – this loop must be stopped manually by selecting the *Loop* button again.

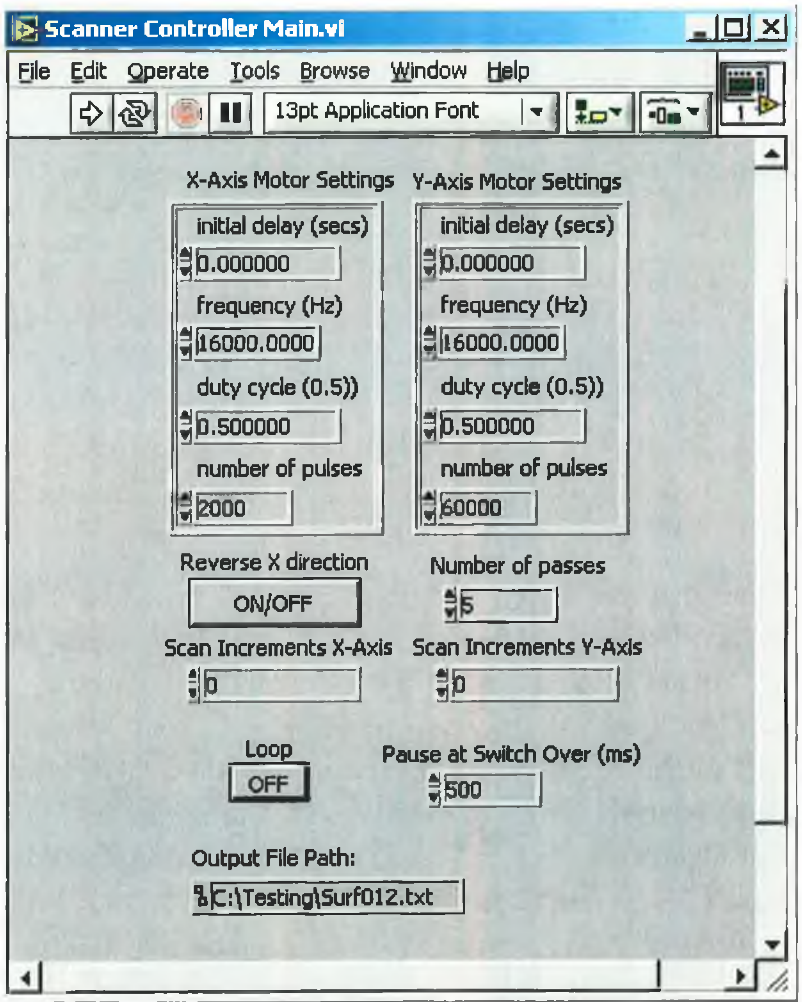

Figure 2.9 - Scanner controller main.VI (front panel)

Table 2.2 – Labview symbols

	This Boolean constant provides a constant FALSE value to the block diagram.
	Integer number, 32 bit.
	This VI writes one point (a logic high or low) to the digital line which controls the Y-axis motor direction.
	Computes the integer quotient and the remainder of the inputs.
	Use the numeric constant to pass a numeric value to the block diagram.
	Returns TRUE if **x** is equal to **y**. Otherwise, this function returns FALSE.
	Returns TRUE if **x** is equal to 0. Otherwise, this function returns FALSE.
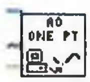	Generates a timed, simple-buffered waveform for the given output channel at the specified update rate.
	Indicates the IVI instrument which it will communicate with, in this case channel 0.
	Single-precision floating-point number which have a 32-bit IEEE single-precision format.
	Long unsigned integer number, 32 bit.
	Waits the specified number of milliseconds before returning the value of the millisecond timer.
	This VI generates a finite pulse train using two counters.
	Gate parameter which contains the gate source, gate signal, gate mode, and reserved parameters.
	Converts a 2D or 1D array of single-precision numbers to a text string and writes the string to a new byte stream file or appends the string to an existing file.
	File path.

Table 2.2 above shows the LabView symbols used in the *Scanner Controller Main* VI.

During initial 3D linear scan testing problems occurred frequently when the signal switched from one motor to the next through the demultiplexor. As the signal was switched from one motor onto the other, the first motor would stall (effectively become stationary with a slight oscillation). It was discovered that adding a slight delay in the program during demultiplexor switching solved this problem. The last configurable parameter in the VI is the output file path. The output file is in an N x M matrix format where N is the number of increments in the Y-Axis and M is the number of passes.

Figure 2.10 shows the first page of the program (known as a block diagram) of the VI described above. The main structure of the program is comprised of a WHILE and FOR loop. The FOR loop controls the number of passes in the linear scan and will continue to trigger the program loop until it has finished out the required number of passes. Inside the FOR loop is a SEQUENCE structure made up of 7 distinct sequences. Each of these sequences represents a part of the control of one individual scan.

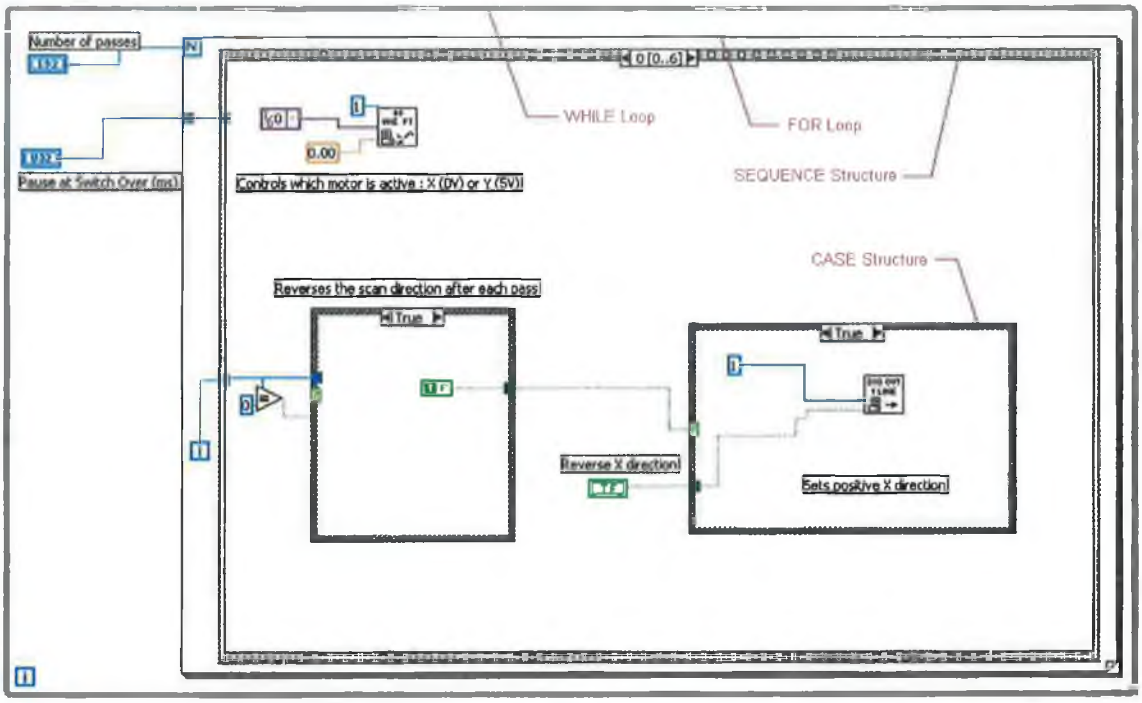

Figure 2.10 - Page one of the data acquisition program (reverse direction condition - true)

Essentially, this VI is a sequence structure and will continue to loop until all of the scan passes have been completed. The VI will write a data point to file after each step, see figure 2.16, and this will be repeated for each pass by the number of increments in each pass before the direction of the Y-axis is changed, see the case structure in figures 2.14 and 2.16.

The WHILE loop will continue to loop the VI as long as the *Loop* option is selected on the front panel. The first CASE structure at the bottom of this VI image will not be active unless the *Reverse X Direction* option is selected. The digital signal output function in the CASE structure outputs a high signal to the DAQ's digital line 1 or DIO1, through Pin_{17}. This is connected to the X-Axis stepper motor controller, Pin_3. This signal will remain high unless the *Reverse X Direction* option is selected. In the top left corner of the figure above is the function which selects which motor (axis) is active. This function writes a single voltage value to the specified analogue output channel, in this case, channel 0. Channel 0 is output to the demux, Pin_6 through Pin_2 of the DAQ card. This analogue signal output icon is located in the top left of the sequence structure, and will output either a 0 or +5V signal depending on the active leadscrew - 0V being the Y-Axis and +5V being the X-Axis.

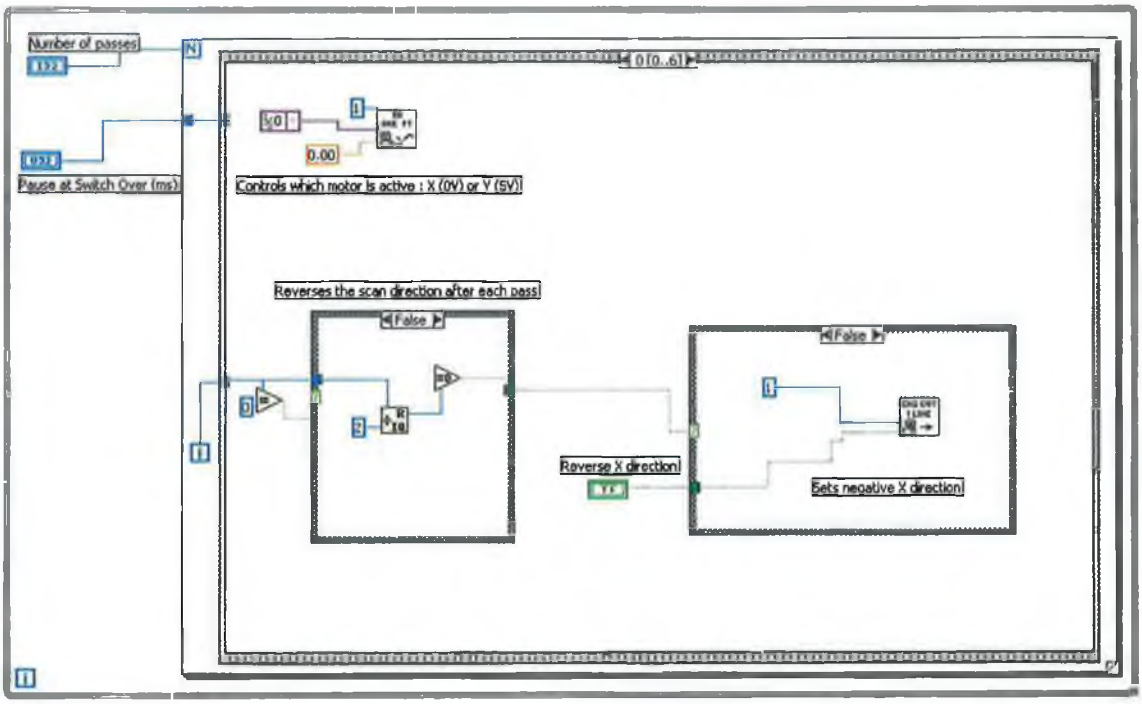

Figure 2.11 - Page one of the data acquisition program (reverse direction condition - false)

Figure 2.11 shows the FALSE of the CASE structures on the first sequence page of the program structure. The second page of the SEQUENCE structure is shown in figure 2.12. This is simply a small time delay to ensure no 'crossover' between the demultiplexor outputs. The delay time was set to 500ms as default but is a user definable setting.

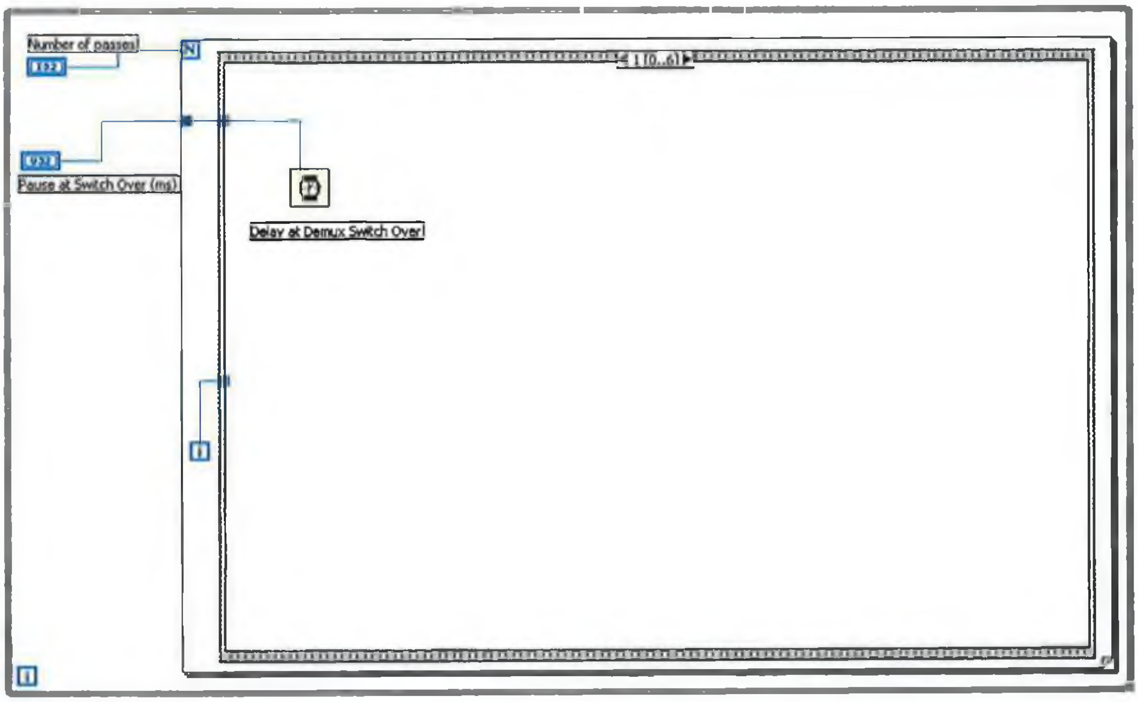

Figure 2.12 - Page two of the data acquisition program

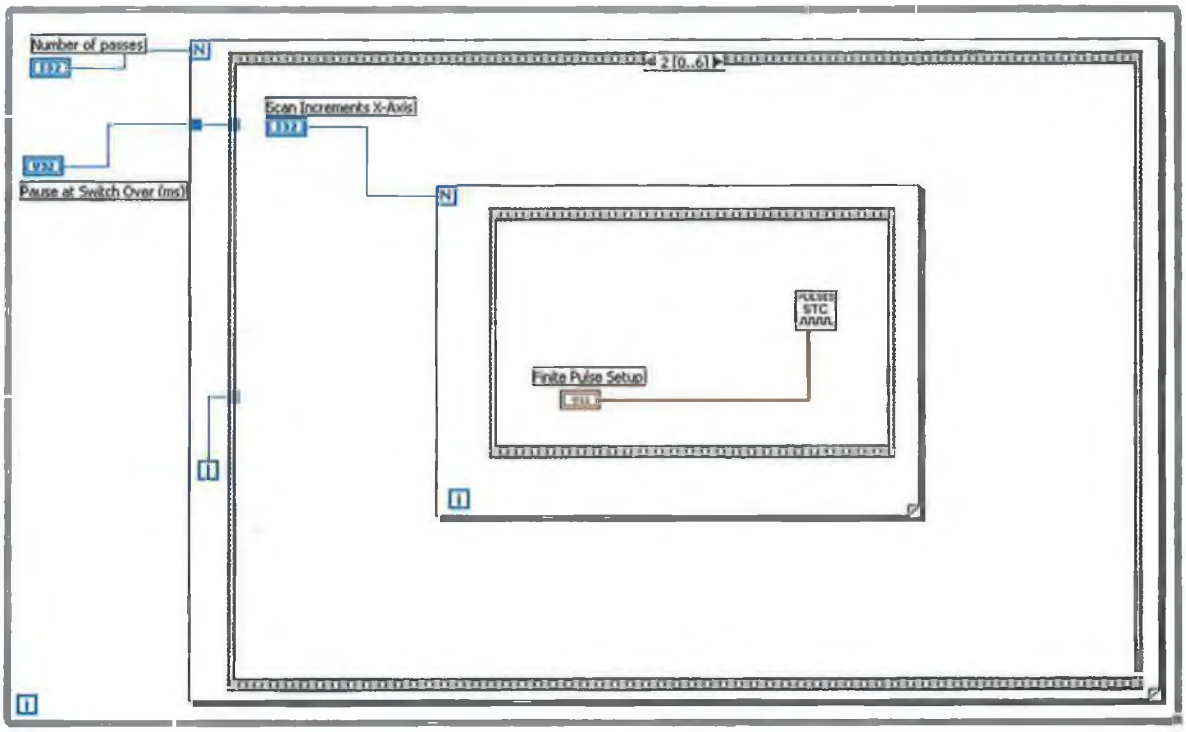

Figure 2.13 - Page three of the data acquisition program

Figure 2.13 shows the third page of the program. This section of the program moves the laser sensor over the target surface by the number of increments selected on the VI front panel.

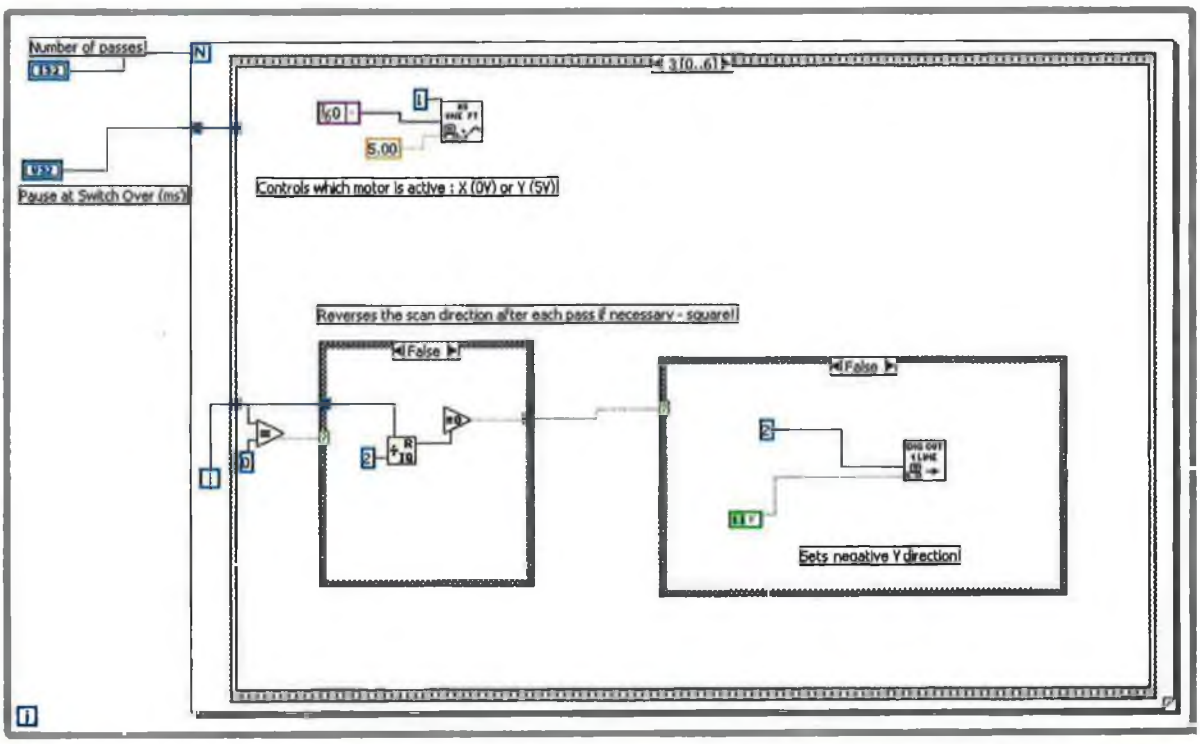

Figure 2.14 - Page four of the data acquisition program (reverse direction condition - false)

Figure 2.14 is similar to the first page of the SEQUENCE structure of the VI but in this case the Y-axis is configured to move rather than the X-axis. On the top left of the sequence the analogue output is visible, this time outputting +5V, again to Channel 0 which is Pin_2 of the DAQ card. Also, the digital output function in the CASE structure sets the direction of the Y-Axis motor on digital channel 2, through Pin_{49}. This is connected to the Y-Axis stepper motor controller, Pin_3 of the motor control board.

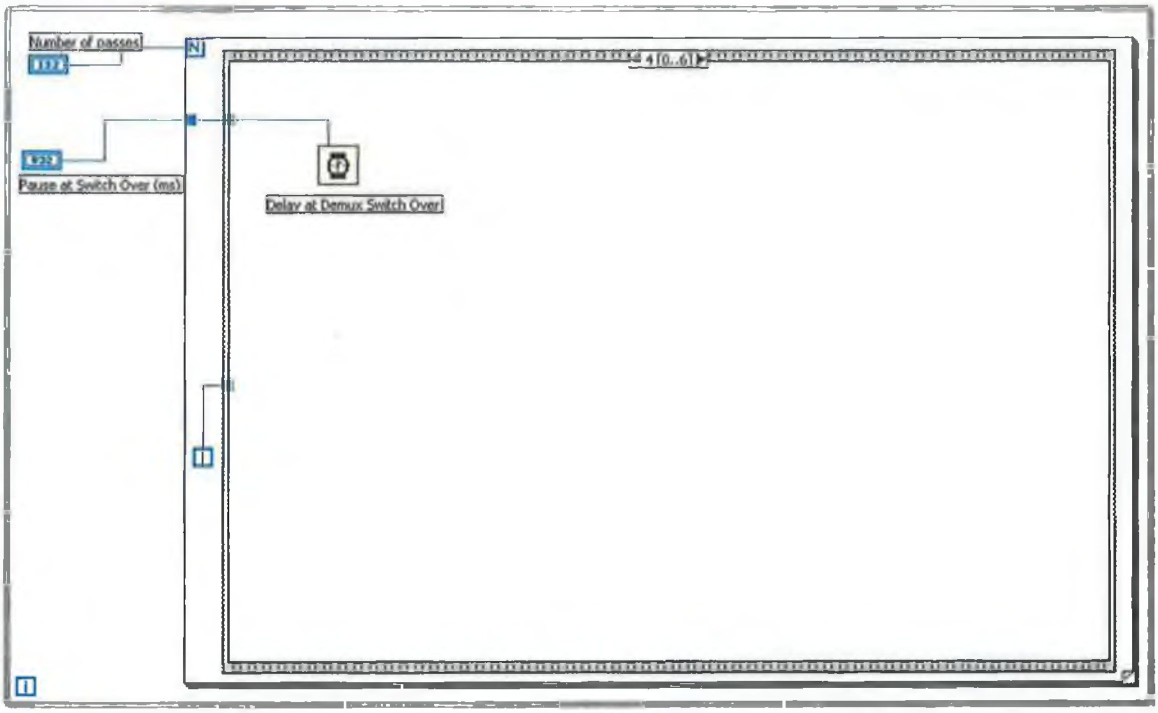

Figure 2.15 - Page five of the data acquisition program

The next sequence in the program, figure 2.15, is similar the second page of the structure - a 500ms delay is executed before the subsequent sequence which moves the Y-Axis. Figures 2.16 and 2.17 show the sixth page of the sequence structure. In this sequence the incremental movement of the Y-axis is controlled, as is the signal acquisition from the laser sensor after each movement. The sequence structure for this, shown in these figures, is made up of 2 pages and is located in a FOR loop which will repeat continuously for the amount of scan increments in the Y-Axis specified on the front panel.

The CASE structure on the bottom of figure 2.16 changes the direction of the Y-Axis, and continuously changes the direction of the Y-axis movement after each pass before saving the scanned data to file. As can be seen from the VI, the system will only capture a data point after the Y-axis has incremented, ensuring that both axes are stationary during data acquisition.

The Write Point to File function collects each acquired data array to the file path set by the user. This file is in matrix format as described earlier.

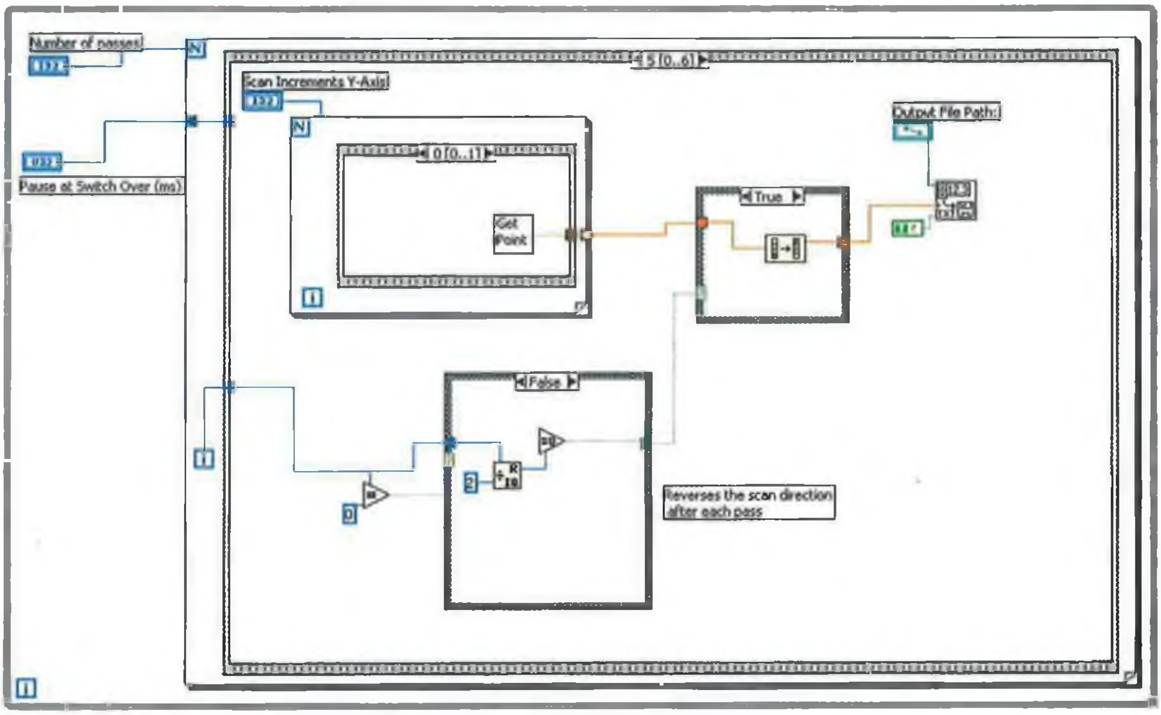

Figure 2.16 - Page six of the data acquisition program (sequence 0)

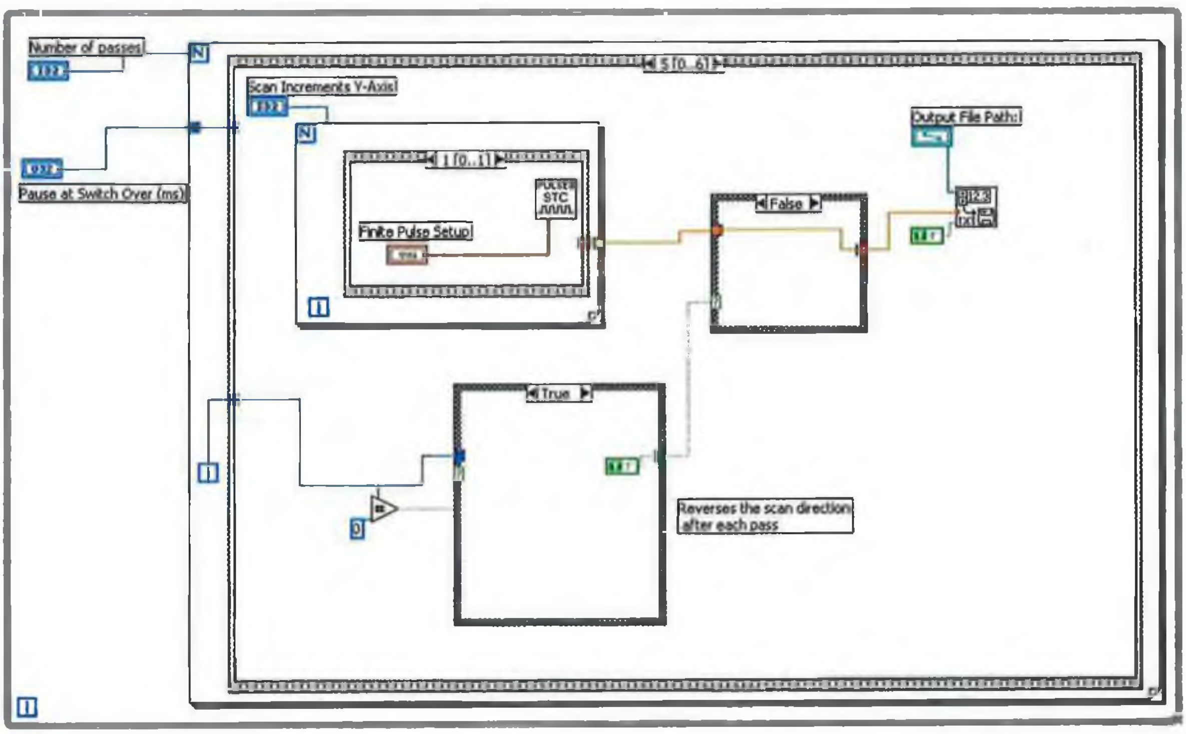

Figure 2.17 - Page six of the data acquisition program (sequence 1)

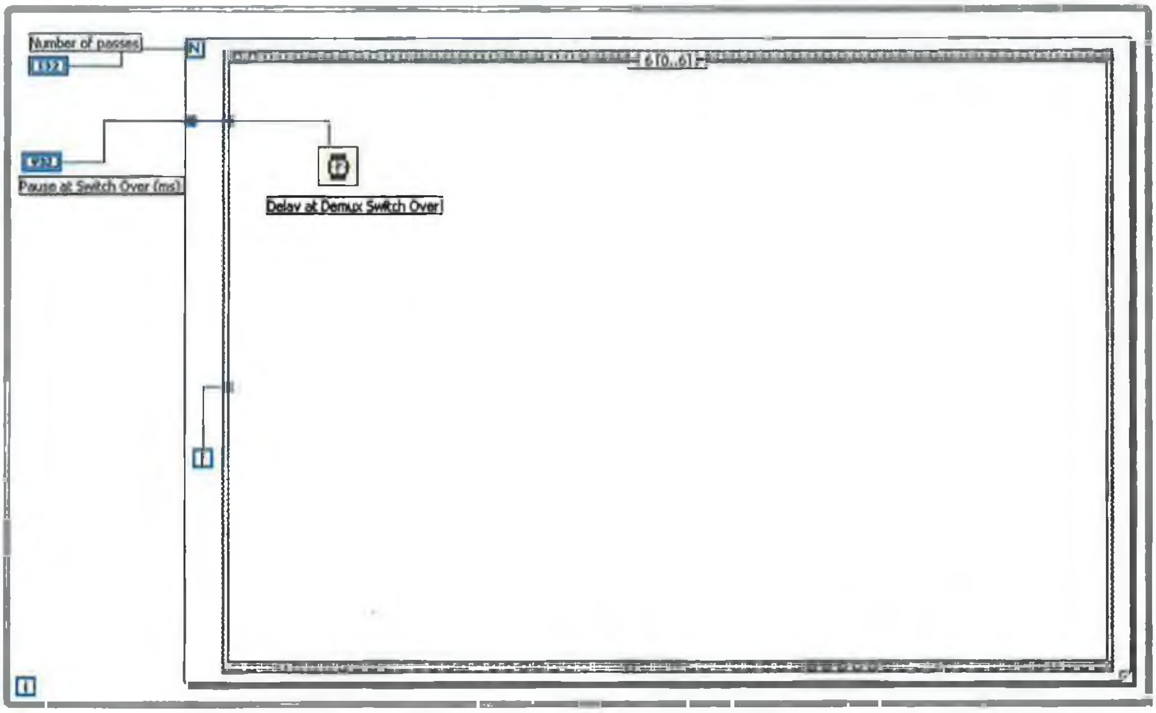

Figure 2.18 - Page seven of the data acquisition program

The last page of the cycle shown in figure 2.18 initialises another time delay of 500ms delay before returning to page 1 of the SEQUENCE structure.

Chapter 3 Experimental set-up and test procedures

This section deals with testing the laser profilometer. Sections 3.1 to 3.4 describe various tests which measure the systems performance, resolution, and deviation over various distances. Sections 3.5 to 3.9 details tests which describe the capability of the profilometer while measuring various surface types and surface roughness.

3.1 X and Y-axis dynamic stability

This test was executed in order to determine signal 'noise' in the output voltage of the displacement sensor during normal operation. Based on the results of the scans (X-axis and Y-axis), the signal acquisition section of the program was developed further so that no scanning would occur during movements causing high levels of vibration.

Experimental setup

In order to compare the recorded data from both the X and Y-axis scan a surface with a well defined varying features was required. For this purpose, an Irish 20 Cent coin was used and set up on the system table as shown in figure 3.1 so that the beam was scanned across an arbitrary area of the surface of the harp, on the tail side of the coin from point A to B. The coin was chosen because its varied profile will clearly define any deviation between the scans across the two axes. Scan length for this test was 6.25mm. A magnified view of the scan line is shown in figure 3.2. The coin was clamped on the measurement table and scanned in the X-axis direction. The coin was then rotated through 90 degrees and scanned in the Y-axis direction. The laser spot was positioned approximately 0.75mm to the right of the harp on the coin for the X-axis scan. The exact start position of the Y and X axis scans relative to one another was not critical as the purpose of this test is to compare vibrational 'noise' of the two axes.

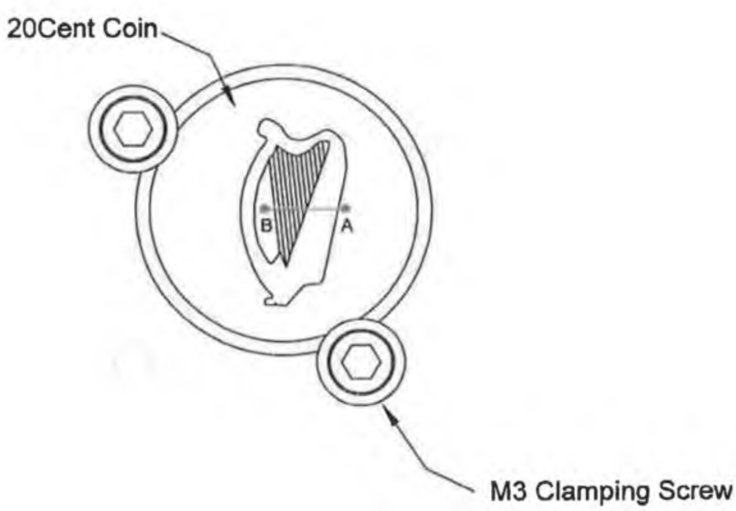

Figure 3.1 - Clamping arrangement of coin showing scan path across an Irish 20 Cent coin

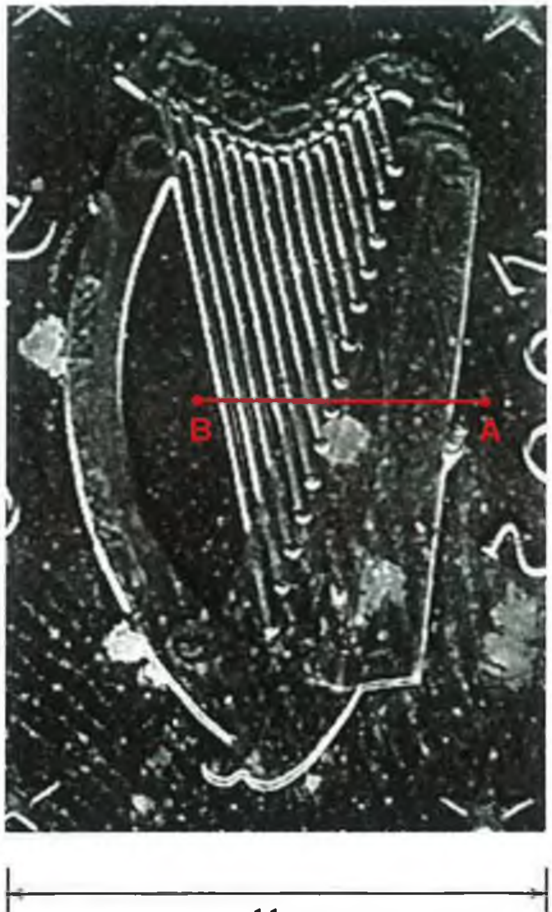

Figure 3.2 - Magnified view of laser scan path across an Irish 20 Cent coin*

*Image taken with a Reichert 344817 microscope

Experimental procedure – (1) Axis Stability Comparison

The laser spot was positioned in location A (see figure 3.2) using the VI *Position Zero Point*. Using the *Scanner Controller Main* VI, the X-axis direction was set to negative and the system settings shown at the end of section 3.1 were selected. During X-axis scans, the laser spot was moved over the coin through the movement of the laser head assembly on the X-axis leadscrew. Once the X-axis had reached point B (2500 clock pulses to motor) the program automatically terminated and a data file *data.txt* was written to the hard drive of the computer. This data was then imported to Microsoft Excel. The laser spot was once again repositioned at point A using the *Position Zero Point* VI (negative movement of 2500 clock pulses) – this procedure was repeated three times and an averaged profile result was calculated. For the Y-axis study, the coin was turned by 90° on the measurement table and clamped in the same manner as for the X-axis scan. The experimental procedure was the same as for X-axis scan with three separate scans taken and averaged. This test was critical in order to develop the control program before testing the systems dynamic height resolution.

The *Scanner Controller Main* VI motor settings for the X and Y-axis dynamic stability tests are shown below:

X-axis motor settings

- Initial delay (s): 0
- Frequency (Hz): 250
- Duty cycle: 0.5
- Number of pulses/increment: N/A
- X-axis motor, step size: 0.0025mm (800 steps/revolution)

Y-axis motor settings

- Initial delay (s): 0
- Frequency (Hz): 250
- Duty cycle: 0.5
- Number of pulses/increment: N/A
- Y-axis motor, step size: 0.0025mm (800 steps/revolution)

3.2 Z_{HEIGHT} dynamic resolution

Testing of the Z-axis resolution or the true vertical resolution of the laser scanning system was achieved by scanning a 1.005mm thick slip gauge mounted on three strips of 0.0508mm thick steel shim. The tolerance on the gauge was ±2μm and the true width of the gauge was measured as 1.007mm with a Mitutoyo FS70 inspection microscope.

Experimental setup

The gauge was laid flat over three strips of 0.0508mm thick shim and clamped to the measurement table using four M3 screws and two aluminium clamping jigs, see figure 3.3. The shims (denoted as S in diagram) were used to ensure that a good surface contact was made across the width of the gauge. This was vital, as the thickness of the gauge would be measured from the top surface of the gauge to the top of the shim. The gauge was aligned with the X-axis of the measurement table, as scanning movement for this experiment was in the Y-axis. Two sets of three scans were run over the slip gauge from point A to point B, see figure 3.3. The lateral resolution (Res_L, Y-axis step size) was set to 2μm for the first set of scans and to 1μm for the second set of scans.

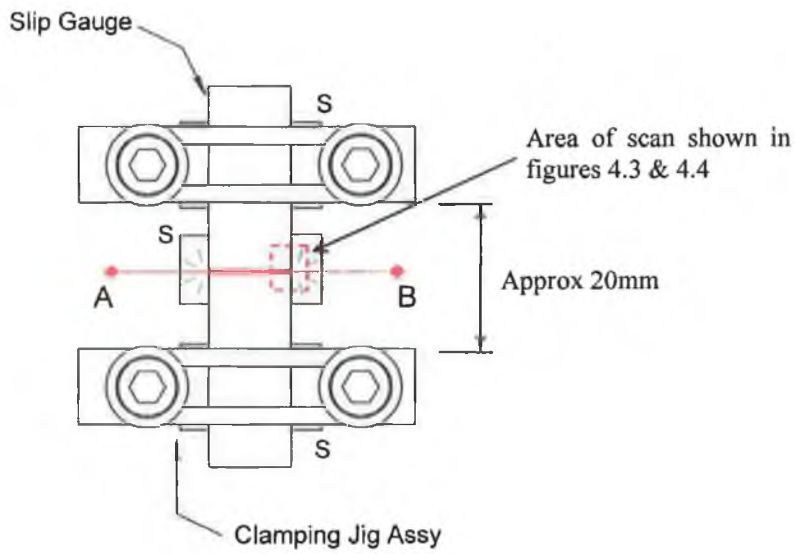

Figure 3.3 - Experimental setup for Z-axis resolution

Experimental procedure

The laser spot was positioned directly over the slip gauge and the vertical linear stage was adjusted so that the laser sensor could scan the complete Z-axis range required. The laser head assembly was then positioned in the X and Y-axis off to one side of the gauge at location A using the *Position Zero Point* VI, see figure 3.3. Two sets of scans were recorded by moving the table in the Y-axis under the laser spot (X-axis kept stationary for all scans). The first scan was made with a lateral step/resolution of 2µm and the second with a step of 1µm. Each scan set was made up of three separate scans run from point A to B, a distance of 15mm. After each scan, the laser spot was repositioned at point A using the *Position Zero Point* VI. For the 2µm step scans a total of 7,500 data points were collected while 15,000 data points were collected for the 1µm step scans. Each pass generated a *data.txt* data file, the contents of which were copied to Microsoft Excel after each pass. Average scan results were calculated and plotted from these data points for the two lateral resolutions.

The *Scanner Controller Main* VI motor settings for the X Z_{HEIGHT} dynamic resolution test are shown below:

X-axis motor settings

- Initial delay (s): 0
- Frequency (Hz): 16000
- Duty cycle: 0.5
- Number of pulses/increment: 42 (2µm Res_L) / 26 (1µm Res_L)
- X-axis motor, step size: 0.039µm

Y-axis motor settings

- Initial delay (s): 0
- Frequency (Hz): 16000
- Duty cycle: 0.5
- Number of pulses/increment: 0
- Y-axis motor, step size: N/A

3.3 X and Y-axis accuracy & repeatability

The lateral accuracy and repeatability of the system was largely influenced by the accuracy and repeatability of the stepper motors and of the leadscrew itself. Too much play in the motors and leadscrew will reduce the overall accuracy and repeatability; also, sticking friction in the stepper motors will have an adverse effect and will result in an increasing error over greater distances. The 1.007mm slip gauge was employed again to measure the X and Y-axis accuracy and repeatability. In order to do this the slip gauge was mounted on the measurement table at a known angle. The laser displacement sensor was designed with a static resolution of 0.25µm which is far more accurate than the achievable X or Y-axis accuracy making it ideal for measuring deviation in the axes movement. By using basic trigonometry, any positional error in either the X or Y-axis could then be recorded by comparing the measured Z_{HEIGHT} to the theoretical height for that location. Lateral accuracy and repeatability of the system is an important factor that must be taken into account when scanning any surface, but it is especially important when scanning over larger areas.

Experimental setup

In order to measure the system accuracy and repeatability of both the X and Y-axis, the 1.005mm slip gauge was mounted on the measurement table at an angle of 26.6° which gave a slope of about 1:2. The angle of the gauge was measured using the displacement sensor as shown. The angular tolerance of this setup is approximately 0.06°. The gauge was scanned prior to testing for each axis and the slope plotted to ensure that it was exactly 1:2 (the slope of the gauge could be adjusted by adjusting the height of the fixing screw on its upper end), see figure 3.4.

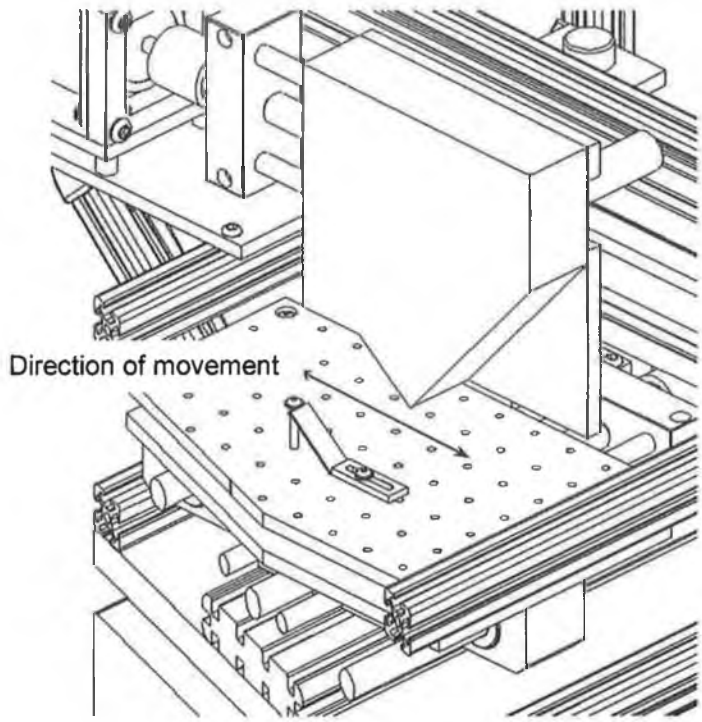

Figure 3.4 - Experimental setup for X-axis repeatability

In order to measure the performance of the X-axis, the gauge was aligned along the X-axis sloping upwards in the positive axis so that the gauge itself would not obstruct the view of the camera, see figure 3.4. Similarly, the gauge was aligned with the Y-axis to measure Y-axis performance as shown in figure 3.5.

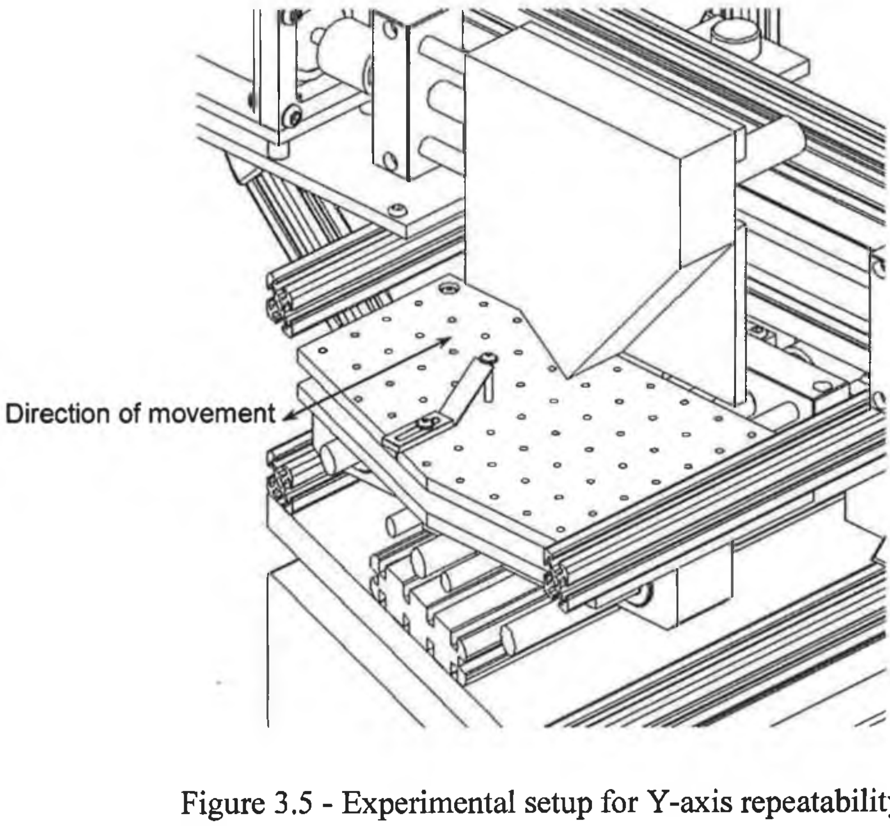

Figure 3.5 - Experimental setup for Y-axis repeatability

A schematic of the gauge set-up is further is shown in figure 3.6. The gauge is set up on the measurement table as shown and the laser spot is moved to position 1, see figure 3.6, beam position 1 in the diagram. The linear stage holding the laser head assembly was adjusted until the output voltage form the sensor head read zero. This voltage was recorded as V_1. The laser spot was then moved along the X-axis to position A (movement X_1 in the diagram) by means of the *Position Zero Point* VI. From point A, the laser spot was moved by the same number of steps back to it's original position on the gauge, movement X_2 in the diagram. Theoretically, the laser spot should now be in the exact same location as before, however due to sticking friction and play in the motor and leadscrew this is not the case. The laser spot ends instead at beam position 2.

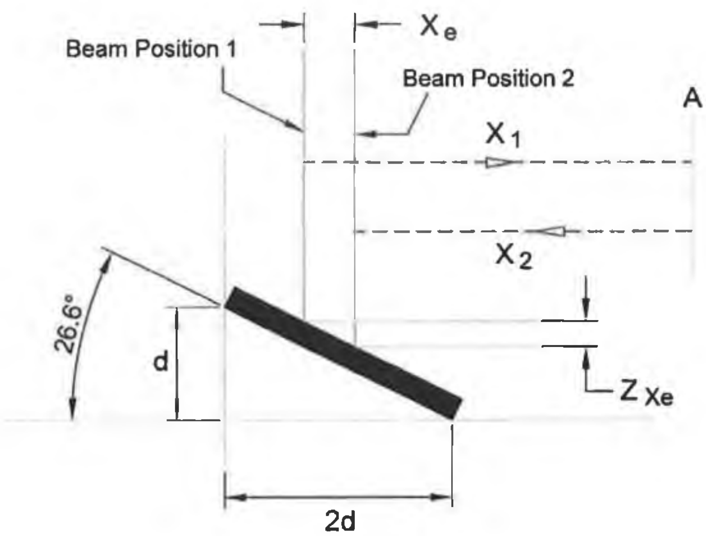

Figure 3.6 - Theoretical setup for repeatability testing

Taking a second reading from the camera sensor output voltage (V_2) and comparing it to V_1 allow calculation of the height variation between the two beam positions of Z_{Xe}. Once Z_{Xe} was calculated it was straightforward to calculate the lateral deviation X_e as:

$$X_e = 2.|Z_{Xe}|$$

eq 3.1

This test was run five times for nine different distances; 2.0mm, 5.0mm, 10.0mm, 20.0mm, 30.0mm, 40.0mm, 50.0mm, 60.0mm and 70.0mm. The Z-axis datum was set to zero at the start of each scan. Motor step size for these tests was set to 0.039μm per step.

The *Scanner Controller Main* VI motor settings for the X and Y-axis accuracy & repeatability test are shown below:

X-axis motor settings

- Initial delay (s): 0
- Frequency (Hz): 16000
- Duty cycle: 0.5
- Number of pulses/increment: 51
- X-axis motor, step size: 0.039μm

Y-axis motor settings

- Initial delay (s): 0
- Frequency (Hz): 16000
- Duty cycle: 0.5
- Number of pulses/increment: 51
- Y-axis motor, step size: 0.039μm

3.4 Measurement of cosine error

This test was used to measure the cosine error of the measurement table in the X and Y-axis, see figure 3.7. This is an important factor to consider since measurement of any part or surface mounted on the measurement table may be affected by the orientation of the table itself with respect to the laser head. This deviation will then be reflected in the recorded scan of that part or surface and will go unseen by the user, this will in effect, induce an error in the measured data points, and the recorded data points may not reflect the actual part or surface. The purpose of this test was to determine the orientation of the measurement table with respect to the laser head. Parts to be scanned could then be positioned in areas of the table known to be the most 'level' thus reducing the cosine error for the scanned parts or surfaces. In addition, the known orientation of the measurement table could be factored into the recorded data during post processing to give a more accurate representation of measured surfaces.

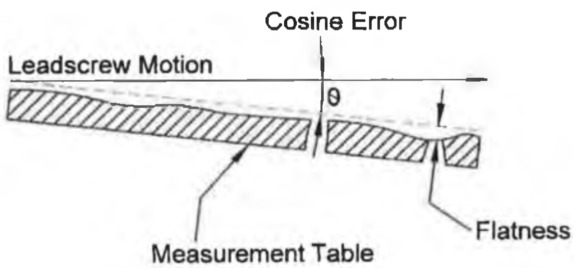

Figure 3.7 - Measurement table flatness and cosine error

Experimental setup

The laser spot was positioned in the 0,0 location of the table, i.e. the zero point of both the X, Y and Z axes is designated by position B in figure 3.8. This point would define the datum 0,0,0 point for the test.

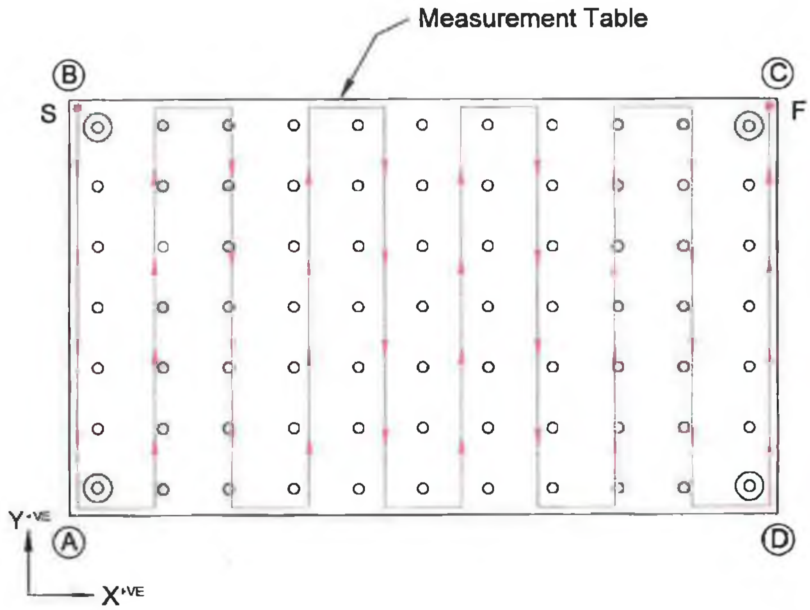

Figure 3.8 - Measurement table scan pattern

In reality, this point was offset by approximately 1mm from both edges of the table to avoid the slightly chamfered edge. This gave a total scan area of 198mm wide by 118mm long. Six data points were recorded for ten separate passes giving a total of sixty data points for the table scan. Motor step size for these tests was set to 0.039μm movement per step.

The *Scanner Controller Main* VI motor settings for the table cosine error test are shown below:

X-axis motor settings

- Initial delay (s): 0
- Frequency (Hz): 16000
- Duty cycle: 0.5
- Number of pulses/increment: 1013760
- X-axis motor, step size: 0.039μm

Y-axis motor settings

- Initial delay (s): 0
- Frequency (Hz): 16000
- Duty cycle: 0.5
- Number of pulses/increment: 604160
- Y-axis motor, step size: 0.039μm

3.5 Surface roughness comparison

A standard test sample with surfaces of known R_a values was used to compare with a series of scans made by the profilometer over the same surfaces. The standard sample used was a Microsurf 315 made by Rubert & Co. of Cheshire, England. An image of the sample piece is shown in figure 3.9. The surfaces profiled were of 3.2μm and 1.6μm R_a. A total of five scans was made over each surface in different areas of the surface so as to give the best possible spread of data. The results for each of the scans and the average across each surface are presented in section 4.5.

Figure 3.9 - Microsurf 315 surface roughness sample

Experimental procedure – Surface Roughness Comparison

The surface roughness test piece was set up on the measurement table as shown in figure 3.10.

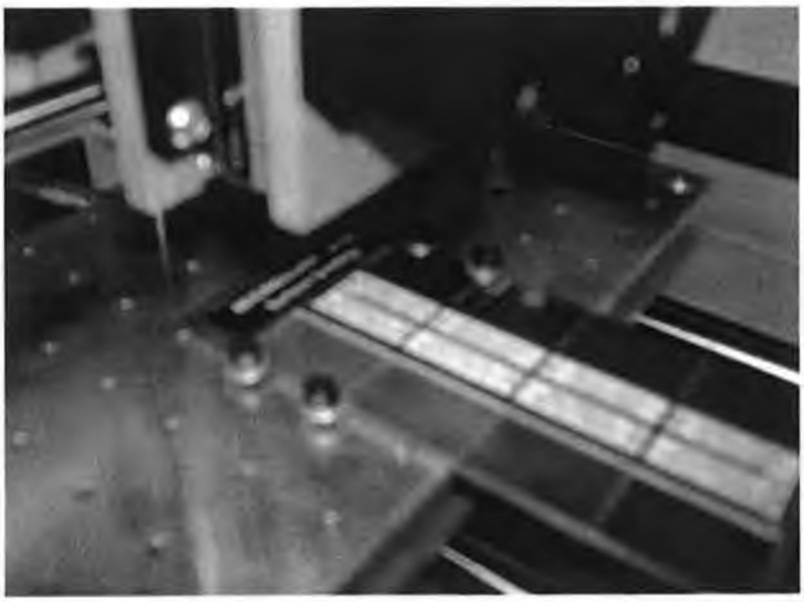

Figure 3.10 - Surface roughness sample set up

The R_a of a surface is total area between the surface profile and the profile's mean line. It is calculated by finding the integral of the absolute value of the surface profile divided by the evaluation length, or the number of data points. Surface R_a is also known as Arithmetic Average (AA) or the Centre Line Average (CLA) and for analogue acquired data is given by the following:

$$R_a = {}^{1}/_{N}.\Sigma^{N}_{n=1} \left| Z_n - Z_{av} \right| \qquad \text{eq 3.2}$$

where:
Z_n = the distance from laser sensor to profile at the n^{th} increment
n = the total number of scan increments

Figure 3.3 shows schematically the Z height points typically used is these measurements.

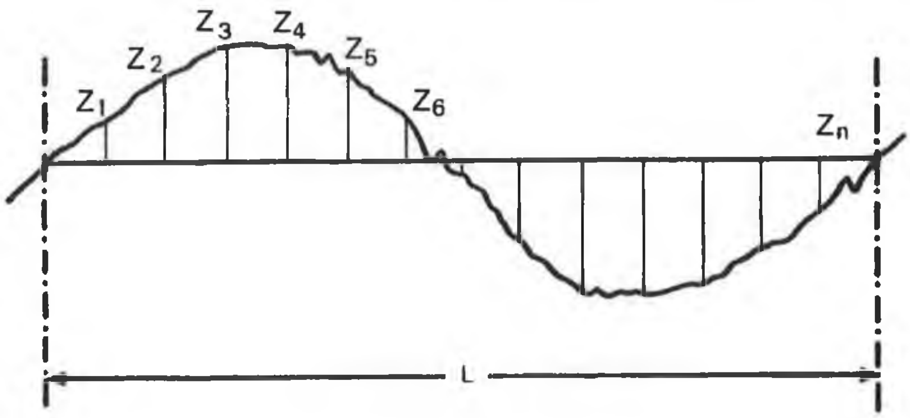

Figure 3.11 - Height data points typically used is roughness parameter measurements[1]

200 data points were recorded on each pass at a lateral resolution of 10μm giving a scan length of 2mm. Motor step size for this test was set to 0.039μm table movement per motor step.

The *Scanner Controller Main* VI motor settings for the surface roughness test are shown below:

X-axis motor settings
- Initial delay (s): 0
- Frequency (Hz): 16000
- Duty cycle: 0.5
- Number of pulses/increment: 258
- X-axis motor, step size: 0.039μm

Y-axis motor settings
- Initial delay (s): 0
- Frequency (Hz): 16000
- Duty cycle: 0.5
- Number of pulses/increment: 258
- Y-axis motor, step size: 0.039μm

3.6 Measurement of table M3 hole scan

The M3 hole scan detailed below is a surface scan over one of the measurement tables M3 fixing holes used for securing samples during inspection. The scan covers an area of 15.21mm^2 (3.9mm x 3.9mm). The imaged surface is presented as for other scans, using colour contouring to show the height gradients and variations.

Experimental setup

The laser spot was positioned at the back left hand side of the hole at location A, see figure 3.12. Each pass was configured with 78 increments of 50µm and the total scan was made up of 78 passes at a distance of 50µm along the X-axis from the previous pass thus giving a square scan of 3.9mm x 3.9mm and a total of 6084 data points. Motor step size for these tests was set to 0.039µm leadscrew movement per step.

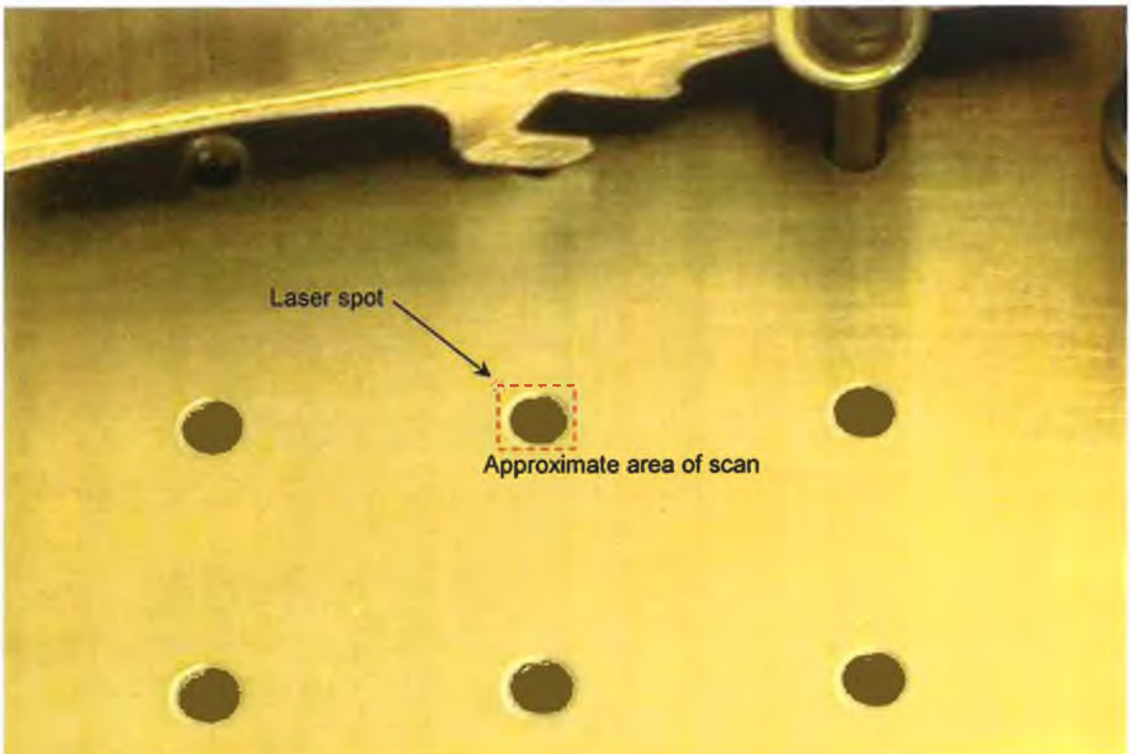

Figure 3.12 - Measurement table M3 hole and scan area

The *Scanner Controller Main* VI motor settings for the M3 hole scan are shown below:

X-axis motor settings

- Initial delay (s): 0
- Frequency (Hz): 16000
- Duty cycle: 0.5
- Number of pulses/increment: 1280
- X-axis motor, step size: 0.039µm

Y-axis motor settings

- Initial delay (s): 0
- Frequency (Hz): 16000
- Duty cycle: 0.5
- Number of pulses/increment: 1280
- Y-axis motor, step size: 0.039μm

3.7 M3 button screw and washer

A hexagonal head M3 button screw and washer in one of the fixing holes was scanned. The scan covers an area of 87.8mm^2 (9.37mm x 9.37mm). The purpose of this test was to try to image a small curved surface and a surface with vertical features. The imaged scan was presented with colour contouring to highlight the height gradients and variations.

Experimental setup

The laser spot was positioned at the back left hand side of the assembly at location. Each pass was configured with 187 increments of 50μm and the total scan was made up of 187 passes displaced at 50μm from each other along the X-axis thus giving a square scan of 9.37mm x 9.37mm and a total of 34,969 data points. Motor step size for these tests was set to 0.039μm leadscrew movement per step.

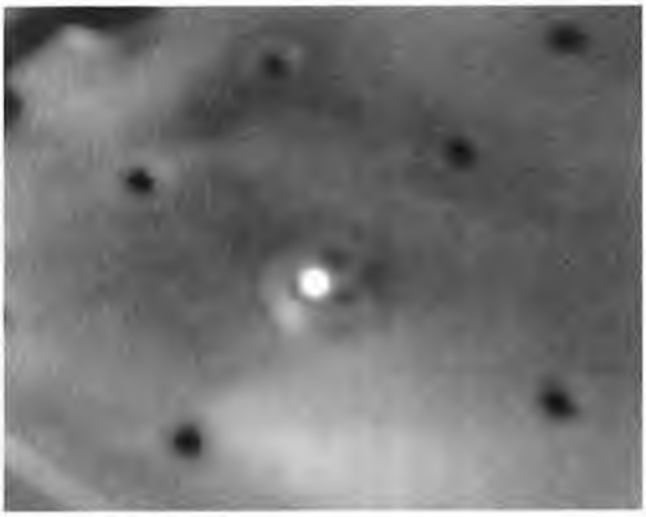

Figure 3.13 - Button screw and washer

The *Scanner Controller Main* VI motor settings for the M3 button screw and washer scan are shown below:

X-axis motor settings

- Initial delay (s): 0
- Frequency (Hz): 16000
- Duty cycle: 0.5
- Number of pulses/increment: 1280
- X-axis motor, step size: 0.039μm

Y-axis motor settings

- Initial delay (s): 0
- Frequency (Hz): 16000
- Duty cycle: 0.5
- Number of pulses/increment: 1280
- Y-axis motor, step size: 0.039μm

3.8 Surface recognition scan

This test details a surface scan across a portion of a 1 Euro coin containing the islands of Ireland and the United Kingdom. The 1 Euro coin was clamped to the measurement table in the same way as the 20 Cent coin in section 3.1. The scan over the feature of the islands covers an area of $6.25mm^2$ (2.5mm x 2.5mm). The purpose of this scan was to compare lateral scan resolutions (Res_L) and determine the lateral resolution offering the best trade off between accuracy, clarity, and speed.

Experimental setup

The 1 Euro coin was clamped to the table using two M3 screws similar to the clamping method used in earlier tests across the 20 Cent coin. The laser spot was positioned approximately 0.10mm to the left of, and above, the island features on the coin, see figure 3.13.

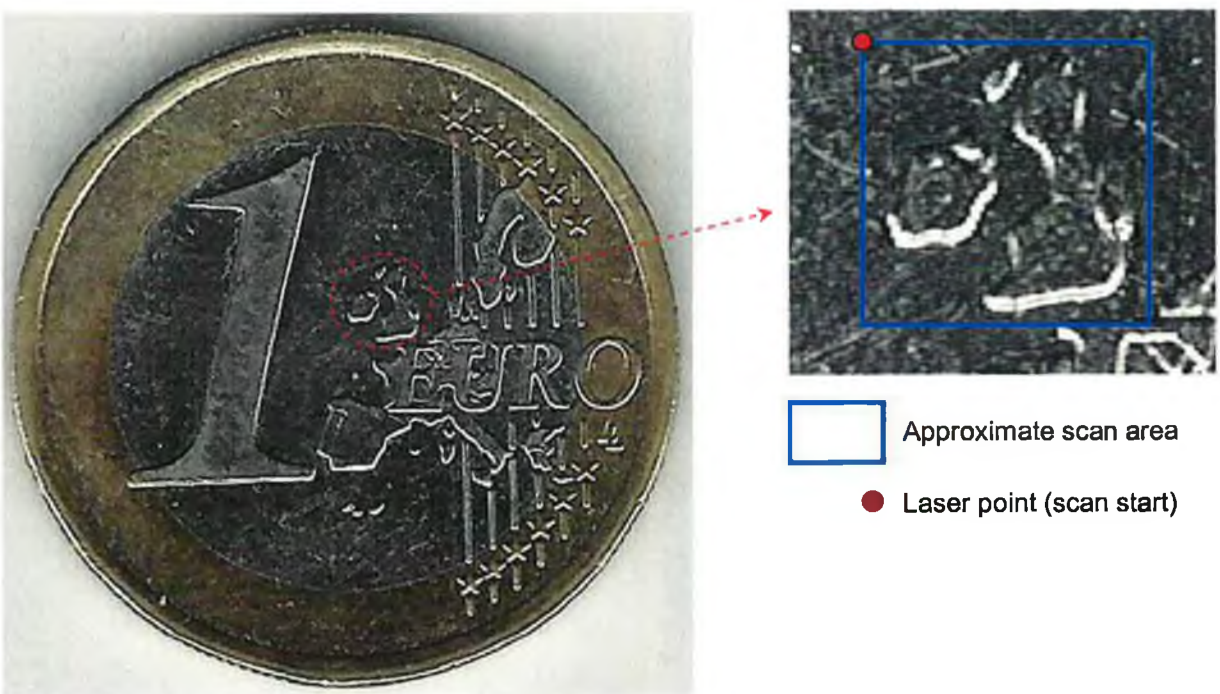

Figure 3.14 - 1 Euro coin scan area

Two scans were run over the area shown above, each at lateral resolutions of 100µm and 50µm giving a total of 625 and 2,500 data points respectively. The different lateral resolution scans correspond to a different scan increment size. Motor step size for these tests was set to 0.039µm leadscrew movement per step.

The *Scanner Controller Main* VI motor settings for the 1 Euro coin scan are shown below:

X-axis motor settings

- Initial delay (s): 0
- Frequency (Hz): 16000
- Duty cycle: 0.5
- Number of pulses/increment: 512 (20µm Res_L) / 1280 (50µm Res_L) / 2560 (100µm Res_L)
- X-axis motor, step size: 0.039µm

Y-axis motor settings

- Initial delay (s): 0
- Frequency (Hz): 16000
- Duty cycle: 0.5
- Number of pulses/increment: 512 (20µm Res_L) / 1280 (50µm Res_L) / 2560 (100µm Res_L)
- Y-axis motor, step size: 0.039µm

3.9 Surface scan fibre optic mould tool

A fibre optic mould tool used for forming fibre optic lenses was scanned with the developed profilometer. The mould was made up of a 'dimple' which had an outer diameter of approximately 400 µm, a raised inner diameter of 250 µm and a height of 100 µm. The dimple was formed in a circular countersink. The scan step size was set 10 µm and the profile is made up of a total of 60 × 60 data points and scanning an area of 3600 µm^2.

Experimental setup

The mould tool was clamped to the measurement table and the laser spot positioned at the top left hand side of the mould dimple. Figure 3.14 shows an SEM micrograph of the mould tool. Location A shows the approximate position of the scan start.

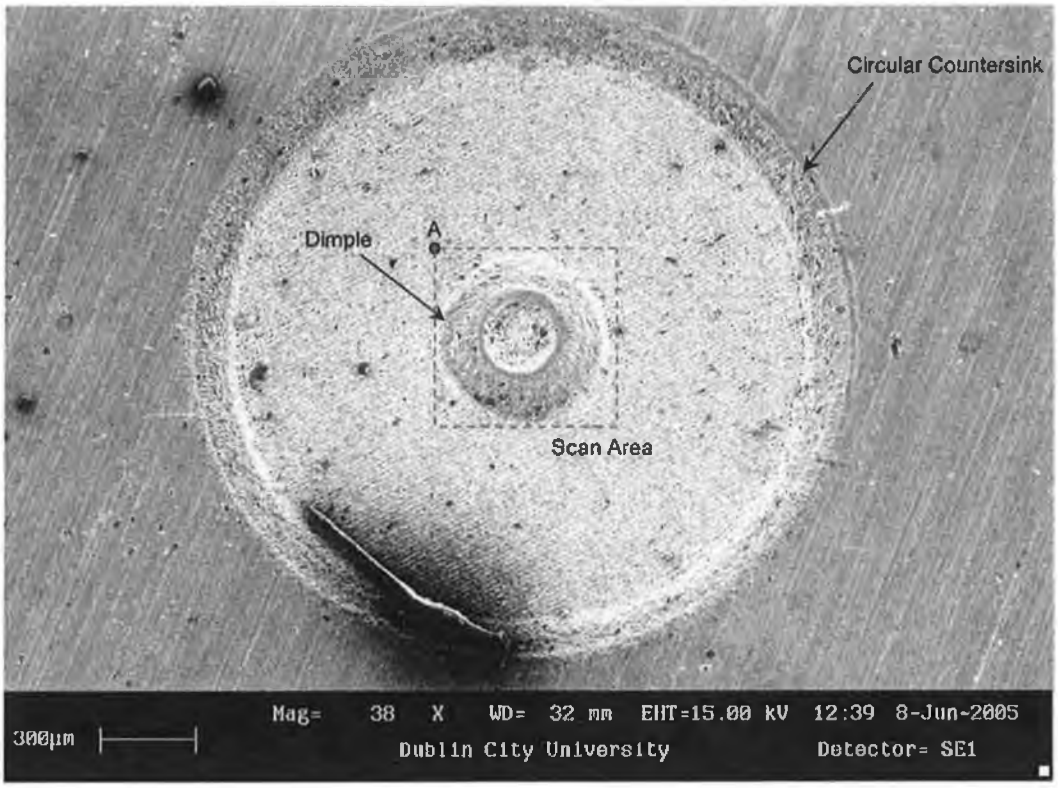

Figure 3.15 - SEM micrograph of the fibre optic mould

The *Scanner Controller Main* VI motor settings for the fibre optic mould tool scan are shown below:

X-axis motor settings

- Initial delay (s): 0
- Frequency (Hz): 16000
- Duty cycle: 0.5
- Number of pulses/increment: 256
- X-axis motor, step size: 0.039µm

Y-axis motor settings

- Initial delay (s): 0
- Frequency (Hz): 16000
- Duty cycle: 0.5
- Number of pulses/increment: 256
- Y-axis motor, step size: 0.039µm

Chapter 4 Results & discussion

4.1 X and Y-axis dynamic stability

(1) Axis Stability Comparison

The average of the recorded height data for the scans was plotted against the X-axis lateral displacements and against the Y-axis lateral displacements, shown in figure 4.2. The figure shows 2-D profiles of the 20 Cent coin across the harp. Comparing the two scans it is clear that the scan along the X-axis contains an excessive amount of vibrational noise as compared with that of the Y-axis scan. The maximum amplitude difference between the two scans differs by approximately 0.050mm.

Vibrational noise from either axis is as a result of an unwanted movement of the laser sensor assembly or measurement table in the Z-axis during controlled movement of both the X and Y axis leadscrews. This can happen for a number of reasons, however, the largest influence on this movement is caused by deviations, inconsistencies, and tolerance/fits in the leadscrew and guide rails. Vibrational errors are more prominent in the X-axis as it is only supported by two guide rails as opposed to the four of the Y-axis. As the laser sensor assembly is moved along the X-axis possible vibrations could occur in the Z-axis plane, around the X-axis (R_X), and also around the Y-axis (R_Y), see figure 4.1.

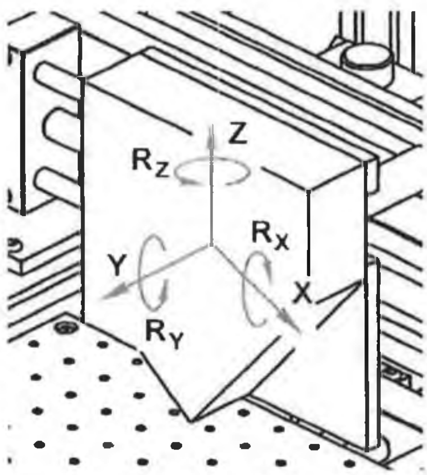

Figure 4.1 - Positional errors affecting the laser sensor assembly

Based on these results it was decided to develop the signal acquisition program so that no signal scanning or point (voltage) acquisition would take place during movement in the X-axis, therefore all data points were recorded after Y-axis movement, see figure 2.8. By adopting this approach it is possible to reduce the amount of vibration from the X-axis, as it was be stationary during signal acquisition thus improving the quality of the recorded data.

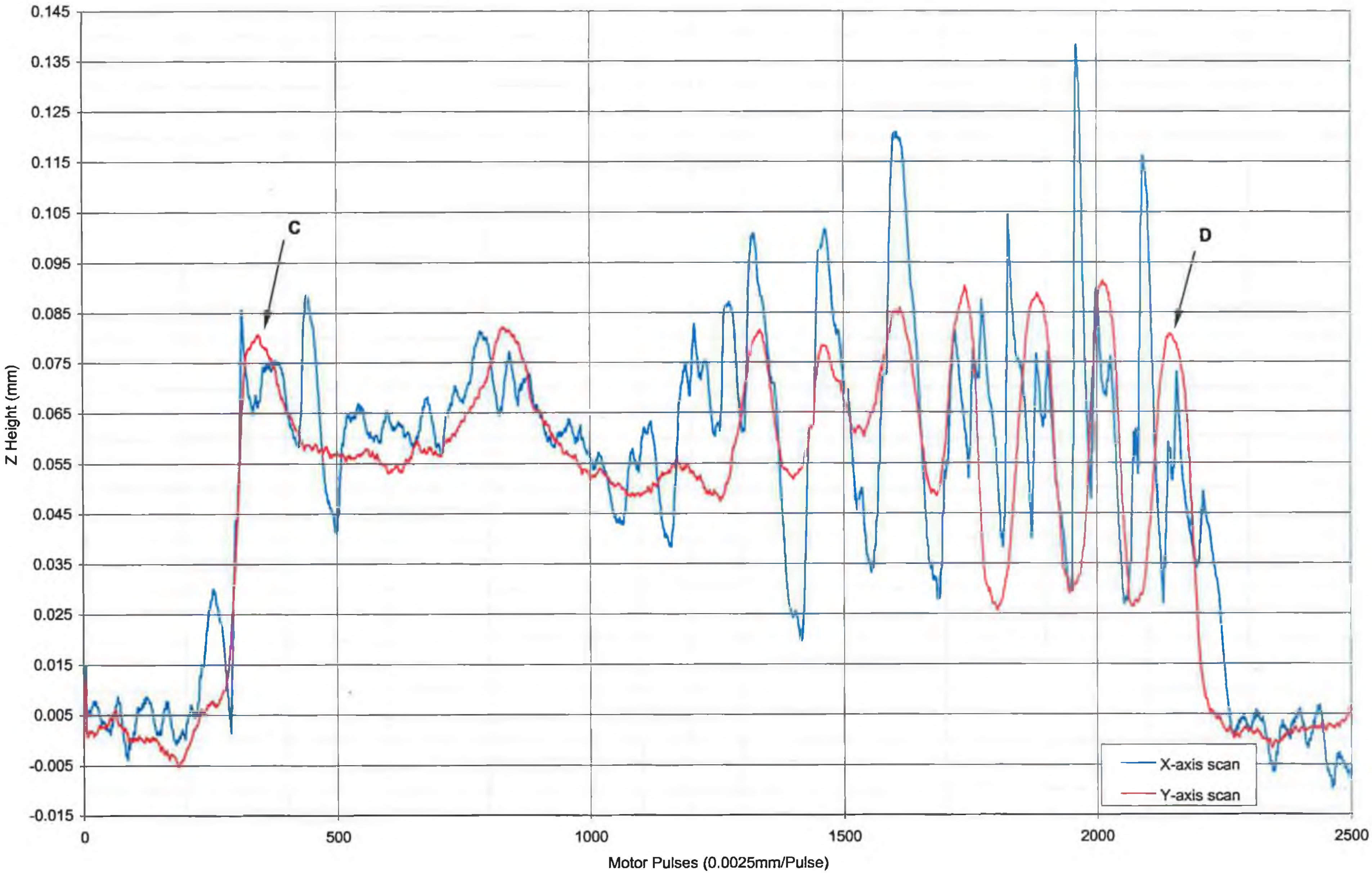

Figure 4.2 - 6.25mm straight line scan over harp on 20 cent coin

4.2 Z_{HEIGHT} dynamic resolution

Looking at figure 4.3 (2µm lateral resolution) it can be seen that the laser sensor has measured the width of the gauge as 1.0085mm (Z height) on the first pass, 1.007µm on the second pass, and 1.0085µm on the third pass, giving an average of 1.008µm over the three scans and a deviation of 1µm in the Z-axis measurement.

Figure 4.4 (1µm lateral resolution) shows the measured width of the gauge as 1.0105µm (Z height) on the first pass, 1.008µm on the second pass, and 1.0095µm on the third pass, giving an average of 1.0093µm over the three scans and a deviation of 2.3µm in the Z-axis.

The slightly increased size of the deviation seen in the second scan above could simply be due to the increased number of scan points taken in this higher resolution scan. Due to the higher number of data points captured a greater deviation between the top and the bottom of the gauge would be expected. Discussion relating to the accuracy and repeatability of the system in both the X and Y-axis is presented in section 4.3.

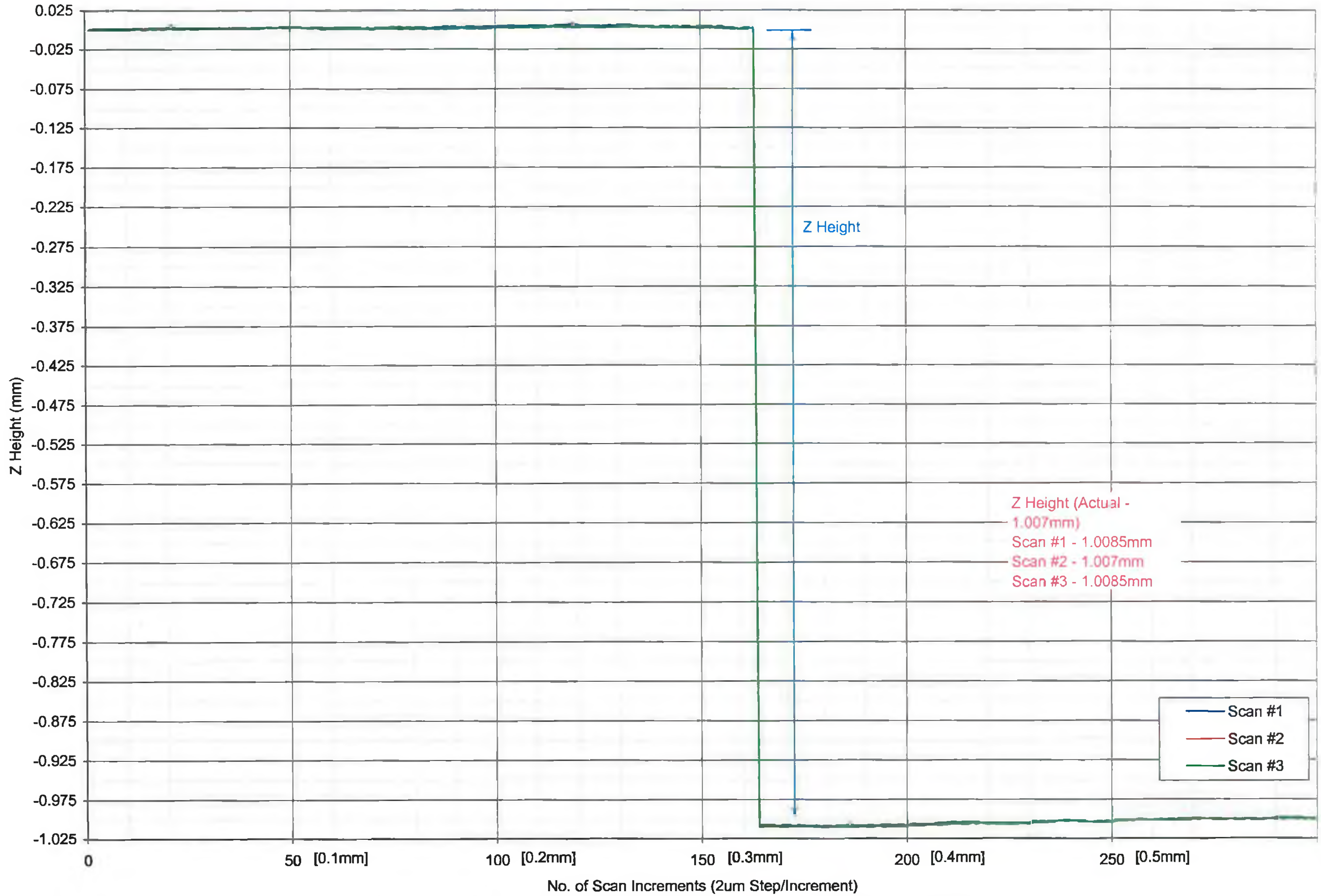

Figure 4.3 - Z Height Resolution Tests, 2um ResL, 1.007mm Slip Gauge

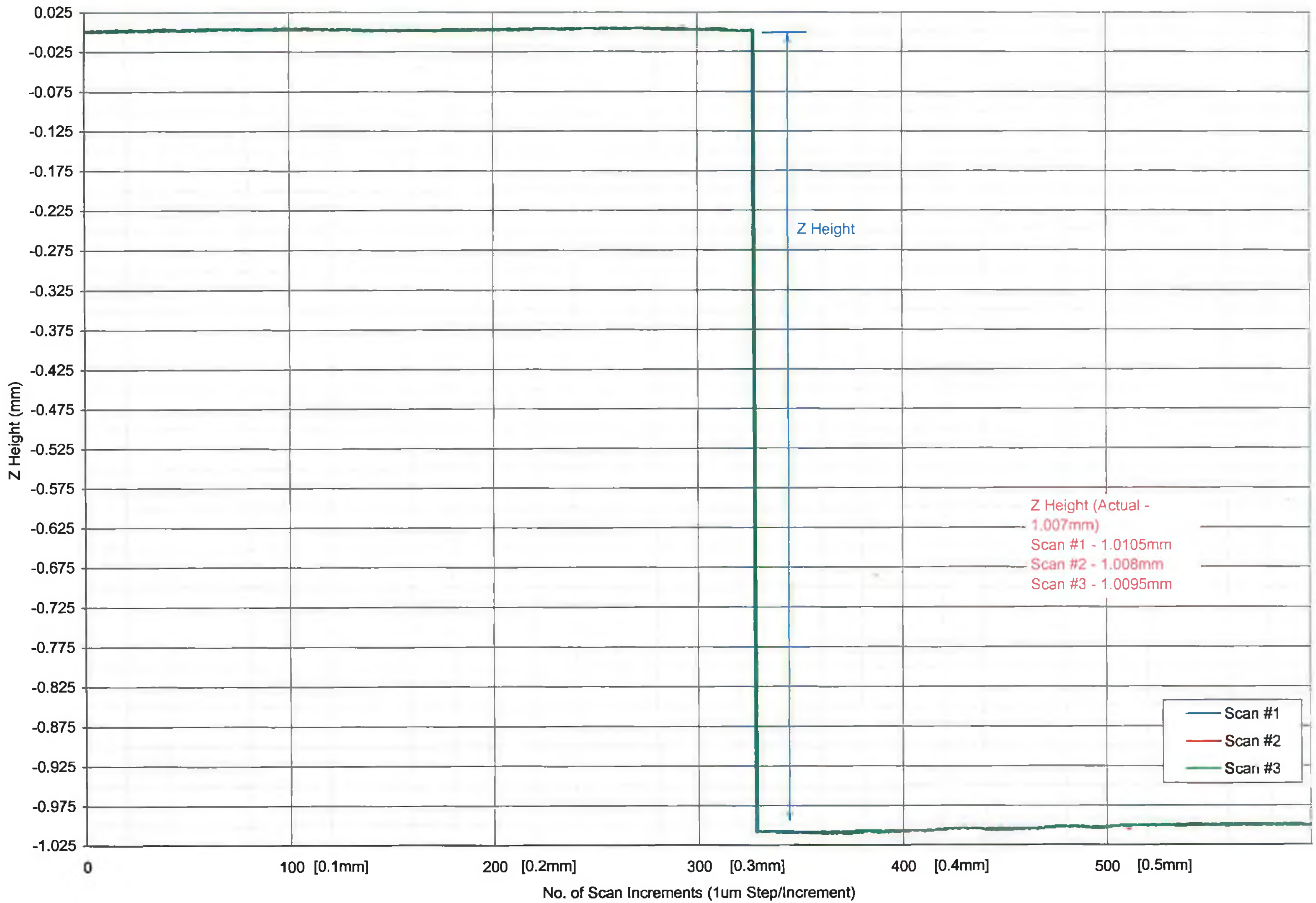

Figure 4.4 - Z Height Resolution Tests, 1um ResL, 1.007mm Slip Gauge

4.3 X and Y-axis accuracy & repeatability

Figure 4.5 shows the plot of the slope of the gauge setup in both the X and Y-axes. A distance of 1mm was scanned and the vertical height across the scan was plotted. The slope sample was adjusted as described until the inclination was recorded at 1:2. Once the sample was set to the correct gradient the bottom fixing screw was tightened to lock it in place and the slope was rescanned to ensure the inclination was correct.

The results from the accuracy and repeatability tests are plotted in figure 4.6, which shows an average of the five scans for both the X and Y-axes. The X-axis accuracy gets worse at a reducing rate as the scan distance increases. It is interesting to note that the X-axis accuracy is slightly better than the Y-axis, reaching a maximum error across the range of just over 8μm, while Y-axis accuracy reaches a maximum of approximately 11μm. The difference in the accuracy of the two axes may be due to a number of reasons. Firstly, the Y-axis motor was an older motor and so may have slightly degraded windings or stators causing the motor to occasionally stall or lose position. Another possible influence on the accuracy of the Y-axis could be caused by the two additional guide rails supporting the measurement table. Any imperfections or misalignment on either of the guide rails may cause the bearings to bind or snag as they move along the rail thus causing a variation in the actual position of the table. Lastly, the leadscrew assembly themselves will have an affect on accuracy as there will be a certain amount of play between the leadscrew and the leadscrew nut. Leadscrew error is given as 0.0013mm/mm. The X and Y axis repeatability is also shown in figure 4.6. The repeatability was calculated by measuring the range of the accuracy deviation for of the five scans.

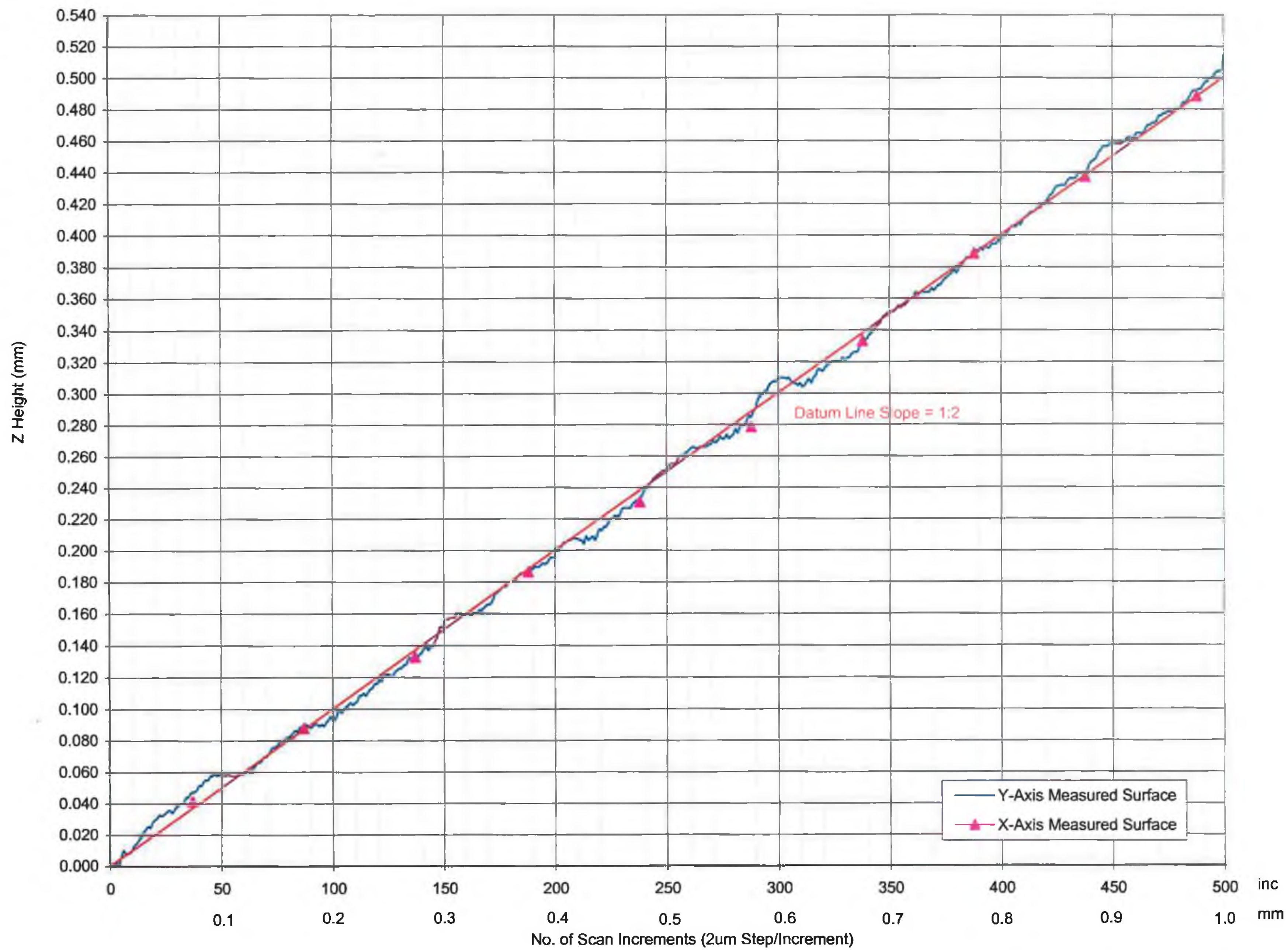

Figure 4.5 - X Y-Axis Repeatability Test Sample Slope [Step size = 3.9E-5mm per Pulse]

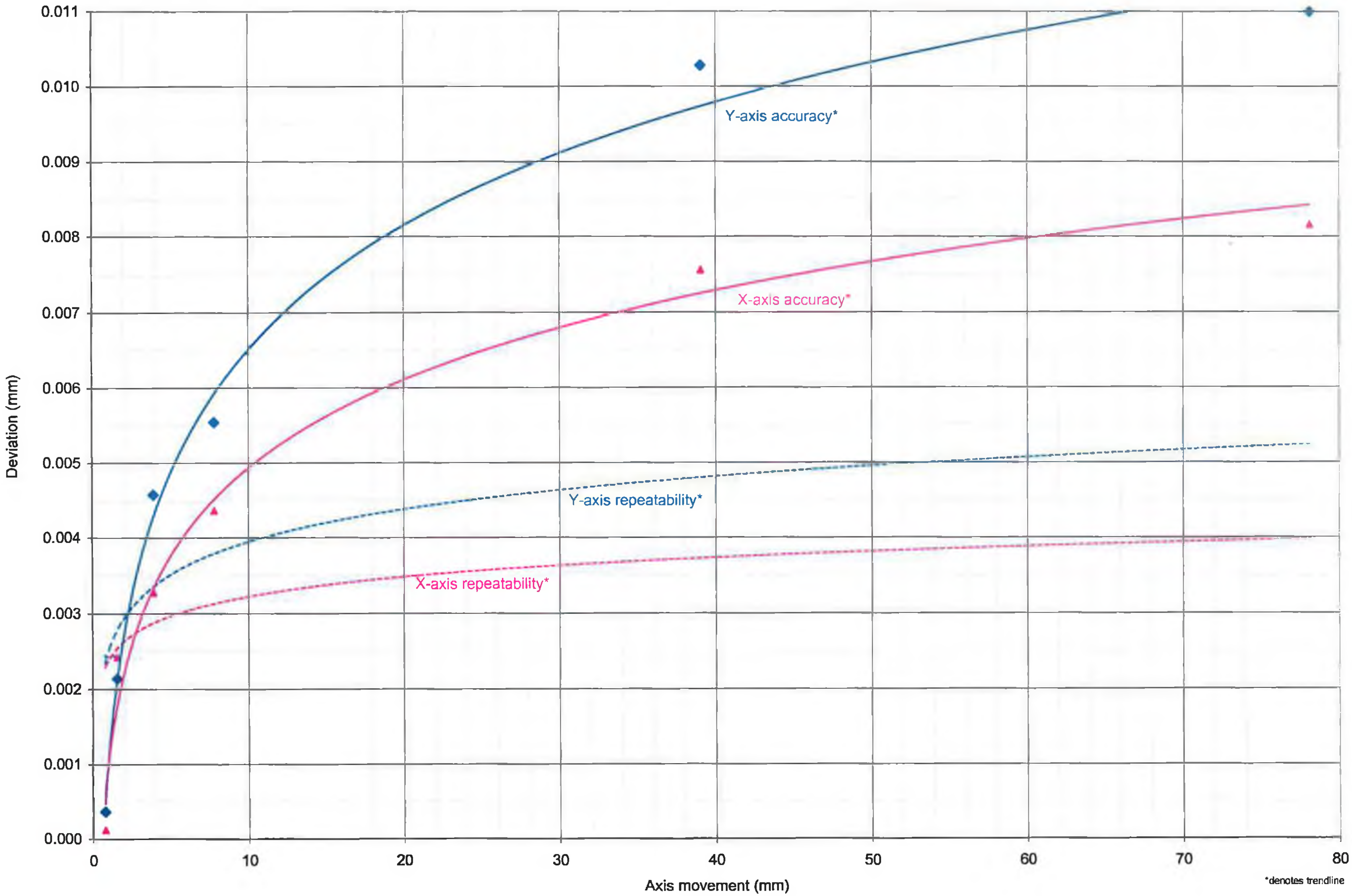

Figure 4.6 - X and Y Axis Accuracy Repeatability

4.4 Measurement of cosine error

The results from the measurement table surface scan are shown in figure 4.7. The colour map represented the heights recorded at each location on the table.

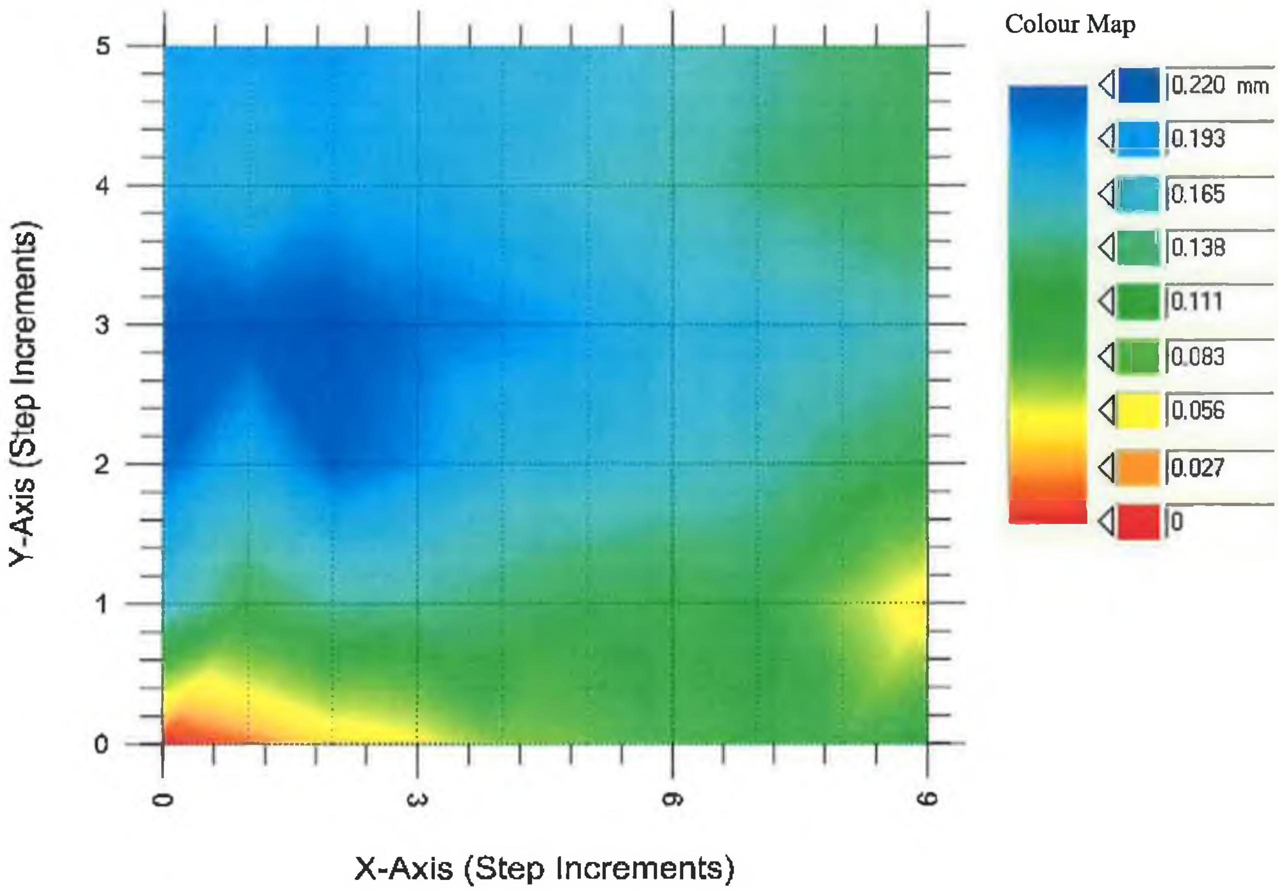

Figure 4.7 - Colour map of measurement table scan

In figure 4.7, the blue areas represent the highest regions of the measurement table surface and the red areas represent the lowest areas with respect to the position of the laser head. The data used to generate the surface above was post-processed to zero the lowest (furthest from laser sensor) data point. The colour map above provides a graphical key showing the height above the zeroed datum. In order to better visualise this data, a contour map of the surface is shown in figure 4.8 and a 3-D image of the scanned data is shown in figure 4.9. This data was then used for setting the mounting locations for the further tests presented in this thesis enabling objects and surfaces to be mounted in the geometrically flattest areas of the table.

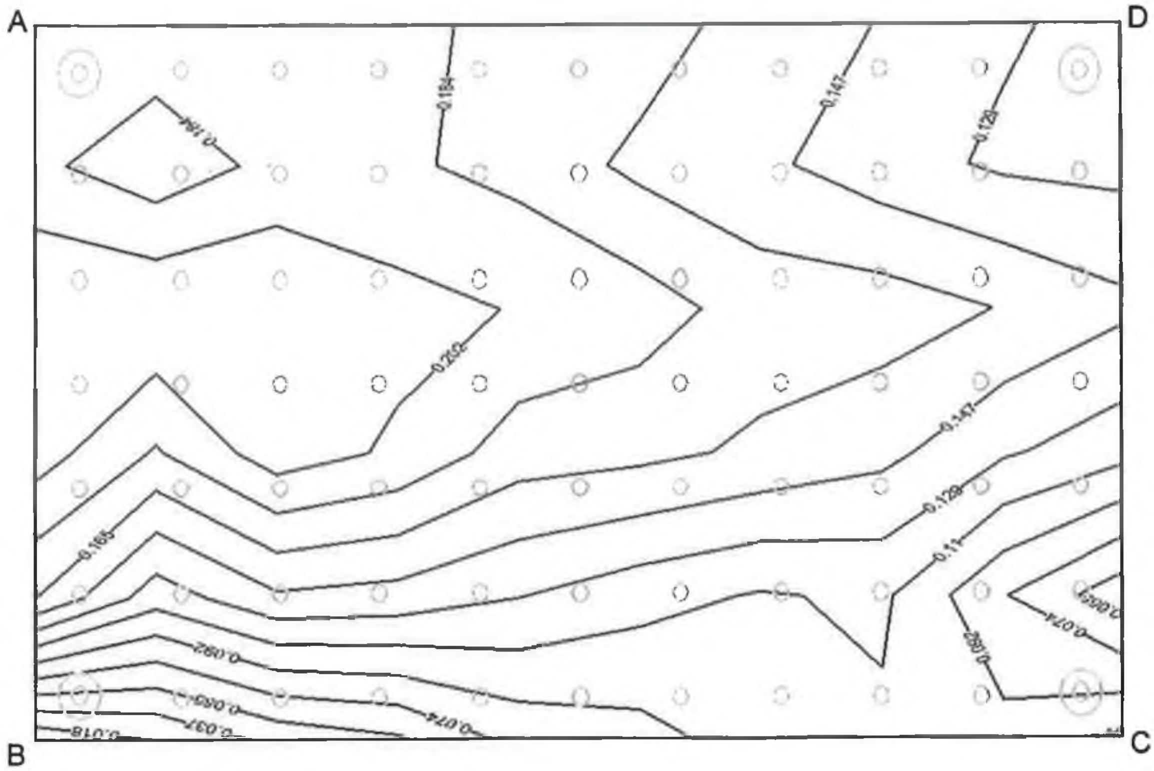

Figure 4.8 - Contour map of scanned measurement table

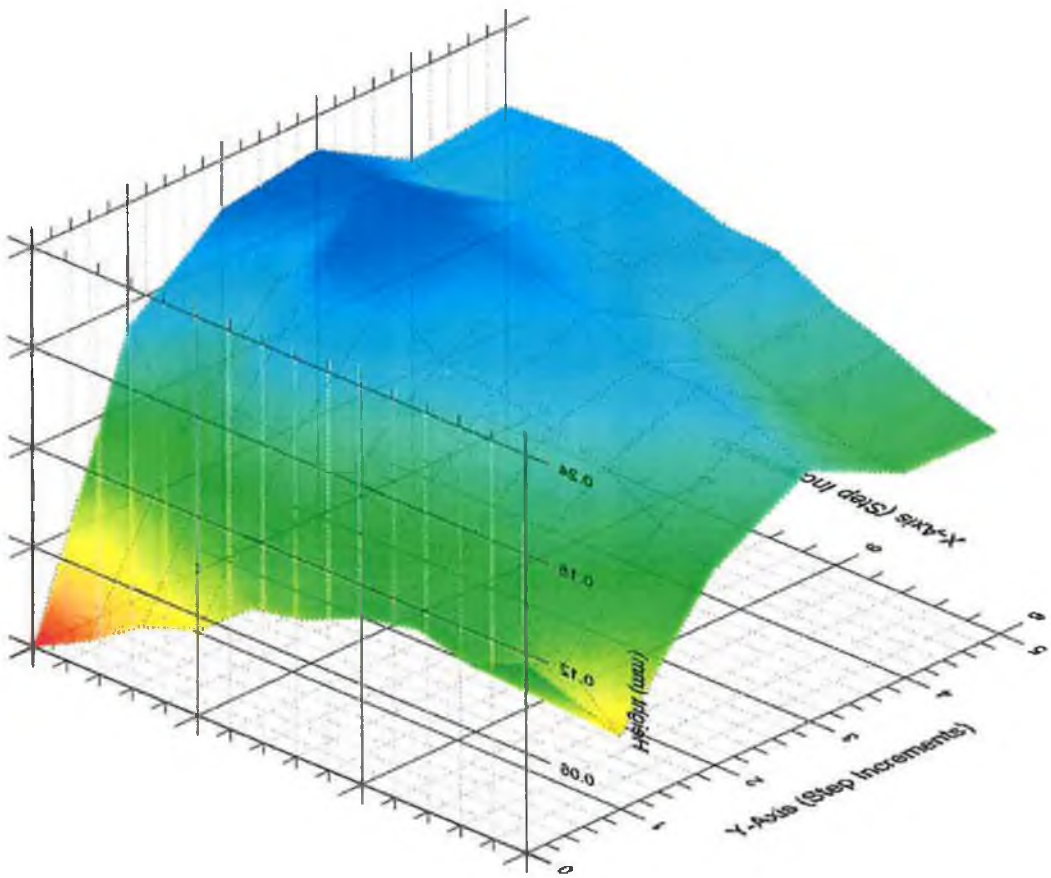

Figure 4.9 - 3-D image of measurement table scan

A portion of the form error of the measurement table can be attributed to the machining process used during its manufacture causing a form error on the surface of the table itself, however, one of the largest factors that may be affecting form error could be misalignment of the measurement table carriage with respect to the laser head carriage assemblies.

Figure 4.10 shows potential sources of misalignment of the three axes of the laser scanning system. For a three axis system there are 18 degrees of freedom. This coupled with the orthogonalities of each of the axes results in a total of 21 potential sources of alignment error in the system.

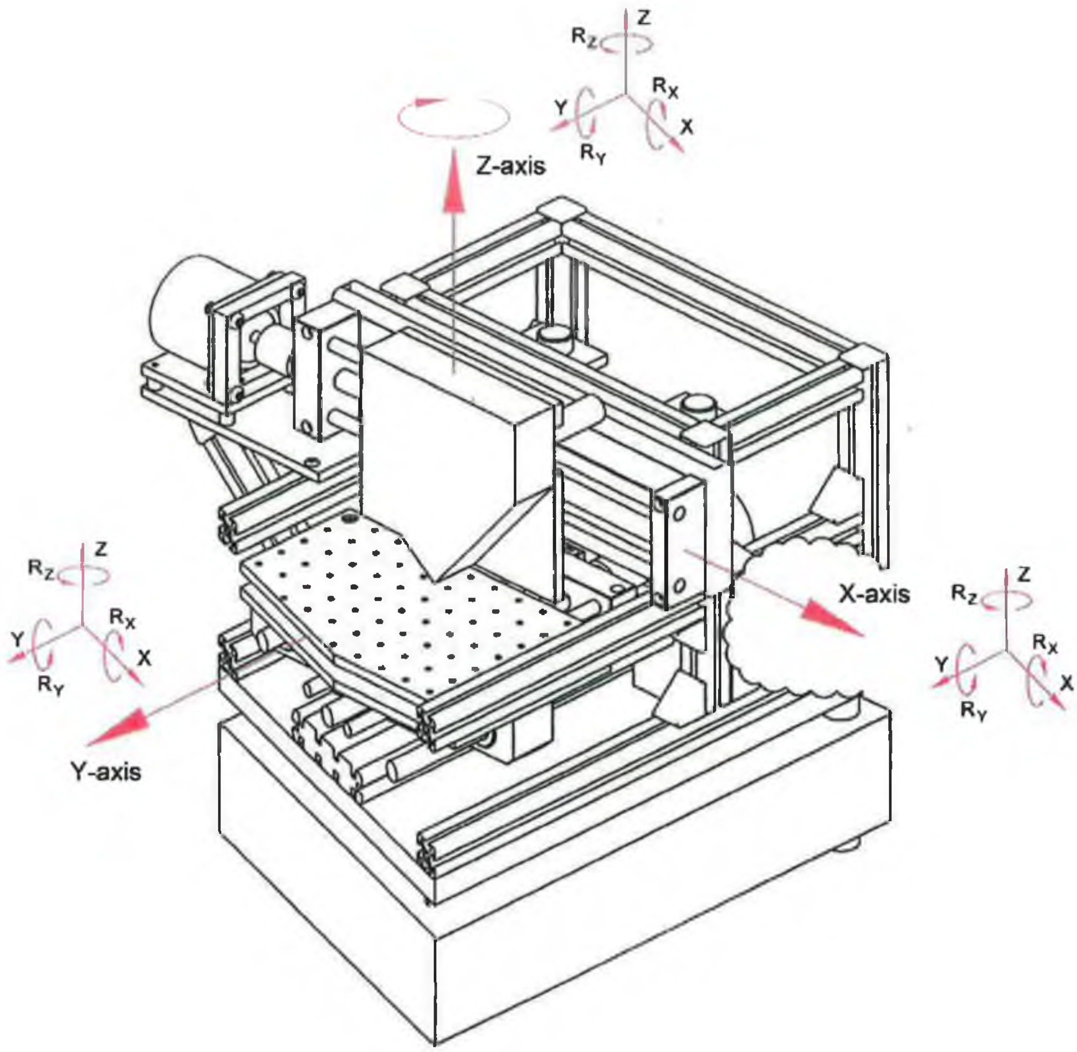

Figure 4.10 - Sources of alignment error in the laser scanning system

From figure 4.9 it is possible to calculate the minimum, maximum, and average cosine error for the X axes. By plotting the edges A-B and D-C, the maximum and minimum cosine error for the X-axis can be calculated, see figure 4.11. In figure 4.11, $\theta X_{A\text{-}B}$ represents the cosine angle in the X-axis along edge A-B of the measurement table. Similarly, $\theta X_{D\text{-}C}$ represents the cosine angle in the X-axis along edge D-C of the measurement table.

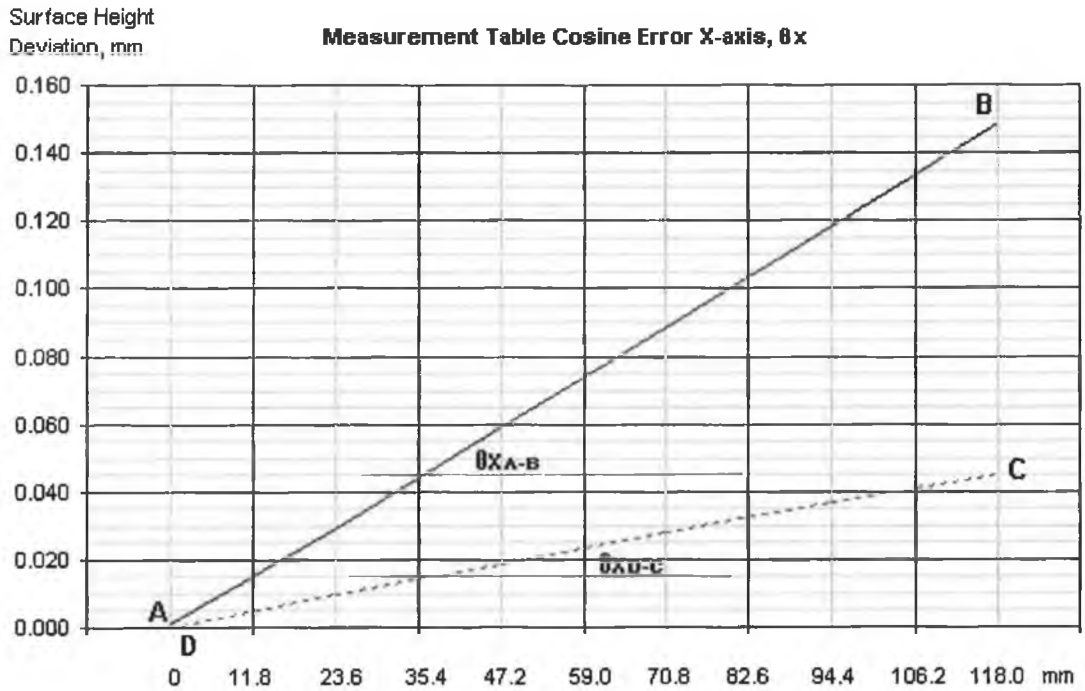

Figure 4.11 - Measurement table cosine error, X-axis

As shown, the maximum cosine error in the X-axis is along edge A-B. The length of the edge in the horizontal is 118mm with a total vertical deviation of 0.148mm thus the cosine error along edge A-B can be expressed as:

$$\theta XA\text{-}B = \mathrm{Sin}^{-1}.\ \frac{0.148}{(118^2 + 0.148^2)^{1/2}} = 0.072°$$

Similarly, the minimum cosine error in the X-axis, along edge D-C, was calculated as follows.

$$\theta XD\text{-}C = \mathrm{Sin}^{-1}.\ \frac{0.045}{(118^2 + 0.045^2)^{1/2}} = 0.022°$$

The average cosine error in the X-axis was then calculated as follows.

$$\theta XAV = \frac{(0.022 + 0.072)}{2} = 0.047°$$

Figure 4.12 below shows the Y-axis cosine error along edges B-C and A-D denoted by θX_{B-C} and θX_{A-D} respectively.

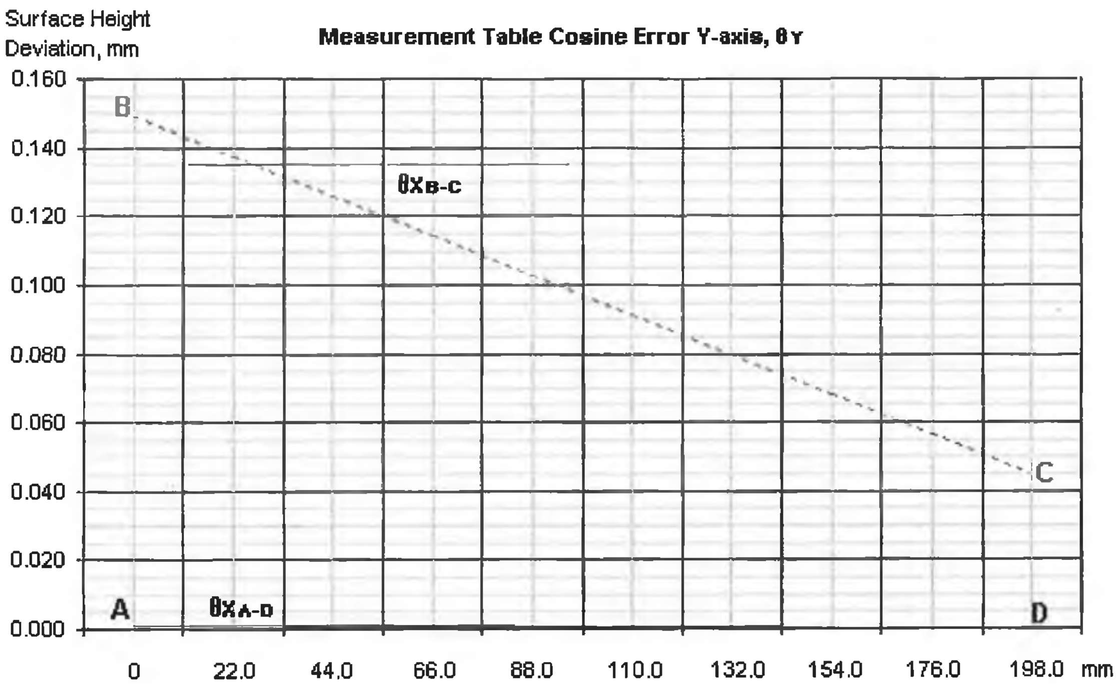

Figure 4.12 - Measurement table cosine error, Y-axis

As can be seen from figure 4.12, the maximum cosine error in the Y-axis is along edge B-C. The length of the edge in the horizontal is 198mm with a total vertical deviation of 0.104mm thus the cosine error along edge B-C can be expressed as:

$$\theta Y_{B-C} = \text{Sin}^{-1}.\ \frac{0.104}{(198^2 + 0.104^2)^{1/2}} = 0.030°$$

Similarly, the cosine error in the Y-axis along edge A-D can be expressed as:

$$\theta Y_{A-D} \approx \text{Sin}^{-1}.\ \frac{0.001}{(198^2 + 0.001^2)^{1/2}} \approx 0°$$

The average cosine error in the Y-axis was then given by:

$$\theta Y_{AV} \approx \frac{(0.030 + 0)}{2} \approx 0.015°$$

4.5 Surface roughness comparison

The surface roughness of the 3.2μm and 1.6μm surface standards is described in this section. The surface test piece was set up as shown in figure 3.9. During each test, five successive scans were made across the surface in different locations so as to record average data from different areas on the sample surface. Scan length was set to 2mm so as to reduce the impact of surface form error on the recorded scans. Unlike instruments such as the Form Talysurf, the laser profilometer is not able to distinguish between surface roughness and form error and so areas of surface inclination or declination will affect the R_a value. A total of 200 data points were recorded during each pass across the surface and the data was entered into equation 3.2 in order to measure the surface R_a.

3.2μm surface scans

The results from the 3.2μm R_a surface scans are detailed below.

Scan #1

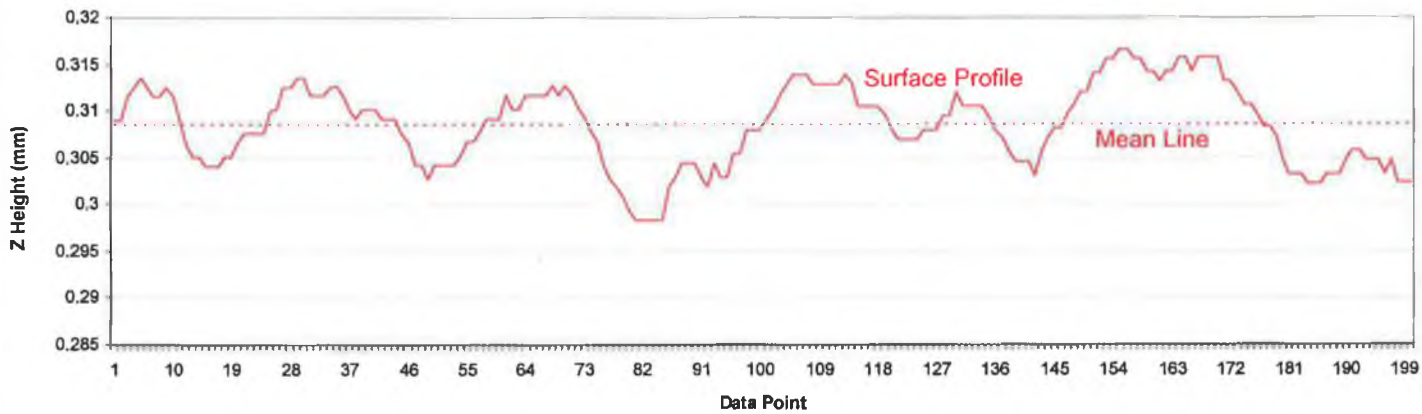

Figure 4.13 - 3.2μm surface, scan #1 recorded profile

Measured R_a value for scan #1 = 3.64μm

Scan #2

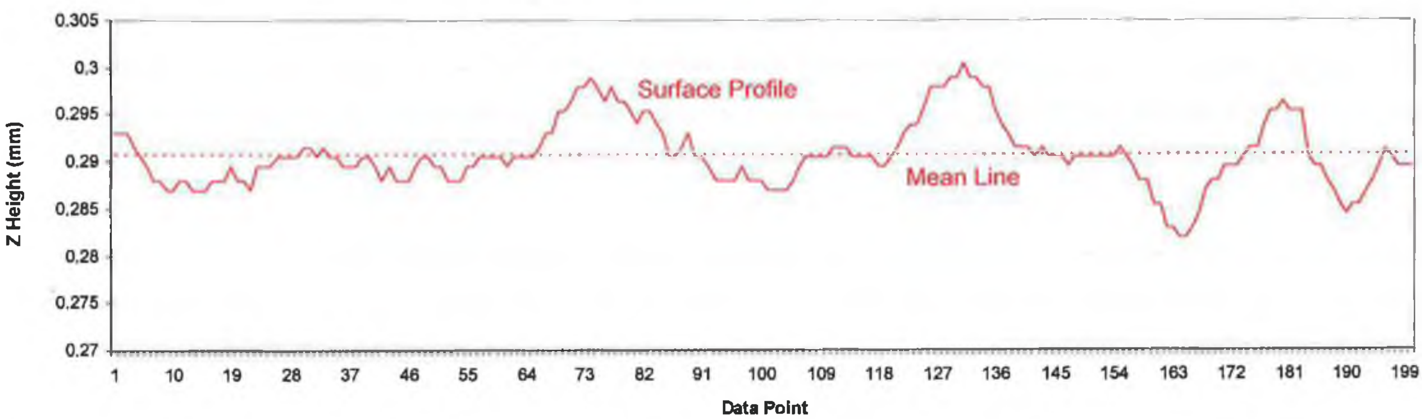

Figure 4.14 - 3.2μm surface, scan #2 recorded profile

Measured R_a value for scan #2 = 2.57μm

Scan #3

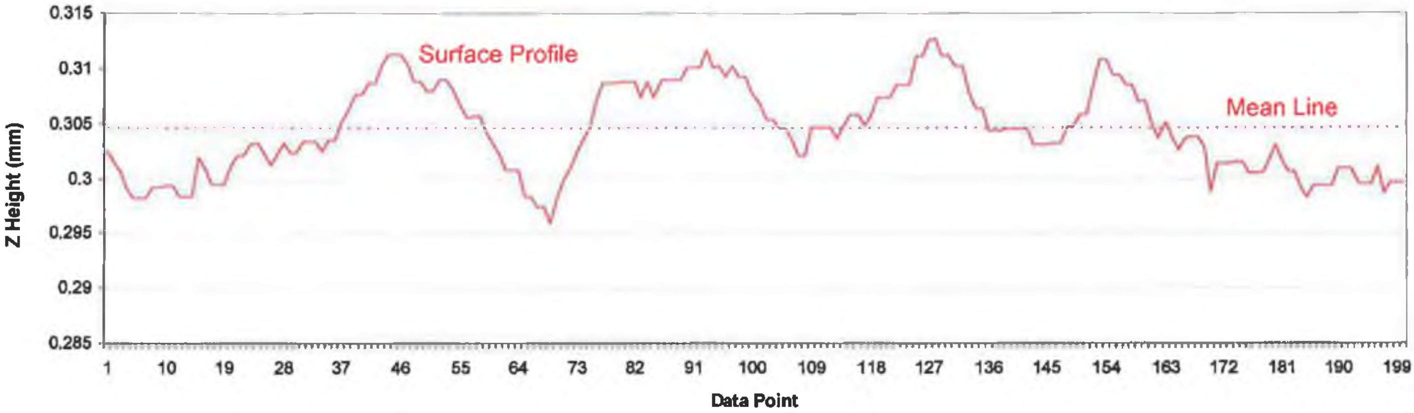

Figure 4.15 - 3.2μm surface, scan #3 recorded profile

Measured R_a value for scan #3 = 3.37μm

Scan #4

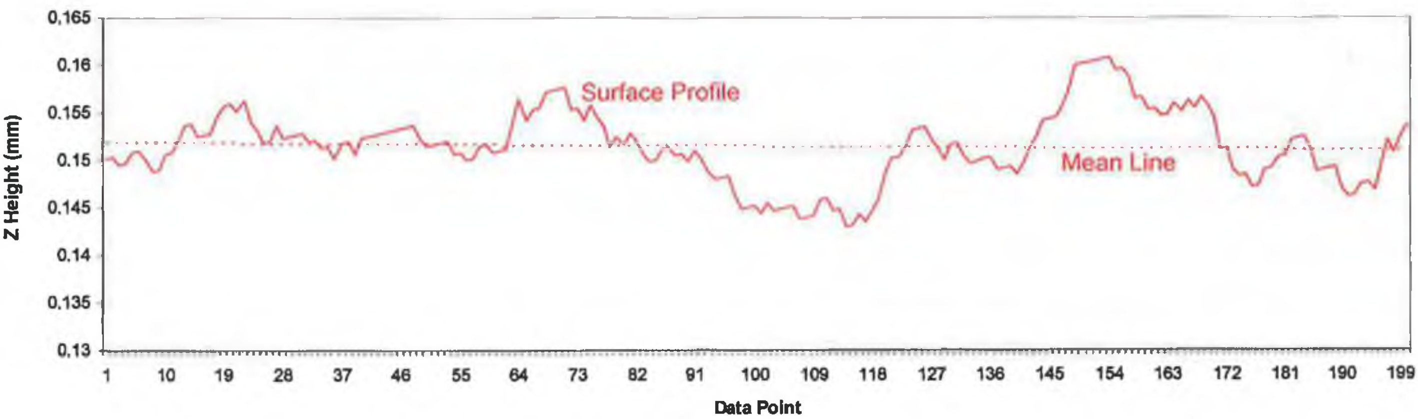

Figure 4.16 - 3.2μm surface, scan #4 recorded profile

Measured R_a value for scan #4 = 2.89μm

Scan #5

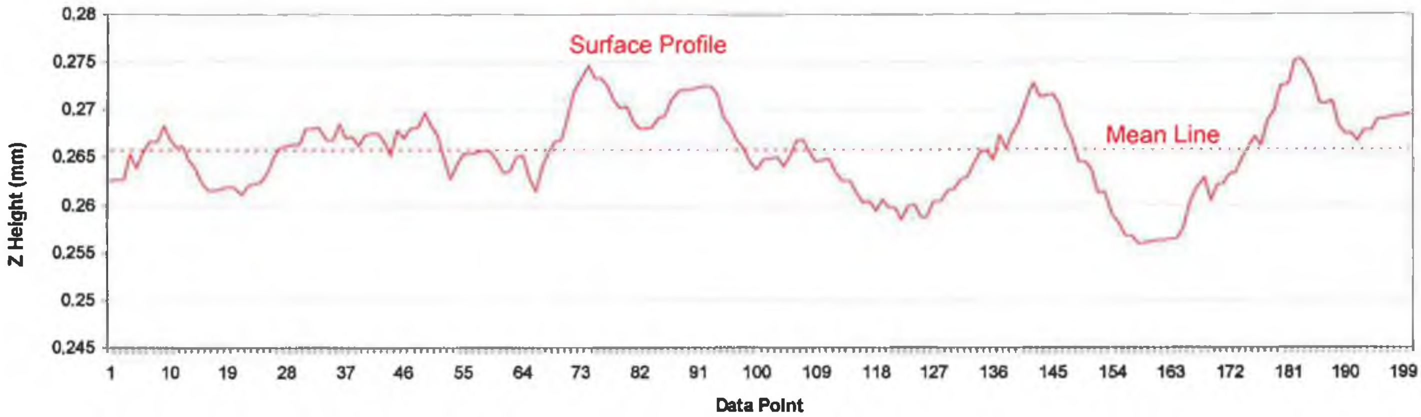

Figure 4.17 - 3.2μm surface, scan #5 recorded profile

Measured R_a value for scan #5 = 3.44μm

The surface R_a values were calculated using eq 3.2:

$$R_a = \frac{|Z_1| + |Z_2| + |Z_3| + |Z_4| + \ldots |Z_n|}{n}$$

Table 4.1 below details each of the recorded R_a values and the average R_a achieved.

Table 4.1 – 3.2μm R_a surface measure R_a values

Scan	Measured R_a(μm)
1.	3.64
2.	2.57
3.	3.37
4.	2.89
5.	3.44
Av.	3.185μm

Error value = |100 - (3.185 / 3.2 * 100)| = 0.47%

From table 4.1 it can be seen that the average measured R_a value compares very well to the actual surface roughness of the test sample giving an error of just 0.47%. However it is important to look at the absolute of the average deviation in order to find the true error.

Table 4.2 - 3.2μm R_a surface measured deviation

Scan	Deviation, Δ(μm)
1.	(+)0.44
2.	(-)0.63
3.	(+)0.17
4.	(-)0.302
5.	(+)0.24
Abs Av.	0.356μm

Error value = 100 - ((3.2 – 0.356) / 3.2 * 100) = 11.25%

Table 4.2 displays the actual deviation for each scan and by calculating the average of the absolute value of each one gives the true error. It is shown that the actual error during scanning of the 3.2μm R_a surface is approximately 11.25%. This can possibly be attributed to two things. Firstly, scanning a surface with an average roughness of 3.2μm, the profilometer is close to it's performance limit - it can be seen from section 4.3 that the Z Height resolution is approximately 2μm @ 1μm Res_L. Another factor which would have a bigger affect on the recorded data is surface form error. By keeping the scan length to 2mm it was possible to reduce any deviation from form error to a minimum, however, given the relatively small surface features, as compared with the scan length, it is probable that the most of the deviation in the scans can be attributed to surface form error.

1.6µm surface scans

The results from the 1.6µm R_a surface scans are detailed below.

Scan #1

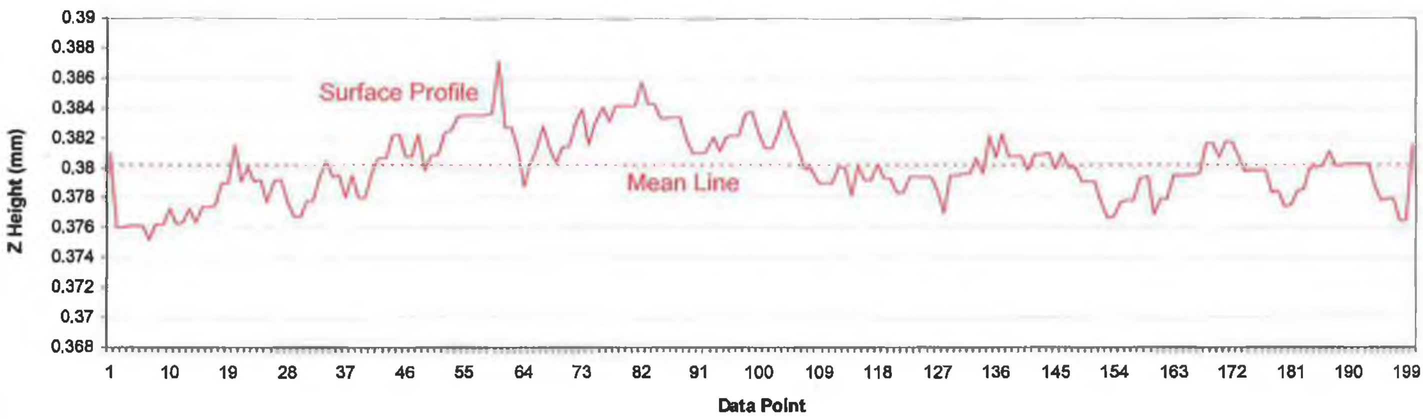

Figure 4.18 - 1.6µm surface, scan #1 recorded profile

Measured R_a value for scan #1 = 1.76µm

Scan #2

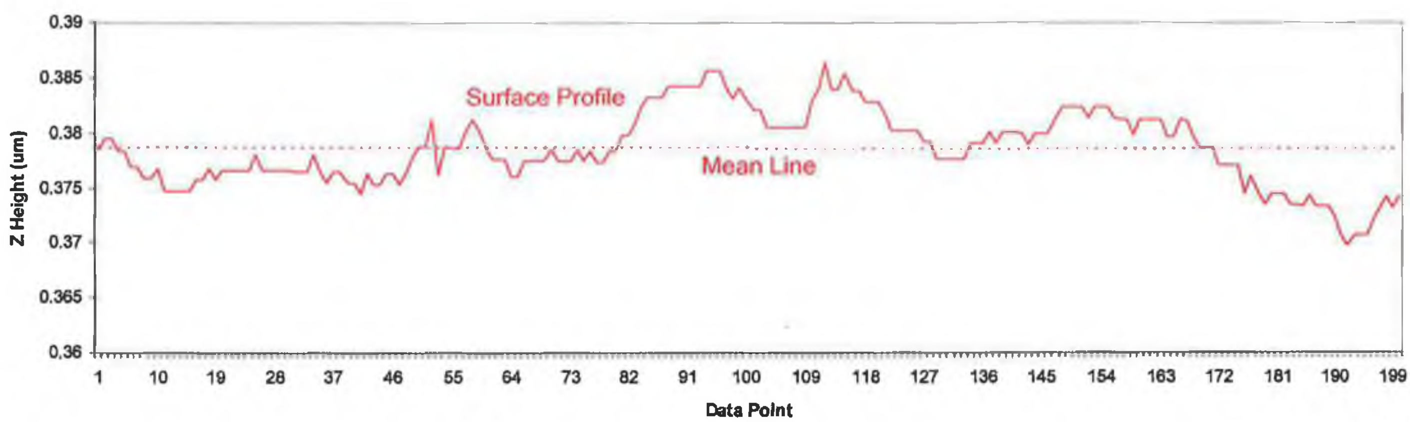

Figure 4.19 - 1.6µm surface, scan #2 recorded profile

Measured R_a value for scan #2 = 2.74µm

Scan #3

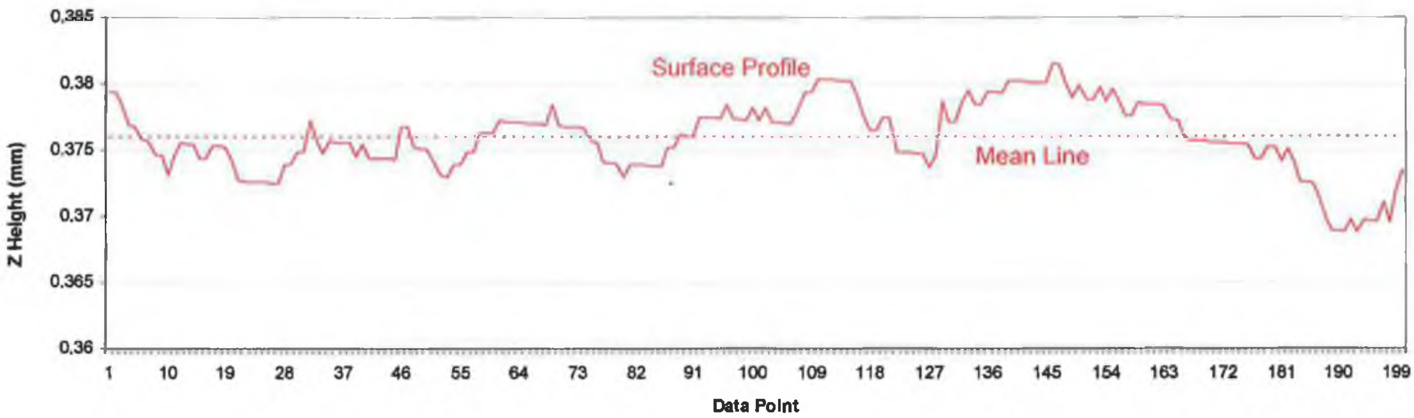

Figure 4.20 - 1.6μm surface, scan #3 recorded profile

Measured R_a value for scan #3 = 2.12μm

Scan #4

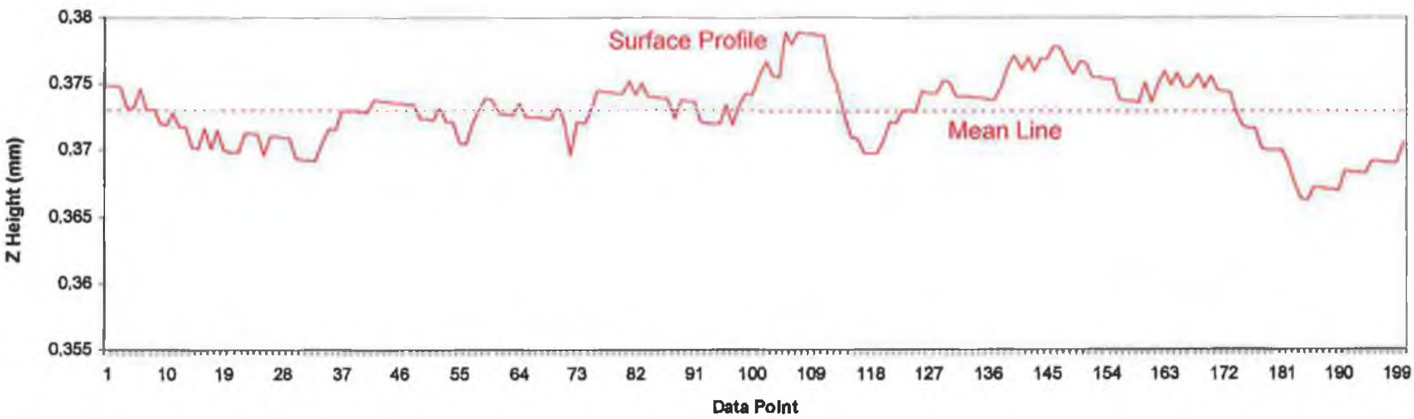

Figure 4.21 - 1.6μm surface, scan #4 recorded profile

Measured R_a value for scan #4 = 2.05μm

Scan #5

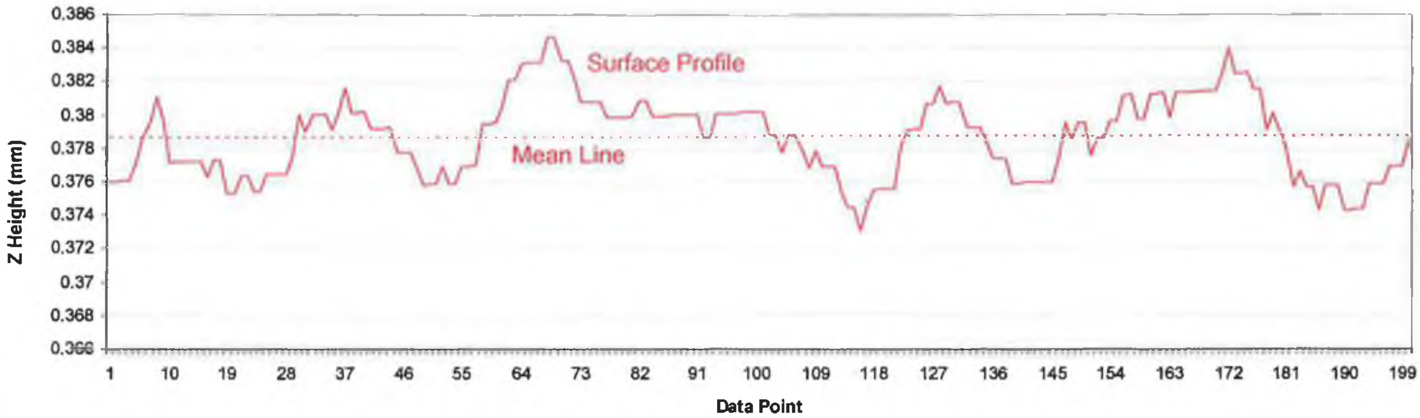

Figure 4.22 - 1.6µm surface, scan #5 recorded profile

Measured R_a value for scan #5 = 2.04µm

The surface R_a values were calculated again using eq 3.2.

Table 4.3 below details each of the recorded R_a values for the 1.6µm R_a surface and the average R_a achieved.

Table 4.3 – 1.6µm R_a surface measure R_a values

Scan	Measured R_a(µm)
1.	1.76
2.	2.74
3.	2.12
4.	2.05
5.	2.04
Av.	2.142µm

The true error can be calculated directly since the deviation of each scan is positive.
Error value = |100 - (2.142 / 1.6 * 100)| = 33.8%

It can be seen from these results that the performance limit of the laser sensor has been exceeded and it cannot accurately profile a surface which has an average roughness less than its vertical resolution. Like the previous scans recorded from the 3.2µm R_a surface, form error would also have had an influence on the recorded data, however in this case it is highly probable that the biggest influence on the scan error is due to the fact that accurate scanning of any surface with a roughness average less than approximately 2-3µm is beyond the capability of the profilometer.

4.6 M3 hole scan

Figure 4.23 below shows an isometric view of the imaged hole. During post processing, the data was shifted to a new datum with the lowest Z_{HEIGHT} set to zero. The centre of the hole was beyond the lower limit of the laser sensor and for most of this region an out of range value was returned.

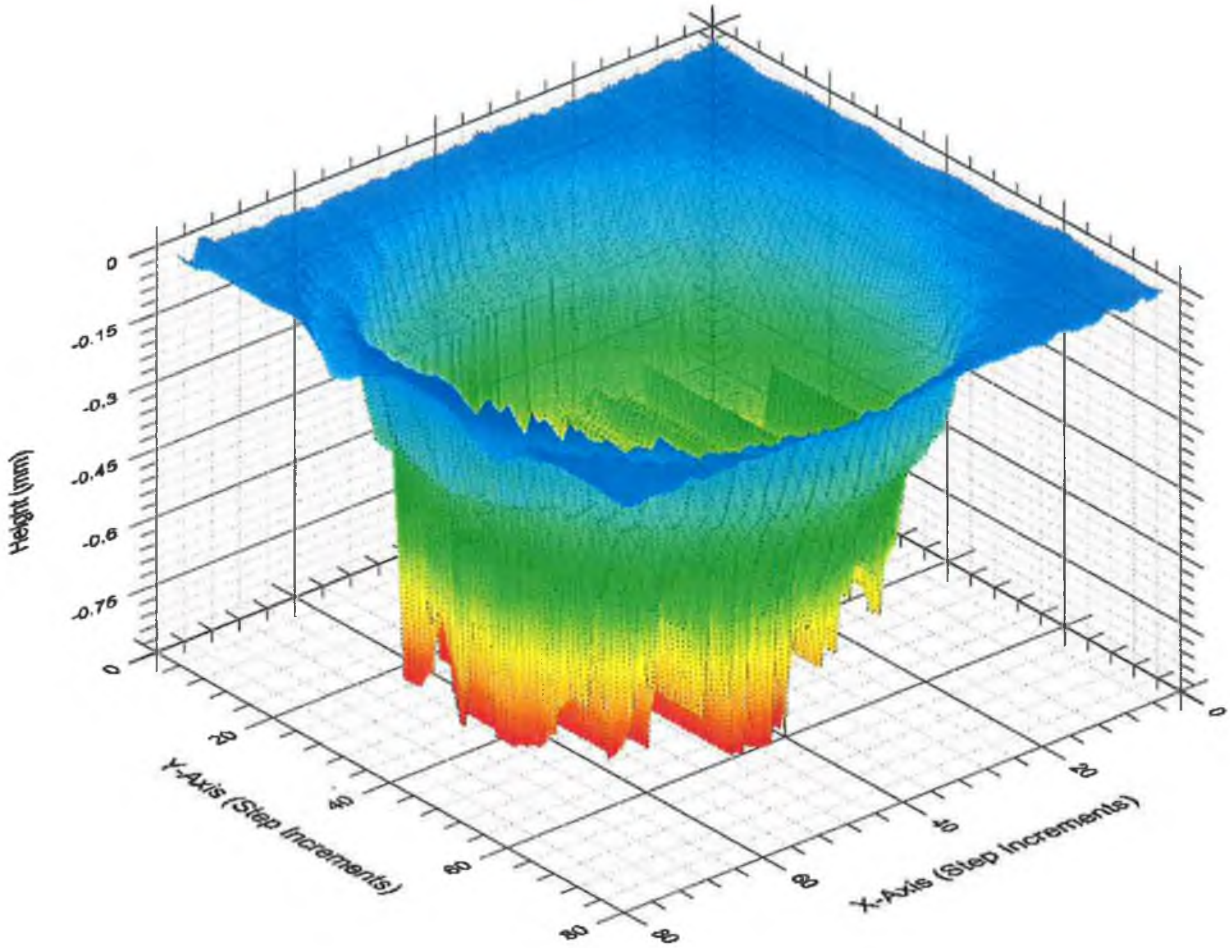

Figure 4.23 - Isometric view of imaged M3 hole

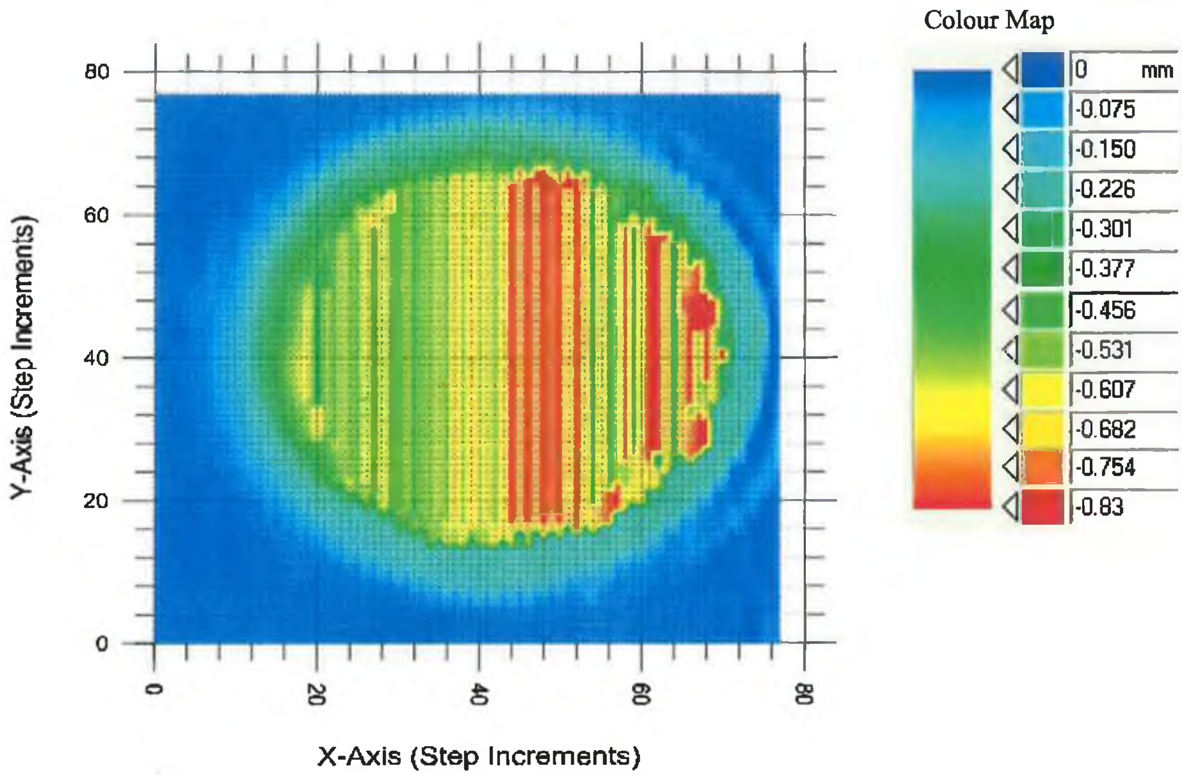

Figure 4.24 - Plan view of imaged M3 hole

Looking at figure 4.24 above, the outline of the hole is clearly visible. The right hand side of this plan view corresponds to the front left of the isometric image in figure 4.23. Figure 4.25 shows the elevation view of this scan. The scanning head passed over the hole from left to right, see figure 4.24 and 4.25. The displacement sensor was orientated such that the optical sensor was in front of the laser spot as the sensor passed over the surface. The bottom right hand side of this scan was out of range as the laser spot went into an out of sight area of view for the optical sensor. This shadow region was caused by the right hand edge of the hole. The top region of the right hand side of the hole was also distorted due to these biased readings from the effect of the shadow zone. The lower left hand side of the scan was at the sensor limit. Sensor readings in this region were due to diffuse laser light reflected from the bottom of the hole.

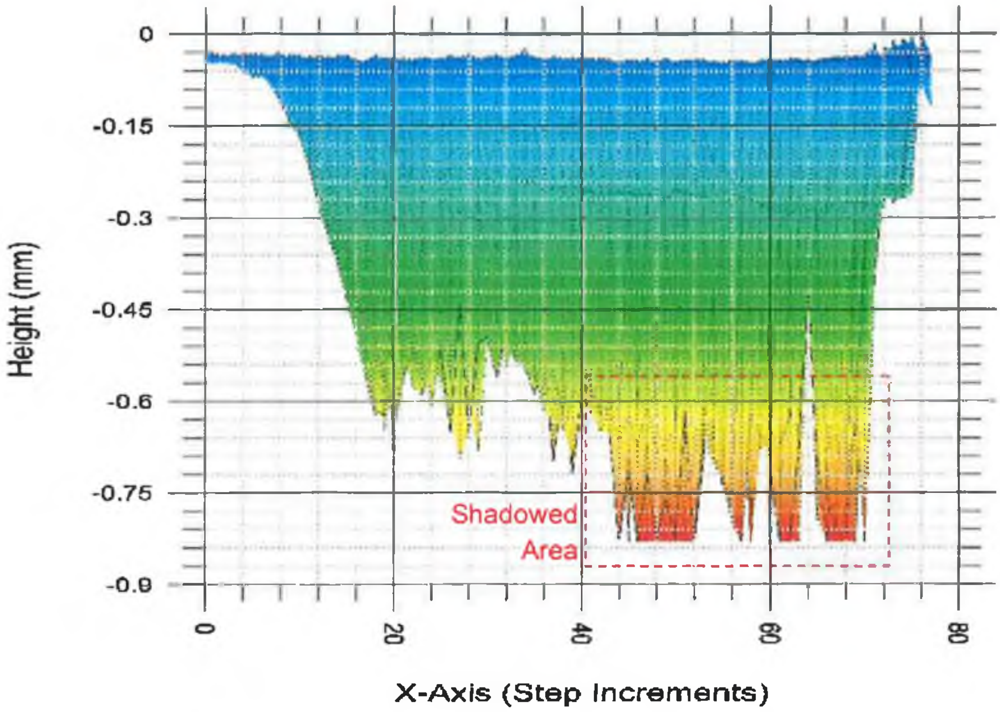

Figure 4.25 - Elevation of imaged M3 hole

Shadowing is also visible at the right hand section of the hole in figure 4.25. The laser spot became obscured by the right hand lip of the hole and so the sensor returned a maximum reading for the regions that it cannot see (a maximum reading will be returned from an 'out of range' state). Variations in this maximum range are due to diffuse light being picked up by the sensors CCD array. Since the diffuse light was detected over a relatively large area on the CCD array, the sensor returned an average value for the depth. The 'shadow' effect is discussed further in section 5.1. The hole also appears to be tapered since the tapered edges above are the chamfered rim of the hole itself appear. Figure 4.26 represents a section through a CAD file of the top portion of one of the holes.

Figure 4.26 - Section through M3 hole

4.6 M3 button screw and washer

Figure 4.27 below shows an isometric view of the button screw and washer assembly.

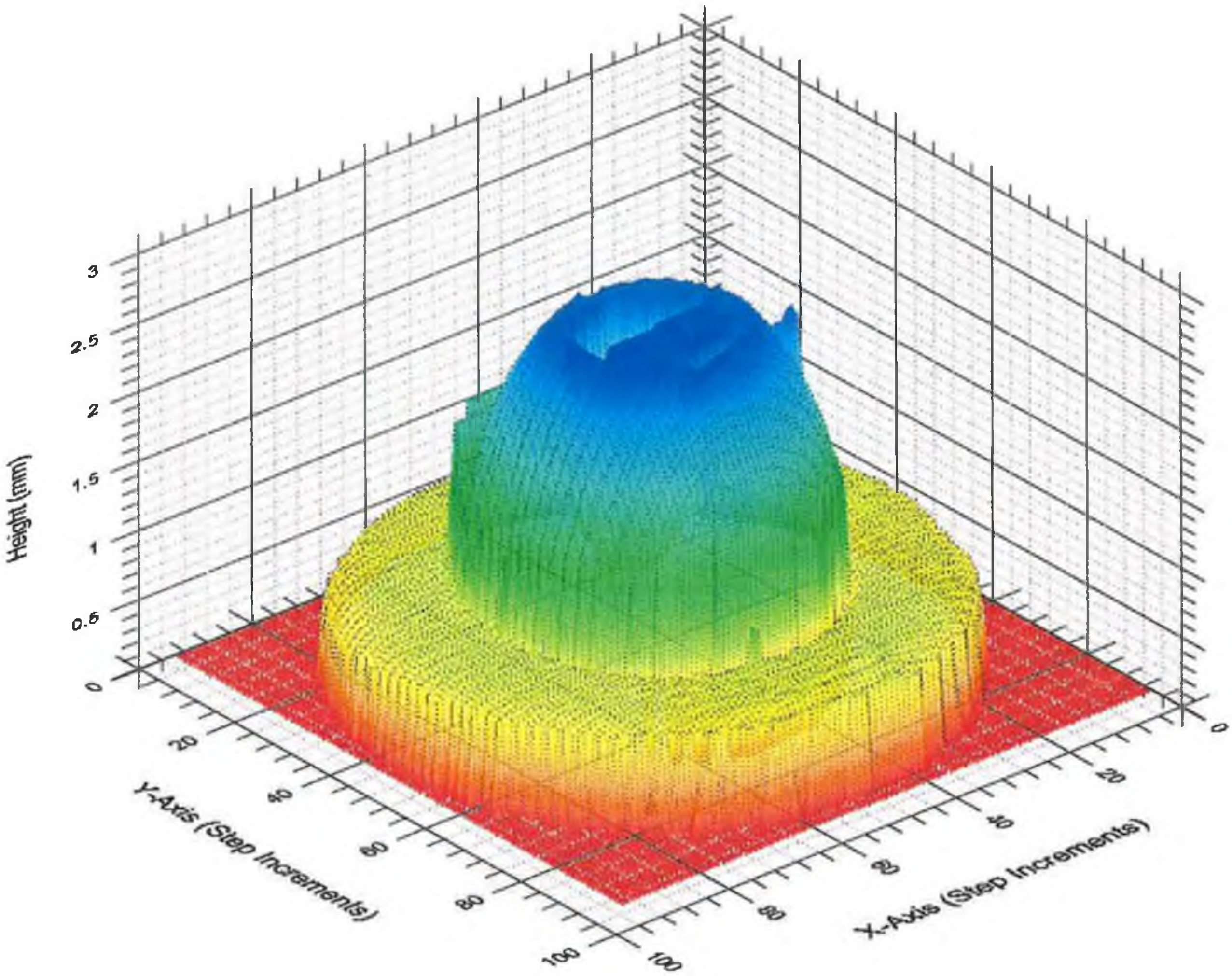

Figure 4.27 - Isometric view of button screw and washer assembly

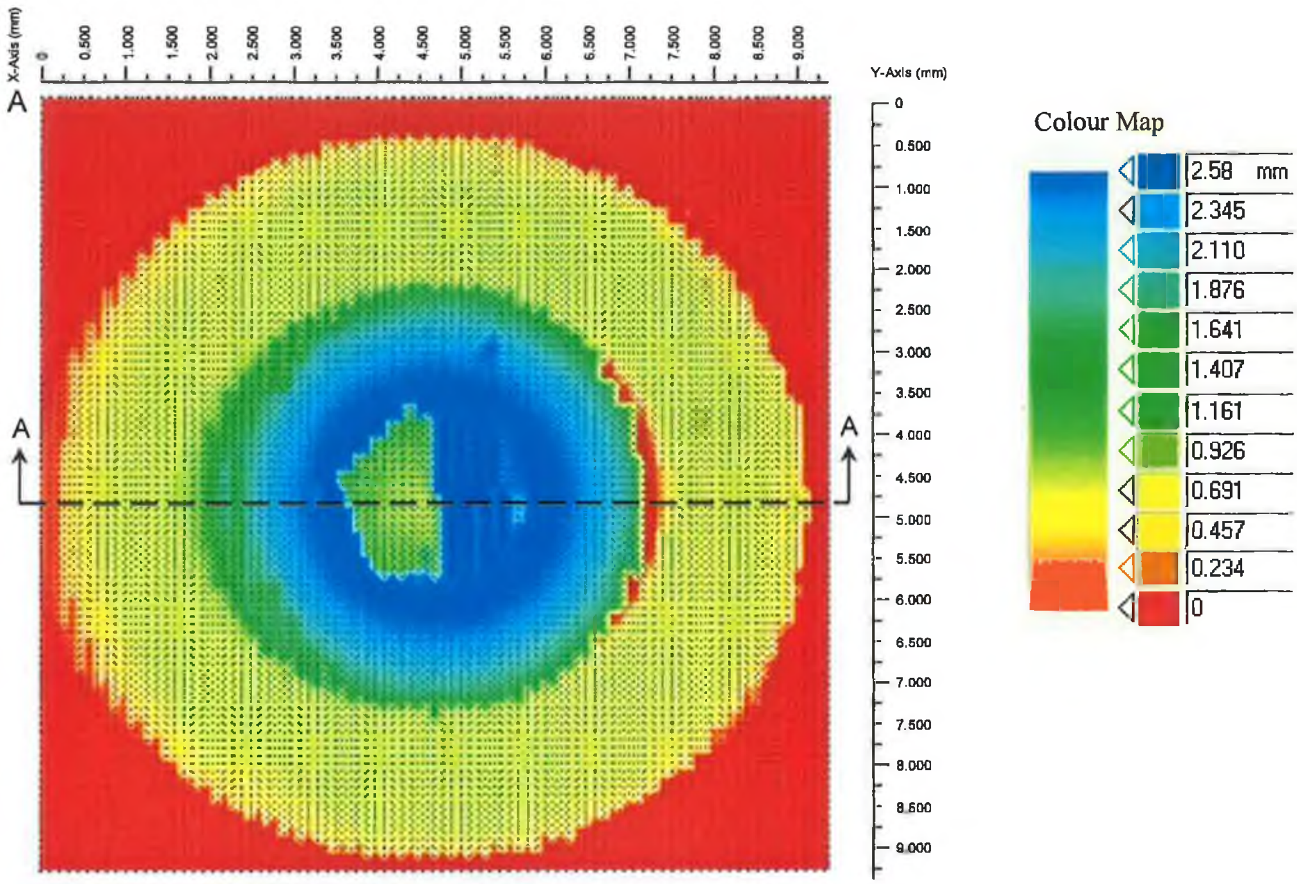

Figure 4.28 - Plan view of screw and washer assembly

Looking at figure 4.28 the areas at the centre of the screw affected by 'shadowing' are clearly visible. To get a better picture of the shadowed region a section through figure 4.28 is shown with the shadowed region marked in red, the incident and reflected beam are marked in broken lines. The shadowed area is created as the reflected light is obstructed by the central edge of the screw.

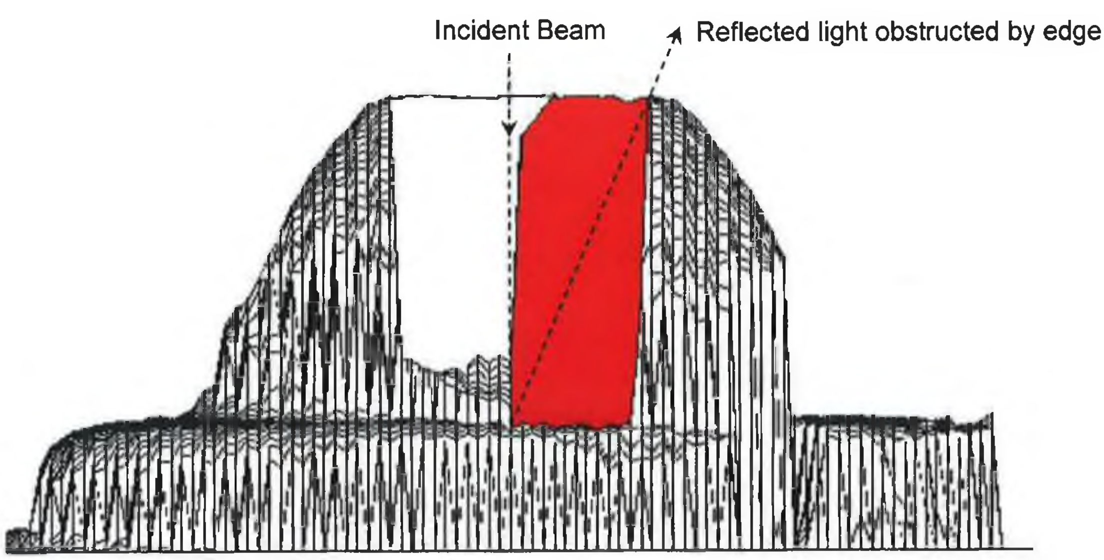

Figure 4.29 - Section A-A through centre of assembly

4.7 Surface scan recognition scan

These results show the ability of the laser profilometer to recognise and visualise surfaces. The first scan across the coin was made using a lateral resolution of 100μm giving a total of 100 scan points per mm^2. Figure 4.20 shows an image of the scanned area.

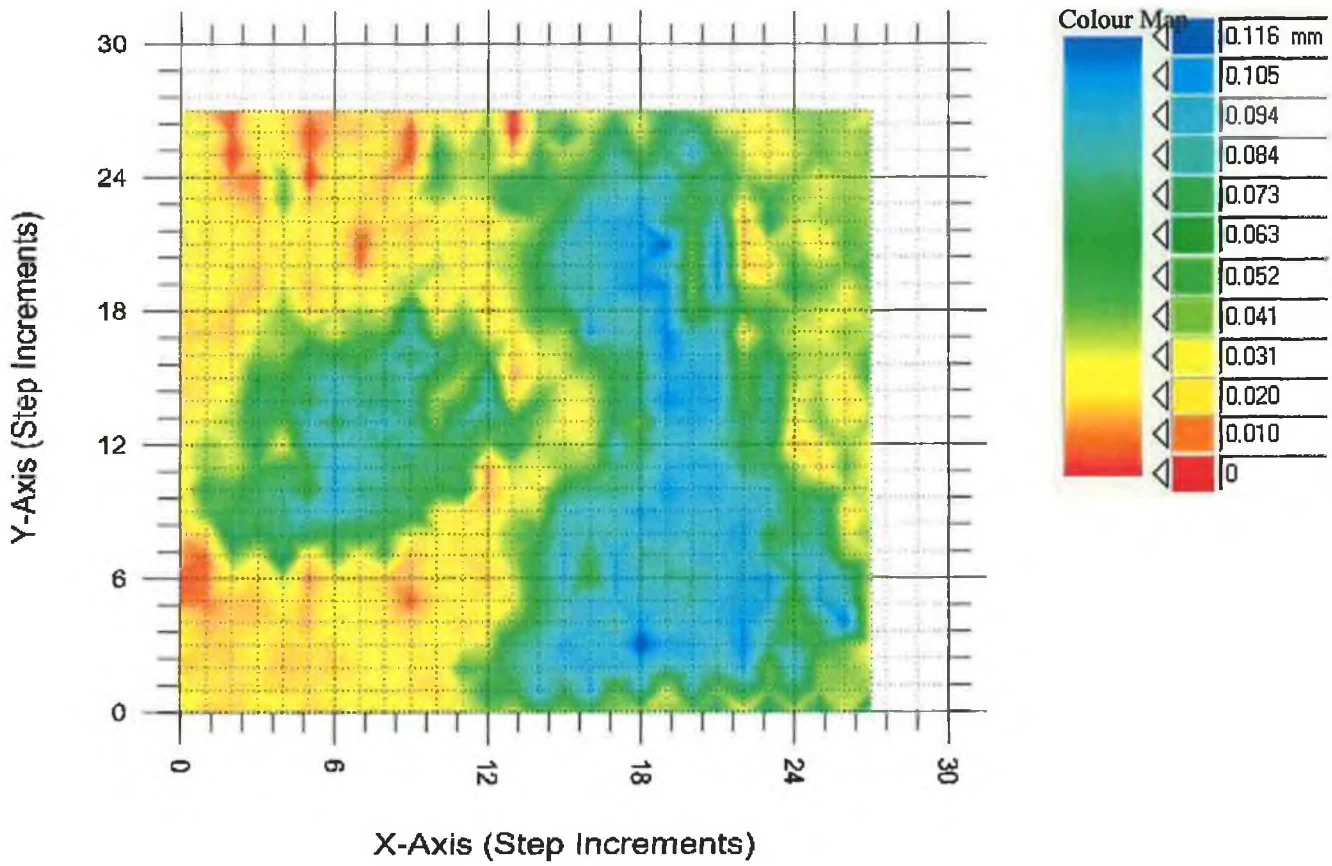

Figure 4.30 - 1 Euro coin scan with 100μm lateral resolution

Looking at figure 4.30 the islands from the scan area are clearly visible, rising approximately 0.1mm from the surface of the coin. The plot is quite 'blocky' as a result of the relatively low lateral resolution, the distance between each scanned point being 0.1mm. Referring to section 4.3, the best achievable lateral accuracy over this scan range (2.5 x 2.5mm) is approximately 4μm.

The second scan across the coin was made using a lateral resolution of 50μm giving a total of 400 scan points per mm^2. Thus, compared with the previous 100μm, the effective resolution has increased by a factor of four. Figure 4.31 shows the resultant image from this scan.

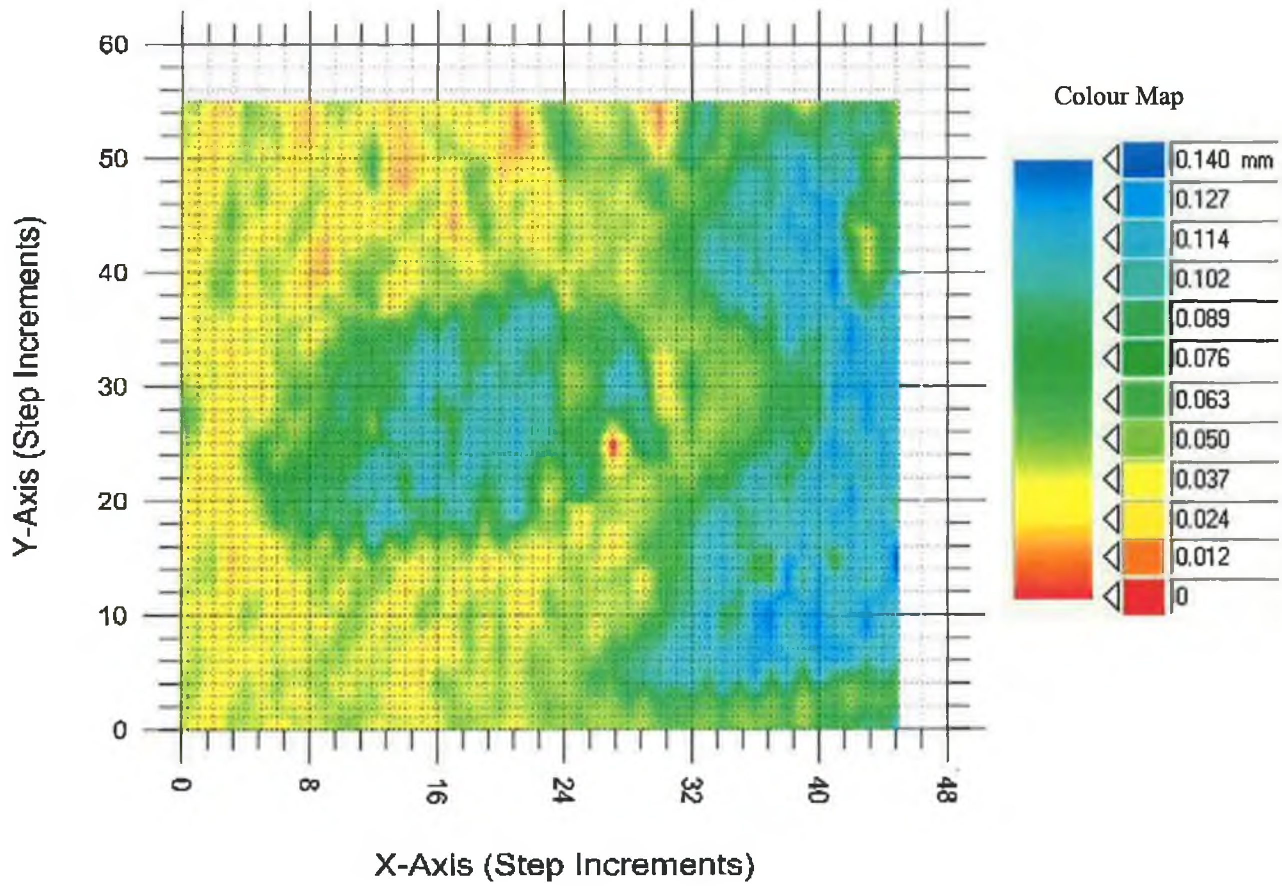

Figure 4.31 - 1 Euro coin scan with 50μm lateral resolution

4.8 Surface scan fibre optic mould tool

Figure 4.32 shows an SEM micrograph of the scanned mould tool.

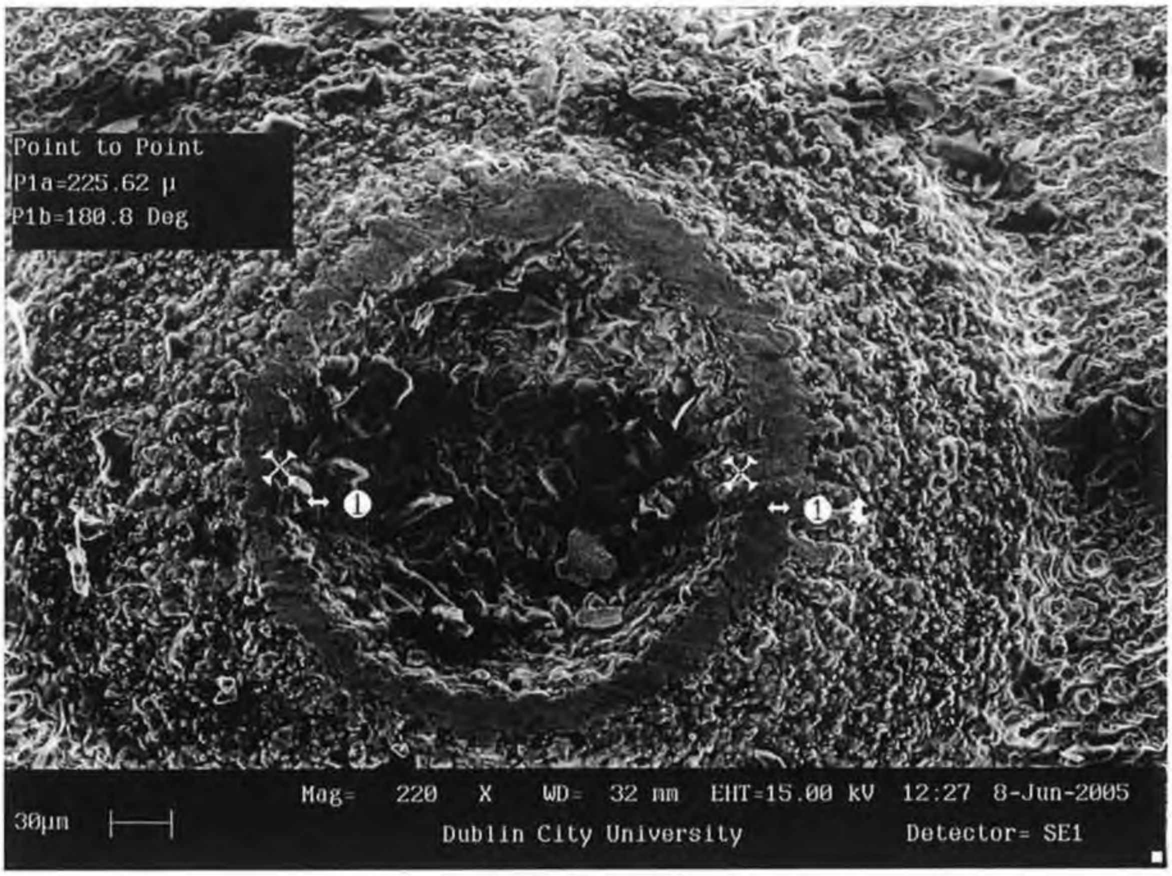

Figure 4.32 - SEM micrograph of fibre optic mould tool

From figure 4.32 it can be seen that the measured diameter of the dimple is approximately 225µm, from edge to edge. Figure 4.33 on the next page shows a 3D scan of the same mould tool from the laser profilometer. A side view is also shown in figure 4.34. The profilometer scan clearly shows the profile of the fibre optic mould. From figure 4.33 the diameter of the mould dimple has been recorded as approximately 227µm.

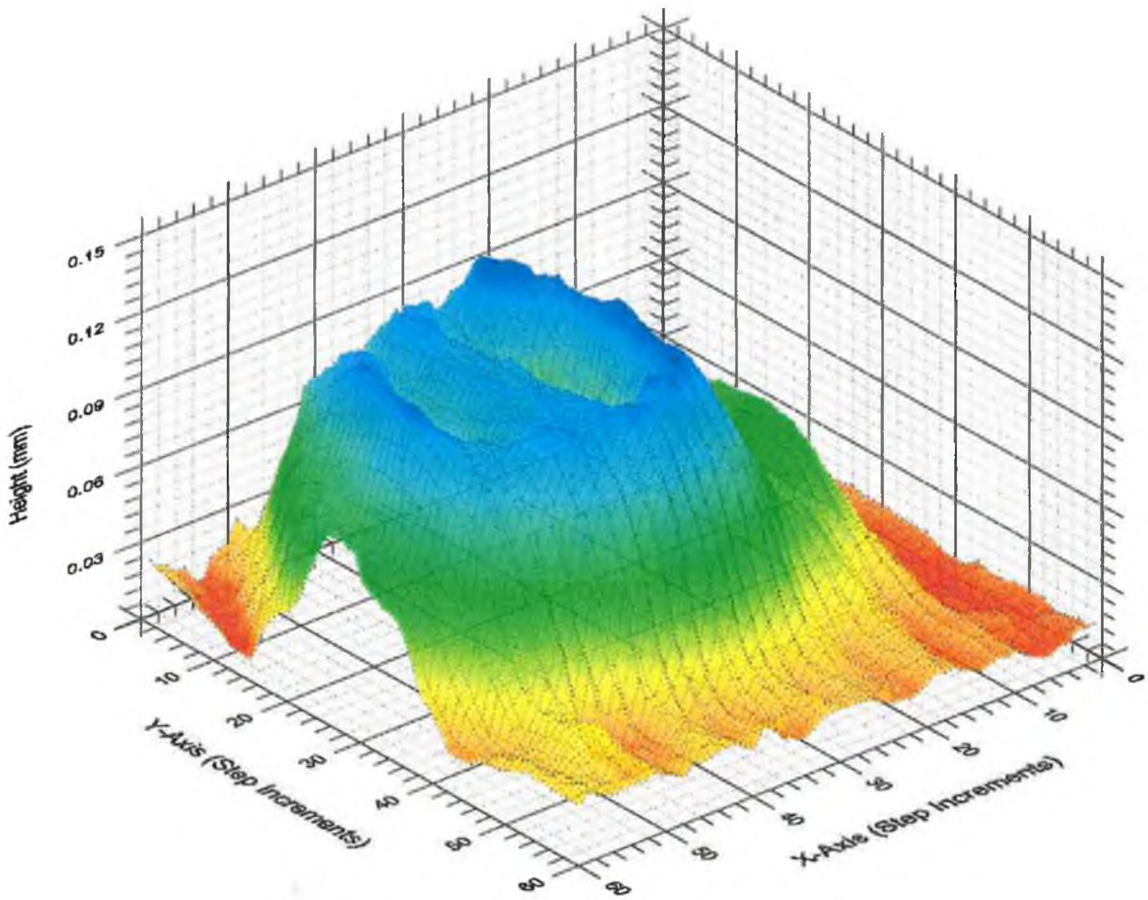

Figure 4.33 - Profilometer scan of fibre optic mould tool, 3D view

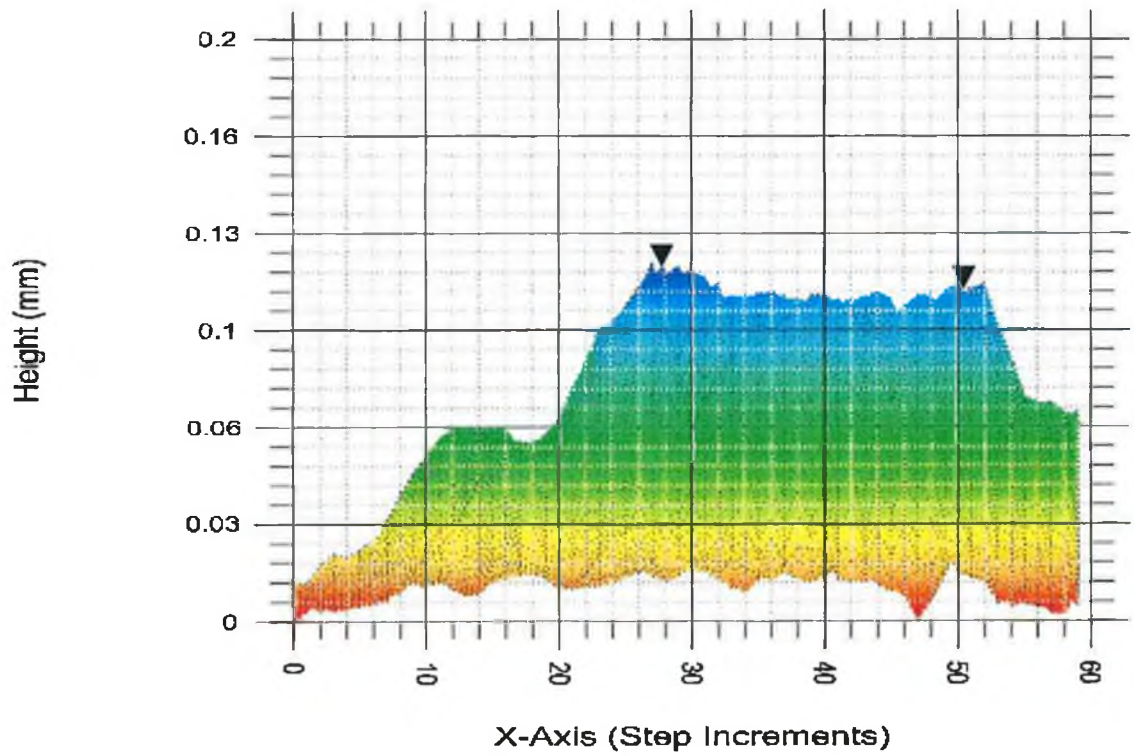

Figure 4.34 - Profilometer scan of fibre optic mould tool, side view

Chapter 5 Conclusions

5.1 Achievements

This thesis presents the development, construction, and testing of a laser based optical profilometer capable of measuring three dimensional surface topographies at a resolution of 2μm. The lateral accuracy of the system was found to be between 5 and 7μm at 10mm movement and between 8 and 11μm at 60mm table movement. The data acquisition for the system has been successfully developed around a raster type scan which only moves one axis at any one time and does not collect data while the laser displacement sensor is in motion, thus limiting unwanted vibrational errors.

The systems dynamic stability during scanning was studied and the dynamic vertical resolution of the system was measured. Leadscrew accuracy and repeatability was also studied and the maximum flatness error across the inspection table of the profilometer was measured. A number of different surfaces were also profiled to characterise and test the capabilities of the profilometer. A surface grinding sample was used to measure the accuracy of the system, and it's limitations during scanning for surface roughness. Scans of a fibre optic mould tool were also compared with SEM images of the same tool. A number of additional scans were run over surfaces to test the recognition capabilities of the profilometer and also to help describe the limitations of the profilometer when scanning larger three dimensional objects.

5.2 System limitations & recommendations for future development

The main limitation of the laser scanning system is its lack of ability to look sideways at the object that it is scanning – it can only see what lies directly beneath it, assuming of course that it lies within the range of the laser sensor. There are two other major limitations to this system. The first is the effect of 'shadow' during scanning of a surface that has a deep feature or hole, which can block the laser spot from the cameras view. Figure 5.1 illustrates the effect of 'shadow' and also one means by which it may be avoided for the scanning of a deep feature. 'Shadowing' will cause an *Out of Range* reading on the laser sensor. The effects of 'shadowing' is clearly visible from test sections 4.5 and 4.6. Figure 5.1 shows two different orientations of the displacement sensor for scanning a deep feature or surface. It should be noted that the feature is assumed to be longer than it is wide. In the first graphic on the left, the movement of the displacement sensor is along the same axis as the recessed surface, i.e. towards or away from the reader. The graphic on the right depicts the displacement sensor scanning across the feature, perpendicular to it's axis. Nevertheless, the same problem of shadowing will occur at the end of each scan as the scan shown in the left hand side will eventually come to a sharp surface at the end of the recessed surface. Scanning a deep hole will present the same problem. One solution to the problem of shadowing would be to scan the target surface from each direction in both axes, however this would require a much more complex axis mechanism to allow the displacement sensor or measurement table to be rotated through 90° and 180°.

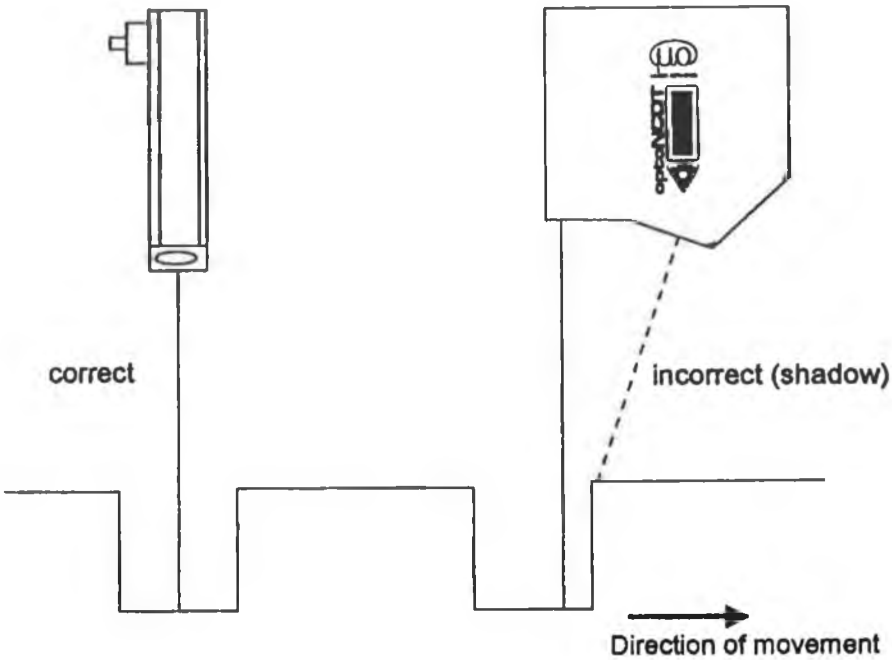

Figure 5.1 - 'Shadow' effect and the correct method to scan a deep feature

The second major constraint on the system it is the adverse effect of the beam spot size on the laser sensors ability to accurately measure sharp or well defined edges – the beam size of the ILD2000 laser displacement sensor used in this profilometer varies between 50 and 130μm depending on the target range. In order to increase the precision with which the system records these types of features the beam spot size should be reduced. However, without additional focusing optics, in general, the smaller the spot size, the lower the measuring range of the laser. In addition, the laser spot will suffer from interference when measuring features that are of the same size or less than the wavelength of the laser light, 0.67μm in this case.

A further limitation of the system is its inability to measure matt surfaces or surfaces with a low reflectivity without first being recalibrated to do so. Differences in the colour of the target will also affect the measurement capability of the laser sensor if it has been optimised for scanning other coloured materials. In order to optimise the system for scanning light or dark materials (for scanning black material gives best linearity) the sensor needs to be used in conjunction with a Micro-Epsilon IF2000 interface card. Since this was not available during this work the laser sensor was not set up to give high linearity while scanning dark surfaces or surfaces with poor reflectivity.

Currently, the system is configured and programmed to scan incrementally, however this is not ideal. It may give a steady platform from which to scan and take data points from, but the speed of scan is reduced. Ideally the system should be able to take data points 'on the move' and continously scan over the target surface while recording the surface features. In order to develop a system that is capable of this a number of important factors must be taken into consideration. Firstly, the systems leadscrews, or other means by which it moves are the platform from which the laser sensor or optical equipment may gather data about the target surface. Any backlash or undesirable freedom of movement in the leadscrews and associated parts will impact on the accuracy of the collected data. It is possible to purchase leadscrews and linear stages that boast incredible precision and accuracy – linear systems with resolutions of less than .005μm and sub-micron repeatability are not uncommon but are very expensive. Similarly, stepper motors ideally should be avoided (due to their relatively high vibration) and should be replaced with high quality brushless DC motors and encoders. This option is costly, but the use of encoders gives the user the advantage of using closed loop control. Assuming that the response time of the signal from the laser sensors and encoders is low, then it is feasible that the system could scan at quite a high rate while still being able to collect accurate data from the surface. By simply sampling the signals from the encoders and laser sensor at a rate defined by the user, it would be possible to quickly generate a series of coordinates, each coordinate made up of three values (X, Y & Z) derived from the sensor and encoder signals and each describing a single point on the target surface. A complete scan of the surface would be in 'point cloud' form and could easily be post-processed, as shown in this work, into a solid model.

The ideal laser scanning system should have relatively few moving parts to cut down unwanted vibrational induced noise and speed up the scanning process. This could be achieved by a system utilising acousto or electro-optics to scan or sweep the laser beam across the target surface. The surface in turn could be passed under the scanning beam on a high performance linear stage while data points would be acquired with a high resolution CMOS camera. The drawback of such a system is that complicated and expensive optics may be required to account for the angle of scan and an advanced data acquisition program would have to be employed to successfully control the system and interpret the recorded data.

Another possible improvement to the systems performance would be to create an automatic post processing function whereby the cosine and form error of the measurement table could be taken into consideration while scanning surfaces clamped to the measurement table surface. Effectively, this would mean adjusting the recorded data for the slope and form error of the surface table, and outputting more accurate data for the scanned surface. Also, a very precise knowledge of the location and contact of the part on the measurement table would also be required.

As can be seen from section 4.5, the system cannot distinguish between surface roughness and from error over larger scan distances. This is an important point since surface form will have an undesirable influence on surface roughness measurements if it is not properly taken into account. It has been shown that the system is reasonably good for surface roughness scans for R_a values greater than 3.0μm; however it should be noted that the surface roughness scans included in this work are over relatively small distances to keep the influence of form error to a minimum. In order to accurately measure surface roughness over larger distances a post processor should be developed, specifically for surface roughness measurement, and which can calculate and remove the effects of form error from the acquired data.

References

[1] Dagnall, H., (1986), Exploring Surface Texture, Rank Taylor Hobson Limited, Leicester, England.

[2] Stedman, M., and Lindsey K., (1988), Limits of Surface Measurement by Stylus Instruments, National Physics Laboratory, Division of Mechanical and Optical Metrology, Middlesex, UK.

[3] Thomas, T.R., (1988), Surface Roughness: The Next Ten Years.

[4] Stedman, M., and Lindsey K., (1988), Limits of Surface Measurement by Optical Probes, National Physics Laboratory, Division of Mechanical and Optical Metrology, Middlesex, UK.

[5] Lindsey, K., (1985), The Assessment of Ultrasmooth Substrates and Overcoatings, Vacuum 35 (10-11), 499-502.

[6] Alexander, S., Hellemans, L., Marti, O., Schneir, J., Elings, V., Hansma, P.K., Longmiro, M., and Gurley, J., (1989), An Atomic-Resolution Atomic-Force Microscope Implemented Using an Optical Lever, J. Appl. Phys. 65(1), 164-167.

[7] Meyer, G. and Amer, N., (1988), Novel Optical Approach to Atomic Force Microscopy, Appl. Phys. Lett. 53(12), 1045-1047.

[8] Keller, D.J. and Chih-Chung, C., (1992), Imaging Steep, High Structures by Scanning Force Microscopy with Electron Beam Deposited Tips. Surf. Sci. 268, 333-339

[9] Baselt, D., (1993), The Tip-Sample Interaction in Atomic Force Microscopy and its Implications for Biological Applications, California Institute of Technology, US.

[10] National Instruments Corporation, (1994), SCB-68 68-Pin Shielded Connector Block Installation Guide.

[11] Engineering Talk, (1999), Contact vs Laser Digitising – No Contest, Background Article.
Web address: [http://www.engineeringtalk.com/news/rat/rat101.html]
Date accessed: Jan 2003.

[12] Quality Online, Suzik, H.A., (1999), Inline Gauging – Choose Between Contact & Non-Contact Systems.
Web address: [http://www.qualitymag.com/articles/1999/sep99/0999f1.html]
Date accessed: Nov 2002

[13] Cielo, P., (1990), On-line Optical Sensors for Industrial Material Inspection, National Research Council, Canada, Industrial Materials Research Institute.

[14] Makosch, G., and, Drollinger, B., (1984), Applied Optics, pp. 4544-4552.

[15] Kohno, T., (1988), On a Few Functions of HIPOSS (High Precision Optical Surface Sensor) and Their Applications, Tokyo Metropolitan Institute of Technology, Department of Mechanical Systems Engineering, Japan.

[16] Leonhardt, K., K., Rippert, and H., Tiziani, (1988), Optical Methods of Measuring Rough Surfaces, Institute of Applied Optics, University of Stuttgart.

[17] Wyant, J., (2002), White Light Interferometry, Optical Sciences Center, University of Arizona, US.

[18] Quality Online (2000), Laser Based System Gives a 3-D Look to Nooks and Crannies, Quality Innovations.
Web address: [http://www.qualitymag.com/articles/2000/apr00/0400qi.html]
Date accessed: Dec 2002

[19] Buse, K, and Luennemann, L., (2000), Wave Front Sensing Using a Birefringent Crystal, University of Osnabrück, Germany

[20] Sullivan, S., (1986), Aquiring Images by Laser Scanning, Lincoln Laser Company, Phoenix, Arizona.

[21] Beary, S., (1996), Development of a Laser Scanning System for the Inspection of Surface Defects, Dublin City University, Dublin, Ireland.

[22] Svelto, O., and Hanna, D., (1982), Principles of Lasers, 2nd ed., Plenum Press, New York.

[23] Downs, M., McGivern, W., and Ferguson, H., (1985), Optical System for Measuring the Profiles of Super-Smooth Surfaces, Precision Engineering, Vol 7, No. 4, pp. 211-215.

[24] Hrabovský M., Bača Z., Horváth P., (2000), Theory of Speckle Displacement and Decorrelation and Its Application in Mechanics. Optics and Lasers in Engineering 32 (4) 395.

[25] Huang, C.C., (1984), Heterodyne Profiling Instrument for the Angstrom Region, Optical Engineering, pp. 365-370.

[26] NASA Technical Brief (1968), Technical Support Package for No. 68-10525, Digital Laser-Beam Deflection Sensor, CFSTI No. PB180565. Washington, D.C.

[27] Marshall, G.F., (1980), Applied Optics and Optical Engineering, Vol 6.

[28] Beiser, L., (1974) Laser Scanning Systems, in Laser Applications (M.Ross, ed.), Vol 2, p90. Academic Press, New York.

[29] Germano, C., (1971), IEEE Trans. Audio Electroacoustics 19 (1), 6.

[30] Hayosh, T., (1976), Motors and Control Systems for Rotating Mirror Deflectors, Proc. SPIE 84, 104.

[31] Hayosh, T., (1976), Technical Considerations of Rotating Mirror Deflectors, Simple and Sophisticated, Proc. SPIE 84, 128.

[32] Mason, N., and, Nelson, J.C., Downs, M., (1988), Measurement of The Profiles of Super Smooth Surfaces Using Optical Interferometry, National Physics Lab, Teddington, UK, and Department of Electrical and Electronic Engineering, University of Leeds, UK.

[33] Sommargren, G., (1981), Applied Optics, pp. 610-618.

[34] Collins, D., White paper on methods of laser scanning, Sch. of Mech. and Manu. Eng., DCU, November 2004.

[35] Collins, D., Brabazon, D., and El Baradie, M., Development of a laser based profilometer using optical triangulation, 22nd International Manufacturing conference, 31st Aug. – 2nd Sept. 2005, IT Tallaght, Dublin, pp. 151-161, ISBN: 0-9551218-0-9.

Appendix A System capability and technical data

Overall System Dimensions (HxWxL):	361mm x 387mm x 400mm
Measurement Table Dimensions:	200mm x 120mm
Maximum Scannable Area:	≈300mm x 210mm
Linear Encoding:	None
Axis Motors:	Vexta, 1.4V(3.8A), 1.8° Step
Laser Source:	Semiconductor Laser, 670nm/1mW Class 2 Laser
Laser Sensor Protection Rating:	IP64
Operating Temperature Range:	0°C to 40°C
Warm-up Period:	20 minutes
Measuring Range:	±2.5mm
Laser Sensor Standoff Distance:	58mm
Linear Stage Range:	±7.5mm
Laser Sensor Resolution (0.005% FSO):	0.25μm
System Z_{HEIGHT} Resolution:	2μm @ 1μm Res_L*
X-Axis Repeatability:	4.5μm over 5mm 8.2μm over 40mm
Y-Axis Repeatability:	>6μm over 5mm 11μm over 40mm
Temperature Stability:	±0.1μm/K
Smallest Spot Size:	
Start of Measurement Range	50μm
End of Measurement Range	130μm
Laser Sensor Sampling Rate:	10kHz
Permissible Incident Light:	30,000 lx
Angle Error for Surfaces Inclined @ 15°:	±0.13%
Angle Error for Surfaces Inclined @ 30°:	±0.3%
Lateral Resolution, Theoretical:	5μm – 3.906 x 10^{-2}μm
Lateral Repeatability:	Refer to section 2.2.3
Lateral Accuracy:	Refer to section 2.2.3
Input Voltage(s):	+12V_{DC}/250mA -12V_{DC}/120mA +5V_{DC}/500mA
Output Voltage:	±5V_{DC} (R_L = 1KΩ)

*Res_L = Lateral (X/Y Axis) Resolution

Appendix B Configurable system settings

Configurable Parameter	Recommended Setting	
Duty cycle:	0.5	X & Y Axes
Initial delay:	0s	
Stepper motor frequency:	16kHz (max 30kHz)	
Number of pulses [per increment] (Res_L) :	User defined	
[Number of] Scan increments:	User defined	
Reverse X Direction:	On/Off	
Number of passes:	User defined*	
Loop Program:	On/Off	
Delay at [demux] switchover:	500ms	
Output file path:	User defined	

*Should be equal to the number of scan increments for a square scan

Appendix C System piece part drawings

Piece Part Drawing Index:

a.	ITM-P5-20x20 45d	(Aluminium Extrusion, 20x20 45d)
b.	ITM-P5-EXT86.12	(Aluminium Extrusion, 20x20x86.12mm)
c.	ITM-P5-EXT100	(Aluminium Extrusion, 20x20x100mm)
d.	ITM-P5-EXT169.4	(Aluminium Extrusion, 20x20x169.4mm)
e.	ITM-P5-EXT210	(Aluminium Extrusion, 20x20x210mm)
f.	ITM-P5-EXT235	(Aluminium Extrusion, 20x20x235)
g.	ITM-P5-EXT395	(Aluminium Extrusion, 20x20x395mm)
h.	LS-MBR	[Linear Stage Mounting Bracket]
i.	LU-MBR	[Laser Unit Mounting Bracket]
j.	LU-MT-BAS	[Laser Unit Measurement Table Base]
k.	LU-MT-LG-MBR	[Laser Unit MT Mounting Bracket]
l.	LU-MT-TOP	[Measurement Table Top]
m.	LVDT-BR-BOT	[LVDT Bracket Bottom]
n.	LVDT-BR-RIS	[LVDT Bracket Riser]
o.	LVDT-BR-TOP	[LVDT Bracket Top]
p.	MT-LG-MBLK	[Measurement Table Linear Guide M.Block]
q.	SM-MBR-BAS	[Stepper Motor M.Bracket Base]
r.	SM-MBR-RIS	[Stepper Motor M.Bracket Riser]
s.	SM-MSURF-FR	[Stepper Motor M.Surface (Frame)]
t.	ST-BP	[Surface Table Bolster Plate]
u.	ST-GR	[Surface Table Granite]

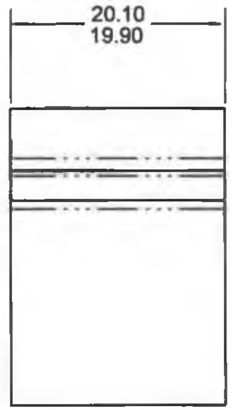

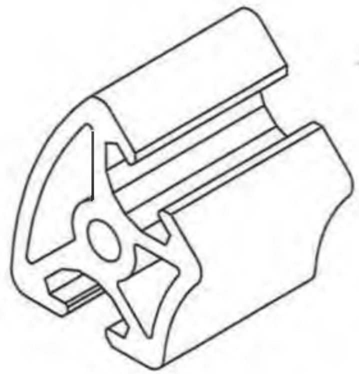

ISOMETRIC VIEW

DCU

TITLE:
ITEM P5 ANGLE EXTRUSION 20mm Wide

DESCRIPTION: ALUMINIUM EXTRUSION, 20x20 45d

MATERIAL: ALUMINIUM

DRAWN BY: D.COLLINS | DATE: 05/12/02

CHECKED BY: N/A | DATE: N/A

FILE NAME:
ITM-P5-20x20 45d

ADDITIONAL NOTES:
1. All dimensions are in mm unless otherwise specified.
2. Do not scale drawing.
3. Break all edges.

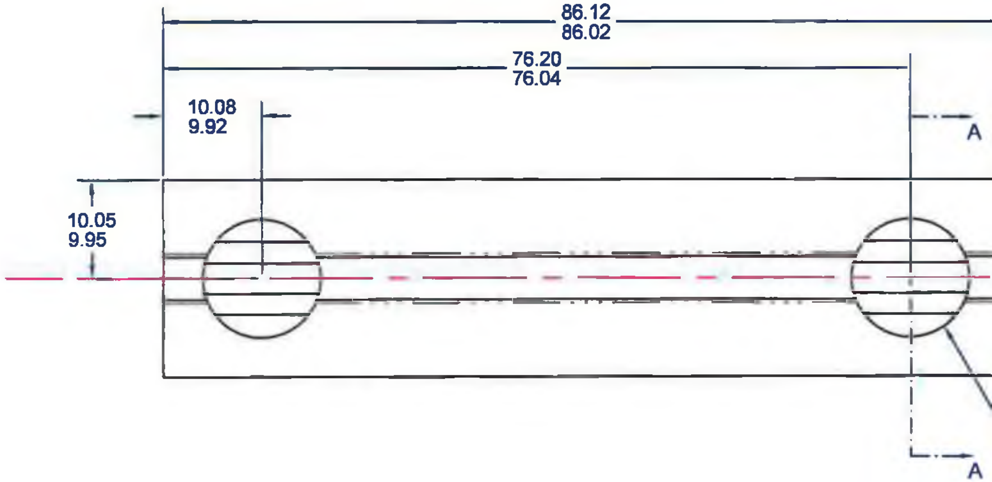

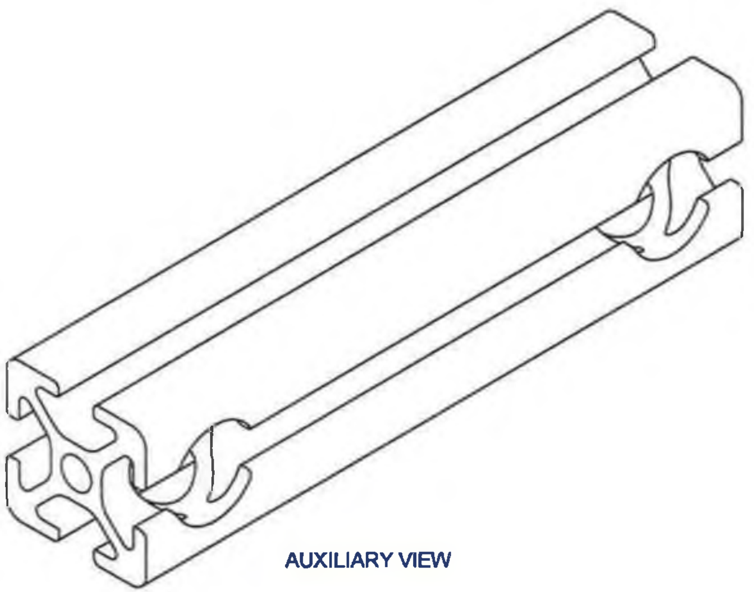

AUXILIARY VIEW

FIT TO A4

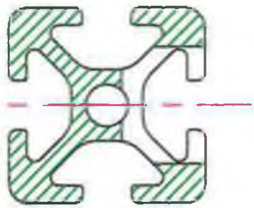

SECTION A - A

Ø12.0 HOLE, 8.5mm DEEP (2) PLCS

DCU

TITLE:
ITEM P5 EXTRUSION 86.12mm Long

DESCRIPTION: ALUMINIUM EXTRUSION, 20x20x86.12mm

MATERIAL: ALUMINIUM

DRAWN BY: D.COLLINS DATE: 14/09/02

CHECKED BY: N/A DATE: N/A

FILE NAME:
ITM-P5-EXT86.12.dwg

ADDITIONAL NOTES:

1. All dimensions are in mm unless otherwise specified.
2. Do not scale drawing.
3. Break all edges.

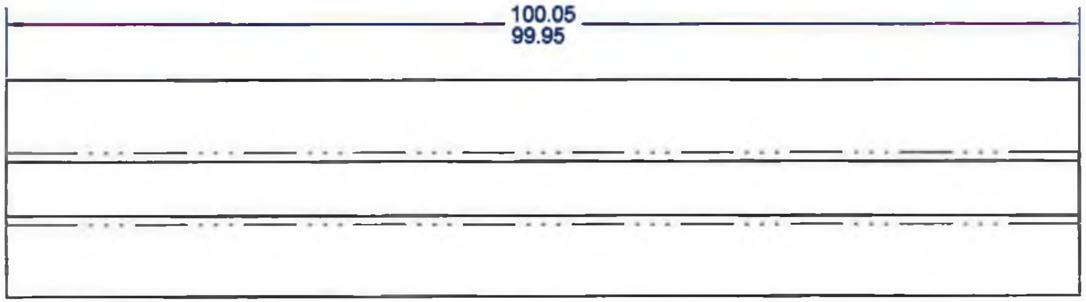

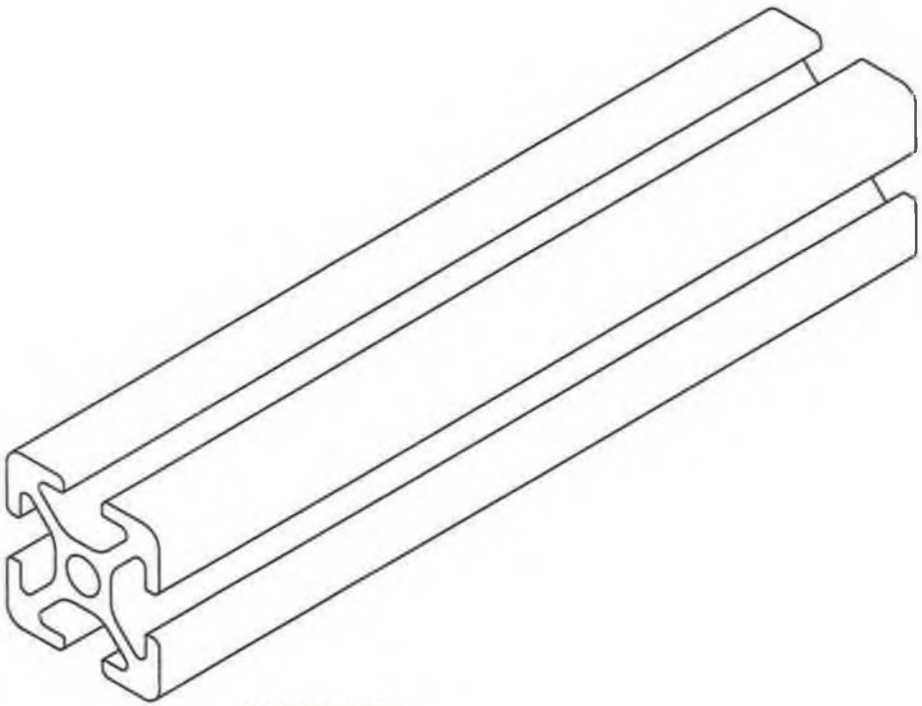

ISOMETRIC VIEW

DCU TITLE: ITEM P5 EXTRUSION 100mm Long	
DESCRIPTION: ALUMINIUM EXTRUSION, 20x20x100mm	MATERIAL: ALUMINIUM
DRAWN BY: D.COLLINS DATE: 14/09/02 CHECKED BY: N/A DATE: N/A	FILE NAME: ITM-P5-EXT100.dwg

ADDITIONAL NOTES:
1. All dimensions are in mm unless otherwise specified.
2. Do not scale drawing.
3. Break all edges.

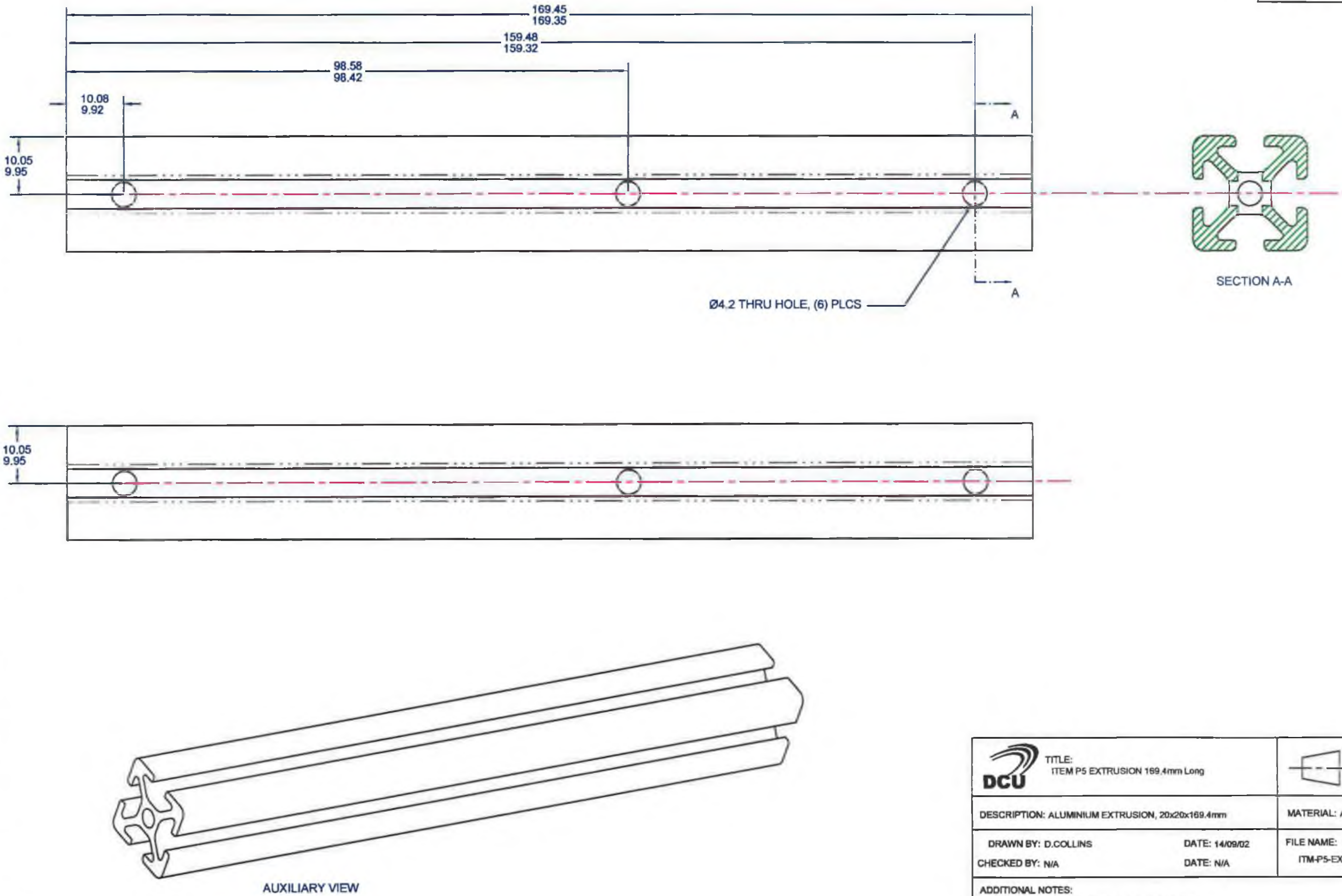

DCU TITLE: ITEM P5 EXTRUSION 169.4mm Long	
DESCRIPTION: ALUMINIUM EXTRUSION, 20x20x169.4mm	MATERIAL: ALUMINIUM
DRAWN BY: D.COLLINS DATE: 14/09/02 CHECKED BY: N/A DATE: N/A	FILE NAME: ITM-P5-EXT169.4.dwg

ADDITIONAL NOTES:
1. All dimensions are in mm unless otherwise specified.
2. Do not scale drawing.
3. Break all edges.

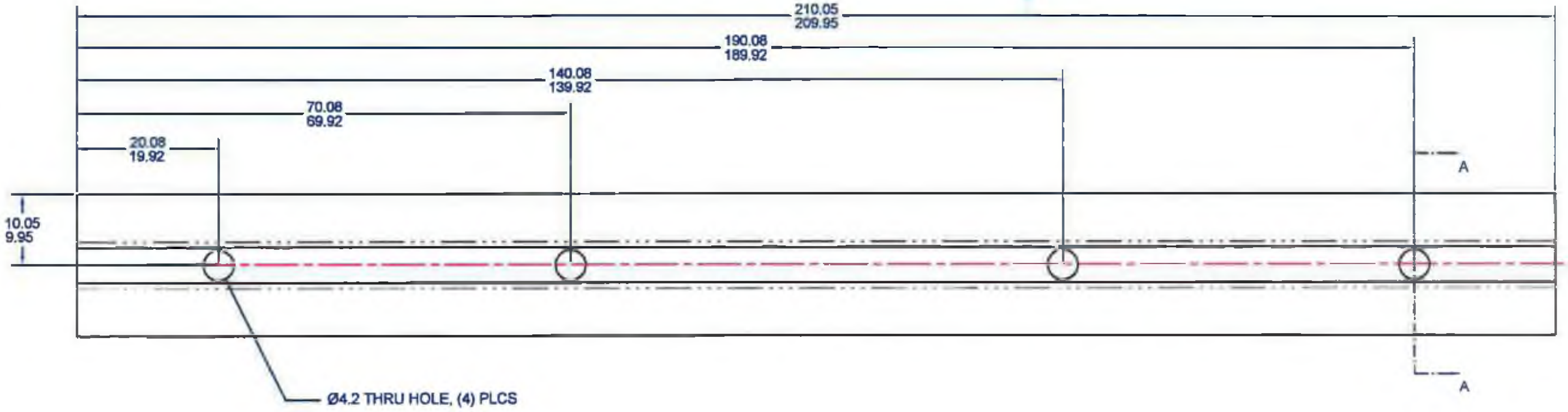

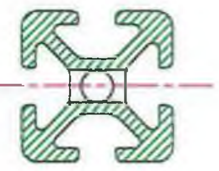

SECTION A-A

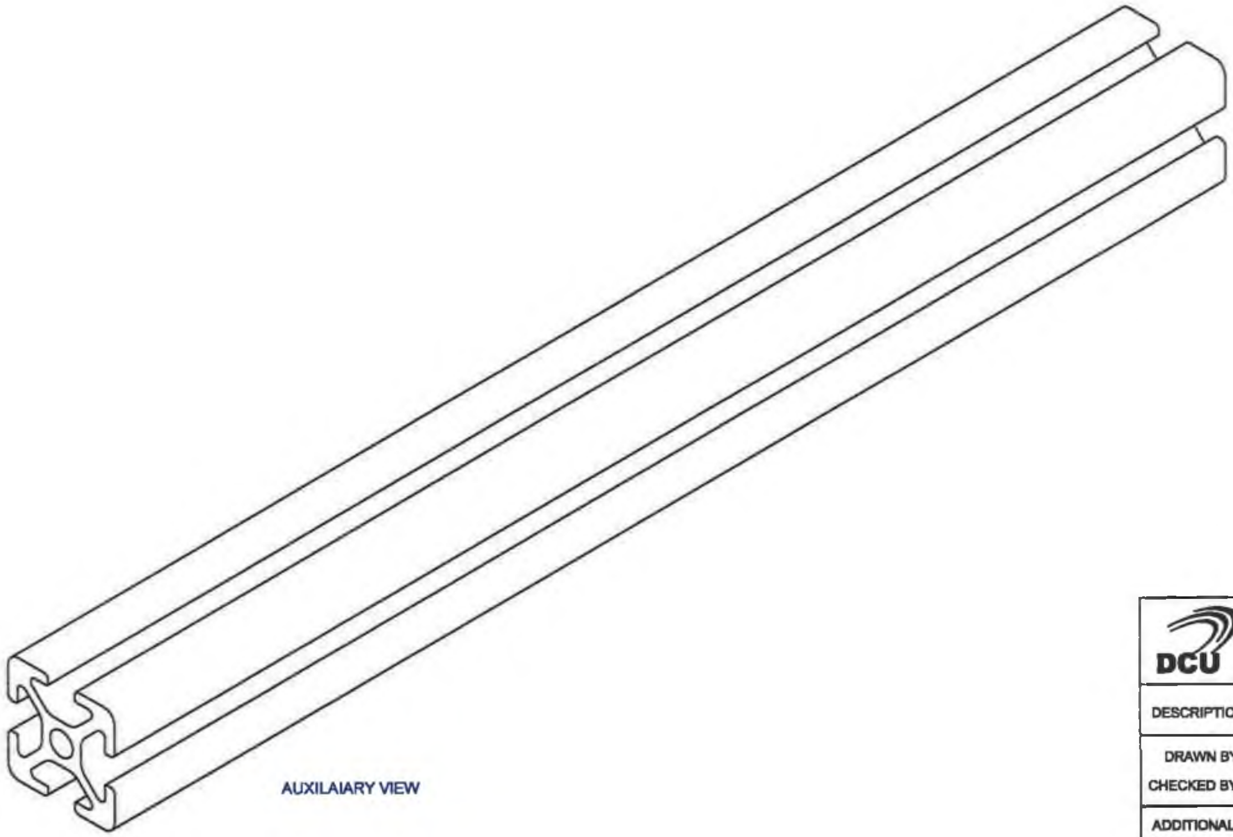

AUXILAIARY VIEW

TITLE: ITEM P5 EXTRUSION 210mm Long	
DESCRIPTION: ALUMINIUM EXTRUSION, 20x20x210mm	MATERIAL: ALUMINIUM
DRAWN BY: D.COLLINS DATE: 14/09/02 CHECKED BY: N/A DATE: N/A	FILE NAME: ITM-P5-EXT210.dwg

ADDITIONAL NOTES:

1. All dimensions are in mm unless otherwise specified.
2. Do not scale drawing.
3. Break all edges.

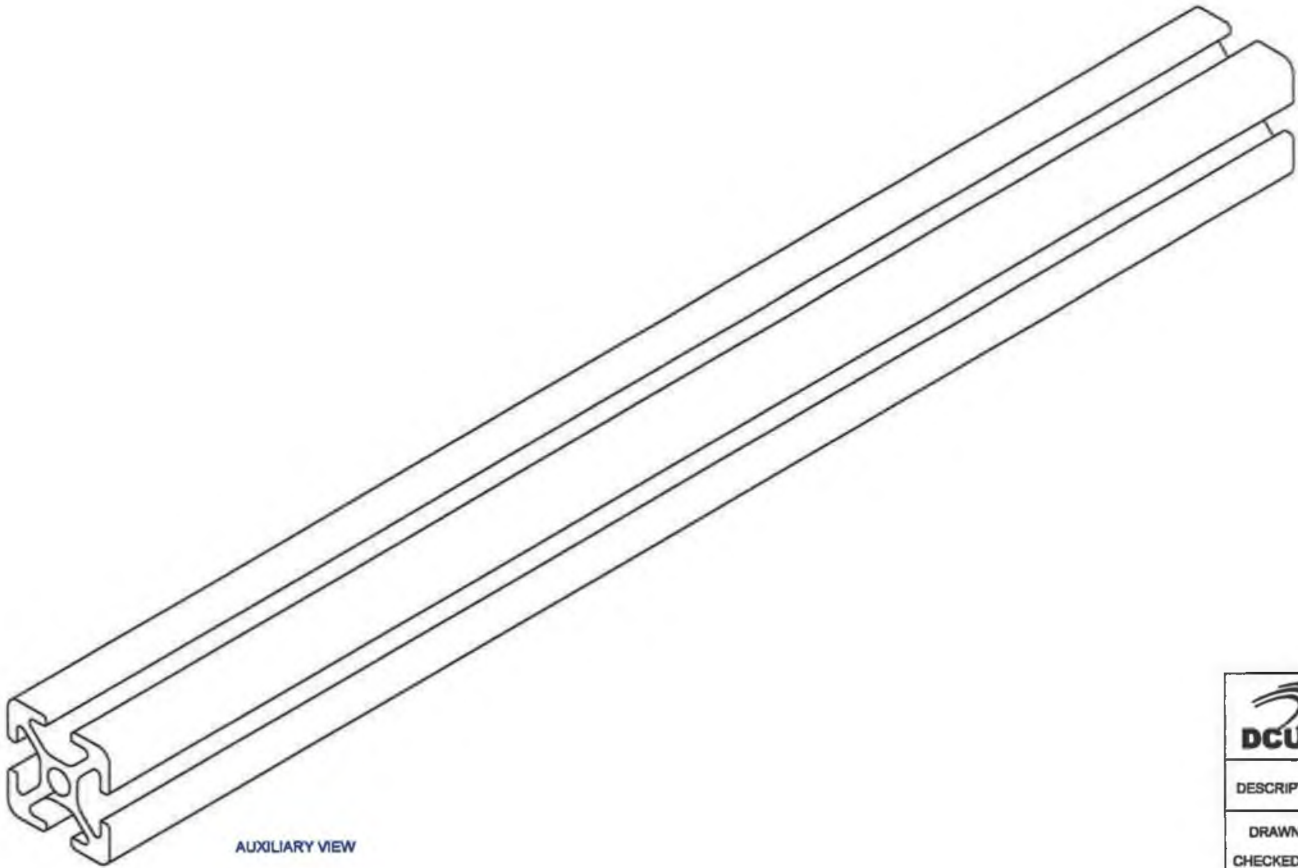

AUXILIARY VIEW

DCU

TITLE:
ITEM P5 EXTRUSION 235mm Long

DESCRIPTION: ALUMINIUM EXTRUSION, 20x20x235mm

MATERIAL: ALUMINIUM

DRAWN BY: D.COLLINS — DATE: 14/09/02

CHECKED BY: N/A — DATE: N/A

FILE NAME: ITM-P5-EXT235.dwg

ADDITIONAL NOTES:

1. All dimensions are in mm unless otherwise specified.
2. Do not scale drawing.
3. Break all edges.

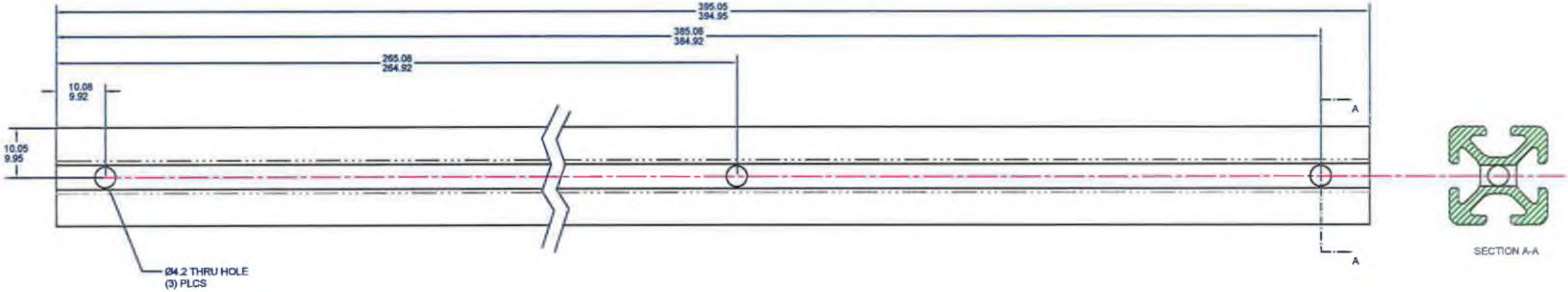

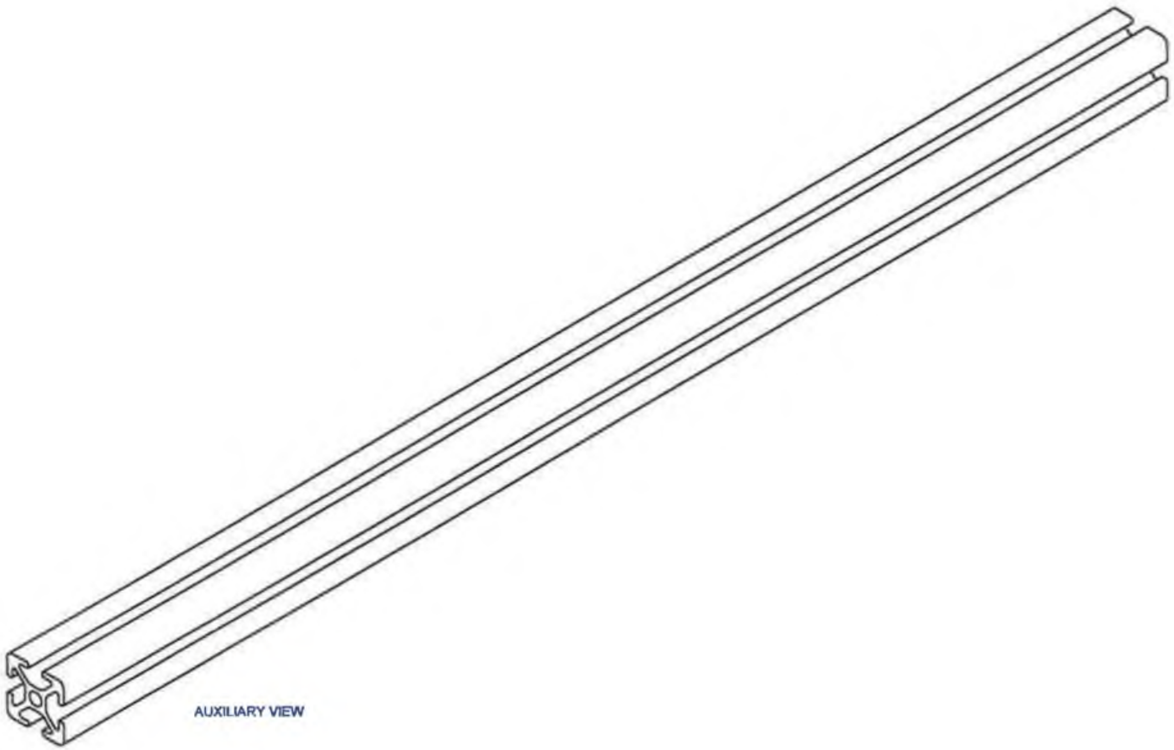

AUXILIARY VIEW

DCU

TITLE: ITEM P5 EXTRUSION 395mm Long	
DESCRIPTION: ALUMINIUM EXTRUSION, 20x20x395mm	MATERIAL: ALUMINIUM
DRAWN BY: D.COLLINS / DATE: 14/09/02	FILE NAME: ITM-P5-EXT395.dwg
CHECKED BY: N/A / DATE: N/A	

ADDITIONAL NOTES:

1. All dimensions are in mm unless otherwise specified.
2. Do not scale drawing.
3. Break all edges.

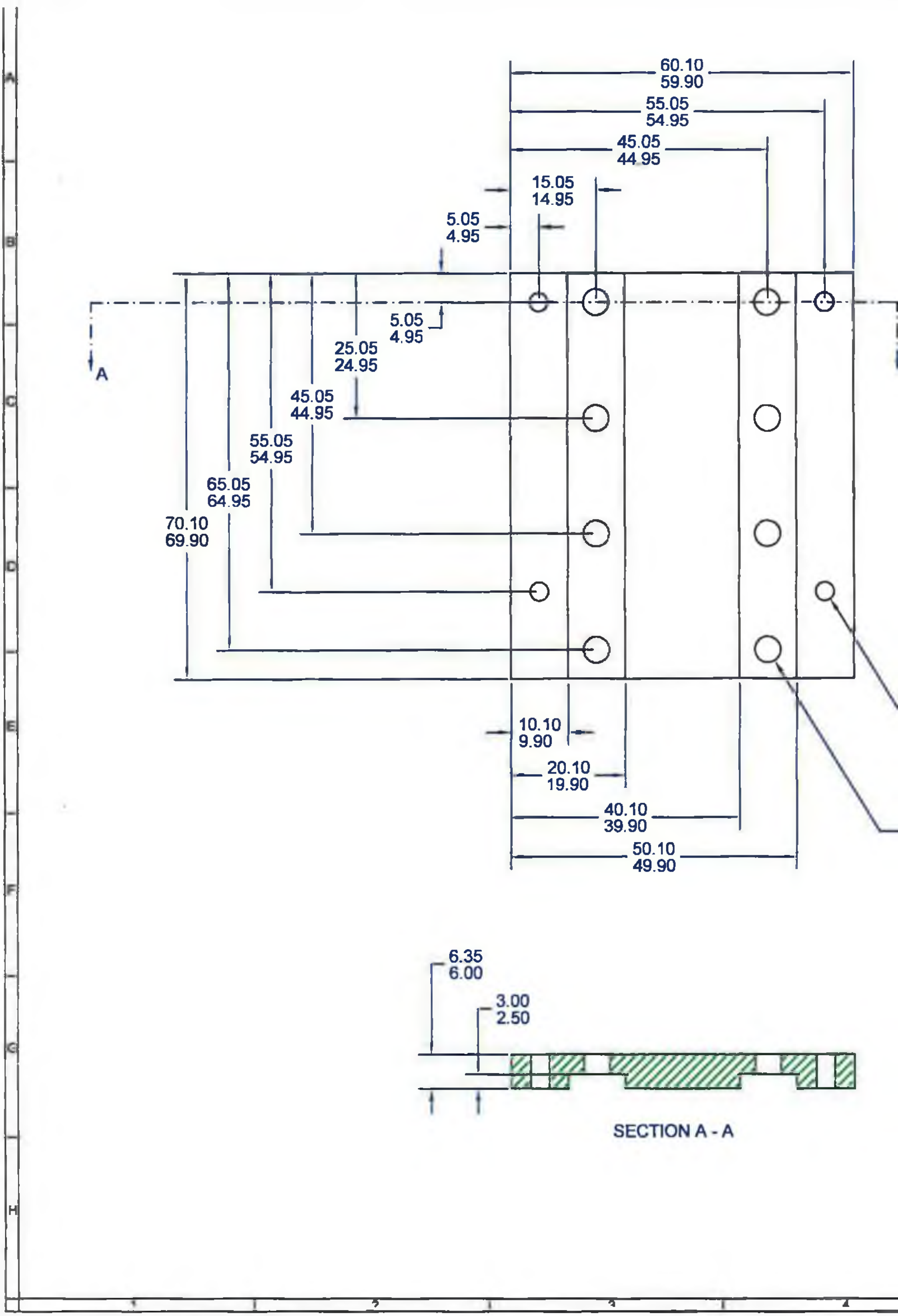

60.10
59.90
55.05
54.95
45.05
44.95
15.05
14.95
5.05
4.95
A
5.05
4.95
25.05
24.95
45.05
44.95
55.05
54.95
65.05
64.95
70.10
69.90
10.10
9.90
20.10
19.90
40.10
39.90
50.10
49.90
6.35
6.00
3.00
2.50

SECTION A - A

A

M4 THRU HOLE
(4) PLCS

Ø4.5 THRU' HOLE
(8) PLCS

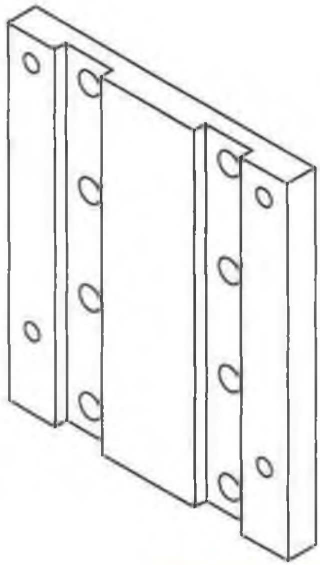

ISOMETRIC VIEW

DCU

TITLE:
LINEAR STAGE MOUNTING BRACKET

DESCRIPTION: MOUNTING BRACKET

MATERIAL: ALUMINIUM

DRAWN BY: D.COLLINS   DATE: 14/09/02

CHECKED BY: N/A   DATE: N/A

FILE NAME:
LS-MBR.dwg

ADDITIONAL NOTES:

1. All dimensions are in mm unless otherwise specified.
2. Do not scale drawing.
3. Break all edges.

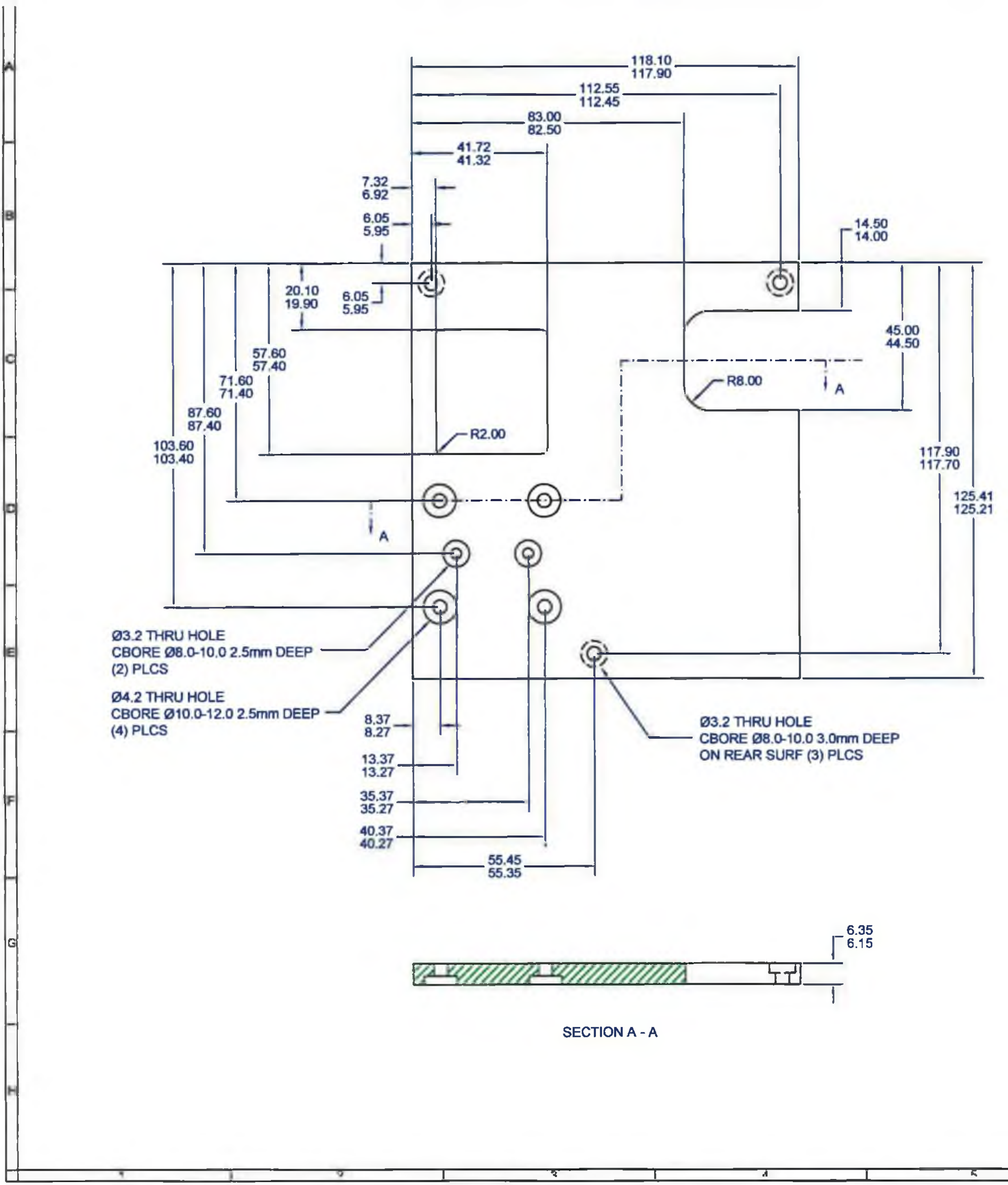
118.10
117.90
112.55
112.45
83.00
82.50
41.72
41.32
7.32
6.92
6.05
5.95
14.50
14.00
20.10
19.90
6.05
5.95
57.60
57.40
71.60
71.40
87.60
87.40
103.60
103.40
45.00
44.50
R8.00
A
R2.00
117.90
117.70
125.41
125.21
A
Ø3.2 THRU HOLE
CBORE Ø8.0-10.0 2.5mm DEEP
(2) PLCS
Ø4.2 THRU HOLE
CBORE Ø10.0-12.0 2.5mm DEEP
(4) PLCS
Ø3.2 THRU HOLE
CBORE Ø8.0-10.0 3.0mm DEEP
ON REAR SURF (3) PLCS
8.37
8.27
13.37
13.27
35.37
35.27
40.37
40.27
55.45
55.35
6.35
6.15
SECTION A - A

FIT TO A4	1 OF 1

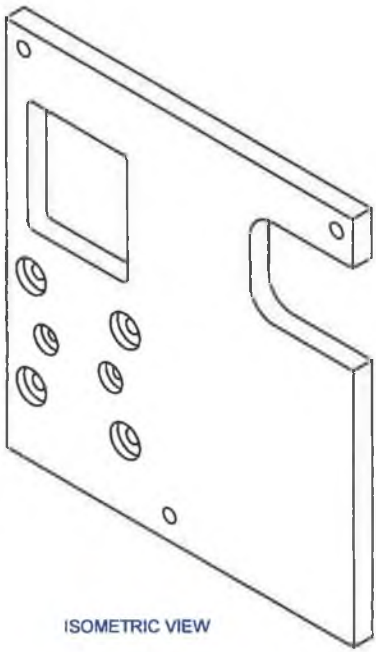

ISOMETRIC VIEW

DCU TITLE: LASER UNIT MOUNTING BRACKET	
DESCRIPTION: MOUNTING BRACKET	MATERIAL: ALUMINIUM
DRAWN BY: D.COLLINS DATE: 14/09/02 CHECKED BY: N/A DATE: N/A	FILE NAME: LU-MBR.dwg

ADDITIONAL NOTES:

1. All dimensions are in mm unless otherwise specified.
2. Do not scale drawing.
3. Break all edges.

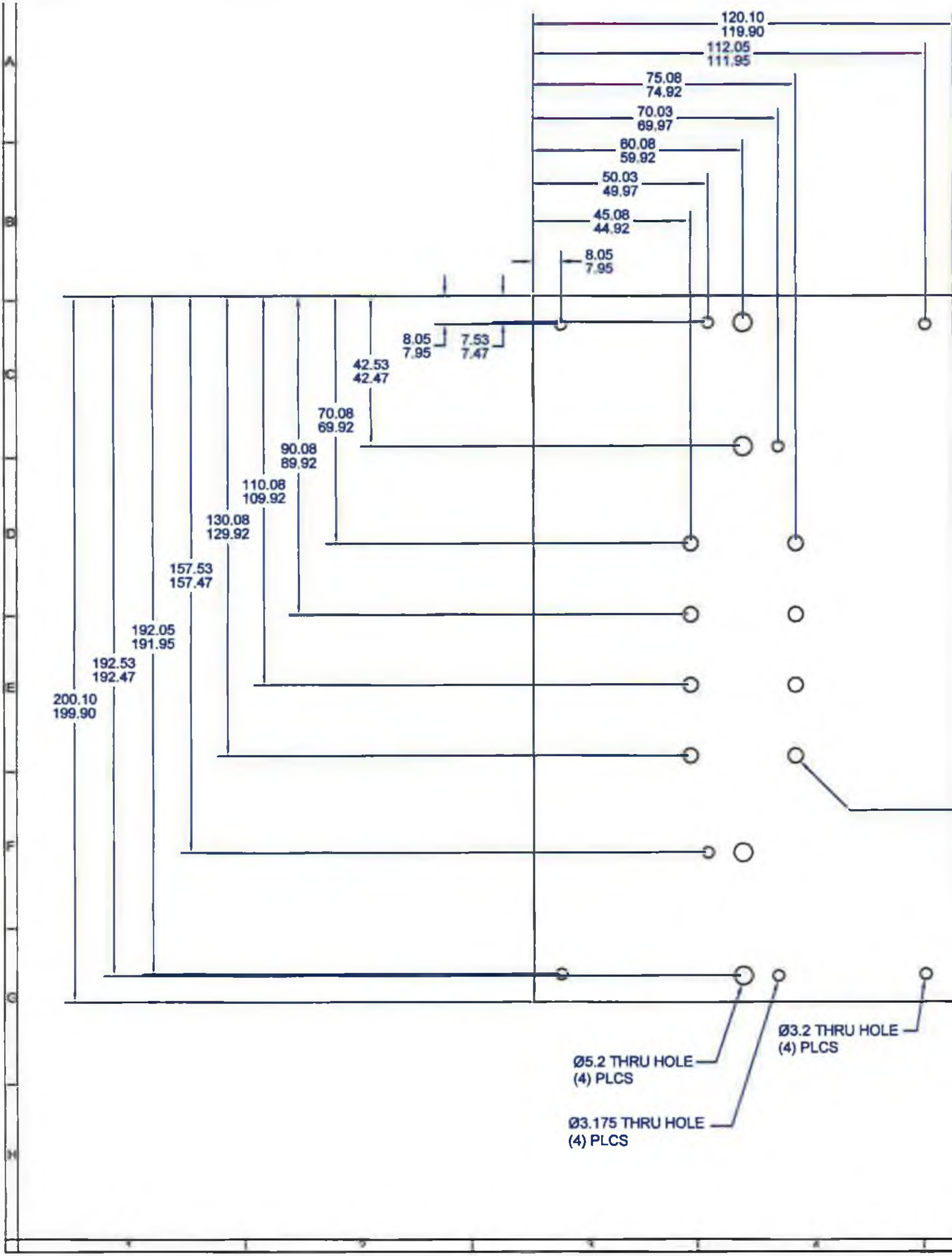

120.10
119.90
112.05
111.95
75.08
74.92
70.03
69.97
60.08
59.92
50.03
49.97
45.08
44.92
8.05
7.95
8.05
7.95
7.53
7.47
42.53
42.47
70.08
69.92
90.08
89.92
110.08
109.92
130.08
129.92
157.53
157.47
192.05
191.95
192.53
192.47
200.10
199.90
Ø3.2 THRU HOLE
(4) PLCS
Ø5.2 THRU HOLE
(4) PLCS
Ø3.175 THRU HOLE
(4) PLCS

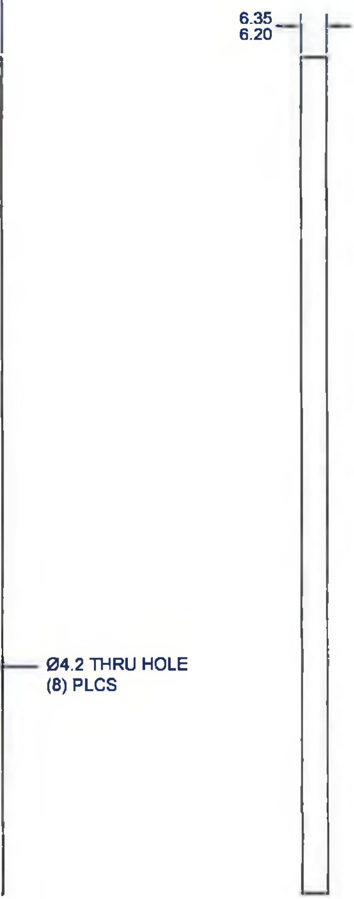

TITLE:
LASER UNIT MEASUREMENT TABLE BASE

DESCRIPTION: MEASUREMENT TABLE BASE

MATERIAL: ALUMINIUM

DRAWN BY: D.COLLINS   DATE: 14/09/02

CHECKED BY: N/A   DATE: N/A

FILE NAME:
LU-MT-BAS.dwg

ADDITIONAL NOTES:

1. All dimensions are in mm unless otherwise specified.
2. Do not scale drawing.
3. Break all edges.

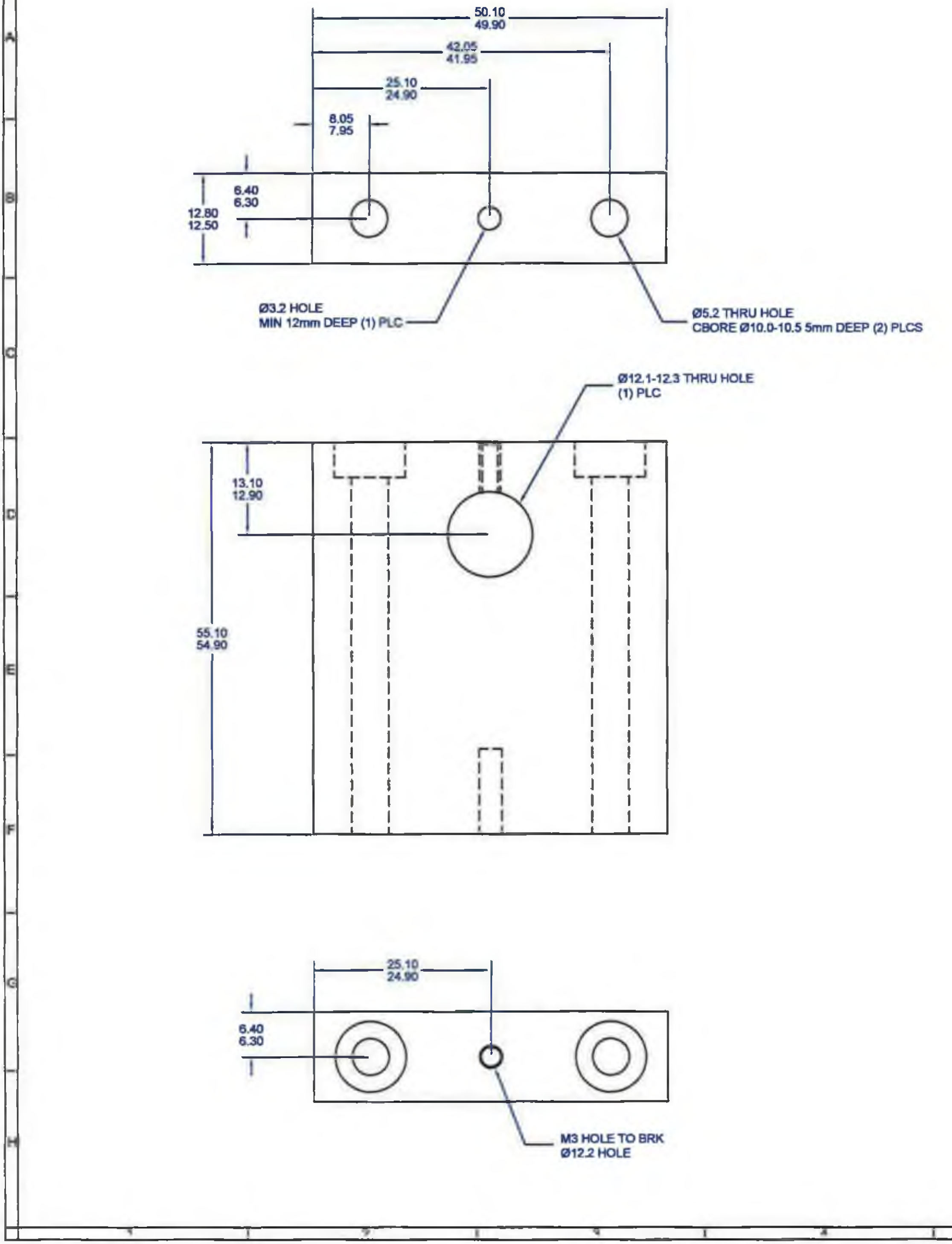
50.10
49.90
42.05
41.95
25.10
24.90
8.05
7.95
6.40
6.30
12.80
12.50
Ø3.2 HOLE
MIN 12mm DEEP (1) PLC
Ø5.2 THRU HOLE
CBORE Ø10.0-10.5 5mm DEEP (2) PLCS
Ø12.1-12.3 THRU HOLE
(1) PLC
13.10
12.90
55.10
54.90
25.10
24.90
6.40
6.30
M3 HOLE TO BRK
Ø12.2 HOLE
A
B
C
D
E
F
G
H

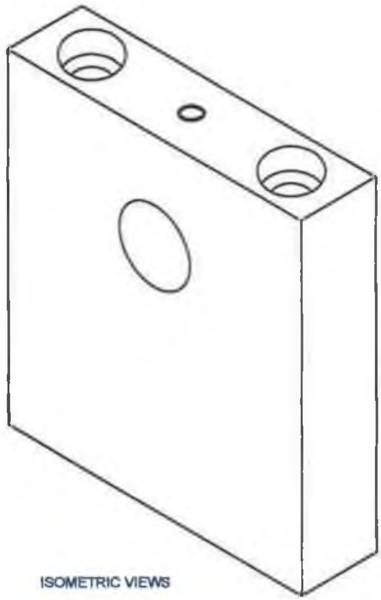

ISOMETRIC VIEWS

TITLE: LASER UNIT MT MOUNTING BRACKET	
DESCRIPTION: MOUNTING BRACKET	MATERIAL: ALUMINIUM
DRAWN BY: D.COLLINS DATE: 14/09/02 CHECKED BY: N/A DATE: N/A	FILE NAME: LU-MT-LG-MBR.dwg

ADDITIONAL NOTES:

1. All dimensions are in mm unless otherwise specified.
2. Do not scale drawing.
3. Break all edges.

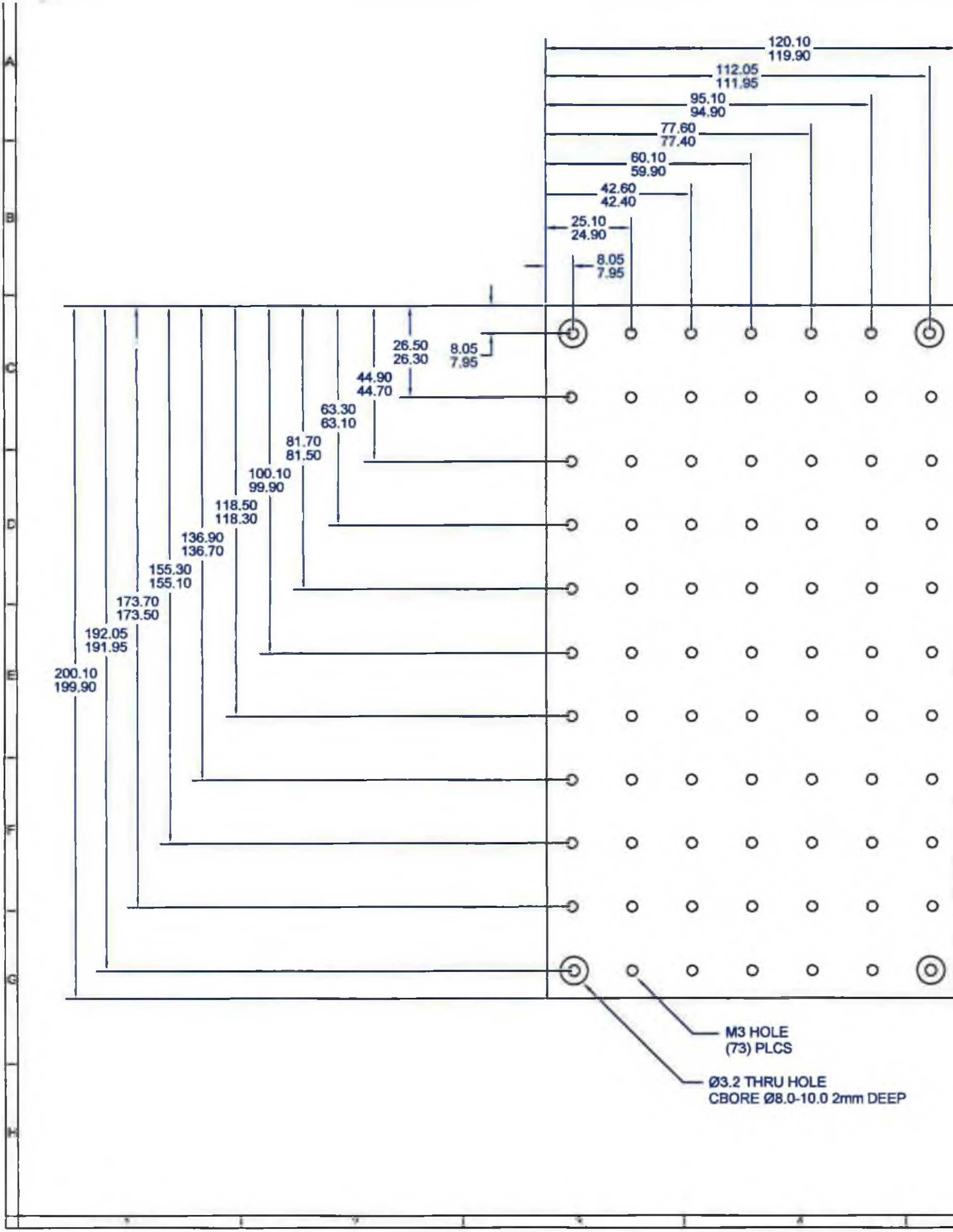

120.10
119.90
112.05
111.95
95.10
94.90
77.60
77.40
60.10
59.90
42.60
42.40
25.10
24.90
8.05
7.95
26.50
26.30
8.05
7.95
44.90
44.70
63.30
63.10
81.70
81.50
100.10
99.90
118.50
118.30
136.90
136.70
155.30
155.10
173.70
173.50
192.05
191.95
200.10
199.90
M3 HOLE
(73) PLCS
Ø3.2 THRU HOLE
CBORE Ø8.0-10.0 2mm DEEP
A
B
C
D
E
F
G
H

FIT TO A4	1 OF 1

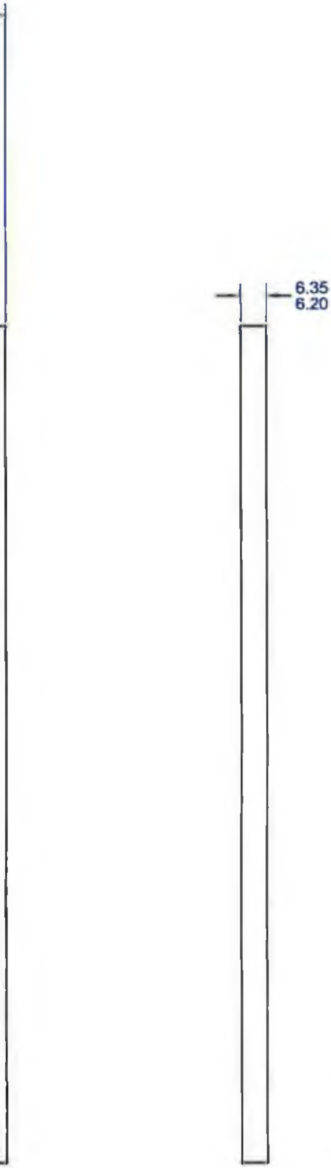

TITLE: LASER UNIT MEASUREMENT TABLE TOP	
DESCRIPTION: MEASUREMENT TABLE TOP	MATERIAL: ALUMINIUM
DRAWN BY: D.COLLINS DATE: 14/09/02 CHECKED BY: N/A DATE: N/A	FILE NAME: LU-MT-TOP.dwg

ADDITIONAL NOTES:

1. All dimensions are in mm unless otherwise specified.
2. Do not scale drawing.
3. Break all edges.

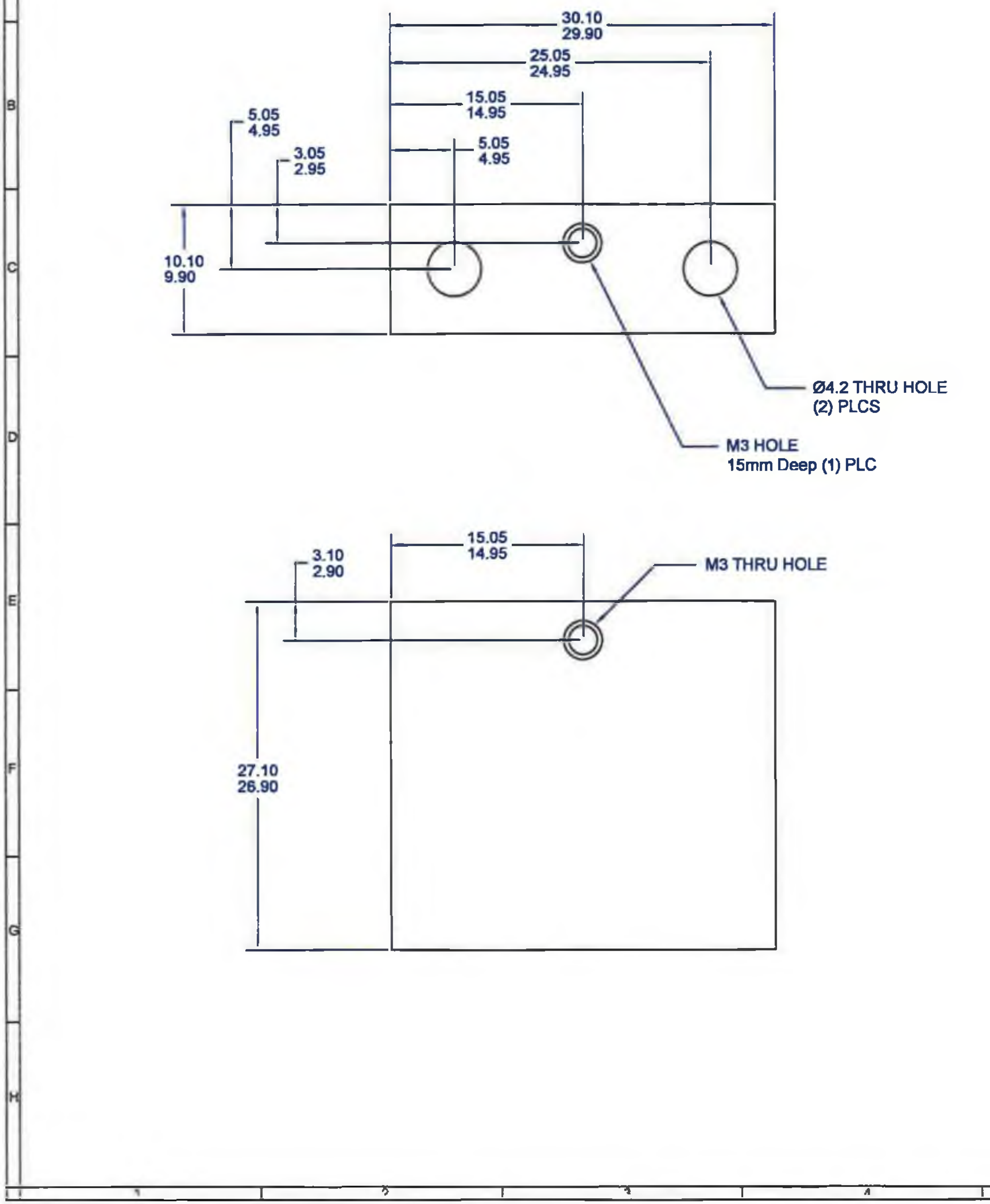

A
B
C
D
E
F
G
H
30.10
29.90
25.05
24.95
15.05
14.95
5.05
4.95
3.05
2.95
5.05
4.95
10.10
9.90
Ø4.2 THRU HOLE
(2) PLCS
M3 HOLE
15mm Deep (1) PLC
15.05
14.95
3.10
2.90
M3 THRU HOLE
27.10
26.90

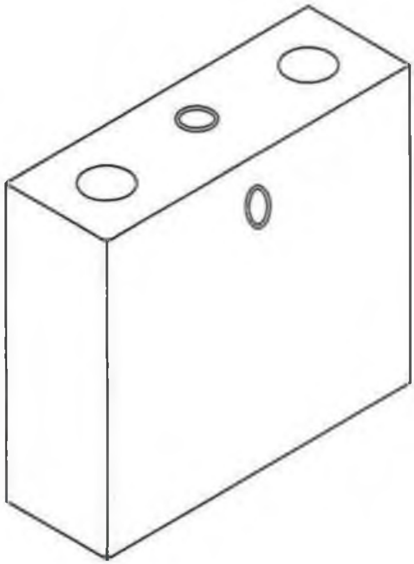

ISOMETRIC VIEW

TITLE: LVDT BRACKET BOTTOM		
DESCRIPTION: LVDT BRACKET		MATERIAL: ALUMINIUM
DRAWN BY: D.COLLINS	DATE: 14/09/02	FILE NAME: LVDT-BR-BOT.dwg
CHECKED BY: N/A	DATE: N/A	

ADDITIONAL NOTES:

1. All dimensions are in mm unless otherwise specified.
2. Do not scale drawing.
3. Break all edges.

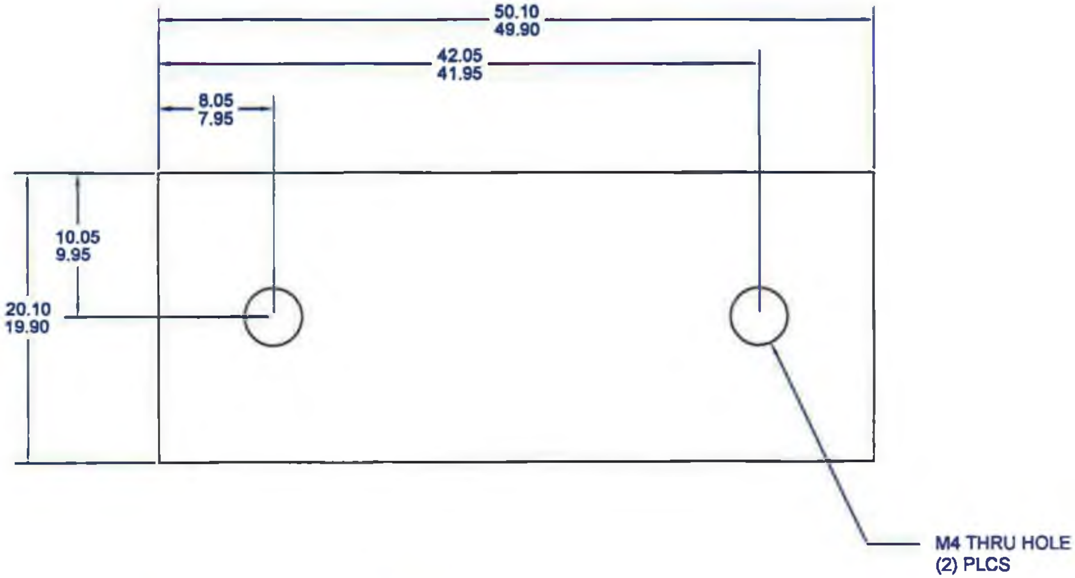
50.10
49.90
42.05
41.95
8.05
7.95
10.05
9.95
20.10
19.90
M4 THRU HOLE
(2) PLCS

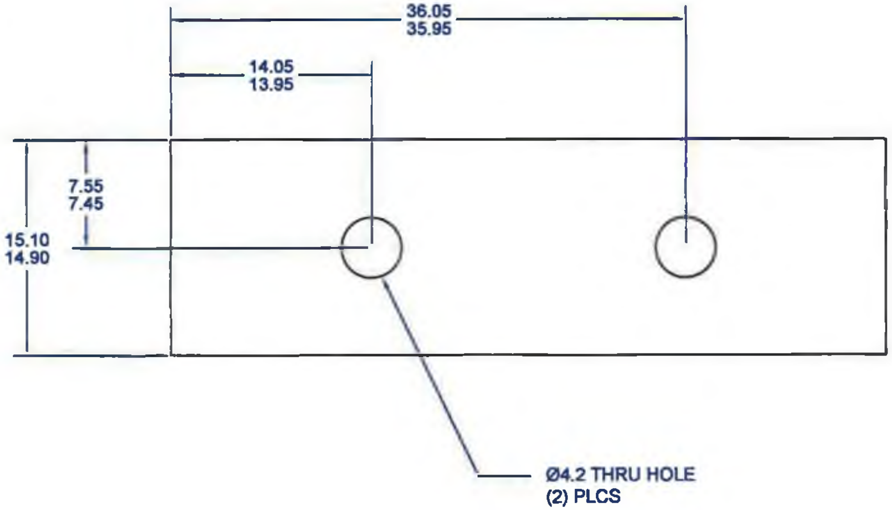
36.05
35.95
14.05
13.95
7.55
7.45
15.10
14.90
Ø4.2 THRU HOLE
(2) PLCS

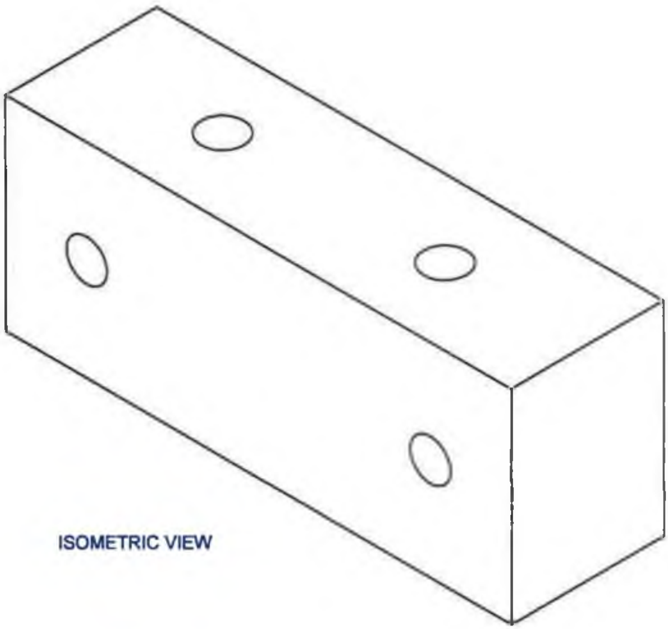

ISOMETRIC VIEW

DCU TITLE: LVDT BRACKET RISER	
DESCRIPTION: LVDT BRACKET	MATERIAL: ALUMINIUM
DRAWN BY: D.COLLINS DATE: 14/09/02 CHECKED BY: N/A DATE: N/A	FILE NAME: LVDT-BR-RIS.dwg

ADDITIONAL NOTES:
1. All dimensions are in mm unless otherwise specified.
2. Do not scale drawing.
3. Break all edges.

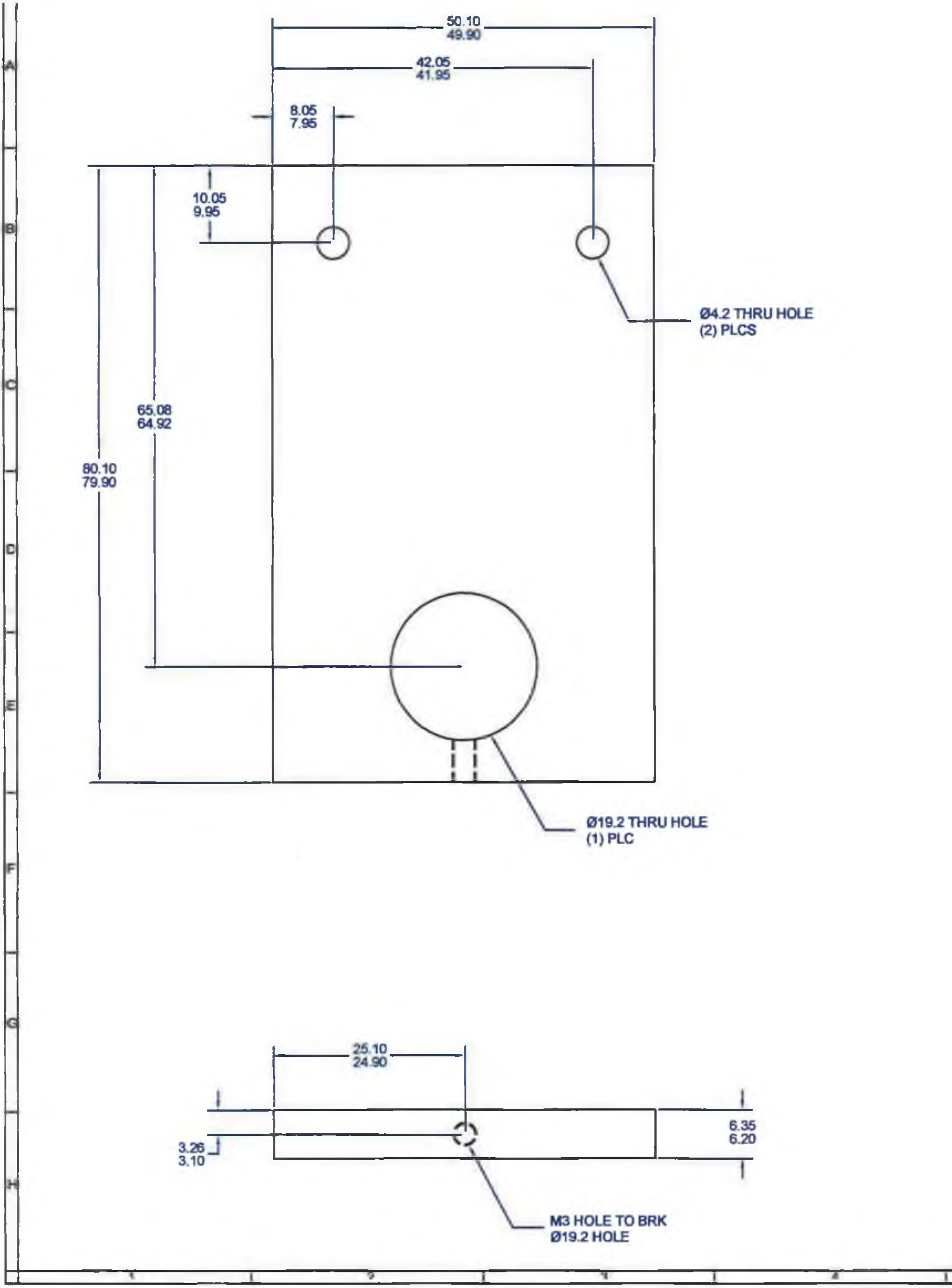

50.10
49.90
42.05
41.95
8.05
7.95
10.05
9.95
Ø4.2 THRU HOLE
(2) PLCS
65.08
64.92
80.10
79.90
Ø19.2 THRU HOLE
(1) PLC
25.10
24.90
3.26
3.10
6.35
6.20
M3 HOLE TO BRK
Ø19.2 HOLE
A
B
C
D
E
F
G
H

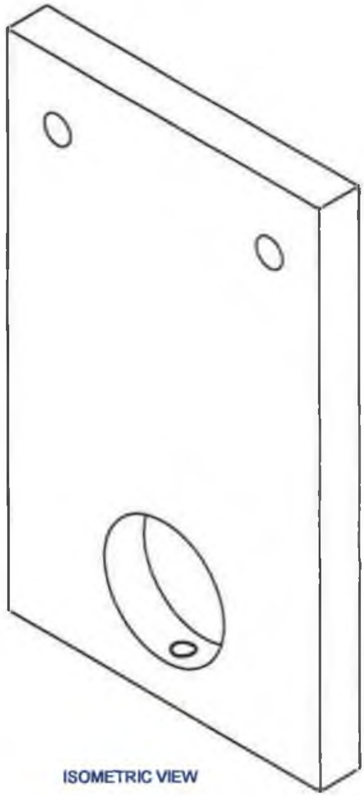

ISOMETRIC VIEW

TITLE: LVDT BRACKET TOP	
DESCRIPTION: LVDT BRACKET	MATERIAL: ALUMINIUM
DRAWN BY: D.COLLINS DATE: 14/09/02 CHECKED BY: N/A DATE: N/A	FILE NAME: LVDT-BR-TOP.dwg

ADDITIONAL NOTES:

1. All dimensions are in mm unless otherwise specified.
2. Do not scale drawing.
3. Break all edges.

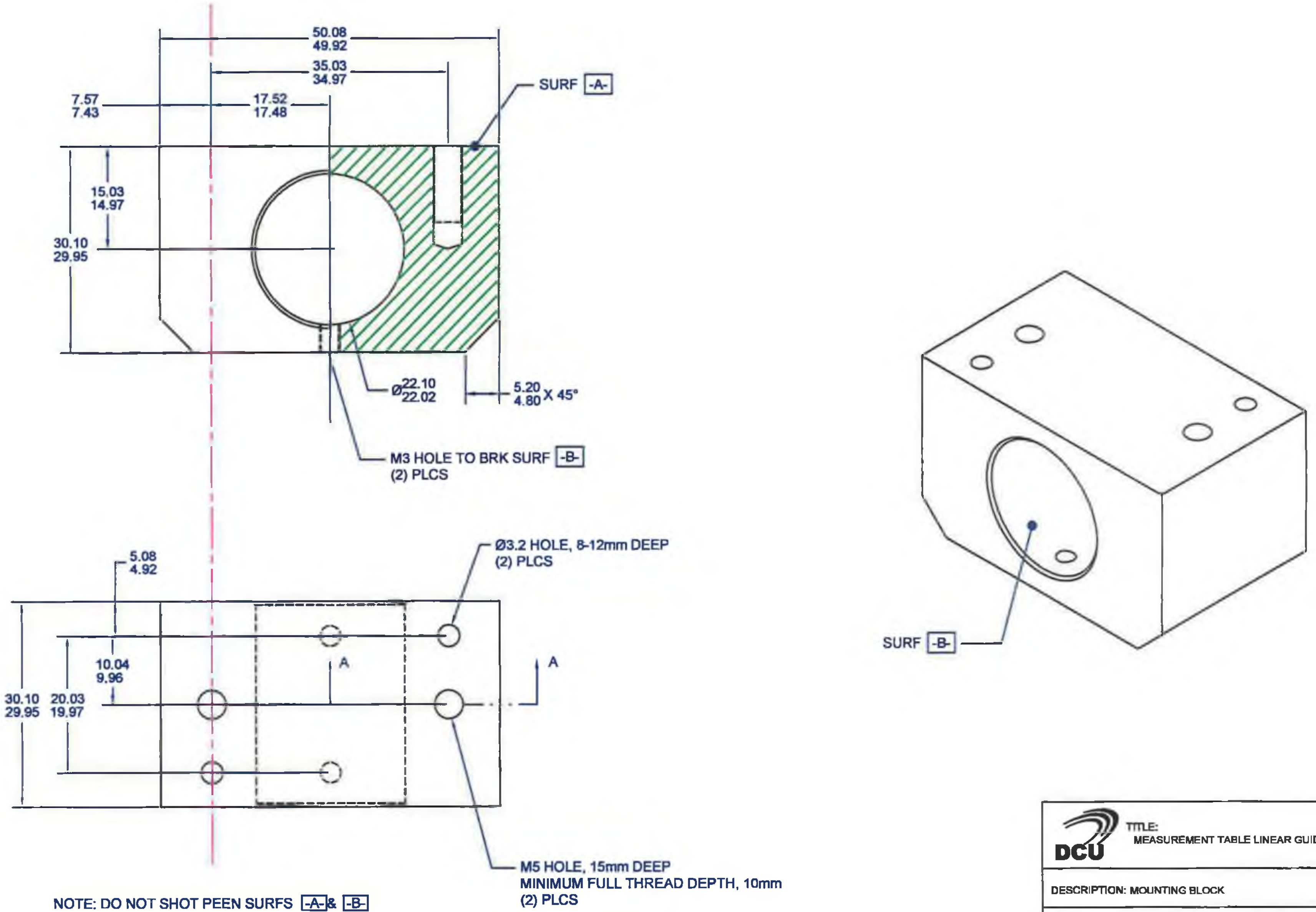

DCU TITLE: MEASUREMENT TABLE LINEAR GUIDE M.BLOCK	
DESCRIPTION: MOUNTING BLOCK	MATERIAL: ALUMINIUM
DRAWN BY: D.COLLINS DATE: 14/09/02 CHECKED BY: N/A DATE: N/A	FILE NAME: MT-LG-MBLK.dwg

ADDITIONAL NOTES:

1. All dimensions are in mm unless otherwise specified.
2. Do not scale drawing.
3. Break all edges.

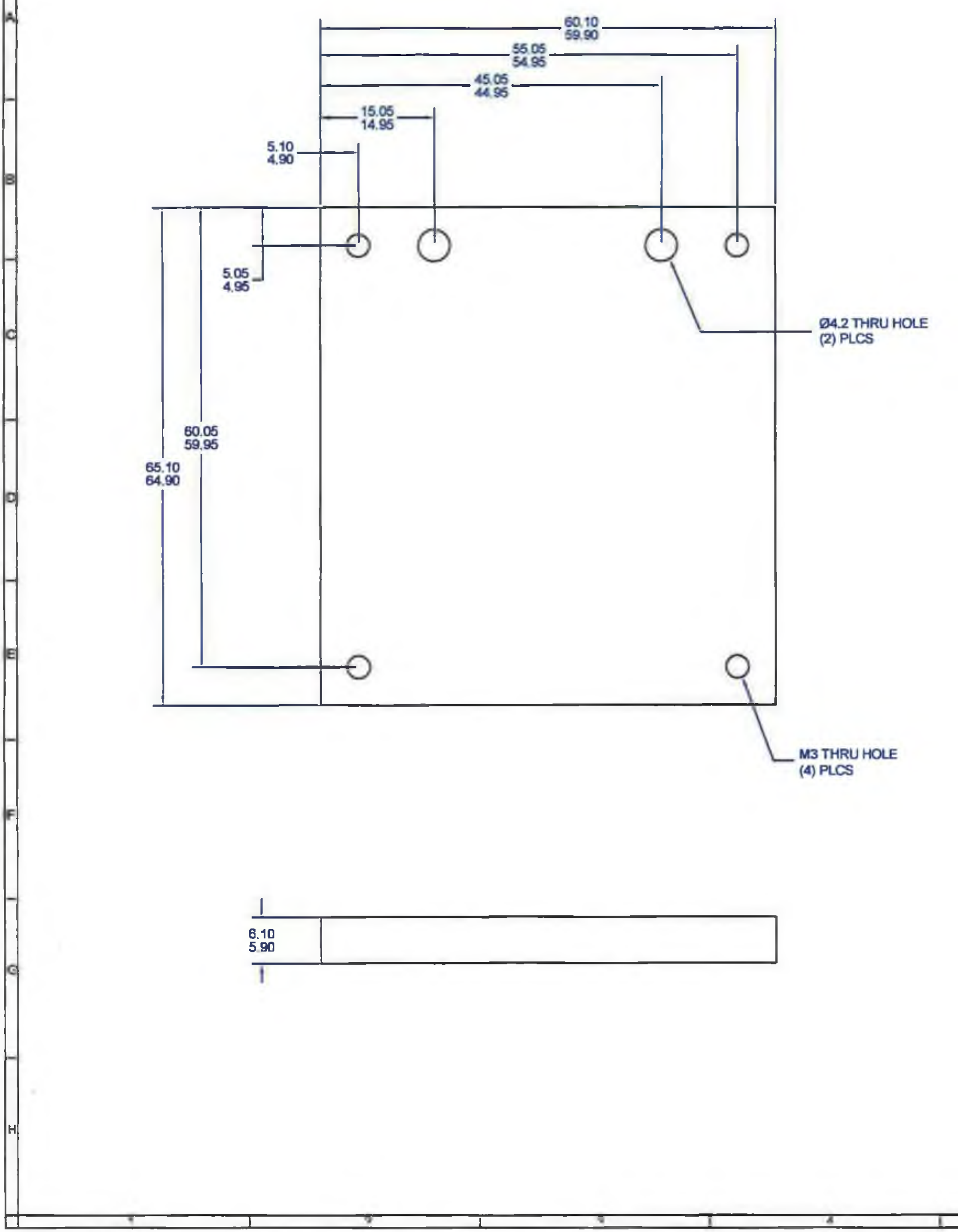
60.10
59.90
55.05
54.95
45.05
44.95
15.05
14.95
5.10
4.90
5.05
4.95
Ø4.2 THRU HOLE
(2) PLCS
60.05
59.95
65.10
64.90
M3 THRU HOLE
(4) PLCS
6.10
5.90

PLOT SCALE	
FIT TO A4	1 OF 1

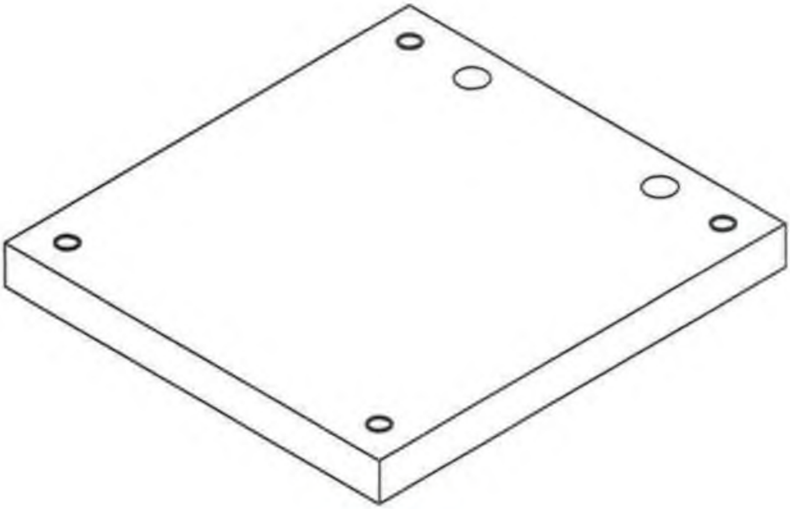

ISOMETRIC VIEWS

DCU TITLE: STEPPER MOTOR M.BRACKET BASE	
DESCRIPTION: MOUNTING BRACKET BASE	MATERIAL: ALUMINIUM
DRAWN BY: D.COLLINS DATE: 14/09/02 CHECKED BY: N/A DATE: N/A	FILE NAME: SM-MBR-BAS.dwg

ADDITIONAL NOTES:

1. All dimensions are in mm unless otherwise specified.
2. Do not scale drawing.
3. Break all edges.

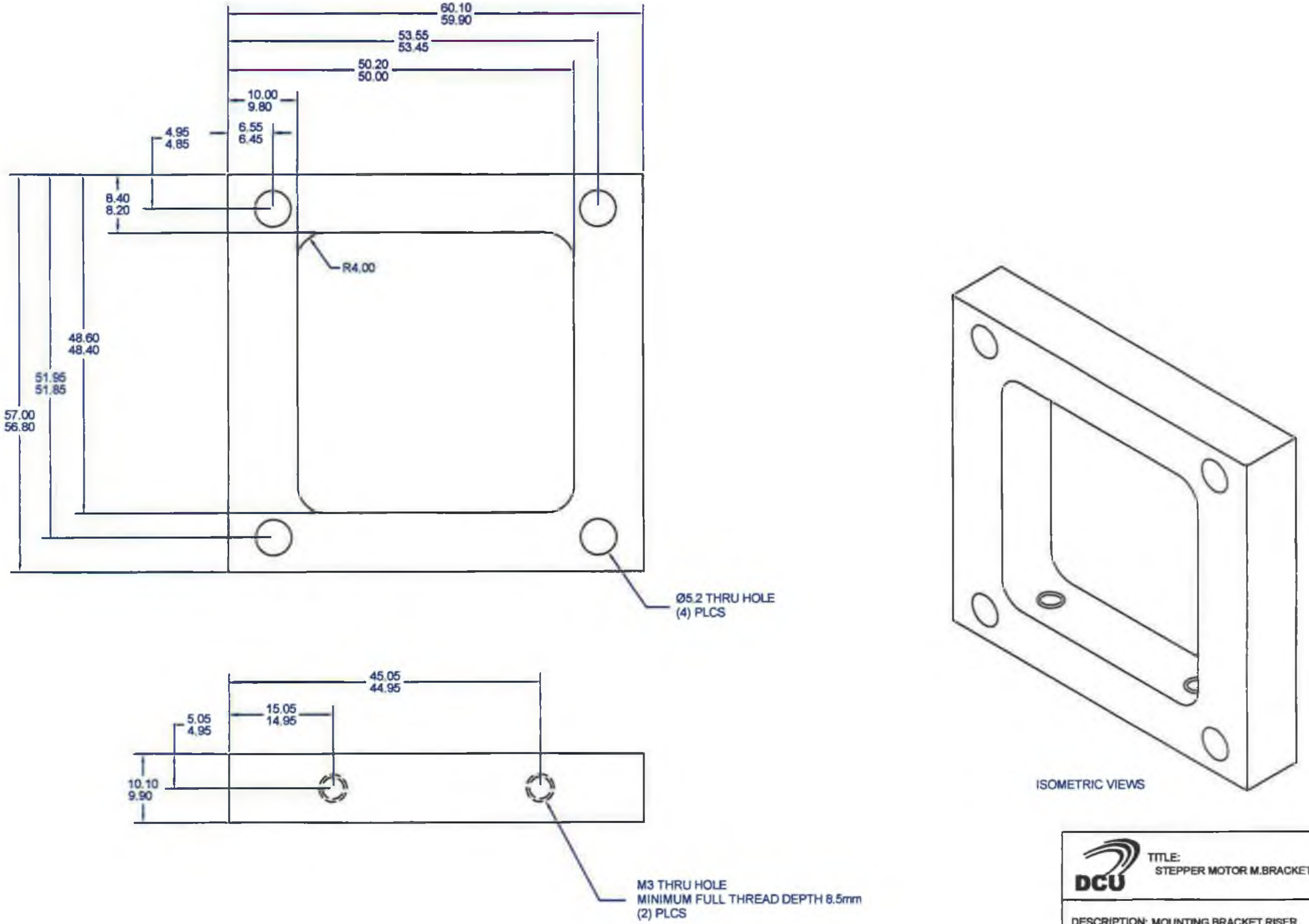

ISOMETRIC VIEWS

DCU

TITLE:
STEPPER MOTOR M.BRACKET RISER

DESCRIPTION: MOUNTING BRACKET RISER

MATERIAL: ALUMINIUM

DRAWN BY: D.COLLINS | DATE: 14/09/02

CHECKED BY: N/A | DATE: N/A

FILE NAME:
SM-MBR-RIS.dwg

ADDITIONAL NOTES:
1. All dimensions are in mm unless otherwise specified.
2. Do not scale drawing.
3. Break all edges.

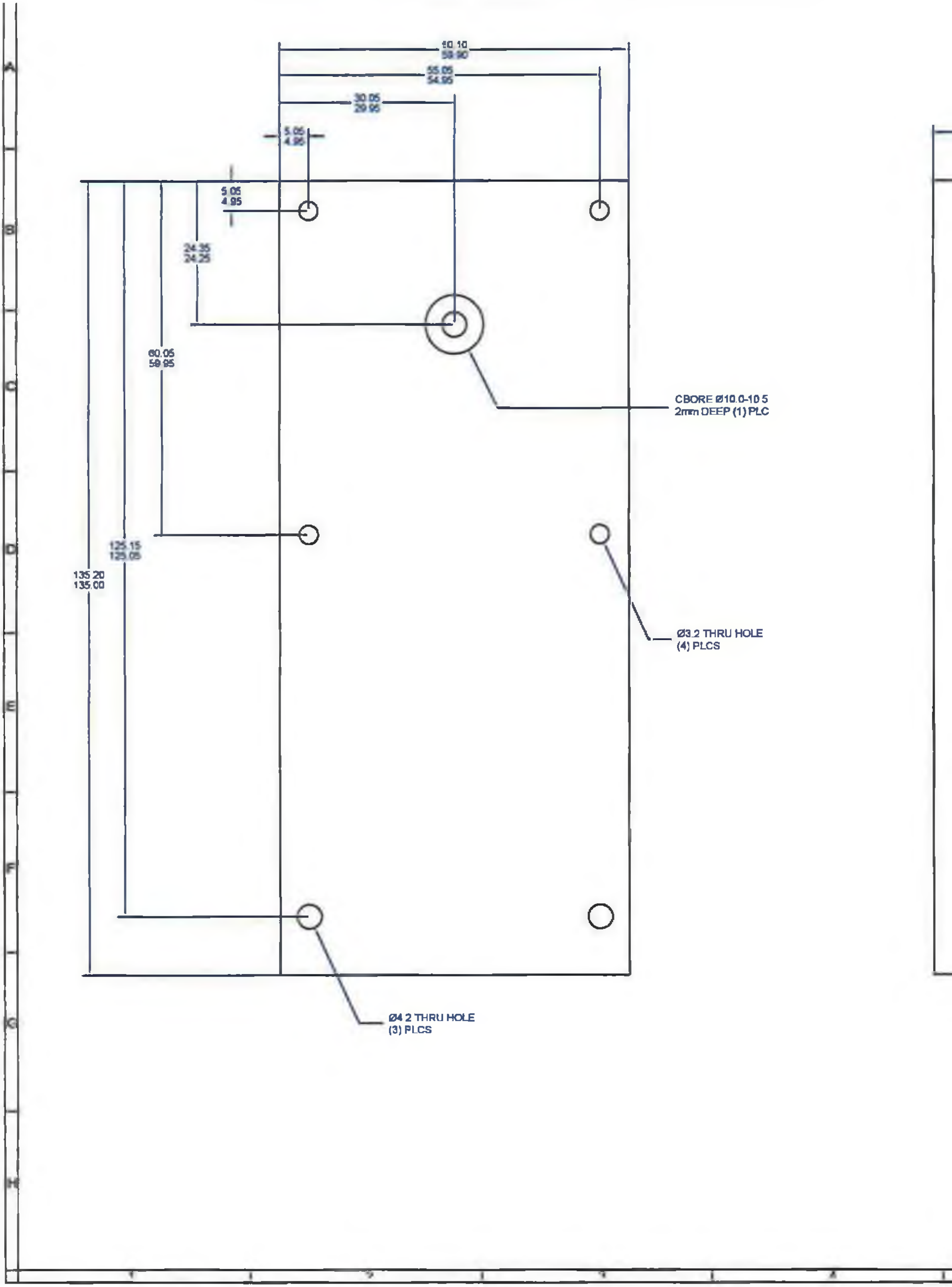
60.10
59.90
55.05
54.95
30.05
29.95
5.05
4.95
5.05
4.95
24.35
24.25
60.05
59.95
125.15
125.05
135.20
135.00
CBORE Ø10.0-10.5
2mm DEEP (1) PLC
Ø3.2 THRU HOLE
(4) PLCS
Ø4.2 THRU HOLE
(3) PLCS
A
B
C
D
E
F
G
H

6.10
5.90

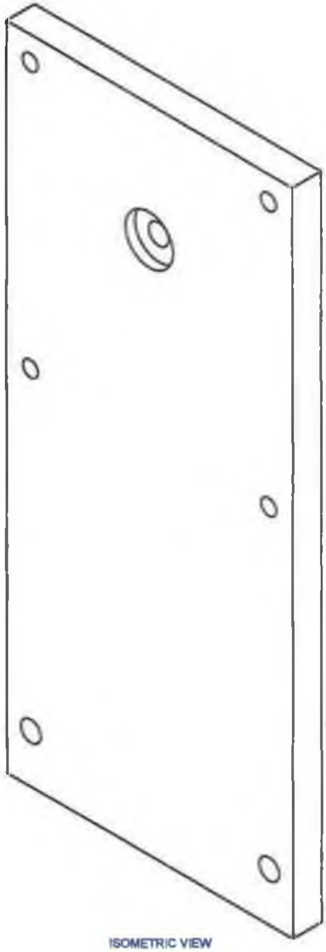

ISOMETRIC VIEW

DCU	TITLE: STEPPER MOTOR M.SURFACE (FRAME)	
DESCRIPTION: MOUNTING SURFACE (FRAME)		MATERIAL: ALUMINIUM
DRAWN BY: D.COLLINS	DATE: 14/09/02	FILE NAME: SM-MSURF-FR.dwg
CHECKED BY: N/A	DATE: N/A	

ADDITIONAL NOTES:

1. All dimensions are in mm unless otherwise specified.
2. Do not scale drawing.
3. Break all edges.

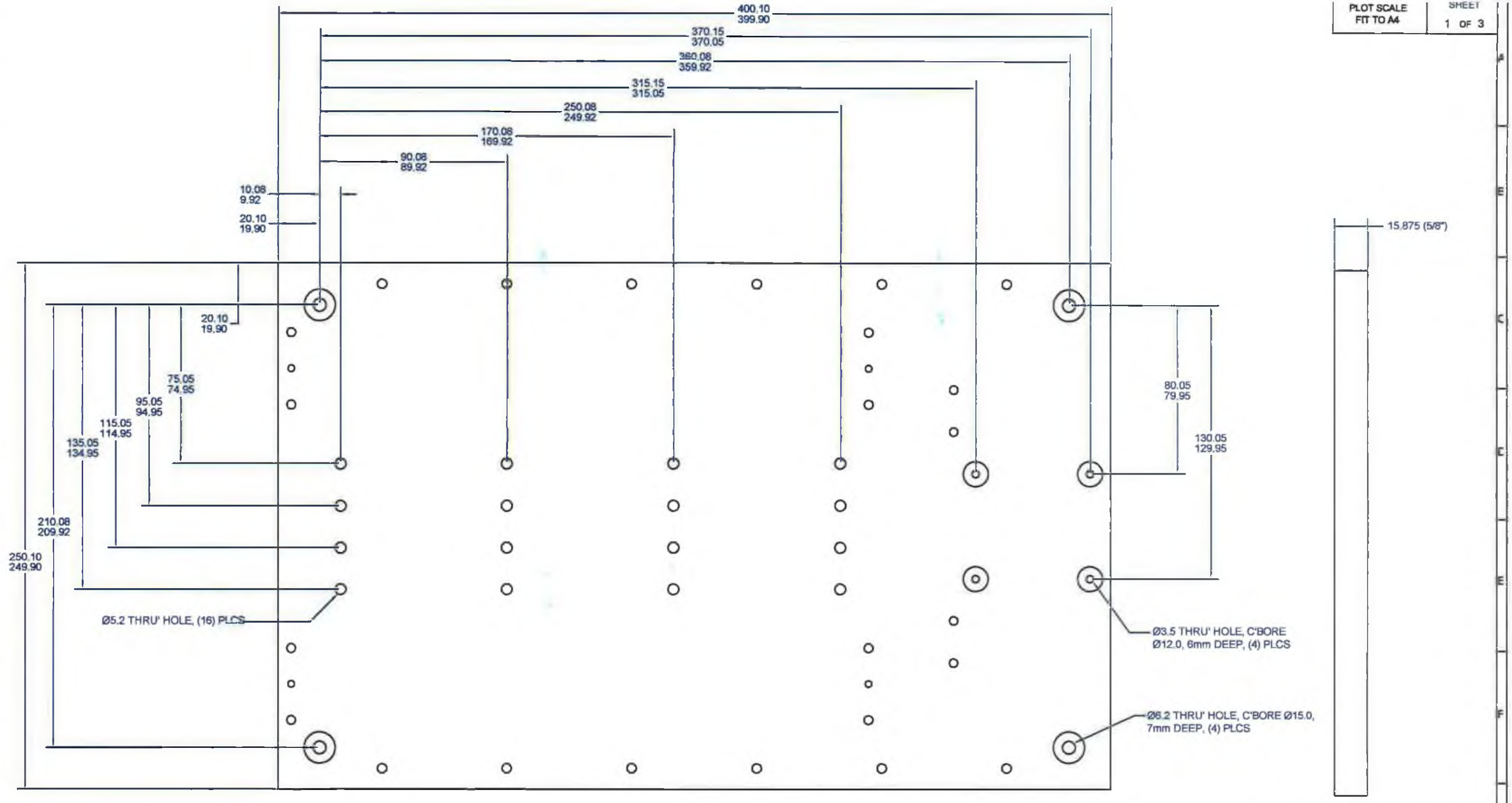

PLOT SCALE FIT TO A4

SHEET 1 OF 3

DCU

TITLE: SURFACE TABLE BOLSTER PLATE

DESCRIPTION: BOLSTER PLATE

MATERIAL: ALUMINIUM

DRAWN BY: D.COLLINS

DATE: 14/09/02

CHECKED BY: N/A

DATE: N/A

FILE NAME: ST-BP.dwg

ADDITIONAL NOTES:

1. All dimensions are in mm unless otherwise specified.
2. Do not scale drawing.
3. Break all edges.

PLOT SCALE FIT TO A4	SHEET 2 OF 3

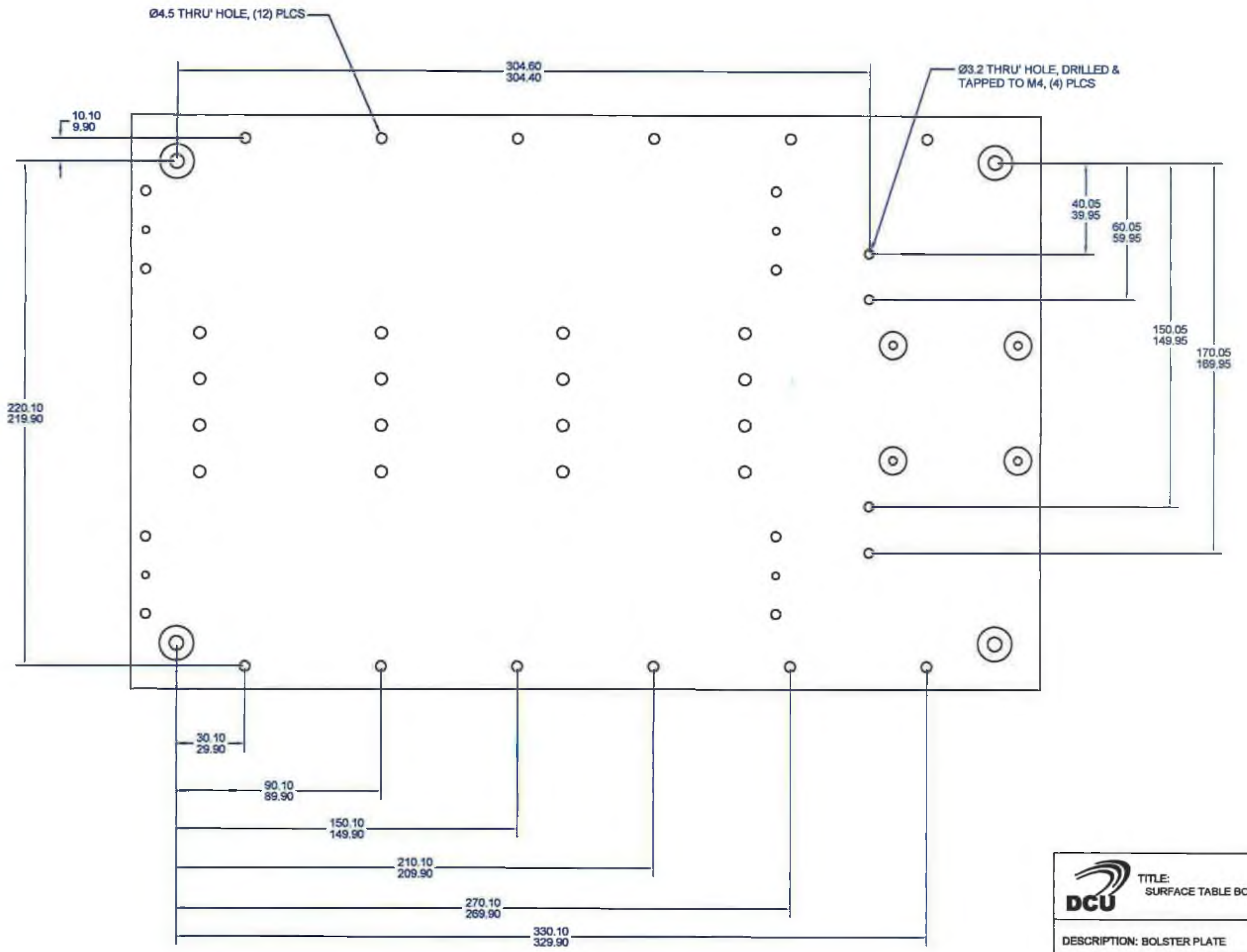

TITLE: SURFACE TABLE BOLSTER PLATE	
DESCRIPTION: BOLSTER PLATE	MATERIAL: ALUMINIUM
DRAWN BY: D.COLLINS DATE: 14/09/02 CHECKED BY: N/A DATE: N/A	FILE NAME: ST-BP.dwg

ADDITIONAL NOTES:
1. All dimensions are in mm unless otherwise specified.
2. Do not scale drawing.
3. Break all edges.

PLOT SCALE FIT TO A4 | SHEET 3 OF 3

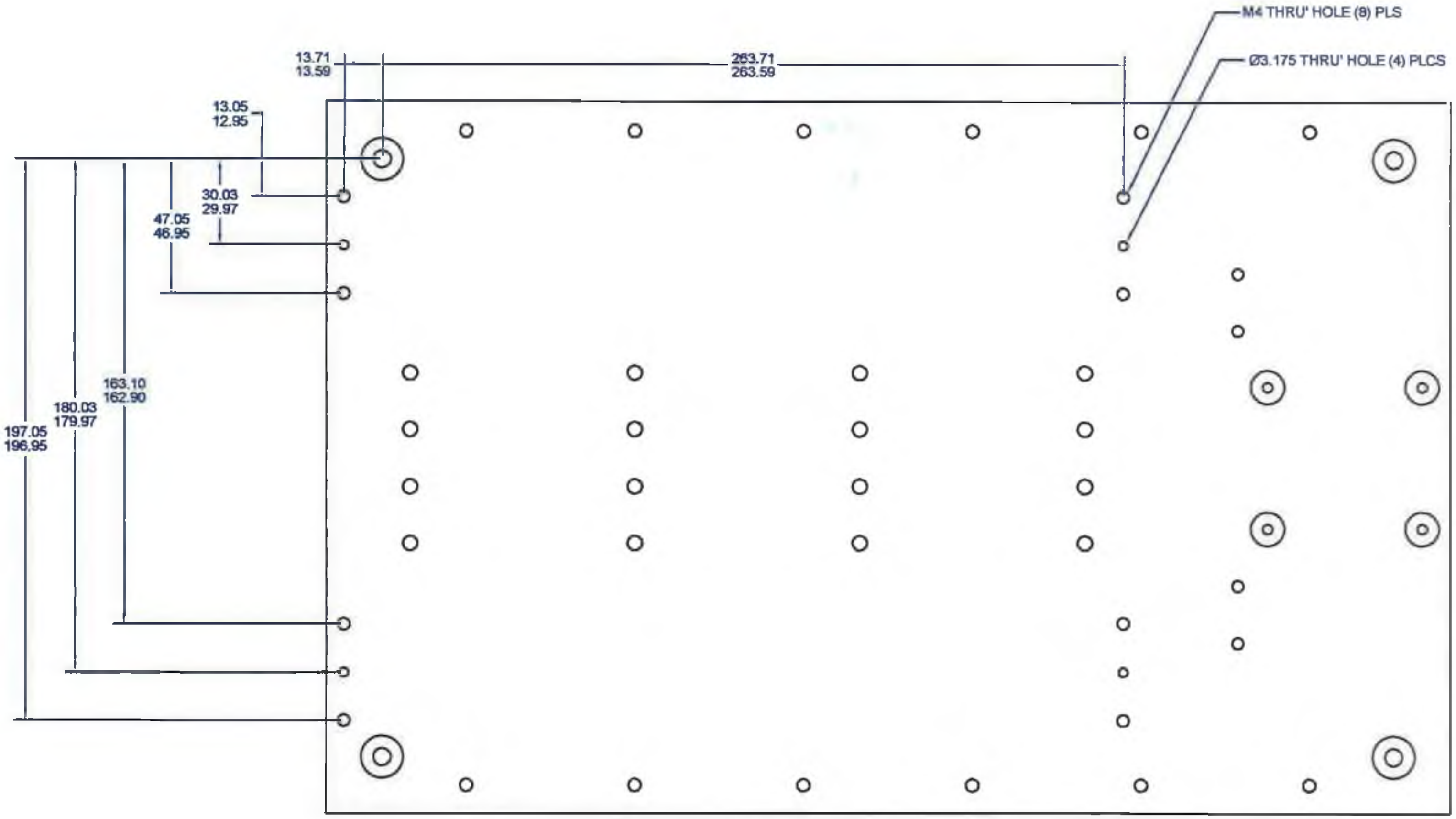

DCU

TITLE: SURFACE TABLE BOLSTER PLATE

DESCRIPTION: BOLSTER PLATE

MATERIAL: ALUMINIUM

DRAWN BY: D.COLLINS | DATE: 14/09/02

CHECKED BY: N/A | DATE: N/A

FILE NAME: ST-BP.dwg

ADDITIONAL NOTES:
1. All dimensions are in mm unless otherwise specified.
2. Do not scale drawing.
3. Break all edges.

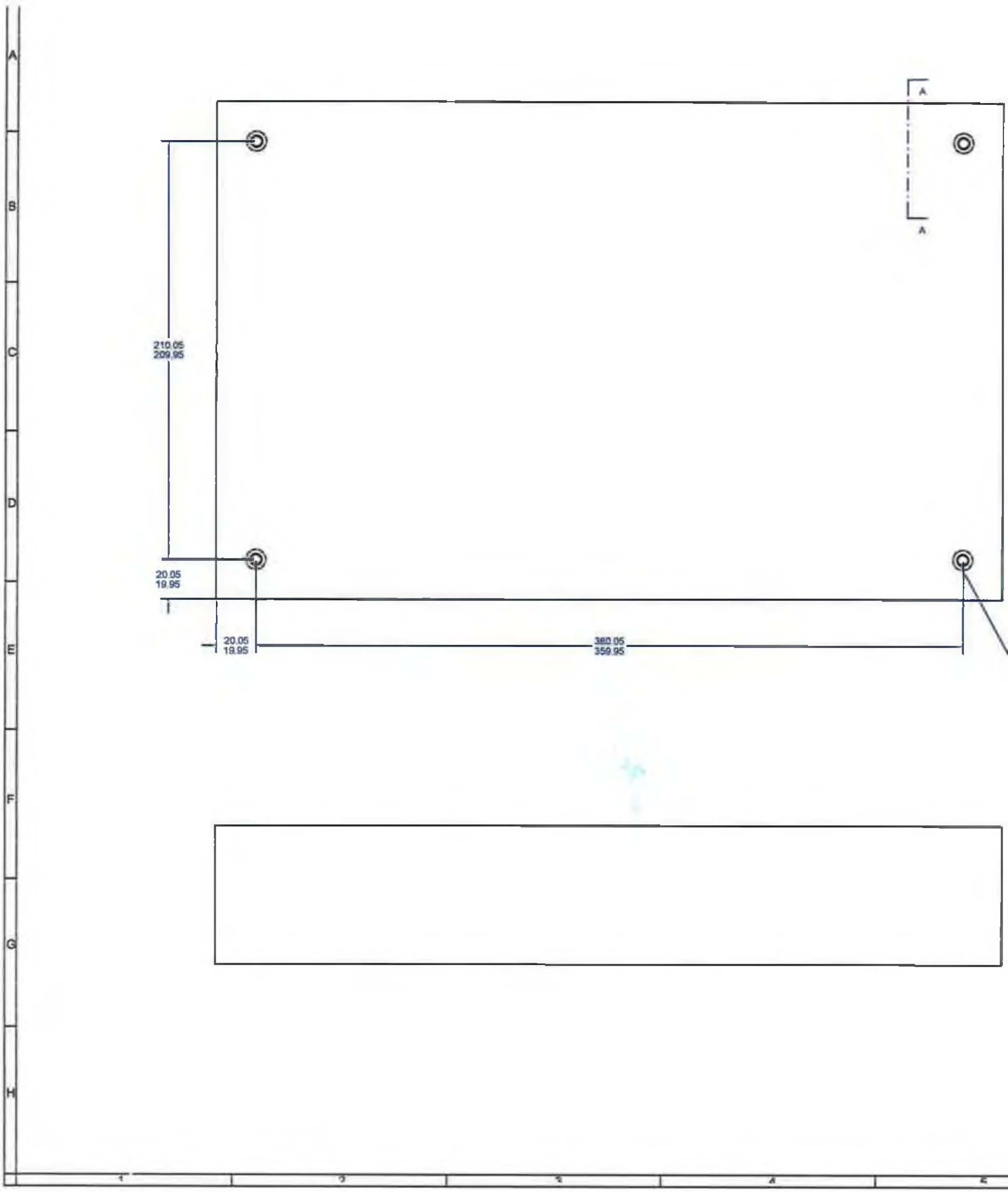
A
B
C
D
E
F
G
H
A
A
210.05
209.95
20.05
19.95
20.05
19.95
359.95

PLOT SCALE FIT TO A4	1 OF 1

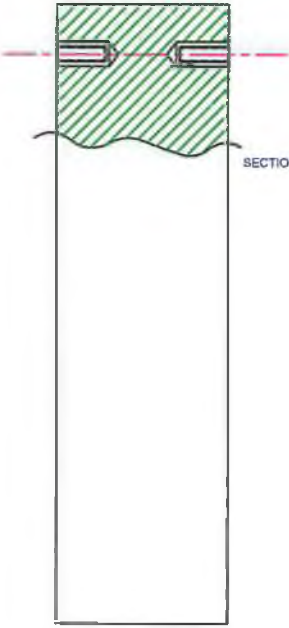

SECTION A-A

Ø10.0-10.5 BLIND HOLE
25mm DEEP, FILL HOLES WITH EPOXY
AND TAP TO M6, MINIMUM FULL THREAD
DEPTH 20mm (6) PLCS

NOTES:
1. DIMENSIONAL TOLERANCES APPLY TO MINOR Ø OF THREADED HOLE
2. POSITIONAL TOLERANCES OF Ø10.0-10.5 HOLE IS ±0.4
3. PART NUMBER - QXD-306-4020K (Kennedy Tooling Granite Lab Grade Inspection Table)
4. MODIFY THE PART PER DRAWING

DCU

TITLE:
SURFACE TABLE GRANITE

DESCRIPTION: SURFACE TABLE

MATERIAL: GRANITE

DRAWN BY: D.COLLINS   DATE: 14/09/02

CHECKED BY: N/A   DATE: N/A

FILE NAME:
ST-GR.dwg

ADDITIONAL NOTES:
1. All dimensions are in mm unless otherwise specified.
2. Do not scale drawing.
3. Break all edges.

Appendix D Wiring diagrams

Wiring Schematic Index:

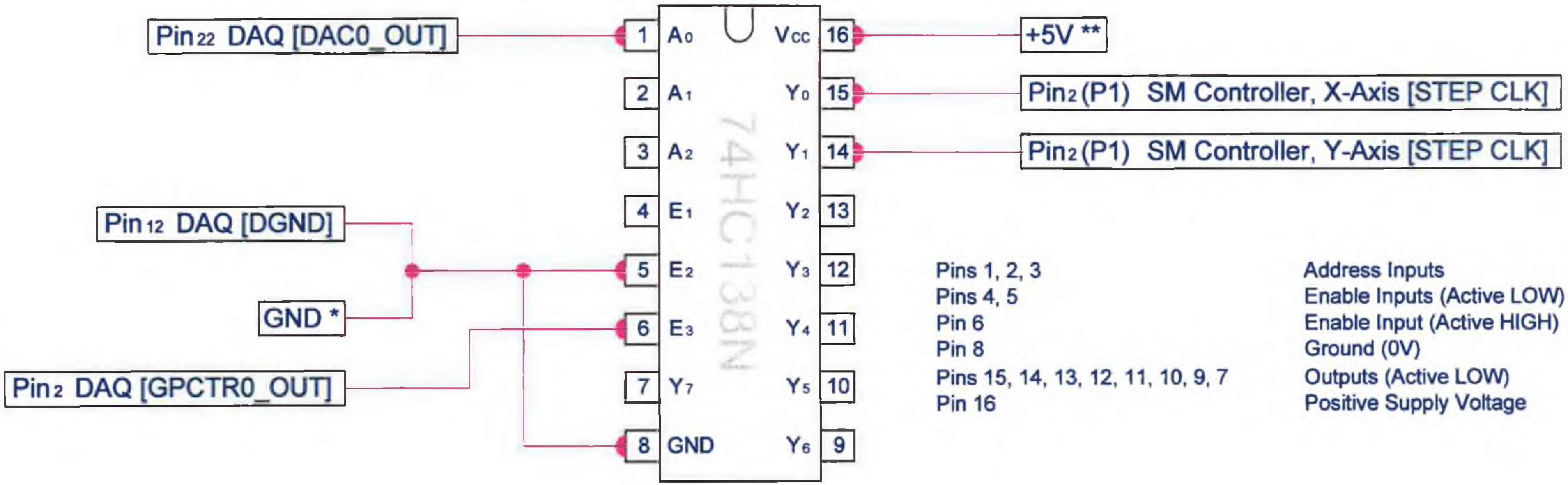

* Connected to Pin 3 (P2) Y-Axis Stepper Motor Controller

** Connected to Pin 4 (P1) Y-Axis Stepper Motor Controller

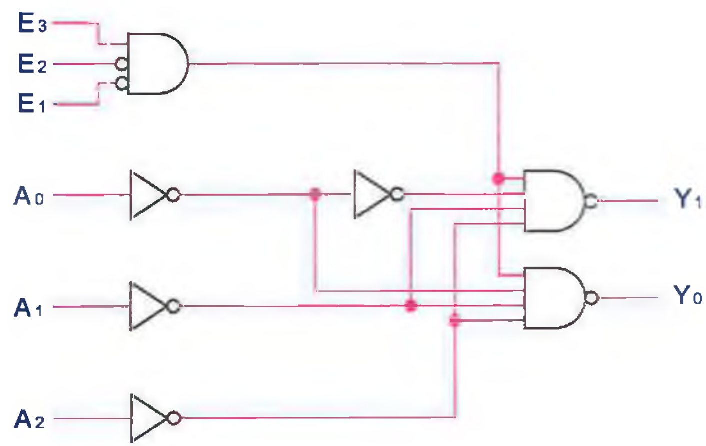

Logic Circuit

DCU

TITLE:
WIRING DIAGRAM #1 - DEMUX WIRING SCHEMATIC

DRAWN BY: D.COLLINS DATE: 18/10/03

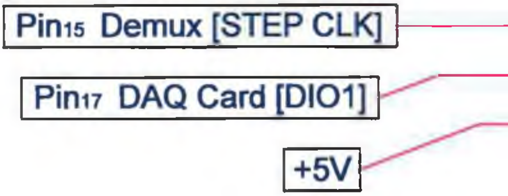

DCU

TITLE:
WIRING DIAGRAM #2 - X-AXIS CONT. WIRING SCHEMATIC

DRAWN BY: D.COLLINS

DATE: 20/10/03

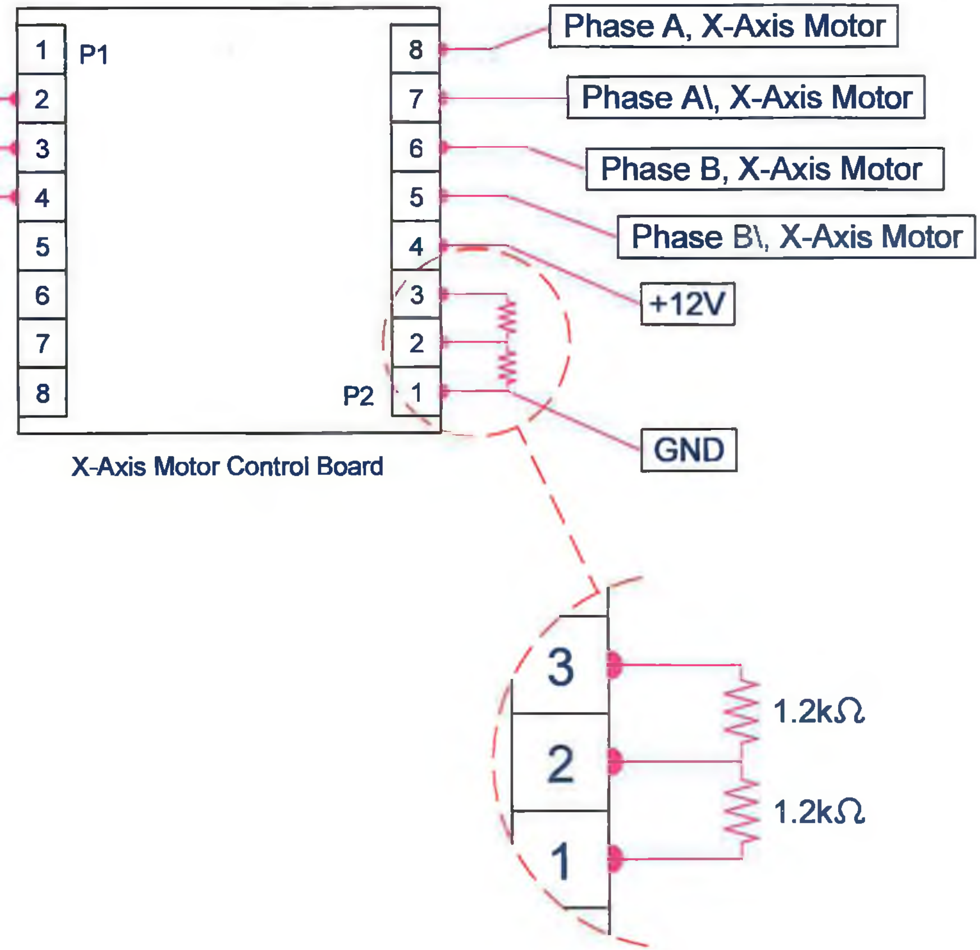

1
2
3
4
5
6
7
8
P1
8
7
6
5
4
3
2
1
P2
Phase A, X-Axis Motor
Phase A\, X-Axis Motor
Phase B, X-Axis Motor
Phase B\, X-Axis Motor
+12V
GND
X-Axis Motor Control Board
3
2
1
1.2kΩ
1.2kΩ

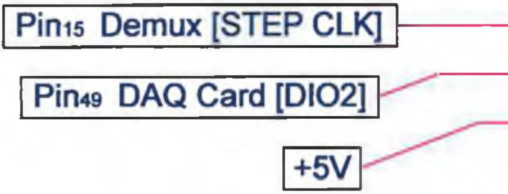

TITLE:
WIRING DIAGRAM #3 - Y-AXIS CONT. WIRING SCHEMATIC

DCU DRAWN BY: D.COLLINS DATE: 20/10/03

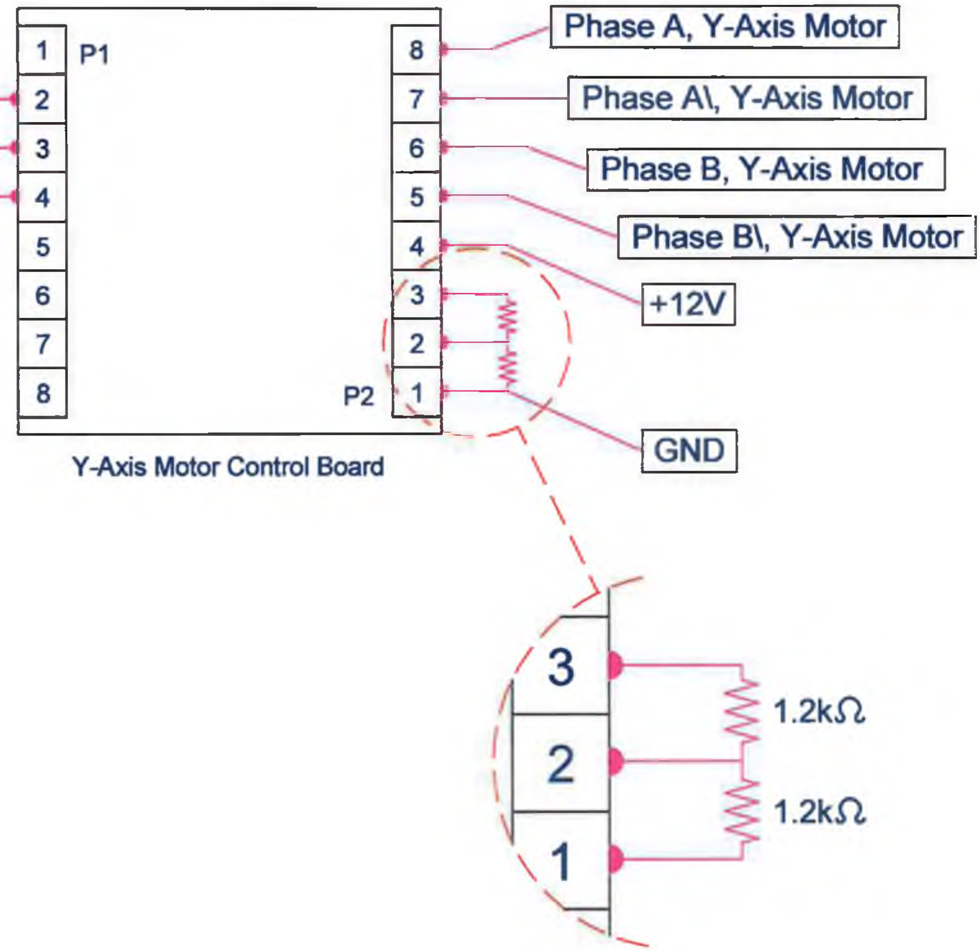

Phase A, Y-Axis Motor
Phase A\, Y-Axis Motor
Phase B, Y-Axis Motor
Phase B\, Y-Axis Motor
+12V
GND
P1
P2
1
2
3
4
5
6
7
8
Y-Axis Motor Control Board
1.2kΩ
1.2kΩ

TITLE:
WIRING DIAGRAM #4 - DAQ CARD BREAKOUT BOX WIRING SCHEMATIC

DCU DRAWN BY: D.COLLINS DATE: 23/10/03

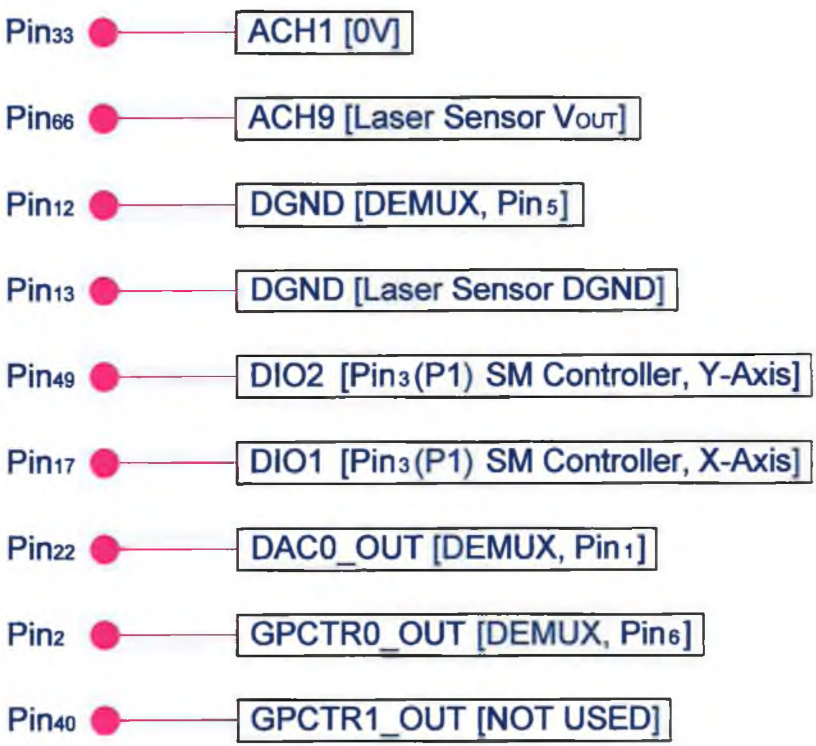

Pin33
ACH1 [0V]
Pin66
ACH9 [Laser Sensor VOUT]
Pin12
DGND [DEMUX, Pin5]
Pin13
DGND [Laser Sensor DGND]
Pin49
DIO2 [Pin3(P1) SM Controller, Y-Axis]
Pin17
DIO1 [Pin3(P1) SM Controller, X-Axis]
Pin22
DAC0_OUT [DEMUX, Pin1]
Pin2
GPCTR0_OUT [DEMUX, Pin6]
Pin40
GPCTR1_OUT [NOT USED]

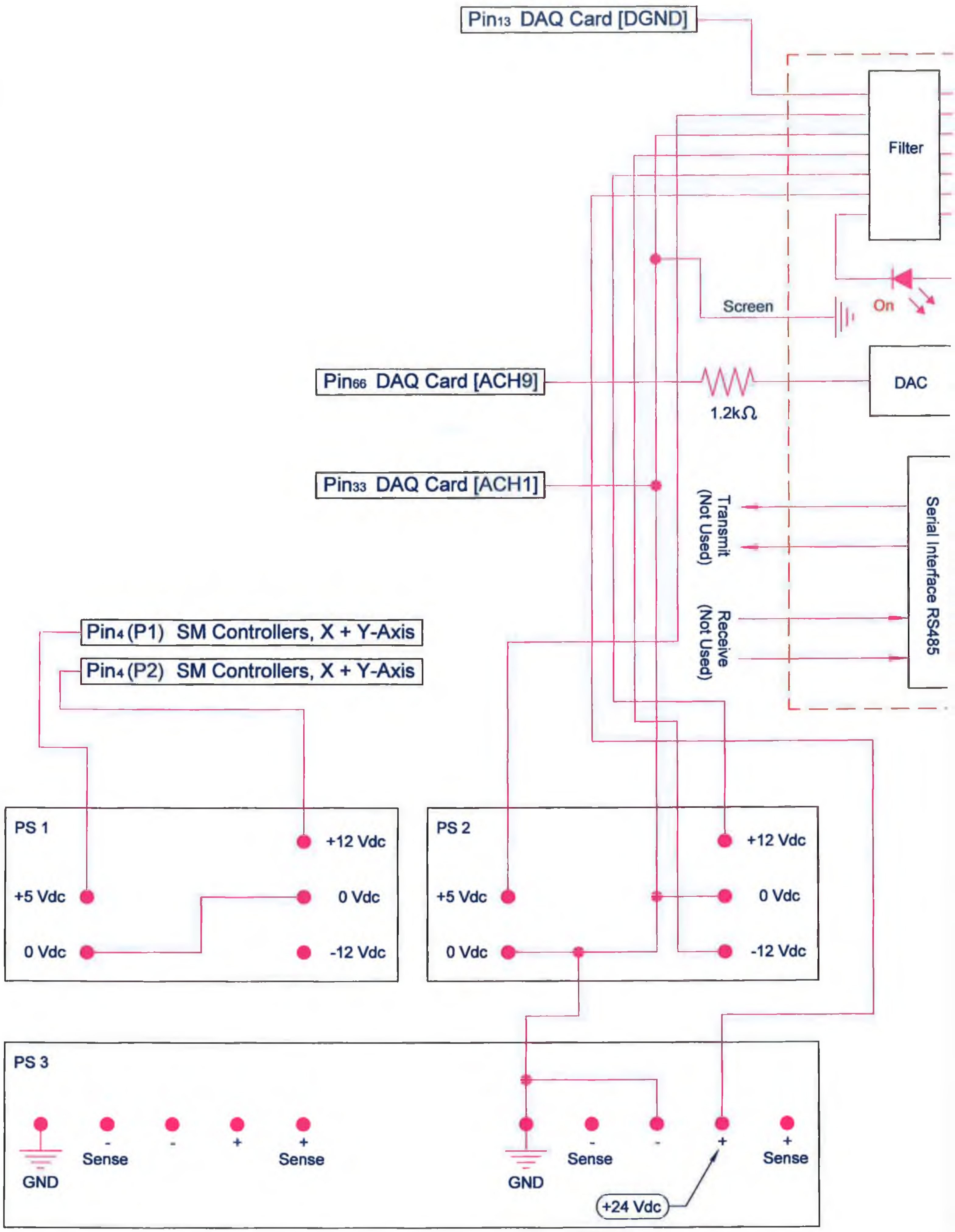

Pin13 DAQ Card [DGND]
Filter
Screen
On
Pin66 DAQ Card [ACH9]
1.2kΩ
DAC
Pin33 DAQ Card [ACH1]
Transmit (Not Used)
Receive (Not Used)
Serial Interface RS485
Pin4 (P1) SM Controllers, X + Y-Axis
Pin4 (P2) SM Controllers, X + Y-Axis
PS 1
+12 Vdc
+5 Vdc
0 Vdc
0 Vdc
-12 Vdc
PS 2
+12 Vdc
+5 Vdc
0 Vdc
0 Vdc
-12 Vdc
PS 3
GND
- Sense
-
+
+ Sense
GND
- Sense
-
+
+ Sense
+24 Vdc

Appendix E System assembly drawings

Assembly Drawing Index:

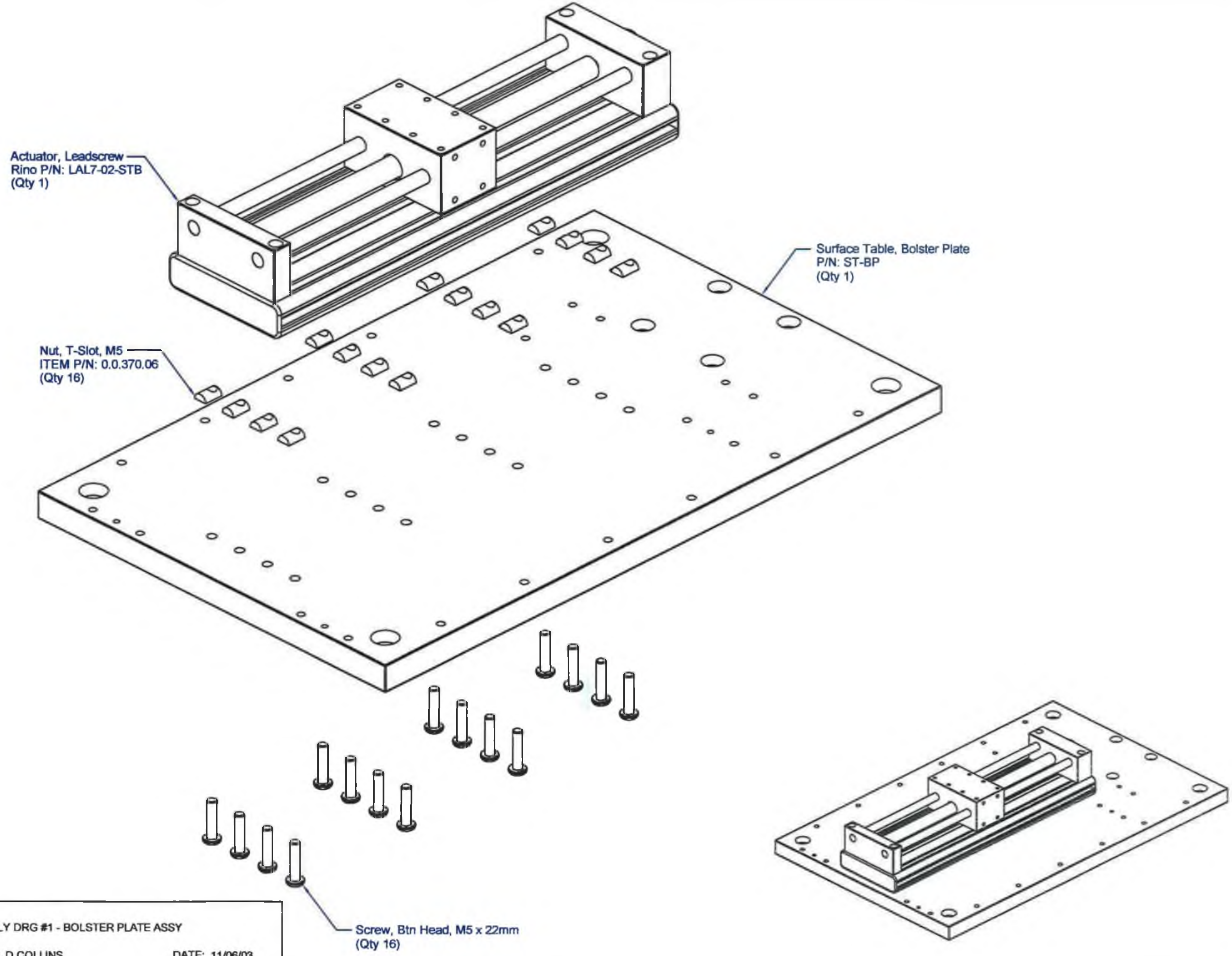

DCU

TITLE:
ASSEMBLY DRG #1 - BOLSTER PLATE ASSY

DRAWN BY: D.COLLINS

DATE: 11/06/03

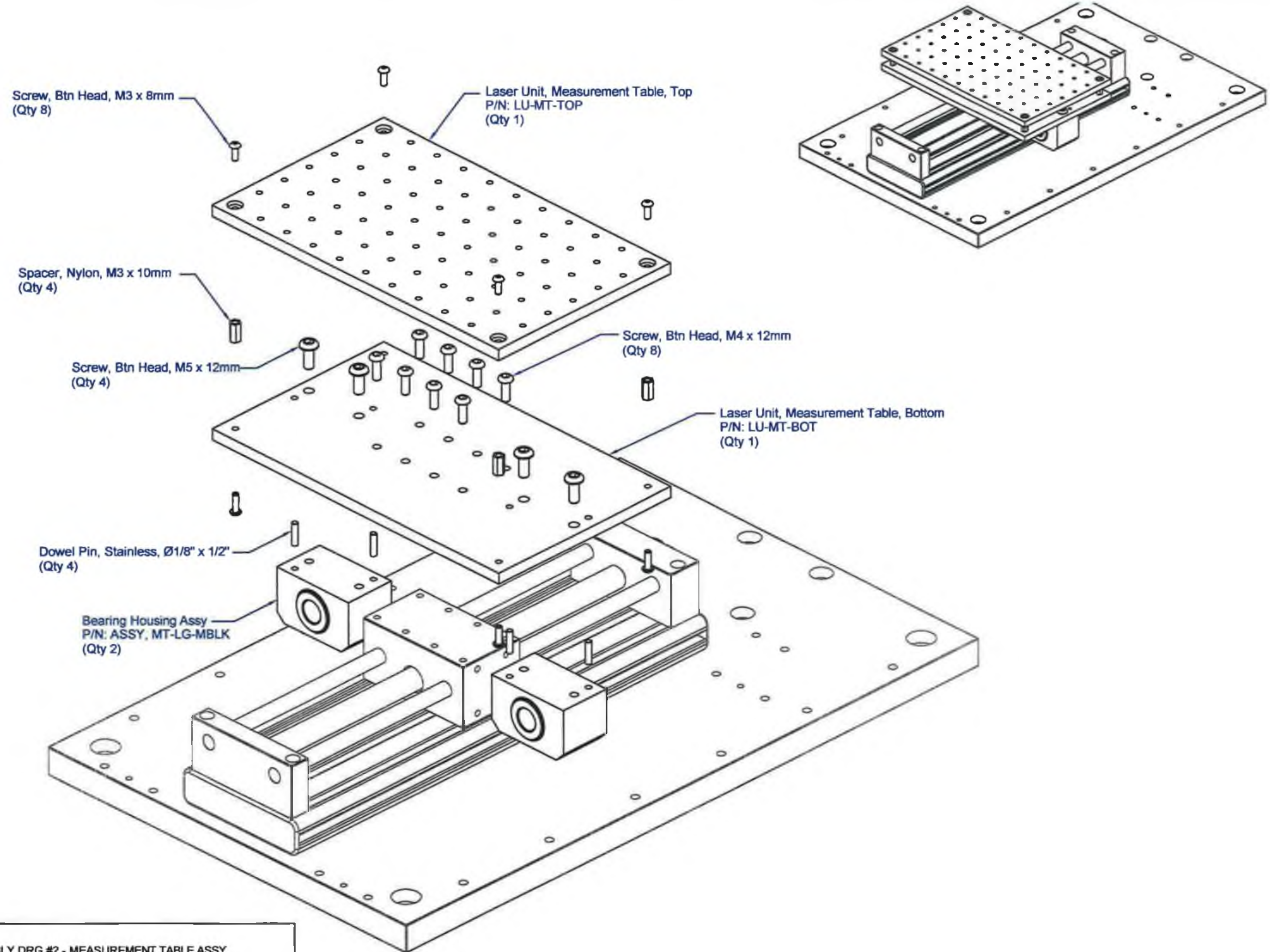

TITLE:
ASSEMBLY DRG #2 - MEASUREMENT TABLE ASSY

DCU DRAWN BY: D.COLLINS DATE: 12/06/03

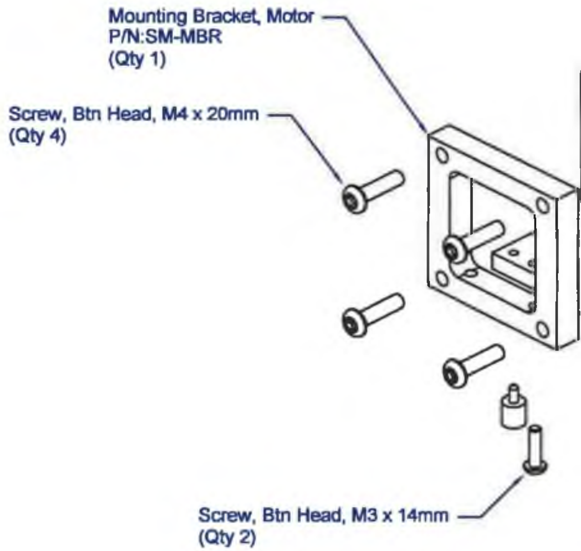

TITLE:
ASSEMBLY DRG #3 - STEPPER MOTOR FRAME ASSY

DRAWN BY: D.COLLINS

DATE: 12/06/03

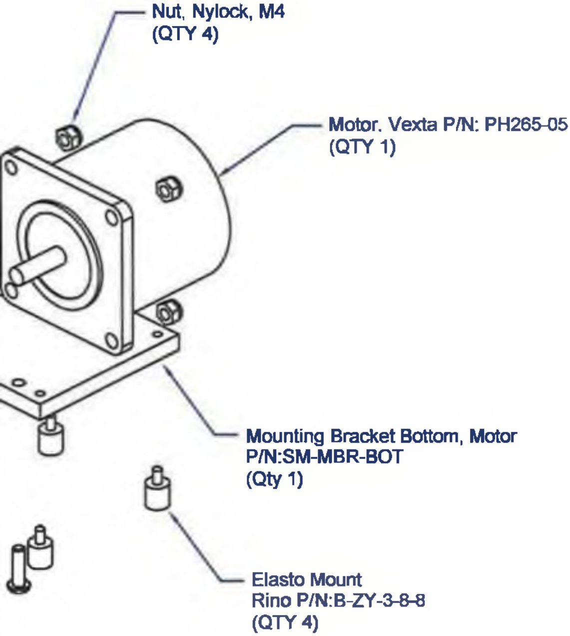
Nut, Nylock, M4
(QTY 4)
Motor. Vexta P/N: PH265-05
(QTY 1)
Mounting Bracket Bottom, Motor
P/N:SM-MBR-BOT
(Qty 1)
Elasto Mount
Rino P/N:B-ZY-3-8-8
(QTY 4)

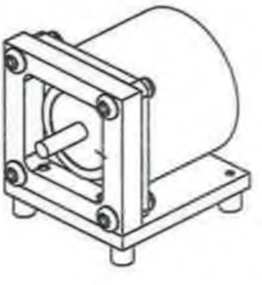

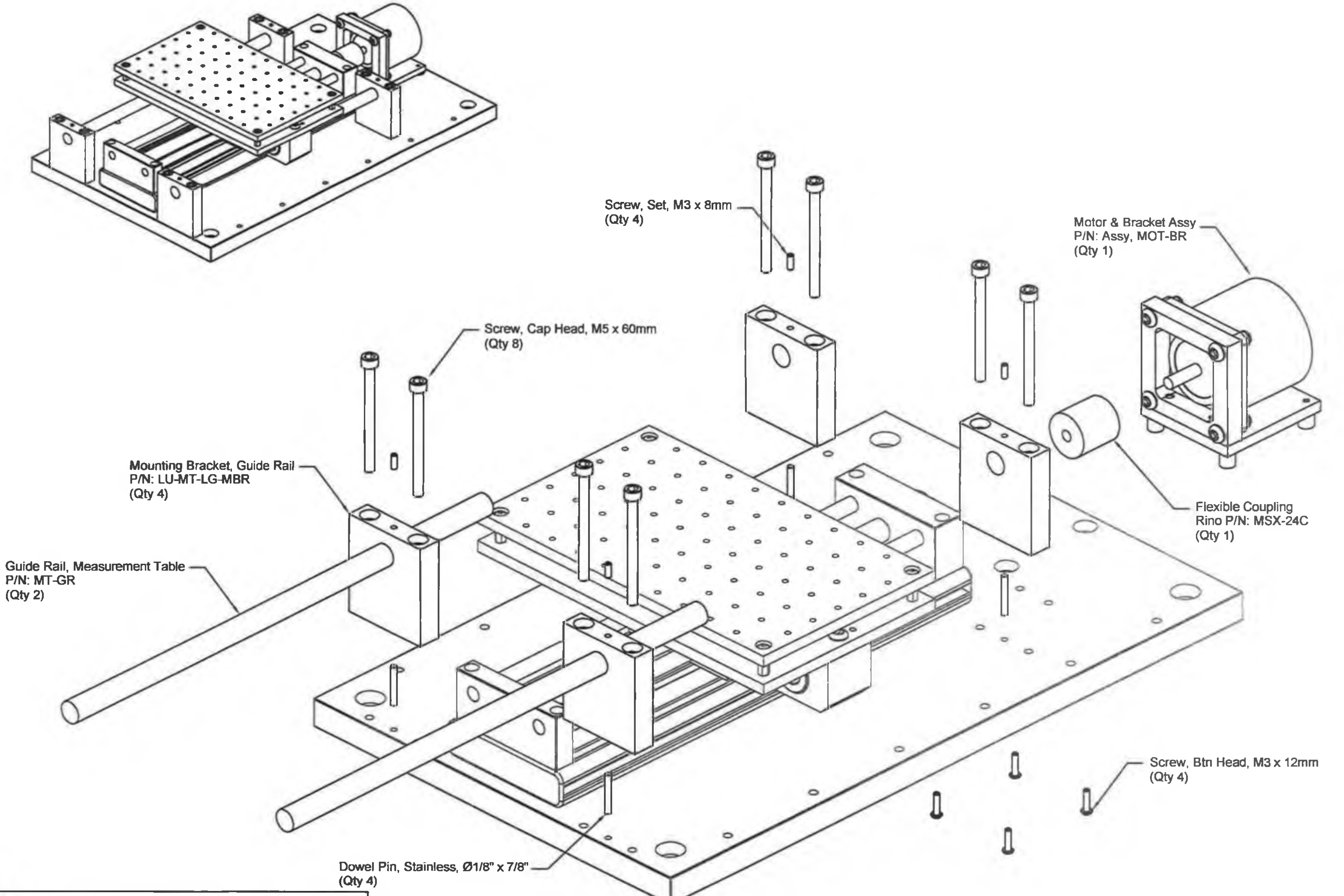

DCU

TITLE:
ASSEMBLY DRG #4 - TABLE GUIDES & Y-AXIS DRIVE MOTOR ASSY

DRAWN BY: D.COLLINS

DATE: 14/06/03

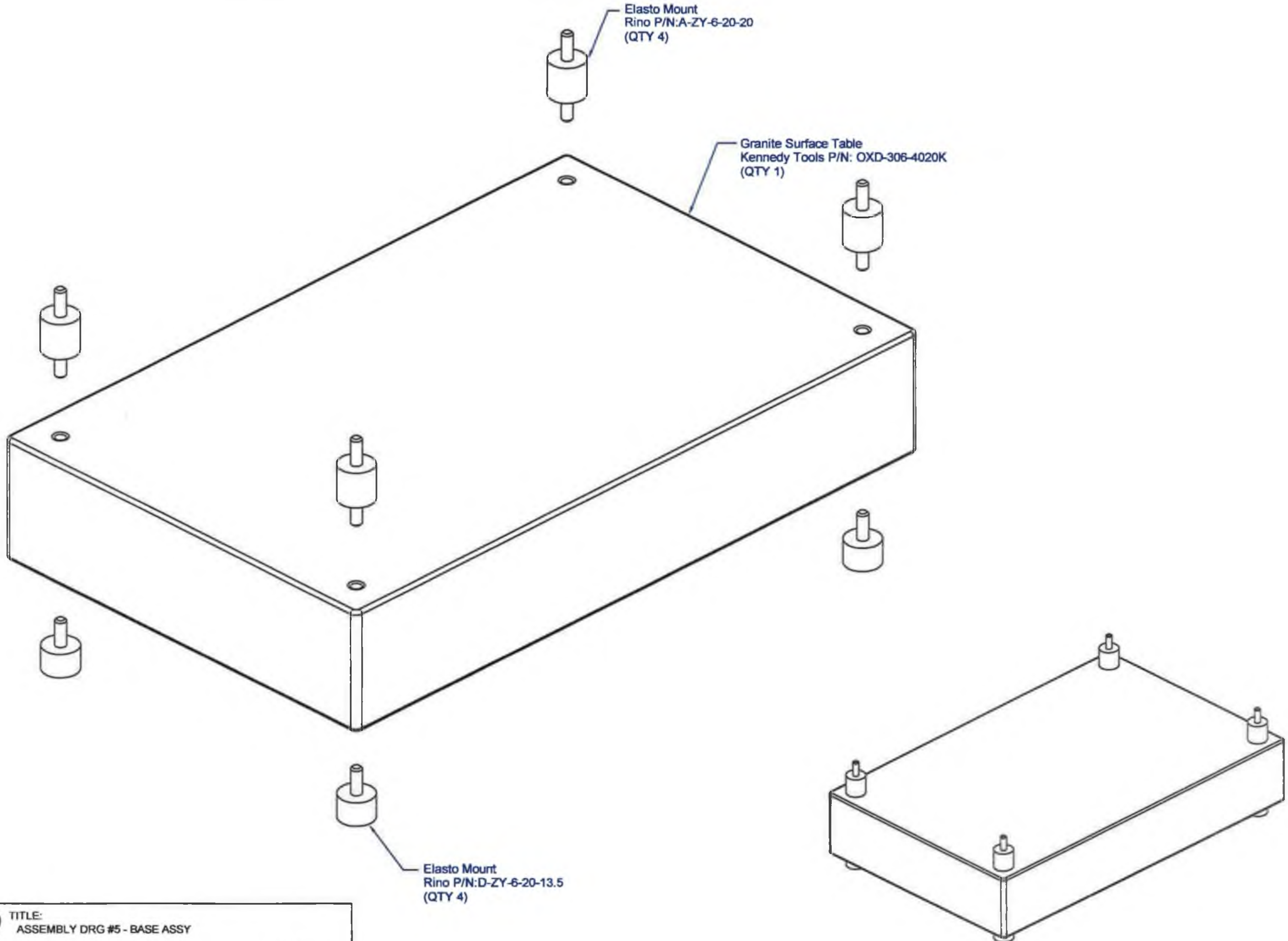

TITLE:
ASSEMBLY DRG #5 - BASE ASSY

DCU DRAWN BY: D.COLLINS DATE: 16/06/03

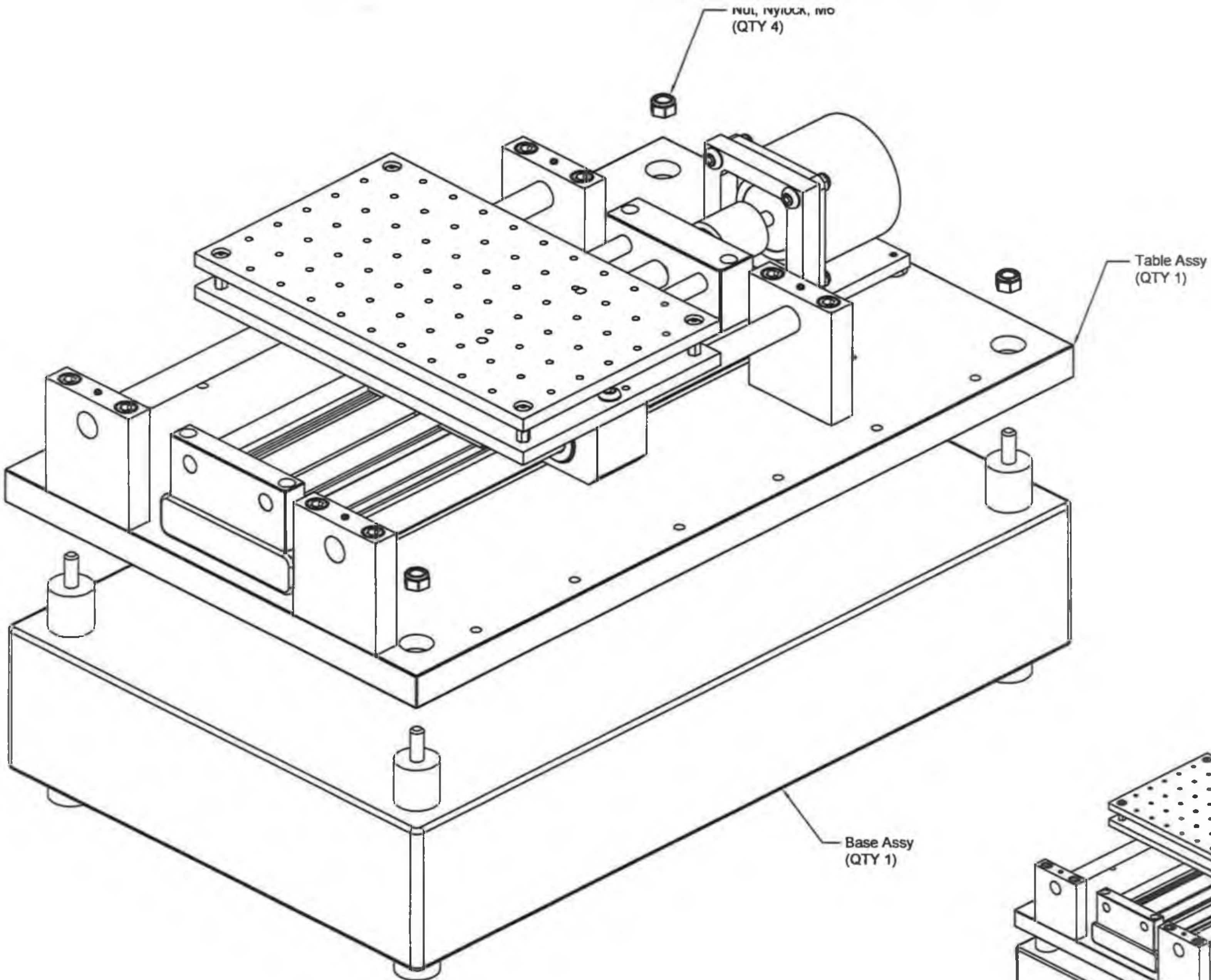

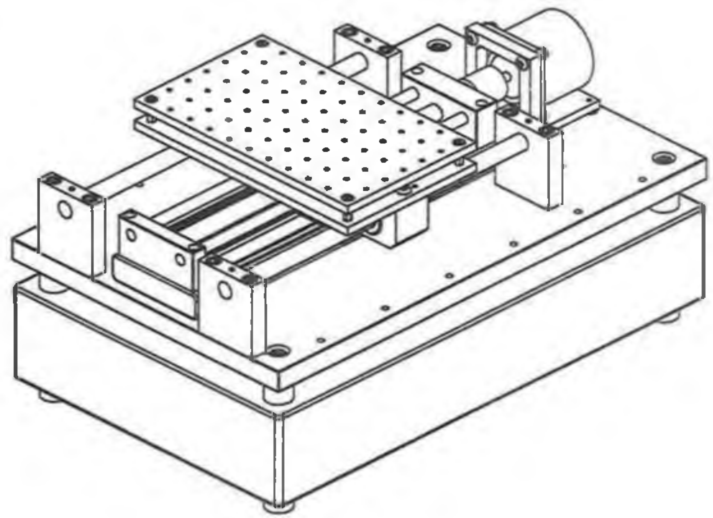

TITLE:
ASSEMBLY DRG #6 - BASE, BOLSTER PLATE & Y-AXIS ASSY

DCU DRAWN BY: D.COLLINS DATE: 17/06/03

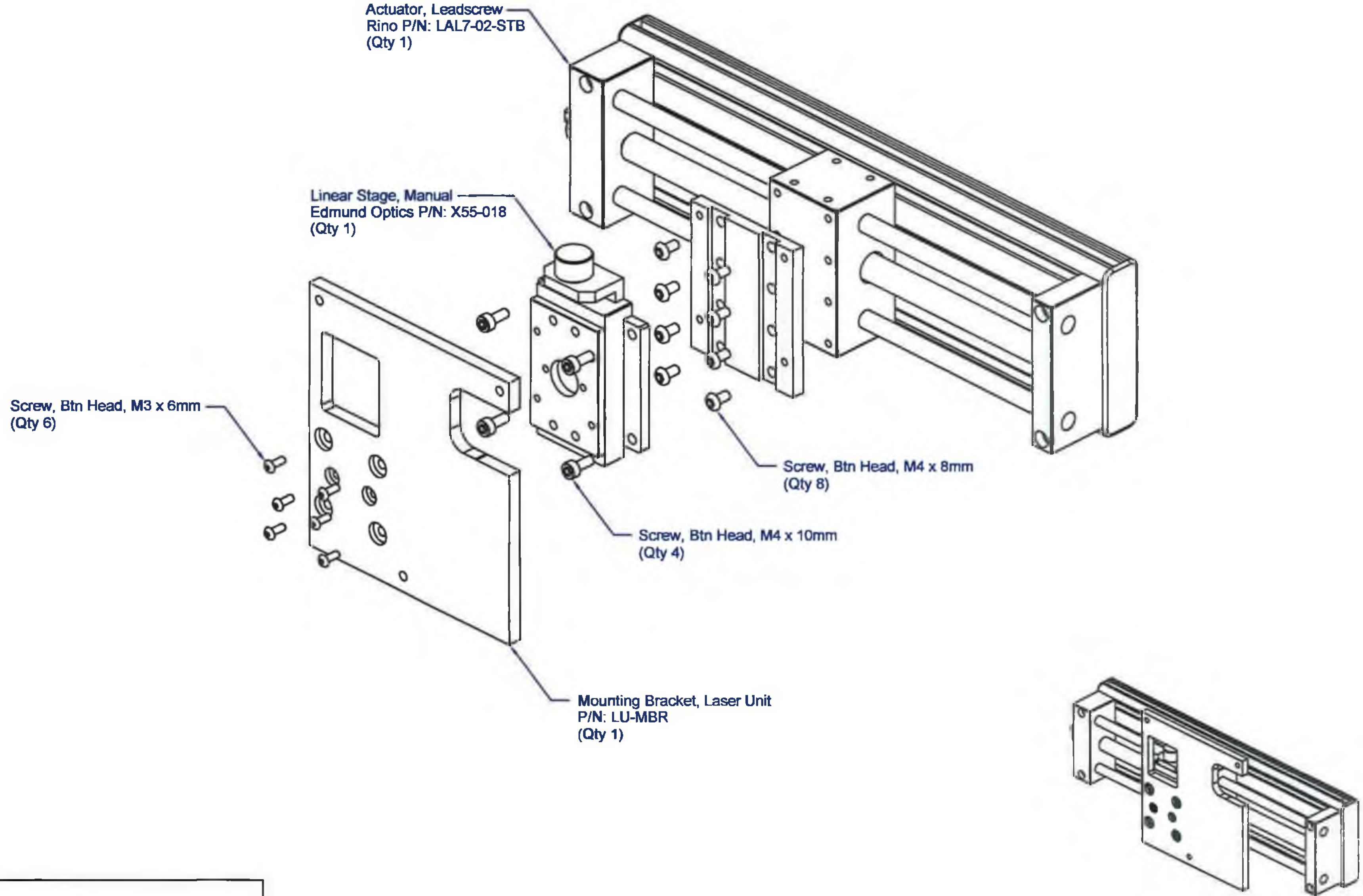

TITLE:
ASSEMBLY DRG #7 - LASER HEAD & X-AXIS ASSY

DCU DRAWN BY: D.COLLINS DATE: 20/06/03

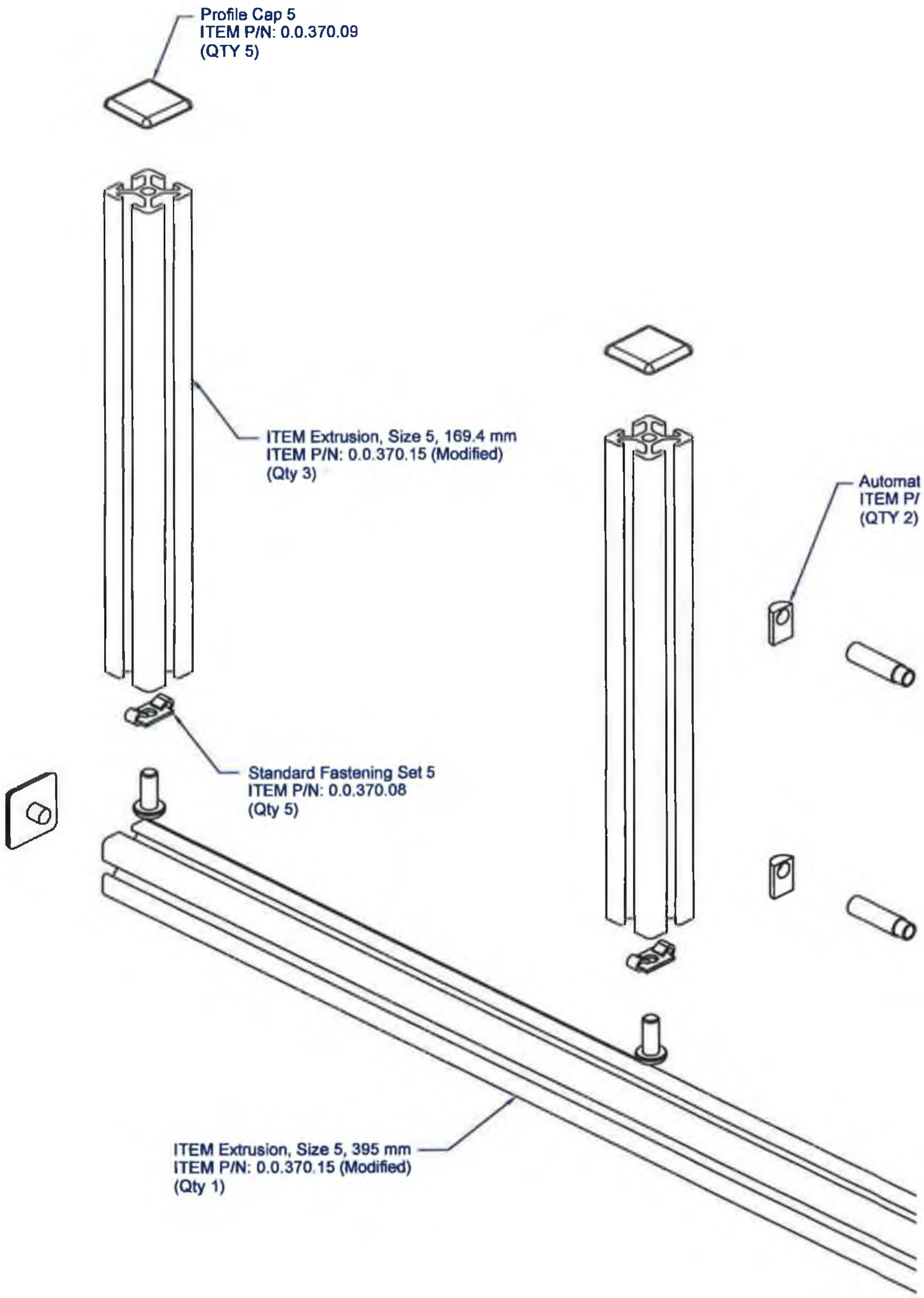

DCU

TITLE:
ASSEMBLY DRG #8 - SIDE FRAME ASSY

DRAWN BY: D.COLLINS

DATE: 22/06/03

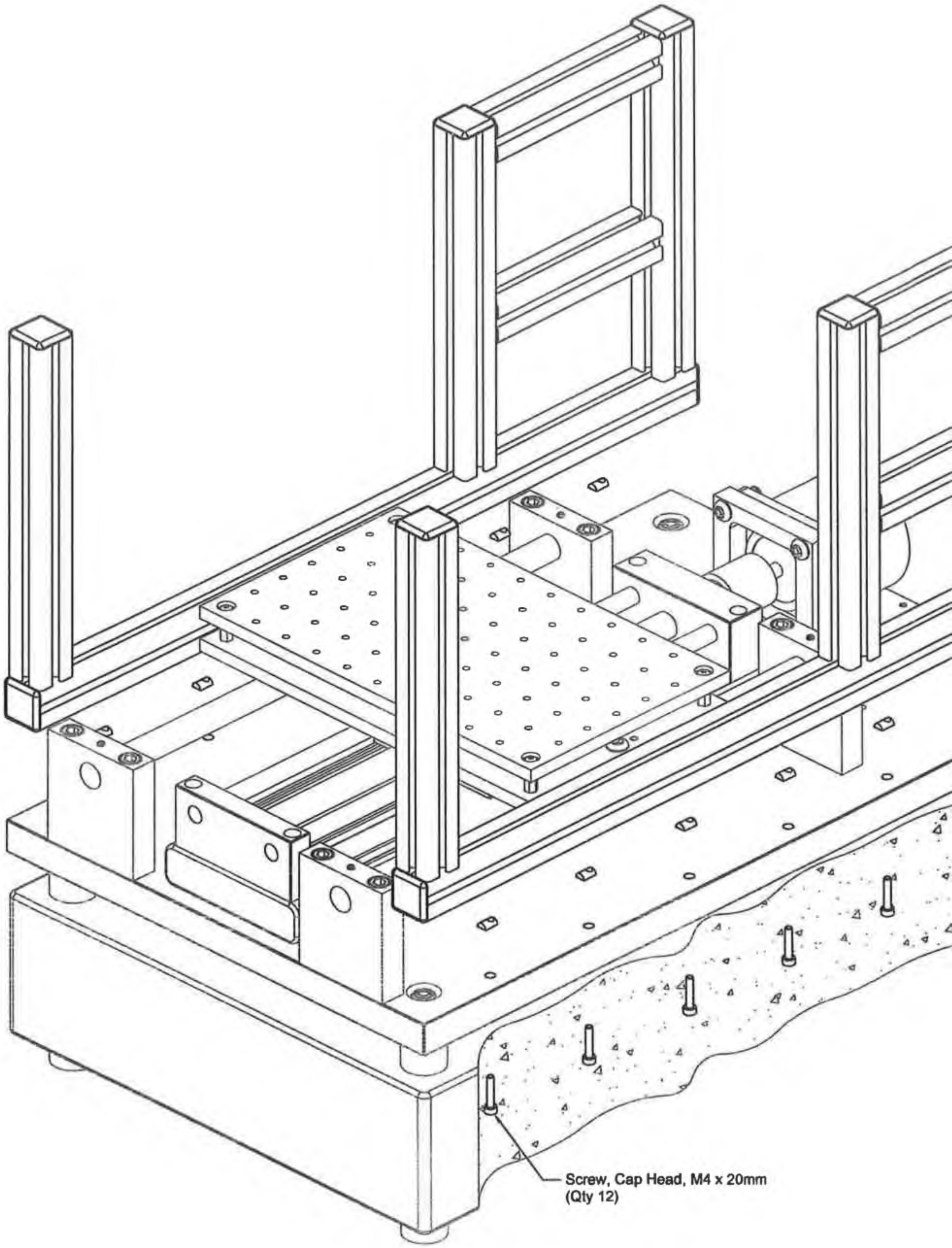

TITLE:
ASSEMBLY DRG #9 - SIDE FRAME & BOTTOM LEVEL ASSY

DCU DRAWN BY: D.COLLINS DATE: 23/06/03

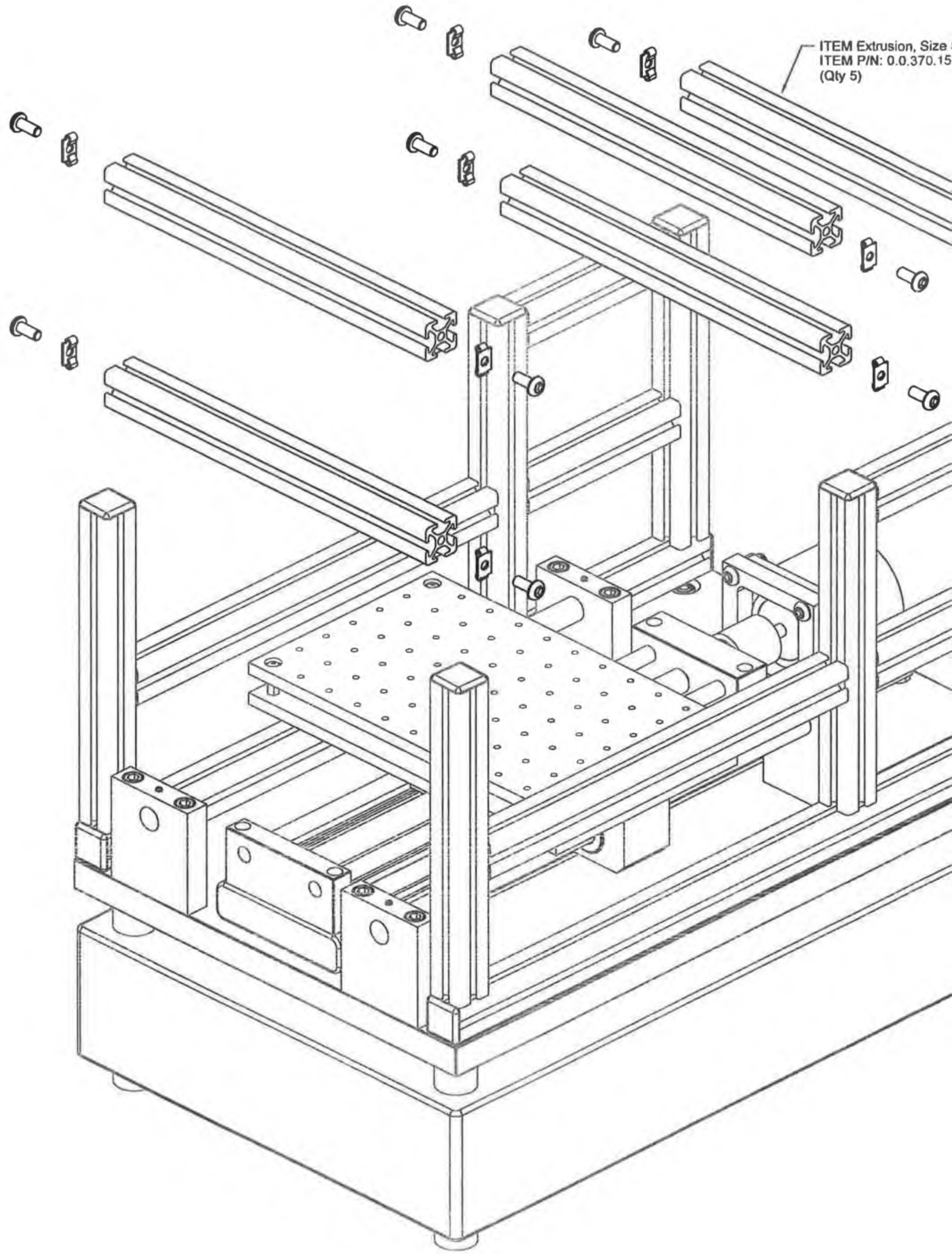

TITLE:
ASSEMBLY DRG #10 - CROSS STRUTS & SIDE FRAME ASSY

DCU DRAWN BY: D.COLLINS DATE: 23/06/03

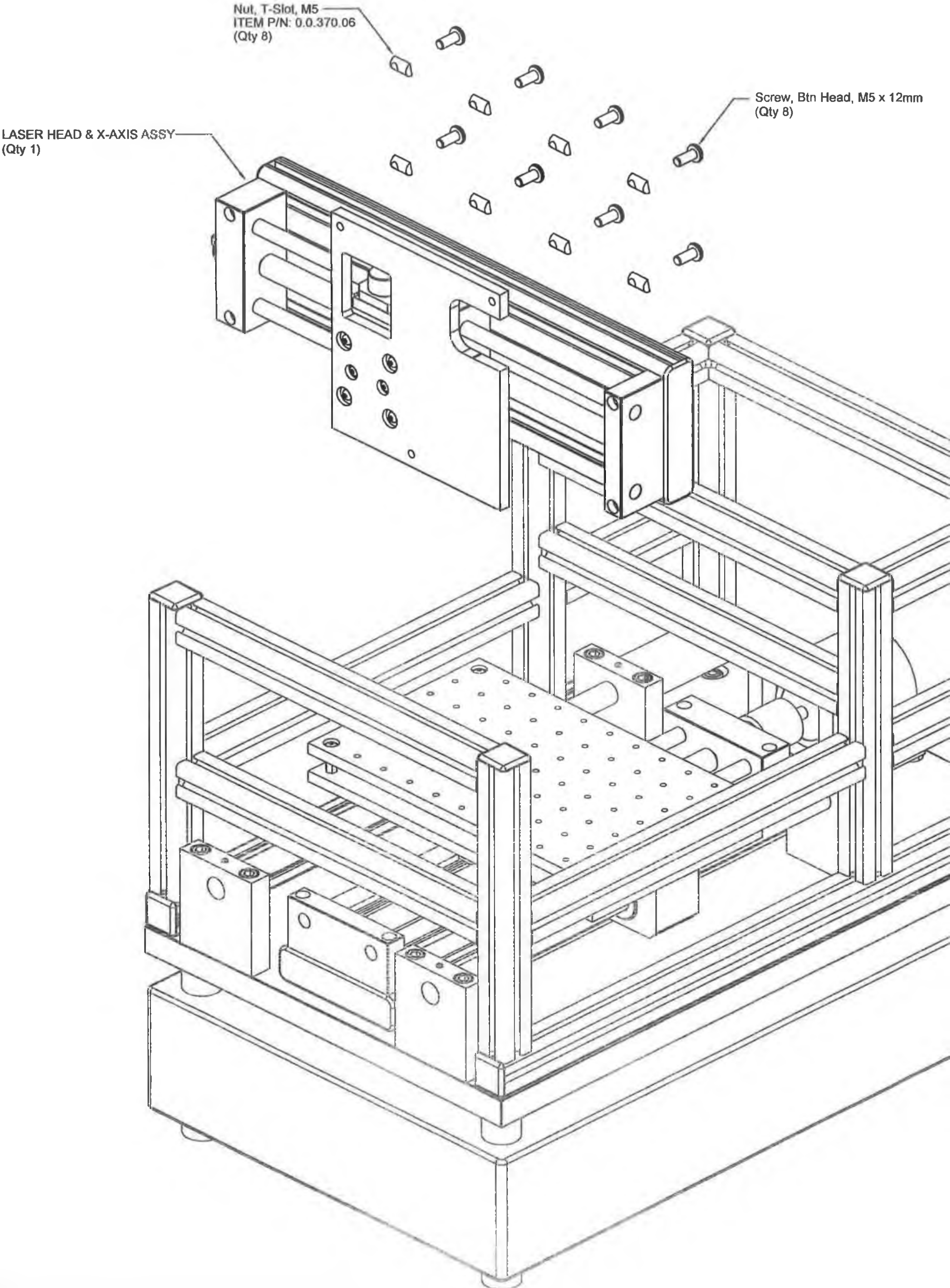

TITLE:
ASSEMBLY DRG #11 - X-AXIS & FRAME ASSY

DRAWN BY: D.COLLINS DATE: 24/06/03

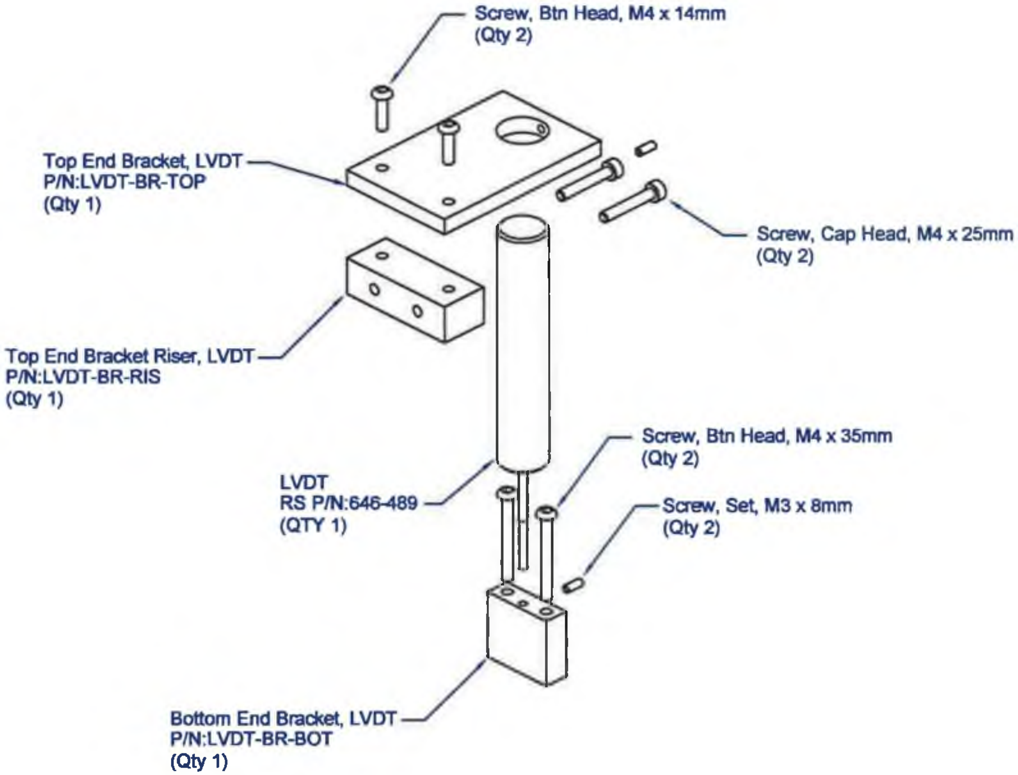

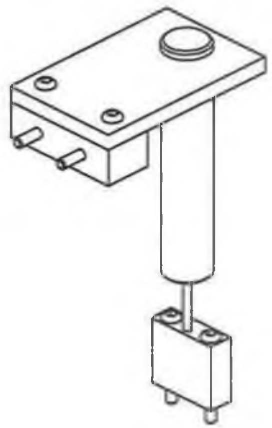

DCU

TITLE:
ASSEMBLY DRG #12 - LVDT ASSY

DRAWN BY: D.COLLINS

DATE: 24/06/03

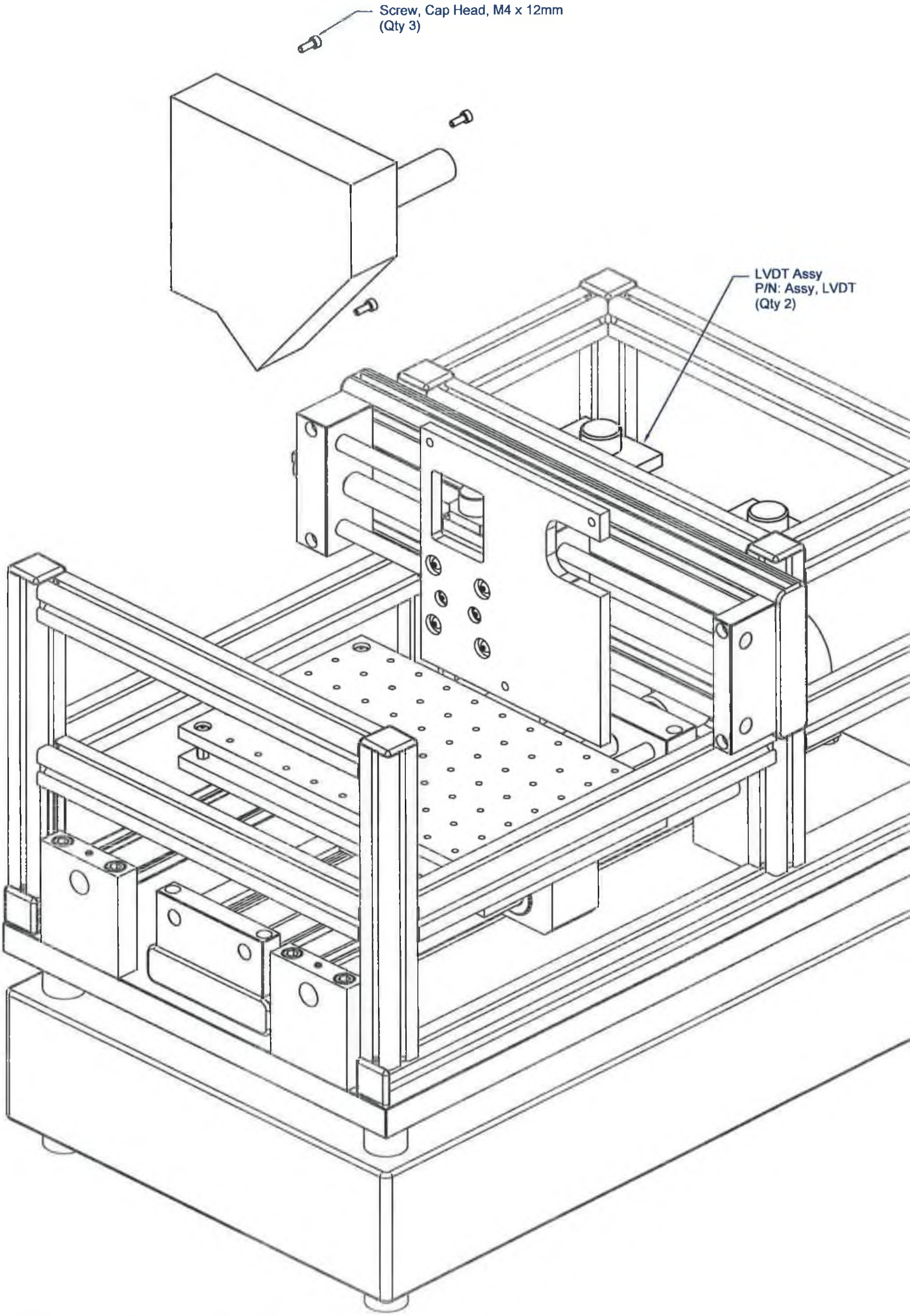

DCU

TITLE:
ASSEMBLY DRG #13 - LASER DISPLACEMENT SENSOR & X-AXIS ASSY

DRAWN BY: D.COLLINS DATE: 24/06/03

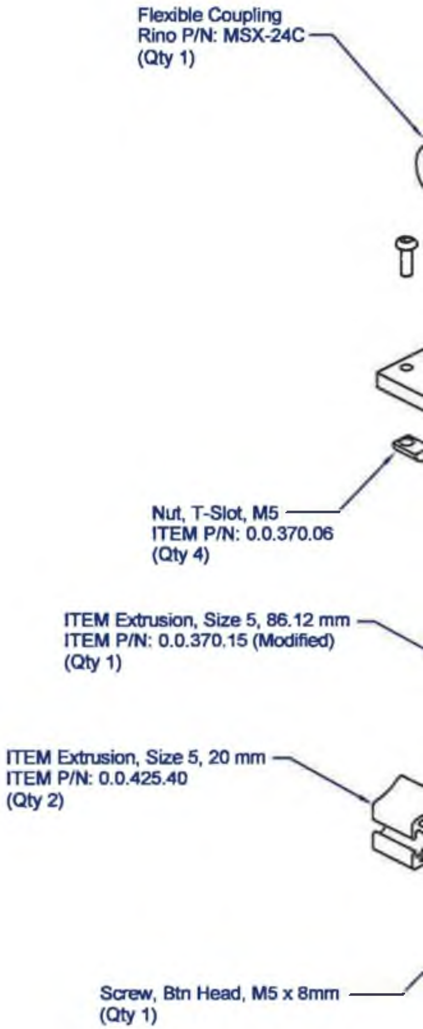

DCU

TITLE:
ASSEMBLY DRG #14 - X-AXIS DRIVE MOTOR ASSY

DRAWN BY: D.COLLINS

DATE: 26/06/03

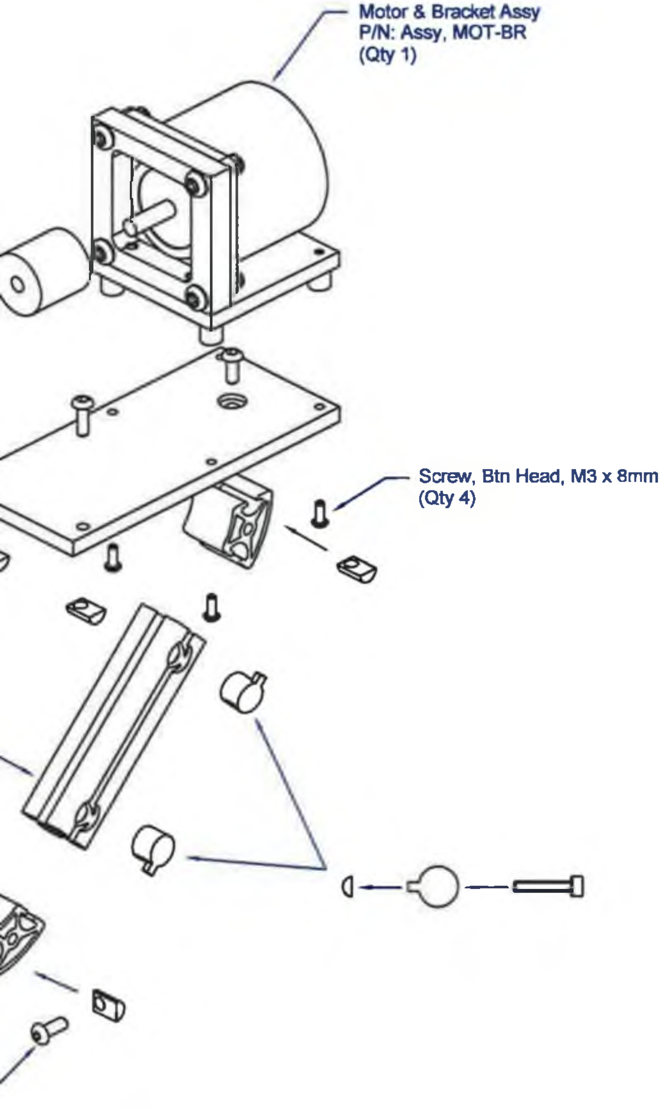
Motor & Bracket Assy
P/N: Assy, MOT-BR
(Qty 1)
Screw, Btn Head, M3 x 8mm
(Qty 4)

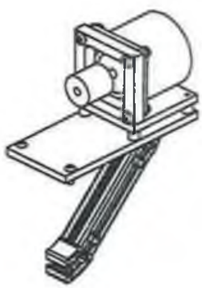

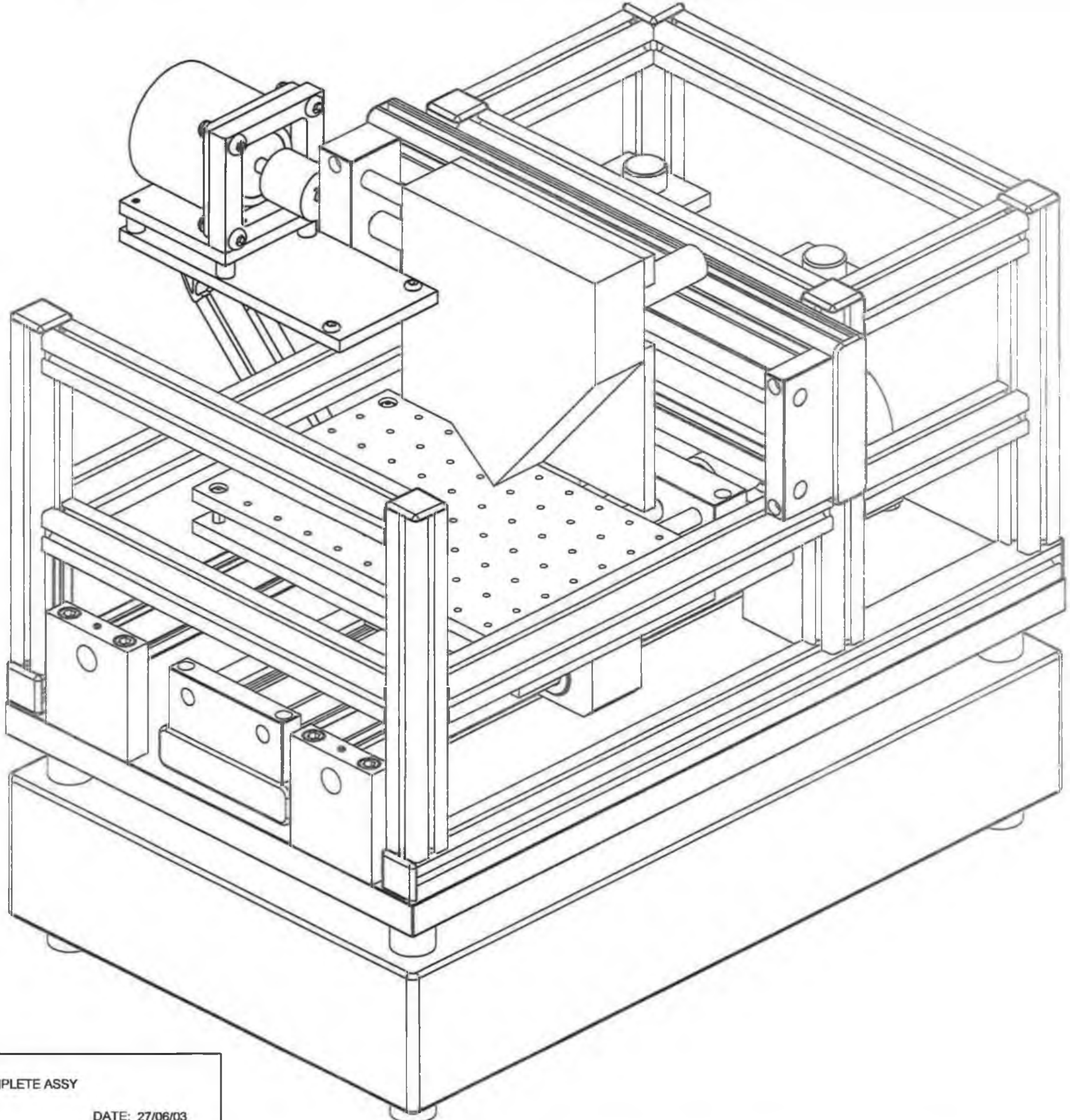

TITLE:
ASSEMBLY DRG #15 - COMPLETE ASSY

DCU DRAWN BY: D.COLLINS DATE: 27/06/03

Appendix F Bill of materials

Part/Description:	Qty
Actuator, Leadscrew, Rino p/n: LAL7-02-STB	2
Automatic Fastening Set, ITEM p/n: 0.0.370.60	4
Bearing Housing Assy, p/n: MT-LG-MBLK	2
Bolster Plate, p/n: ST-BP	1
Dowel Pin, Stainless, Dia1/8" x 1/2"	4
Dowel Pin, Stainless, Dia1/8" x 7/8"	4
Elasto Mount, Rino p/n: B-ZY-3-8-8	8
Elasto Mount, Rino p/n: A-ZY-6-20-20	4
Elasto Mount, Rino p/n: D-ZY-6-20-13.5	4
Extrusion, Size 5, 169.4mm Long, ITEM p/n: 0.0.370.15 (Modified)	6
Extrusion, Size 5, 395mm Long, ITEM p/n: 0.0.370.15 (Modified)	2
Extrusion, Size 5, 100mm Long, ITEM p/n: 0.0.370.15 (Modified)	4
Extrusion, Size 5, 210mm Long, ITEM p/n: 0.0.370.15 (Modified)	5
Extrusion, Size 5, 86.12mm Long, ITEM p/n: 0.0.370.15 (Modified)	1
Extrusion, Size 5, 20mm Long, ITEM p/n: 0.0.425.40 (Modified)	2
Flexible Coupling, Rino p/n: MSX-24C	2
Granite Surface Table, Kennedy p/n: OXD-306-4020K	1
Guide Rail, Measurement Table, p/n: MT-GR	2
LabVIEW DAQ Card, p/n: PCI-6024E	1
LabVIEW DAQ Card, Breakout Box, p/n: SCB-68	1
Linear Stage, Manual, Edmund Optics p/n: X55-018	1
LVDT, RS p/n: 646-489	2
Measurement Table, Top, p/n: LU-MT-TOP	1
Measurement Table, Bottom, p/n: LU-MT-BOT	1
Mounting Bracket, Motor, p/n: SM-MBR	2
Mounting Bracket Bottom, Motor, p/n: SM-MBR-BOT	2
Mounting Bracket, Guide Rail, p/n: LU-MT-LG-MBR	4
Mounting Bracket, Laser Unit, p/n: LU-MBR	1
Motor, Vexta p/n: PH265-05	2
Nut, Nylock, M4	8
Nut, Nylock, M6	4
Nut, T-Slot, M4, ITEM p/n: 0.0.370.06	12
Nut, T-Slot, M5, ITEM p/n: 0.0.370.01	28
Philips 3-to-8 Line Decoder/Demultiplexer; Inverting	1
Profile Cap 5, ITEM p/n: 0.0.370.09	10
Screw, Btn Head, M3 x 6mm	6
Screw, Btn Head, M3 x 8mm	12
Screw, Btn Head, M3 x 12mm	4

Screw, Btn Head, M3 x 14mm	4
Screw, Btn Head, M4 x 8mm	8
Screw, Btn Head, M4 x 10mm	4
Screw, Btn Head, M4 x 12mm	8
Screw, Btn Head, M4 x 14mm	4
Screw, Btn Head, M4 x 20mm	8
Screw, Btn Head, M4 x 35mm	4
Screw, Btn Head, M5 x 8mm	1
Screw, Btn Head, M5 x 12mm	12
Screw, Btn Head, M5 x 22mm	16
Screw, Cap Head, M4 x 12mm	3
Screw, Cap Head, M4 x 20mm	12
Screw, Cap Head, M4 x 25mm	4
Screw, Cap Head, M5 x 60mm	8
Screw, Set, M3 x 8mm	8
Spacer, Nylon, M3 x 10mm	4
Standard Fastening Set 5, ITEM p/n: 0.0.370.08	20
Universal Fastening Set 5, ITEM p/n: 0.0.0370.07	2
Stepper Motor Control Board, IM483	2
Top End Bracket, LVDT, p/n: LVDT-BR-TOP	2
Top End Bracket Riser, LVDT, p/n: LVDT-BR-RIS	2